DSWA-TR-98-7

Technical Report

Vacuum Opening Switch Development

Approved for public release; distribution is unlimited.

November 1999

Prepared for:
Defense Threat Reduction Agency
45045 Aviation Drive
Dulles, VA 20166-7517

DNA001-93-C-0227

Phil Greene, et. al.

Prepared by:
Pulse Sciences, Inc.
600 McCormick Street
San Leandro, CA 94577

CUT HERE AND RETURN

DISTRIBUTION LIST UPDATE

This mailer is provided to enable DTRA to maintain current distribution lists for reports. (We would appreciate you providing the requested information.)

- ❑ Add the individual listed to your distribution list.
- ❑ Delete the cited organization/individual.
- ❑ Change of address.

Note:
Please return the mailing label from the document so that any additions, changes, corrections or deletions can be made easily. For distribution cancellation or more information call DTRA/ADM (703) 325-1036.

NAME: _____

ORGANIZATION: _____

OLD ADDRESS	NEW ADDRESS
_____	_____
_____	_____
_____	_____

TELEPHONE NUMBER: ( ) _____

DTRA PUBLICATION NUMBER/TITLE	CHANGES/DELETIONS/ADDITIONS, etc.) *(Attach Sheet if more Space is Required)*
_____	_____
_____	_____
_____	_____

DTRA or other GOVERNMENT CONTRACT NUMBER: _____

CERTIFICATION of NEED-TO-KNOW BY GOVERNMENT SPONSOR (if other than DTRA):

SPONSORING ORGANIZATION: _____

CONTRACTING OFFICER or REPRESENTATIVE: _____

SIGNATURE: _____

DEFENSE THREAT REDUCTION AGENCY
ATTN: ADM
45045 AVIATION DRIVE
DULLES, VA 20166-7517

DEFENSE THREAT REDUCTION AGENCY
ATTN: ADM
6810 TELEGRAPH ROAD
ALEXANDRIA, VA 22310-3398

REPORT DOCUMENTATION PAGE

Form Approved OMB No. 0704-0188

1. AGENCY USE ONLY *(Leave blank)*	2. REPORT DATE	3. REPORT TYPE AND DATES COVERED
	NOVEMBER 1999	Technical 930930 - 970831

4. TITLE AND SUBTITLE

Vacuum Opening Switch Development

5. FUNDING NUMBERS

C - DNA 001-93-C-0227
PE - 4662
PR - AB
TA - AJ
WU - DH00014

6. AUTHOR(S)

Phil Greene, Sid Putnam, Phil Spence, Joe Lidestri, John Goyer (PSI), Tom Hughes and Tom Genoni (MRC)

7. PERFORMING ORGANIZATION NAME(S) AND ADDRESS(ES)

Pulse Sciences, Inc.
600 McCormick Street
San Leandro, CA 94577

8. PERFORMING ORGANIZATION REPORT NUMBER

PSIFR-2700-01

9. SPONSORING/MONITORING AGENCY NAME(S) AND ADDRESS(ES)

Defense Special Weapons Agency
6801 Telegraph Road
Alexandria, VA 22310-3398

EST/Ware

10. SPONSORING/MONITORING AGENCY REPORT NUMBER

DSWA-TR-98-7

11. SUPPLEMENTARY NOTES

This work was sponsored by the Defense Special Weapons Agency under RDT&E RMC Code B 4662 D GE 00014 3300 A AB 25904D.

12a. DISTRIBUTION/AVAILABILITY STATEMENT

Approved for public release; distribution is unlimited.

12b. DISTRIBUTION CODE

13. ABSTRACT *(Maximum 200 words)*

Results are present from an experimental and theoretical investigation of the operation of the Density Controlled Opening Switch (DCOS), a potential long conduction time opening switch candidate for induction store drivers of advanced high current simulators. The DCOS has two conduction modes of practical interest: a self-opening mode and a mode suitable for control of opening by external gating of the injected ion source. With available experimental hardware these modes were studied with conduction times $\lesssim$ 2 ms, electron current densities up to 2000 A/cm2 and total currents up to ~200 kA. Scaling models for both modes were developed incorporating results of experiments and simulations. The drop of switch impedance observed at later times was identified as due to radial expansion of the current channel rather than gap closure by density electrode plasmas. A second task of the program demonstrated efficient power coupling to a load through an opened low density erosion switch on the DECADE-2 module.

14. SUBJECT TERMS		15. NUMBER OF PAGES
Inductive Energy Stores	Plasma Erosion Opening Switch	200
Vacuum Opening Switch		16. PRICE CODE
Density Controlled Opening Switch		

17. SECURITY CLASSIFICATION OF REPORT	18. SECURITY CLASSIFICATION OF THIS PAGE	19. SECURITY CLASSIFICATION OF ABSTRACT	20. LIMITATION OF ABSTRACT
UNCLASSIFIED	UNCLASSIFIED	UNCLASSIFIED	SAR

CLASSIFIED BY:

N/A since Unclassified

DECLASSIFY ON:

N/A since Unclassified

PERFORMING ORGANIZATION NAME(S) AND ADDRESS(ES) (Continued):

Mission Research Corporation
735 State Street
Santa Barbara, CA 93101

PREFACE

The experimental work on the Density Controlled Opening Switch (DCOS) was conducted by Joseph Lidestri during the first year of the program. Mr. Lidestri is currently with the Department of Biochemistry and Molecular Biophysics at Columbia University, New York. Philip Greene continued the experimental DCOS work until its conclusion. Assistance in magnetic field coil design by Vernon Bailey of Pulse Sciences, Inc. is gratefully acknowledged. The power flow task on DECADE MODULE 2 at Primex Physics International was performed by Philip Spence, Philip Greene and John Goyer. Dr. Goyer is currently with Maxwell Technologies, Inc. in San Diego, CA.

CONVERSION TABLE

Conversion factors for U.S. Customary to metric (SI) units of measurement.

MULTIPLY → / ← TO GET	BY → / ← BY	TO GET → / ← DIVIDE
angstrom	1.000 000 X E -10	meters (m)
atmosphere (normal)	1.013 25 X E +2	kilo pascal (kPa)
bar	1.000 000 X E +2	kilo pascal (kPa)
barn	1.000 000 X E -28	meter^2 (m^2)
British thermal unit (thermochemical)	1.054 350 X E +3	joule (J)
calorie (thermochemical)	4.184 000	joule (J)
cal (thermochemical/cm^2)	4.184 000 X E -2	mega joule/m^2 (MJ/m^2)
curie	3.700 000 X E +1	*giga becquerel (GBq)
degree (angle)	1.745 329 X E -2	radian (rad)
degree Fahrenheit	t_k = (t°f + 459.67)/1.8	degree kelvin (K)
electron volt	1.602 19 X E -19	joule (J)
erg	1.000 000 X E -7	joule (J)
erg/second	1.000 000 X E -7	watt (W)
foot	3.048 000 X E -1	meter (m)
foot-pound-force	1.355 818	joule (J)
gallon (U.S. liquid)	3.785 412 X E -3	meter^3 (m^3)
inch	2.540 000 X E -2	meter (m)
jerk	1.000 000 X E +9	joule (J)
joule/kilogram (J/kg) radiation dose absorbed	1.000 000	Gray (Gy)
kilotons	4.183	terajoules
kip (1000 lbf)	4.448 222 X E +3	newton (N)
kip/inch^2 (ksi)	6.894 757 X E +3	kilo pascal (kPa)
ktap	1.000 000 X E +2	newton-second/m^2 (N-s/m^2)
micron	1.000 000 X E -6	meter (m)
mil	2.540 000 X E -5	meter (m)
mile (international)	1.609 344 X E +3	meter (m)
ounce	2.834 952 X E -2	kilogram (kg)
pound-force (lbs avoirdupois)	4.448 222	newton (N)
pound-force inch	1.129 848 X E -1	newton-meter (N·m)
pound-force/inch	1.751 268 X E +2	newton/meter (N/m)
pound-force/foot^2	4.788 026 X E -2	kilo pascal (kPa)
pound-force/inch^2 (psi)	6.894 757	kilo pascal (kPa)
pound-mass (lbm avoirdupois)	4.535 924 X E -1	kilogram (kg)
pound-mass-foot^2 (moment of inertia)	4.214 011 X E -2	kilogram-meter^2 (kg·m^2)
pound-mass/foot^3	1.601 846 X E +1	kilogram/meter^3 (kg/m^3)
rad (radiation dose absorbed)	1.000 000 X E -2	**Gray (Gy)
roentgen	2.579 760 X E -4	coulomb/kilogram (C/kg)
shake	1.000 000 X E -8	second (s)
slug	1.459 390 X E +1	kilogram (kg)
torr (mm Hg, 0° C)	1.333 22 X E -1	kilo pascal (kPa)

*The becquerel (Bq) is the SI unit of radioactivity; 1 Bq = 1 event/s.
**The Gray (GY) is the SI unit of absorbed radiation.

TABLE OF CONTENTS

TABLE OF CONTENTS (continued)

FIGURES

FIGURES (continued)

FIGURES (continued)

FIGURES (continued)

FIGURES (concluded)

TABLES

SECTION 1
INTRODUCTION

This report presents the results of the Advanced Switch Study Program at Pulse Sciences, Inc. (PSI). Most of the effort of the program was devoted to the operation and scaling of the Density Controlled Opening Switch (DCOS) concept for potential applications to long-conduction-time opening switches ($\gtrsim$ 1 μsec) of advanced simulators. A second part of the program addressed load power coupling through an opening switch for near-term applications to the DECADE simulator development and involved experiments on the DECADE MODULE-2 (DM-2). The DM-2 experiments demonstrated efficient load coupling and practically useful results for plasma radiation source development for the DECADE simulator. The DCOS studies achieved current density goals and conduction currents in the 100 kA range with up to 2 μsec time durations for conduction, opening and high impedance before re-strike. A conduction mode suitable for external control of opening was obtained, a new mechanism for the impedance drop of the switch was identified, and models for scaling the self-opening and gating modes were developed. Although considerable progress in understanding the DCOS operation was made and the switch remains a promising candidate for long conduction time applications, some empirical aspects still remain to be resolved before the switch can be a priori engineered with confidence.

1.1 BACKGROUND.

The original concept for DCOS was developed at PSI in 1985 and was based on the realization that opening switches required to fully exploit the advantages of an induction store/vacuum opening switch simulator design would need to conduct for long times (e.g., several microseconds or more) and open over timescales of 100 nsec or so -- timescales differing by more than an order of magnitude. It was felt that these requirements would be difficult to achieve with a single plasma condition determined at the start of conduction. The DCOS idea is basically to use an externally gated ion source with ion currents injected that are needed to support the peak current levels during conduction, followed by an externally triggered rapid reduction in the ion current to open the switch, as could be obtained with magnetic or other gating techniques. This approach in principle decouples the conduction time dynamics from the opening phase. A sketch of the DCOS concept is given in Figure 1-1 which also shows a coupling arrangement for a ring diode load. In Figure 1-2 a possible arrangement for integration of DCOS switches in a radial transmission line feed section near the load region of an advanced simulator is shown. Both of these figures illustrate a potentially important feature of DCOS -- the load current does not flow through the switch and no plasma is ejected from the switch into the load region.

A first study of the DCOS was funded at PSI by the Defense Nuclear Agency a decade ago and gave a surprising result; namely, the discovery of a natural or self-opening

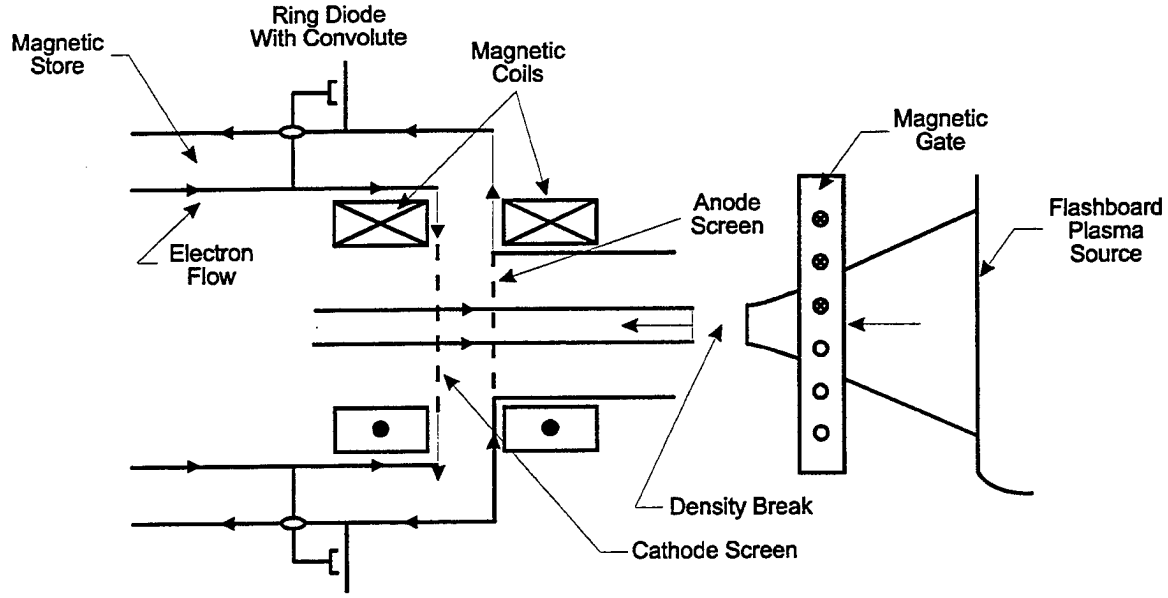

Figure 1-1. Illustration of the DCOS concept.

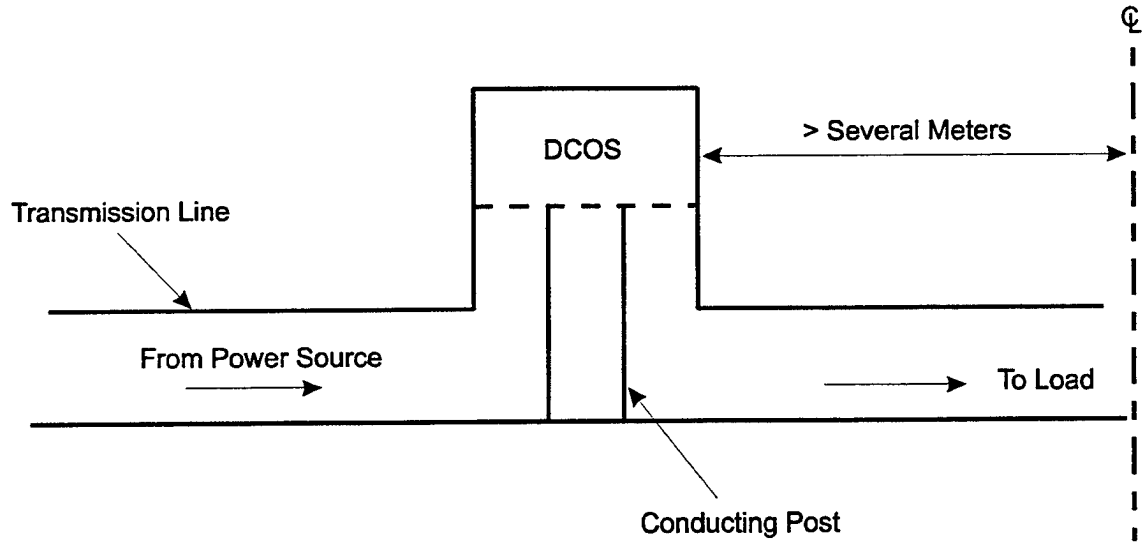

Figure 1-2. Possible arrangement of an individual switch of an azimuthal array of DCOS switches in a simulator.

mode with conduction times of $\gtrsim$1 μsec at currents of ~100 kA[1]. Other accomplishments of the program were demonstration of the DCOS concept at low ion and electron current densities and demonstration of a magnetic gating technique. Theoretical support for the program was subcontracted to Dr. Robert Kares, then of Berkeley Research Associates, who began one-dimensional numerical simulations of the DCOS. His work in the program showed another unanticipated result -- an opening mechanism essentially due to heating of the background plasma electrons by the space-charge-limited electrons emitted from the cathode[2]. The heating was postulated to be due to a two-stream instability at the time. The heated background electrons tend to stream out of the gap to the anode, leaving a net positive charge to restrict the background electron flow, similarly to what happens in the plasma-in-a-box problem. The net positive charge in the gap in turn raises the potential in the gap above the anode potential (a potential hump), thereby reducing or shutting off the injected ion flow since the ions are injected at anode potential. Ions stream out of the gap toward the anode and cathode, and the gap opens. This work was met with some skepticism in the community at the time, but spawned several additional studies by Kares and the Naval Research Laboratory group[3]. Certainly, the opening mechanism discovered by Kares is one that will happen, provided the background electrons are adequately heated in interacting with the emitted or current carrying electrons.

Though not the original DCOS concept, a natural opening mechanism can provide an ideal switch if understood and scalable to desired parameter regimes. On the other hand, external gating or control of the conduction time remains attractive and has possible advantages for synchronization of an array of switches as might be required by large high current simulators.

1.2 OUTLINE OF PROGRAM.

The objective of the program was basically to obtain a better understanding of the DCOS, both in the natural opening mode and in one suitable for external gating, and assess the scalability of the switch to advanced simulator applications. The program was specifically directed toward long conduction times (> 1 μsec) which were of interest for advanced simulator designs at the time of contract award. The program proposed to use the hardware from the previous program with refurbishment and some modifications, so the highest total current levels achievable were in the 100-200 kA range and driving voltages $\lesssim$ 50 kV. The program was also limited to electrical and relatively simple plasma diagnostics (B-dot and Langmuir probes, ion collectors); no funding was included for spectroscopy or interferometric diagnostics. In any case, these electrical and plasma diagnostics had not been fully exploited in the original program and were able to provide considerably more understanding of the switch operation than existed.

(1) L. Demeter, et al., Vacuum Opening Switch Technology Development, DNA-TR-89-277, July 1991, Defense Nuclear Agency, Alexandria, VA 22310-3398.
(2) R. Kares, J. Appl. Phys. 71, 2155 (1992).
(3) R. Kares, et al., J. Appl. Phys. 71, 2168 (1992).

The original program had demonstrated control of conduction current by the injected ion current over a 7 μsec time scale with low total current and peak electron current density, j_e, of ~120 A/cm^2, but with evidence of cathode emission limitations. Simulator scaling suggested that $j_e \gtrsim 1000$ A/cm^2 is required to integrate DCOS in a sufficiently compact form for a practical simulator. The overall program plan was to start with low j_e and ion-current density, j_i, and then scale the electron current density to practical levels. This work was first conducted using a glass cross hardware for visual access, starting with a 90° bend to transport the plasma to the switch gap and eliminate any neutrals from the plasma flashboard surface. The hardware was also used to study basic switch issues such as cathode emission limitations and transparency of electrode meshes with both positive and negative biases. A gated micro-channel plate camera was implemented with the glass cross to infer plasma motion. The maximum j_i obtainable with the bend was ~ 6 A/cm^2 and total currents in this configuration were limited to $\lesssim$ 2 kA. The bend was then removed and j_i ~100 A/cm^2 was obtained with total currents up to ~25 kA. With the bend removed, j_e ~ 2000 A/cm^2 was achieved in the opening mode. Finally, the experiments were moved to a coaxial metallic switch chamber and a larger bank with both flashboard and coaxial gun sources to operate with total currents $\lesssim$ 200 kA.

A key issue of current density scaling was electrode plasma generation and motion which should be dependent on electron and ion current densities or fluences on the electrodes. Aside from electrode plasma generation, other issues of current density scaling were cathode emission limitations, formation of potential humps and shut-off of ion flow (which should be dependent upon the j_e/j_i ratio) and the actual attainable j_e/j_i ratio itself.

There were several issues pertinent to scaling of the total current: (1) effects of the inductive electric field on the potential distribution across the gap during the rise of current in the two low impedance conduction modes of primary interest, (2) the minimum levels of external longitudinal magnetic fields necessary to preserve switch operation and MHD stability of the discharge, and (3) current penetration of the higher density plasma channels. Scaling studies were conducted at several current levels to characterize the effects of plasma cross-section, gap length, magnetic field level, ion source profiles, and electrode boundary conditions (meshes).

A conduction mode suitable for external gating was not obtained until near the end of the experimental program. Since there was no assurance that the power-coupling-to-a-load task could be successfully achieved within the remaining funds, it was suggested to the sponsor that the power-coupling task be directed toward more immediately relevant interests of the current DSWA simulator development program. It was proposed that a plasma erosion opening switch (PEOS) operating in the lower density regimes of DCOS be tested on DM-2 to investigate improved power coupling

to a load. The switch was designed to operate in the bi-polar or modified bi-polar modes as opposed to the magneto-hydrodynamic (MHD) or electromagneto-hydrodynamic (EMH) regimes of the opening switches of DM-1[4]. Additionally, successful results in reducing the DM-2 current risetime would provide a very useful technique to simply and inexpensively reduce the current risetime to near peak current for a plasma radiation source (PRS) load, should the direct drive implosion time be too long for high quality pinches. The suggestion was approved and the last task of the program was conducted on DM-2 at Primex Physics International.

1.3 PROGRAM RESULTS.

1.3.1 DCOS Results.

Two low impedance conduction modes of practical interest were investigated in the program. In these modes the gap impedance is low during conduction as desired, and the voltage across the gap is largely inductive during the risetime of the current. The first mode exhibited self-opening after conduction times from 200 - 900 nsec for parameters of the experiments; Figure 1-3(a) is an example of such a mode obtained with the metallic coaxial system driven by the large bank charged to 30 kV, a cable gun as the ion source, and anode aperture radius of 5.1 cm. The figure shows curves of the current (I_{AK}) and voltage across the switch, V_{AK}. The current rises to 80 kA over ~ 900 nsec, followed by an opening with a peak current fall rate ~ 4.4 times faster than the current rise rate during conduction, giving a peak voltage during opening of ~ 60 kV. [This voltage is measured at an upstream monitor position which is directly appropriate for connection to a load circuit.] The "opened" current is reduced to 25% of the peak conduction current and persists for ~ 0.5 μsec. The other low impedance conduction mode is suitable for external gating and was obtained when the larger flashboard was moved closer to the anode than with opening modes. Figure 1-3(b) shows such a mode with a 30 kV charging voltage where the current rises to ~ 95% of the peak current (~ 175 kA) over ~ 1.5 μsec and the gap "resistive" voltage at that time is ~ 10 kV for nearly another 0.5 μsec.

A high impedance mode was also observed typically when the voltage was applied at early times ($\lesssim$ 1.5 μsec) after the injected plasma had reached the cathode and the injected ion current density was low ($\lesssim$ 5 A/cm^2). In this mode the current was clamped or slowly rising over 1-2 μsec, roughly following the injected ion current, and the voltage across the gap was nearly the charging voltage.

(4) B. Weber, et al., Physics of Plasmas 2 (10), 3893 (1995).

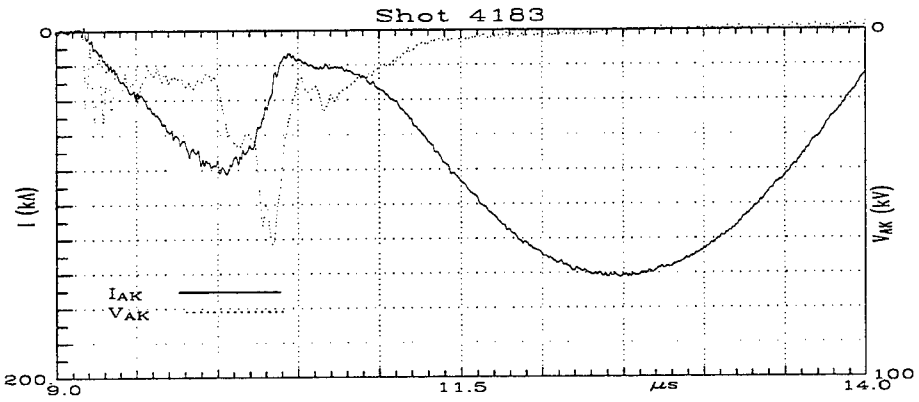

Figure 1-3(a). Self-opening switch mode with -30 kV charging voltage and cable gun ion source.

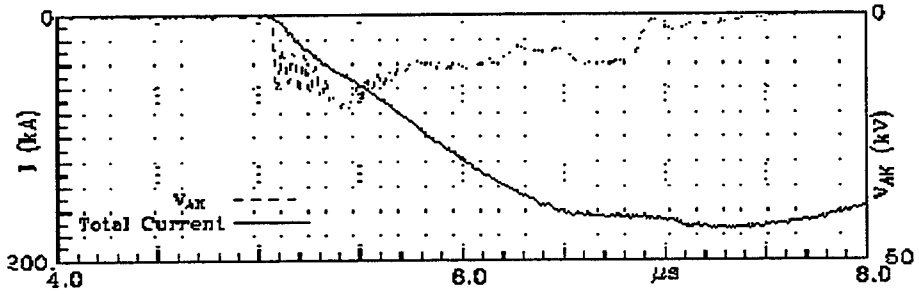

Figure 1-3(b). Switch mode for external gating with -30 kV charging voltage and large flashboard ion source.

The current profiles for all modes eventually show an impedance drop starting at times depending on the mode and particular experimental parameters. Prior to the program it was suspected that the impedance drop was due to high density-electrode plasmas moving across the gap and essentially closing the bi-polar sheath(s); i.e., the usual model of gap closures in high current diodes. Experiments of the program have shown that the impedance drop observed in the DCOS does not have the features associated with the conventional model and instead correlates with a radial expansion of the current channel. This new model of the impedance drop derives both from gated imaging of the luminous cathode plasma and from B-dot probes at various radii. The rate of current channel expansion is reduced by increasing the longitudinal magnetic field level, use of a conducting mesh across the anode aperture through which the plasma is injected into the switch, and by increasing the radius of the initial plasma channel.

The electron current density in the expanded channel annuli is typically low (~10's A/cm^2), but can extend over relatively large areas. The channel expansion rates can be sufficiently low, e.g., to allow operation in the low impedance modes over ~ 2 μsec. Simulations suggest that the radial expansion is driven by a potential hump formed by heating of the background electrons. The net positive charge of the hump generates a radial electric field accelerating ions outward from the channel and then longitudinally across the gap, thereby filling the annulus with the low density ion back-ground necessary to obtain the observed electron current densities.

1.3.1.1 *Scaling of the Self-Opening Mode*. A major objective of the program was to ascertain the scaling of the self-opening mode, given its practical simplicity. From the work of the program a model can be developed for scaling of the mode which incorporates results from both simulations and experiments. The model assumes the basic phenomenology of the simulations in which a potential hump is formed by heating of the background electron population. The potential hump then restricts or shuts off the ion flow, leading to an opening event as the ion "reservoir" of the gap is depleted.

Simulations with the gap initially filled with plasma all show very low impedance when the voltage is applied, consistent with experimental results in the self-opening mode. Experimentally, though, voltage does appear across the gap during the conduction phase due to the inductance of the switch. [This inductance is not included in a one-dimensional simulation or was negligible in the limited two-dimensional simulations.] The voltage across the gap remains low until the magnitude of the potential hump is of the order of the injected ion kinetic energy.

A model of Kares, et al.[3] gives an upper limit on the magnitude of the potential hump. Using this model and setting the hump potential equal to the injected ion kinetic energy gives a limit on the j_e/j_i ratio around which ion flow is restricted:

$$\frac{j_e}{j_i} < \frac{1}{2}\sqrt{\frac{M}{Zm}}\left(\frac{1}{1+\gamma}\right) \qquad (1.1)$$

where M is the ion mass, Z the ion charge number, m the electron mass, and γ a parameter which accounts for the effects of trapped electrons in the potential hump ($\gamma \leq 1$). Taking $\gamma = 0.3$ from simulations, the formula gives j_e/j_i ratios of 17, 57, and 41 for H^+, C^+, and C^{++} respectively. Simulations with low driver bank voltages (1 kV) and "long" current risetimes ($\gtrsim$ 200 nsec), or $dj_e/dt \lesssim 0.6 \times 10^9$ A/cm^2/sec, generally agree with the model and show current "clamping" at $j_e/j_i \sim 15$ for H^+ or an opening. The injected ion current is relatively unimpeded until the j_e/j_i ratio approaches that of the above formula.

Simulations with higher voltage ($\geq$ 5 kV) and shorter risetimes (~ 100 nsec), or $dj_e/dt > 3 \times 10^9$ A/cm^2/sec, show openings with a higher j_e/j_i ratio at opening than the Kares

formula values, i.e., j_e/j_i ~ 25-30 for cases with injected H^+ ion current density relevant to experimental self-opening conditions ($j_i \gtrsim 10$ A/cm^2). Figure 1-4 shows an example of such a simulation by T. Hughes where the peak j_e/j_i ratio is ~ 30*.

Experiments with self-opening modes also show j_e/j_i ~ 25-30 at the time of opening in cases where the ion current density is reasonably uniform over the channel cross-section and with no evidence of appreciable channel expansion. The ion current density used in the experimental ratio is that around the time of application of voltage, but measured without applied voltage, and pertains to cases where the injected ion current is nearly constant or increases over the time of conduction. (See, e.g., Figure 3-33). With good openings, the experimental values of dj_e/dt exceed 10^9 A/cm^2/sec, i.e,, are in the fast risetime range of the simulations.

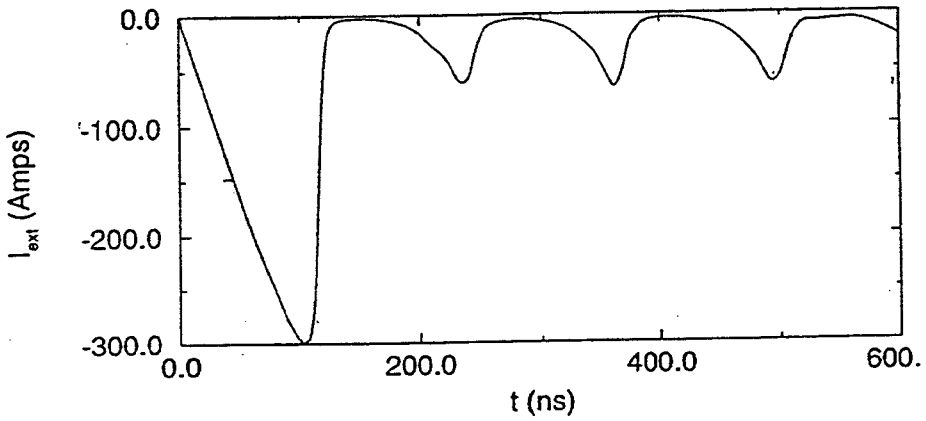

Figure 1-4. Voltage and current versus time for simulation with initial capacitor voltage of 5 kV. Injected hydrogen ion current density is 10 A/cm^2, AK gap is 1 cm, area of channel is 1 cm^2 and external inductance is 1.47 μH.

With the above discussion in mind, simple formulas for scaling the peak current, I_p, and conduction time, t_c, of the self-opening mode can be given:

$$I_p \sim j_i(0)\,\eta\,A \qquad (1.2)$$

$$t_c = [j_i(0)\,\eta\,A\,L_T]/V_c$$

*In simulations which allow space charge limited electron emission from the anode in response to the electric field of the potential hump (the likely experimental condition), the current after opening does not drop to the near zero level of Figure 1-4, but to $\lesssim$ 1/2 the peak current.

where j_i (0) is the ion current density of the time of application of the voltage, A is the channel cross-sectional area, L_T the total system inductance (bank and switch), V_c is the charging voltage, and η the peak j_e/j_i ratio. From experiments and hydrogen plasma simulations η ~ 25-30. The above formulas assume that the ion current density is uniform in radius and nearly constant over the conduction time, $dj_e/dt \gtrsim 10^9$ A/cm^2/sec, the bank external resistance is negligible, and that the cathode is fully ignited at the on-set of conduction. The latter condition was typically realized experimentally when the ion current was collected by the cathode for a duration of $\gtrsim 2$ μsec and j_i (0) $\gtrsim$ 10 A/cm^2 at the time the voltage was applied.

There are two points worthy of note regarding the scaling formulas above. First, the parameters used in simulations (e.g. Figure 1-4) show conduction times before opening of 50-100 nsec; i.e., nearly an order of magnitude shorter than experimental results. The discrepancy is due to the small channel area of the simulations (~ 1 cm^2) and, in the inductively-limited conduction time formula above, it is of course the total current which determines the time. The other remark is that simulations do show higher η values than 25-30 in certain cases which may be practically exploitable. For example, a C^+ simulation with the same injected ion velocity as the H^+ simulations (13 cm/μsec) reaches the Langmuir-Child bi-polar value of ~ 150 at opening.

To conclude the discussion of scaling of the self-opening mode we consider an example of long conduction time parameters envisioned in the original DSWA advanced switch procurement as goals for one of an array of opening switches for a very high current simulator. The desired conduction time was 1.5 μsec, current ~ 2 MA and opening voltage $\geq$ 1.5 MV. Assuming a voltage multiplication ratio of two, a driver voltage of 750 kV is required and with j_e ~ 2 kA/cm^2, the ion current density for H^+ would be 67 A/cm^2 or ~ 25 A/cm^2 for C^{++}. Both j_i values are quite accessible. The current channel radius required is ~ 18 cm and a total inductance of ~1 μH would give the desired conduction time.

The example is of course a significant extrapolation from experimentally accessible parameters of this program. A relevant experiment for scaling assessment was conducted with DCOS using the high voltage driver bank EYESS at Physics International Co. in the previous program. Although the conduction time had to be shorter (~ 0.5 μsec) because of bank parameters, opening voltages $\geq$ 1 MV were obtained with a remarkably long FWHM of the opened voltage ($\gtrsim$1 μsec).

1.3.1.2 *Scaling of A Gating Mode*. A low impedance mode suitable for external gating is in principle demonstrated in Figure 1-3(b). The simulations and analytic models of conduction discussed above suggest a method for realizing the mode. To be conservative, the limit on the j_e/j_i ratio from the Kares model is assumed. We use doubly-ionized carbon, the most practically advantageous ion with $j_e/j_i \lesssim 40$, and the main output component of DSWA gun sources used in the DECADE program. [The

experimental observation that this mode was obtained when the flashboard source was moved closer to the anode may be in part due to a dominant carbon output at time of voltage application.] As long as $j_e/j_i \lesssim 40$ the ion flow should then be relatively unimpeded and the current should follow the ion source current. The peak current and time to reach it are obtainable from the same formulas as used for the opening mode scaling, but with $\eta \sim 40$ and C^{++}. Near the time of peak current, the ion source needs to be gated to reduce the ion current density by only a factor of ~2 to achieve opening if H^+ results can be scaled to C^{++}.

This scaling of this model for a gating mode has not been established experimentally; the mode was obtained essentially empirically late in the DCOS work, so the mode needs verification. In particular, to conduct an experimental scaling study, the ion current density with radius needs to be measured over the entire aperture and the ion species determined. Simulations which include the region between the anode and ion source are also highly desirable. Further work is also needed on gating techniques -- the first DCOS program established a magnetic gating technique with ion current densities up to ~ 60 A/cm^2. An interesting possible technique for gating large area ion sources was suggested by experiments in the program on effective transparency of meshes with positive or negative external biases. The transparency of a mesh in the ion source stream was reduced, e.g., by a factor of 2.6 with application of a negative 500 volt bias.

1.3.1.3 *Scaling-Related Results*. The effects of several switch parameters on the current profile were studied in the program to elucidate switch behavior. A brief summary of the results is given below.

Current Density Scaling Effects. A wide range of electron current densities was covered in the program, from ~ 100 A/cm^2 to ~ 2000 A/cm^2. There was no evidence in the data that pointed to high density electrode plasma closure as the cause of the impedance drop over the ~ 2 μsec times of the experiments. As mentioned above, the impedance drop was associated with radial expansion of the current channel and low electron current density flow outside the main channel over large areas. After opening, the current in the main channel typically clamped over μsec or so time scales and the current increased mostly just outside the central channel. Two-dimensional simulations with electrode emission allowed outside the main channel showed ions accelerated outward from the central channel by the potential hump and a doubling of the total current compared to the case with emission allowed only within the injected plasma channel.

The other current density scaling issue was the j_e/j_i ratio at opening which has been discussed above.

Total Current Scaling. Current scaling was studied in the program at current levels from a few hundred amperes to the 100 kA level. In general there was no evidence of significant changes in switch operation or the character of the various modes as the

total current increased. The modes generally scaled with anode aperture area when the sources had reasonably uniform current density over the aperture area.

The data suggest that beam pinching due to self-field effects at higher current levels and/or lower applied fields does not substantially alter the phenomenology and that opening events are not necessarily associated with MHD instability, as was postulated in the first DCOS program. If anything, centroid motion appears to have been caused at times by an opening event, rather than being the cause.

Radial sheathing of the current in the higher conductivity of plasmas associated with the low impedance modes undoubtedly occurs during the early conduction times and was observed in the gated camera images and in a two-dimensional simulation. The simulation also showed that the cathode emitted uniformly over its cross-section even though the current in the plasmas evolved into a radial sheath away from the cathode. The experiments in general showed no evidence that existence of a radial sheath diffusing into the center of the current channel significantly perturbs the overall discharge behavior.*

Cathode Emission. Ignition properties of several cathode types were studied (stainless foils, meshes, and carbon velvet/fiber emitters). Application of voltage early in time after the injected plasma reached the cathode ($\lesssim$ 1.5 μsec) resulted in a high impedance mode where the current rose rapidly over $\lesssim$ 100 nsec to low values dependent upon the applied voltage and cathode type, and more or less followed the ion current profile thereafter until the start of impedance drop. The gap voltage was nearly the full charging voltage. Simulations were unable to reproduce the behavior of the high impedance mode and were only able to obtain a high voltage initially by applying voltage before the plasma fully crossed the gap. The low ion dose at the cathode when voltage was applied and the simulation results suggest that the cathode was initially emission-limited for the high impedance mode. The cathodes were fully ignited at the time of voltage application for the practically important low impedance modes.

Scaling With Gap Length. There are two aspects of switch behavior which are potentially affected by the gap length -- the conduction time before a self-opening event and the time to start of the impedance drop. If the potential hump is nearly symmetric across the entire gap, the gap length may determine the total charge of the ion reservoir which is depleted once injection is restricted or shut off. Certainly the time before the impedance drops is related to gap length if the conventional electrode plasma closure model is relevant. The data shows that an effective average closure velocity of 4-6 cm/μsec/electrode pertains to the start of impedance drop for the high

*One can speculate that a mechanism exists with a sheathed conduction channel to increase the effective diffusion rate. As the current density becomes high enough to reach the Kares model limit, the annulus effectively becomes a higher impedance path and current is shunted inward. Additional simulations with longer running time are needed to further study this issue.

impedance mode. These effective velocities are very large compared to those expected from a thermally driven plasma generated by energy deposition in the electrodes. The mechanism identified experimentally with the impedance drop is radial expansion of the current channel, as mentioned previously, and this mechanism also can exhibit a linear dependence on length. The ions are likely "pumped out" of the initial current channel around localized potential humps or preferentially near the center of the gap if the hump extends symmetrically across the gap. In any case, the ions must be accelerated longitudinally to fill the extended channel annulus across the entire gap to allow electron current densities observed in the experiments and simulations.

Experimental data on the conduction time and time to start of impedance drop for the low impedance self-opening mode did not exhibit a dependence on gap lengths for gaps $\gtrsim$ 8 cm. It is also noteworthy that, although the impedances typically dropped steadily after opening and a delay, the gaps frequently showed significant "resistive" impedance near peak current up to ~ 2 μsec after start of conduction. This resistive impedance, lasting for 100's of nsec, appeared when the current rise flattened at these late times. In other words, the gap was not shorted out even though the current had nearly peaked.

Magnetic Field Effects. An applied longitudinal magnetic field is incorporated in the DCOS for several reasons: (1) efficient transport of ions from the source to the switch and control of ion current density, (2) suppression of MHD instability growth (kink), and (3) control of beam pinching due to self-magnetic fields. In Section 3 several curves are given illustrating the influence of the applied field shape and peak amplitude upon the ion source peak current density and time profile.

Satisfying the Krushal-Schafranov (K-S) condition to stabilize kink motion is not particularly difficult for switch parameters of interest. The K-S criterion for stability is

$$\frac{2\pi a B_z}{L B_\theta} > 1 \qquad (1.3)$$

where a is the current channel radius, B_z the applied longitudinal field, L the length of the gap and B_θ the self-magnetic field at the channel edge. Using the scaling example above with a current of 2 MA, j_e ~ 2 kA/cm^2, and L = 20 cm, the K-S criterion is $B_z >$ 4 kG.

The effect of beam pinching on the gap behavior was not addressed in the limited two-dimensional simulations of the program. As mentioned previously, experimental conditions where some beam pinching likely occurred showed no significant change in the current profiles of the opening mode. Certainly, if pinching occurs with a largely diffuse current channel, the j_e/j_i ratio should be preserved. Limitation of beam pinching requires a higher B_z value than the K-S criterion and is likely the dominant criterion for the minimum applied field level. For example, if $B_z/B_\theta \gtrsim 1/2$, the 2 MA conduction

current of the scaling example above requires $B_z \gtrsim 11$ kG. Empirical tests are still needed to establish the minimum field level for an actual switch design.

An additional important effect of the applied field pertains to the current channel expansion related to impedance drop. Limited two-dimensional simulations mentioned above showing expansion of the current channel had $B_z \sim 2$ kG, and the ion motion was not adiabatic or tied to field lines. Increasing the B_z field reduces the ion gyro-radius and expansion rates. Experimentally, increasing the field to > 4 kG eliminated outer channel current loops and improved agreement between probes at various radii. The minimum Bz field level to limit current channel expansion over time scales of interest should be largely dependent on the peak j_e/j_i ratio according to the Kares model of the maximum potential hump amplitude. Beam self-fields should also inhibit channel expansion.

In summary, all the important scaling issues related to current density and total current scaling of DCOS have been addressed in the program. The self-opening mode appears scalable over a wide range of parameters and has been demonstrated experimentally to be "robust" in that it works over large admixtures of ion source velocities and charge densities, is reproducible if the ion source is reproducible, and is not highly sensitive to the magnetic field level, gap length, current rise rate, ion source current profiles, cleanliness of the system, etc. Existence of a gating mode has also been established empirically, but needs more diagnosis and simulations including the anode-flashboard region.

The major experimental problem of the program which limited actual switch performance was the non-uniformity of the ion sources over the larger areas. Scaling of switch operation to higher total currents and longer conduction times should include careful diagnosis of the radial distribution of the ion current density to insure its uniformity over the aperture. Use of multiple guns or segmented large area flashboards would help insure this uniformity for larger source areas.

1.4 SUMMARY OF THE DM-2 POWER FLOW EXPERIMENTS.

As explained in the program outline above, the last task of the program addressed power flow through an opened plasma erosion type switch (POS) using the DM-2 driver at Primex Physics International. The switch was designed to operate in the bi-polar or modified bi-polar mode[4], as opposed to the magneto-hydrodynamic regimes of DM-1 opening switches. The basic idea behind this departure from the conventional POS design was to obtain a larger effective gap after opening to reduce launched electron flow and allow more efficient power transfer to the load. The approach was to operate with a lower density (~ 10^{12} cm^3) plasma (which implied the bi-polar modes) and design the switch parameters for conduction with low current density at the electrodes in order to minimize or avoid generation of electrode plasmas. This combination offered the possibility of clearing out most of the switch plasma during opening, resulting in a large effective switch gap and longer opened times. Aside from

demonstrating opening with large switch gaps and efficient power transfer to loads, the DM-2 experiments were designed to provide a convenient and inexpensive technique for pulse sharpening of potential use to DECADE plasma radiation source (PRS) development.

Efficient power flow through the low density POS was demonstrated for inductive loads, including those representative of DECADE QUAD PRS feed designs, and for a high impedance diode load. A ~ 100 nsec reduction in the ~ 300 nsec direct drive current risetime was obtained without significant reduction in the peak load current. Figure 1-5 shows such a result from a shot with a 48 nH inductive short load. The curves show current profiles upstream (I1A) and downstream (ISA) of the switch region and the voltage across the switch. Launched electron currents in the load region just downstream of the switch were maximally 10-15% of the anode current during opening and less than 5% after opening with the inductive loads. Near the load region there was no measurable difference between load and drive current after opening.

Limited experiments with a resistive (diode) load of 1-2 ohms showed that the switch initially opened to an impedance > 2 ohms with sheath flow $\lesssim$ 17% of the downstream anode current. There was no apparent closure or re-strike of the opened switch for > 300 nsec.

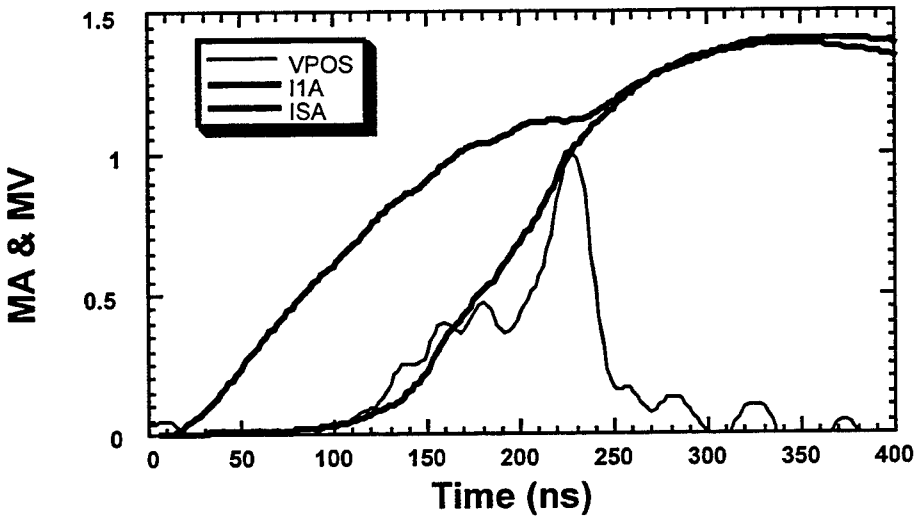

Figure 1-5. Current and voltage waveforms for shot 436.

1.5 REPORT ORGANIZATION.

The following sections of the report describe the program results in detail. Because of near-term interest, the DM-2 results are presented first in Section 2. The DCOS experimental results follow in Section 3, and the simulation work for the DCOS program by T. Hughes and T. Genoni in Section 4 concludes the report.

SECTION 2
POWER FLOW THROUGH AN OPENED POS

2.1 OVERVIEW - MOTIVATION.

The final contract SOW task addressed power coupling through an opened DCOS to a load. Absent a fully developed high current coaxial version of the switch to test, the experiment was designed to incorporate a main feature of DCOS (specifically, a reduced plasma density in the final conduction and opening phases) in a coaxial geometry. In addition, the experimental design attempted to limit the electron energy deposition in the anode electrode of the switch to a level below that generally accepted as the electrode plasma initiation threshold in order to limit the formation of dense electrode plasmas that could contaminate the switch plasma and thereby reduce the opened time of the switch and influence the trajectories of launched electron flow from the switch region.

DM-2 was chosen as the test bed for these experiments for several reasons: (1) DM-2 offered 1-2 MA drive current levels, considerably above the ~ 100 kA test bed level available at PSI, (2) the switch parameter regime could be chosen to provide pulse sharpening to the DM-2 direct drive output pulse that could be of potential use in various DECADE PRS drive scenarios, thus making the work relevant to immediate and near-term needs of the larger DSWA DECADE program, and (3) the tests could benefit from the loan of DM-2 variable inductance short circuit load hardware and extensive current diagnostics built originally for the DECADE Quad PRS direct drive power flow risk reduction experiment.

The experiment was basically successful in demonstrating efficient power flow through an opened low density POS to (1) various inductive short circuit loads covering an inductance range representative of typical Quad PRS feed designs, and (2) a high impedance diode load with a geometric impedance 2/3 that of the switch region, had it been fully opened. Measurement of anode and cathode currents both upstream and downstream of the switch showed launched electron flow from the switch region of typically less than 100 kA for all configurations. Shots with the high impedance diode load showed no apparent closure or re-strike of the opened switch for the roughly 400 nsec time that switch voltage and current were recorded. Questions remain as to the location of the launched electron sheath and the distribution of losses between electron and ions, but the good overall power transmission characteristics of the opened low density plasma switch opens another power conditioning option for a DECADE PRS driver that can speed the current load risetime without resorting to water output line modifications, such as a power doubler.

The remainder of this report section contains a discussion of the experiment design (Section 2.2), a description of the hardware and diagnostics (Section 2.3), summaries of the experimental results with analyses and discussions of various features and observations (Section 2.4), and an overall summary and conclusion (Section 2.5) that

it is hoped will motivate more investigation of low density non-MHD switches by the community for use in, e.g., reducing the direct drive pulse risetime for DECADE PRS loads or reducing conduction time requirements on faster opening, higher density, switches presently used in the DECADE large area bremsstrahlung mode.

2.2 EXPERIMENTAL DESIGN.

For the switch and power coupling to be relevant to the pulse sharpened PRS direct drive option for DECADE QUAD, the following characteristics were considered in the design of the DM-2 POS:

- $\gtrsim$ 50 nsec conduction time;
- $\gtrsim$ 1/3 MA conduction current before opening;
- > 200 nsec "opened" time;
- Erosion opening of the full vacuum gap so that "launched electrons" are minimized and the switch could be located upstream of a low loss vacuum convolute.

We wanted the switch to "erode" away the first $\geq$ 50 nsec of the current pulse, and then open to transfer the current efficiently to the load.

In selecting the switch parameters we first considered the conduction phase scaling laws following Weber, et al[(1)].

Conduction limits for radial current flow in cylindrical geometry

1. Bi-polar	$I_{BP} = (M/Zm)^{1/2} (2\pi r \ell)$ nev
2. Modified bi-polar	$I_{MBP} = 1.02 \times 10^{-2}$ r $n^{1/2}$
3. Electromagneto-hydrodynamic (EMH)	$I_{EMH} = 1.64 \times 10^{-9}$ r $(\ell \dot{I}$ n$)^{1/2}$
4. Magneto-hydrodynamic (MHD)	$I_{MHD} = 1.39 \times 10^{-5} (r^2 \ell^2 \dot{I}^2$ n$)^{1/4}$

Where M is the ion rest mass, Z is the average ion charge state, m is the electron rest mass, r is the radius of the inner conductor, ℓ is the axial length of conduction, n is the electron number density, e is the proton charge, v is the average ion velocity, and the EMH and MHD cases assume a linear current ramp, $I(t) = \dot{I}\,t$. Of these mechanisms, only the bi-polar or modified bi-polar opening mechanisms were expected to achieve the condition of a large opened gap.

These limits on conduction currents correspond to the currents at which an opening based upon that mechanism begins. For the MHD and EMH cases this means that the plasma or the current in the plasma has been displaced by the axial length of the initial plasma. In the BP and MBP cases, there is nominally no disturbance in the

(1) B. Weber, et al., Phys. Plasmas, Vol. 2, No. 10, p. 3893 (1995).

plasma until the conduction limit is reached. When the limit is reached, erosion causes a gap in the plasma to be formed at the electrode, and the switch begins to open. Achieving these conditions without entering the MHD or EMH conduction regime and without significant heating of the switch electrodes during the erosion opening phase dictates use of large radius, low density switches.

For DM-2, existing circuit and hardware flange points and existing plasma guns dictated some of the switch parameters. The rate of rise of the DM-2 current is approximately $\dot{I} = 6.7 \times 10^{12}$ A/s, (~2 MA in 300 nsec). The most practical POS plasma sources for the tests were cable guns similar to those used in the switch in the DM-1 module for the bremsstrahlung diode. The typical output of these guns are C++ ions, and the average velocity is in the range of 2 to 5 cm/μsec. At NRL on Gamble I, under conditions similar to those used on DM-2, the velocity of the cable gun plasma was inferred to be ~3.6 cm/μsec[1]. The most practical radius for the inner conductor was 33.5 cm, the radius used in hardware for the joint PSI/PI power flow tests on DM-2.

Plugging in r = 33.5 cm, $v = 3.6$ cm/μs, Z = 2, M = 2×10^{-23} g, and $\dot{I} = 6.7 \times 10^{12}$ A/s, the above equations for the conduction limits become,

1. Bi-polar $I_{BP} = 1.27 \times 10^{-8} \ell n$
2. Modified bi-polar $I_{MBP} = 3.42 \times 10^{-1} n^{1/2}$
3. Electromagnetohydrodynamics $I_{EMH} = 1.42 \times 10^{-1} (\ell n)^{1/2}$
4. Magnetohydrodynamics $I_{MHD} = 2.08 \times 10^{2} (\ell^2 n)^{1/4}$

The scaling models for the four regimes, at axial lengths of 10, 20 and 30 cm, are plotted in Figures 2-1 a, b, and c. From these graphs it is apparent that a plasma density of 1-2×10^{12} cm^{-3} is required for a bi-polar conduction current of ~0.5 MA. This density was within the achievable range of the available cable gun sources. For the intermediate condition shown of ℓ = 20 cm, a density of 1.6×10^{12} cm^{-3} was expected to begin to open at a current of ~0.4 MA, after ~60 nsec of conduction with $\dot{I} = 6.7 \times 10^{12}$ A/sec.

Bi-polar erosion was expected to be able to sweep most of the plasma out of the electrode gap, resulting in a long open time of the switch provided that electrode plasma contamination of the switch could be minimized. Since the conduction current scales with the initial plasma density, control of the injected plasma density controls the conducted current. The low average current density was expected to reduce anode plasma generation and thus minimize electron flow "launched" onto trajectories that graze the anode.

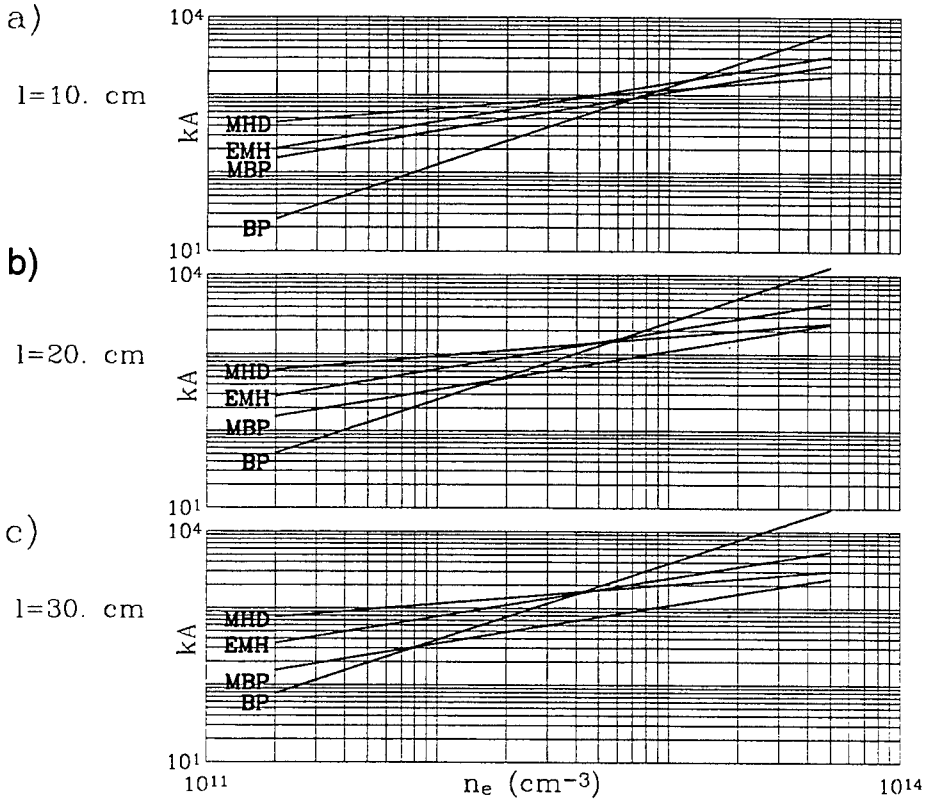

Figure 2-1. Opening currents for four mechanisms with a switch r = 33.5 cm, v = 3.6 cm/μs, Z = 2, M = 2 x 10^{-23} g, and $\dot{I}$ = 6.7 x 10^{12} A/s.

Assuming conditions on DM-2 equivalent to the several low inductance DECADE Quad PRS conceptual designs, with a downstream single-module inductance of ~40 nH and $\dot{I}$ = 8 x 10^{12} A/s, and assuming that the anode radius is ~37 cm for a radial AK gap of ~3.5 cm, the average anode dose delivered by energetic electron deposition during the switch opening phase is very roughly estimated to be < 50 Joules/gram.

$V_{max} < L\dot{I}$ = 40 nH x 8 x 10^{12} A/s = 320 kV

I_{peak} = 500 kA

Area = 37 cm x 2π x 20 cm = 4650 cm^2

J_{peak} = 108 A/cm^2

Fluence = 108 A/cm^2 x 320 x 10^3 V x 60 x 10^{-9} s = 2.1 J/cm^2

Dose/Fluence = 17 @ 320 kV

Dose ≃ 35 J/g

This estimated anode dose is less than the threshold level[2] for anode plasma formation.

To check on the expected MHD effect, an estimate of the displacement of a thin current sheet in the plasma may be given by[1]

$$\dot{x} = \frac{1}{10r}\sqrt{\frac{Z}{\pi M_i}}\,\frac{1}{n}d/dt\sqrt{\left(\int dt\left(n\int I^2 dt\right)\right)} \qquad (2.1)$$

With the assumption that the density is constant and the current is I(t) = $\dot{I}$t, the displacement of the current sheet as a function of time can be written as

$$x(t) = \frac{1}{20r}\sqrt{\frac{Z}{2\pi M_i n}}\,\dot{I}t^2 \qquad (2.2)$$

For the same conditions as those used previously, with t = 60 nsec, a current sheet is displaced by only ~4.4 cm at n = $1x10^{12}$ cm^{-3}, and ~14 cm at n = $1x10^{11}$ cm^{-3}. For a current which is distributed throughout the plasma, the JxB force is reduced from the thin current sheet case, and the displacement for any portion of the plasma is also reduced. Thus no significant axial switch plasma motion was expected compared to the 10's of cm planned switch length.

To make better estimates of the density required for the tests on DM-2, we used a simple equivalent circuit model of the switch on DM-2 shown in Figure 2-2. In this model, a number of assumptions are made. The driver voltage used is from the Lee Schlitt conservative design for the DECADE Quad. This voltage is not exactly the same as for the DM-2 module alone, but it is sufficiently similar for the purposes of this model. It is assumed that the switch has no inductance and acts only as a variable resistor. Magnetic insulation is not included in the model. (The effect of magnetic insulation in the experiment is to increase the rate of the transfer of current from the switch to the load.) In addition, the only opening mechanism assumed is bi-polar erosion. This assumption is appropriate for calculating the time erosion of the switch begins, but as the switch current continues to rise other mechanisms will begin to play a part.

The POS model can be set for no current flow, current flow across a fixed vacuum gap, or with an initial plasma fill. The model assumes an initial dI/dt based upon the initial driver voltage and the initial current paths allowed. The voltage drop across R_{Driver} is calculated, and the remaining voltage drops are calculated based upon the conditions. The current is stepped up by the dI/dt value, and a new dI/dt is calculated

(2) T. Sanford, et al., J. Appl. Phys., Vol. 66, No. 1, p. 10 (1989).

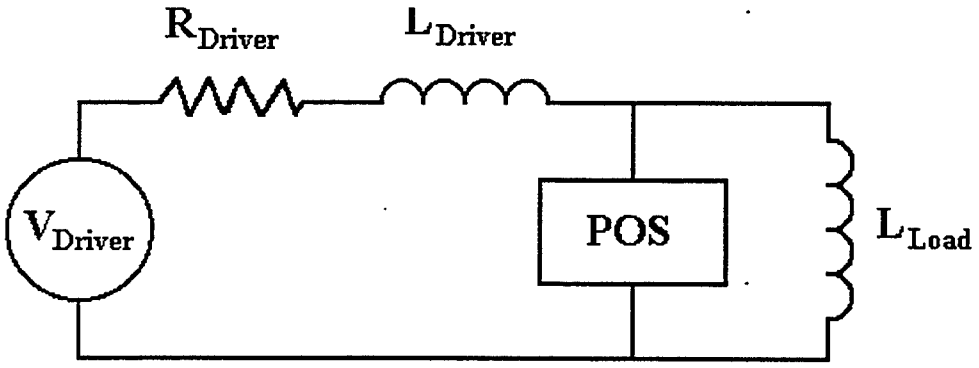

Figure 2-2. Equivalent circuit.

by the voltage drop across one of the inductances. Since the model is not fully self-consistent, calculation of the voltage drops varies with the relative inductances of the load and driver to avoid a numerical instability.

The opening mechanism for the switch is assumed to be simple bi-polar erosion of the plasma, and there are no MHD or EMH effects included. With bi-polar current flow, the maximum ratio of electron to ion currents is given by

$$J_e/J_I = (M/Zm)^{1/2} \tag{2.3}$$

where M is the ion mass, Z is the average ion charge state, and m is the electron mass. Assuming quasi-neutrality of the plasma, the injected ion current density is $n_e e v_{ion}$, and if the electron current density exceeds this value, ions will be accelerated out of the AK gap. Using the fact that the total current is approximately equal to the electron current, the bi-polar current limit can be written as

$$I_{BP} = (M/Zm)^{1/2} (2\pi r\, \ell)\, n_e e v_{ion} \tag{2.4}$$

where n_e is the electron number density, e is the electron charge, v_{ion} is the incident ion velocity, and $(2\pi r\, \ell)$ is the area of the switch. If the switch current exceeds I_{BP}, a gap is eroded in the plasma. The velocity of the gap sheath across the plasma is estimated by simple erosion.

$$dX_s/dt = (J_i - e n_e v_{ion})/(e n_e) \tag{2.5}$$

where J_i is given by Equation 2.3. Using Equations 2.3 and 2.4 this sheath velocity can be rewritten as

$$dX_s/dt = (I/I_{BP} - 1)\, v_{ion} \tag{2.6}$$

The gap as a function of time is the time integral of the sheath velocity from the moment I_{BP} is exceeded.

The relationship between the current in the switch and the voltage across the switch is calculated assuming that the current flow is across an effective vacuum gap, with non-relativistic, bipolar, Child-Langmuir current density.

$$J_e = 1.865\ (\varepsilon_o\ 4/9)\ (2e/m)^{1/2}\ V_o^{\ 3/2}/d^2 \qquad (2.7)$$

When ε_o is the electric permittivity of free space in SI units, e is the electron charge in coulombs, m_e is the electron mass in kg, V_o is in volts, and d is in cm, the current density is given in A/cm^2. When the gap is initially filled with plasma, the bi-polar sheath is assumed to be equal to 0 and there is no voltage across the switch. If the current exceeds the bi-polar current limit, a gap is eroded in the plasma, and the voltage drop across the switch is defined by Equation 2.7. If the switch current subsequently drops below I_{BP}, the gap closes at the rate given by the sheath velocity above.

For the tests on DM-2, r = 33.5 cm and ℓ = 20 cm. The ions are assumed to be doubly ionized carbon, Z = 2, and $M_I = 2.x10^{-23}$ g. The driver R is 0.6 ohms, L_{Driver} is 75 nH, and L_{Load} is 24 nH. Figure 2-3 shows the currents and voltages for the case where the switch is not allowed to carry any current. In Figures 2-4 and 2-5 are the currents and voltages for two values of I_{BP} with an assumed ion velocity of 3.6 cm/μsec. Plotted beneath the calculated currents and voltages are the width of the eroded gap in the plasma and the sheath velocity as functions of time.

The I_{BP} value of 0.5 MA chosen in Figure 2-4 is the value estimated to be optimal by the "back-of-the-envelope" calculations. However, from Figure 2-5 it is clear that a lower bi-polar current limit produces a more desirable condition because of the rate at which the gap opens in the plasma. From Equation 2.6 it is clear that the current must be significantly above the bi-polar current limit to cause fast erosion of the plasma. Although the current limit in Figure 2-5 is only 0.1 MA, it conducts up to 0.75 MA due to the time it takes the gap to open.

The model for the erosion in this circuit model is overly simplistic, and under-estimates the sheath velocity for most of the time. As the current in the switch increases beyond the bi-polar limit, the modified bi-polar limit will be reached, and enhanced erosion of the plasma will occur and increase the opening rate of the switch. Although this simple circuit model only predicts the preliminary stage of the opening process, it does indicate that the switch parameters are in the right regime for the intended experiment.

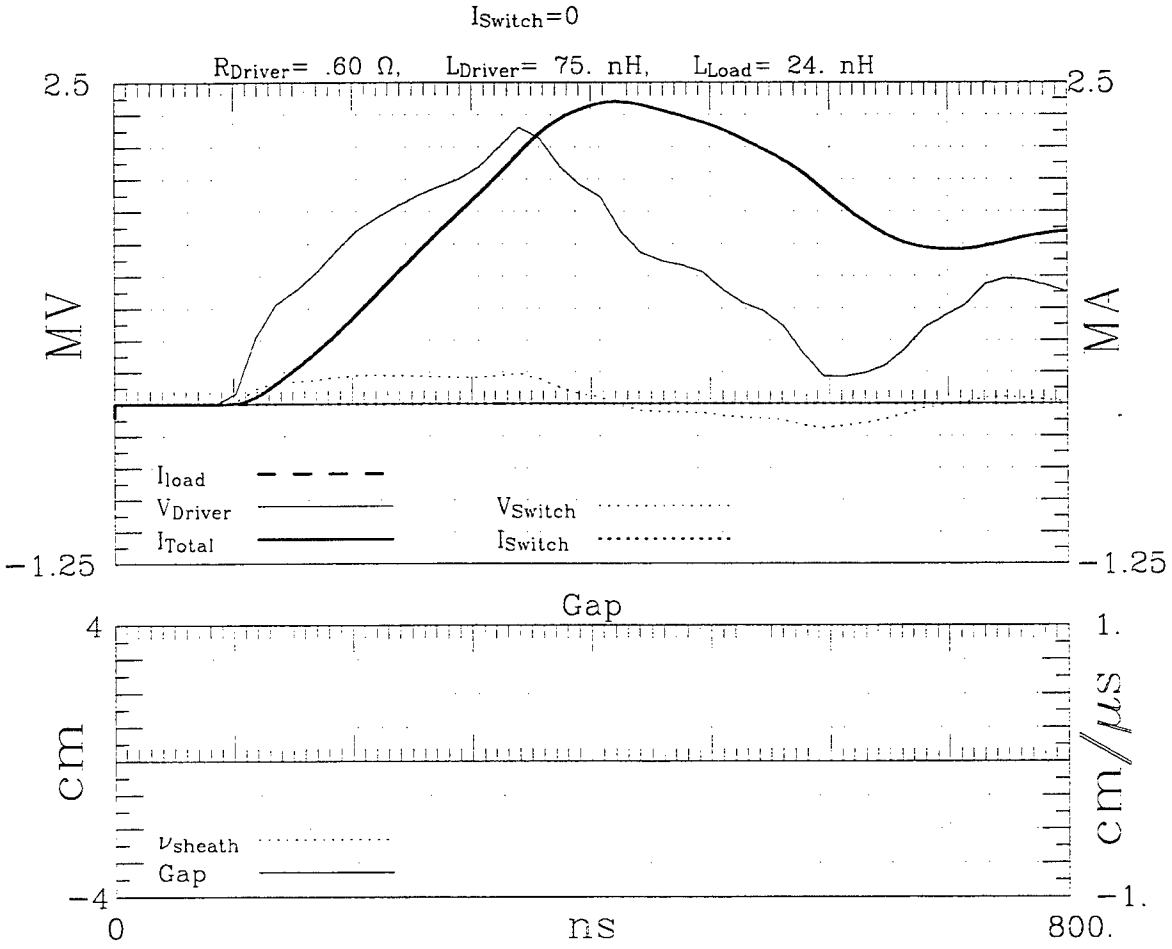

Figure 2-3. Calculated currents and voltages when the switch carries no current.

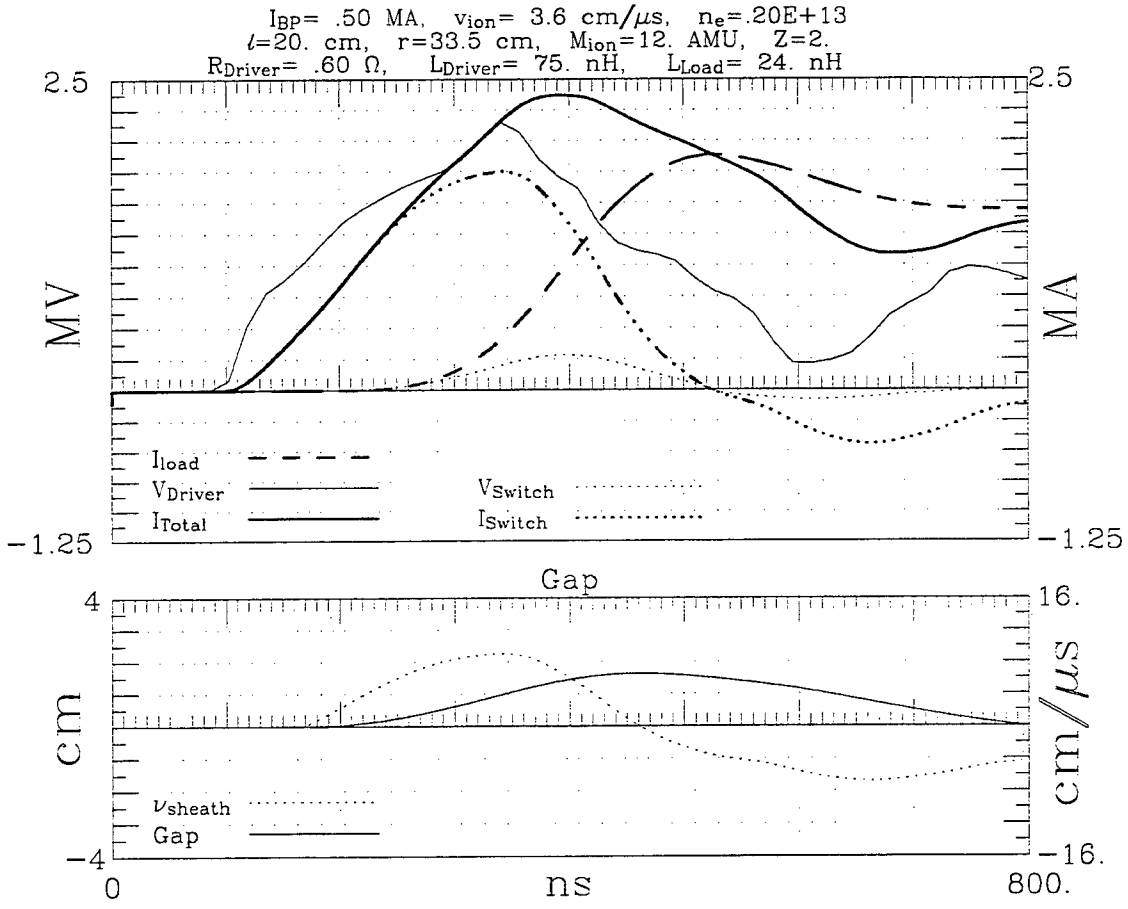

Figure 2-4. Calculated currents and voltages with a bi-polar current limit of 0.5 MA.

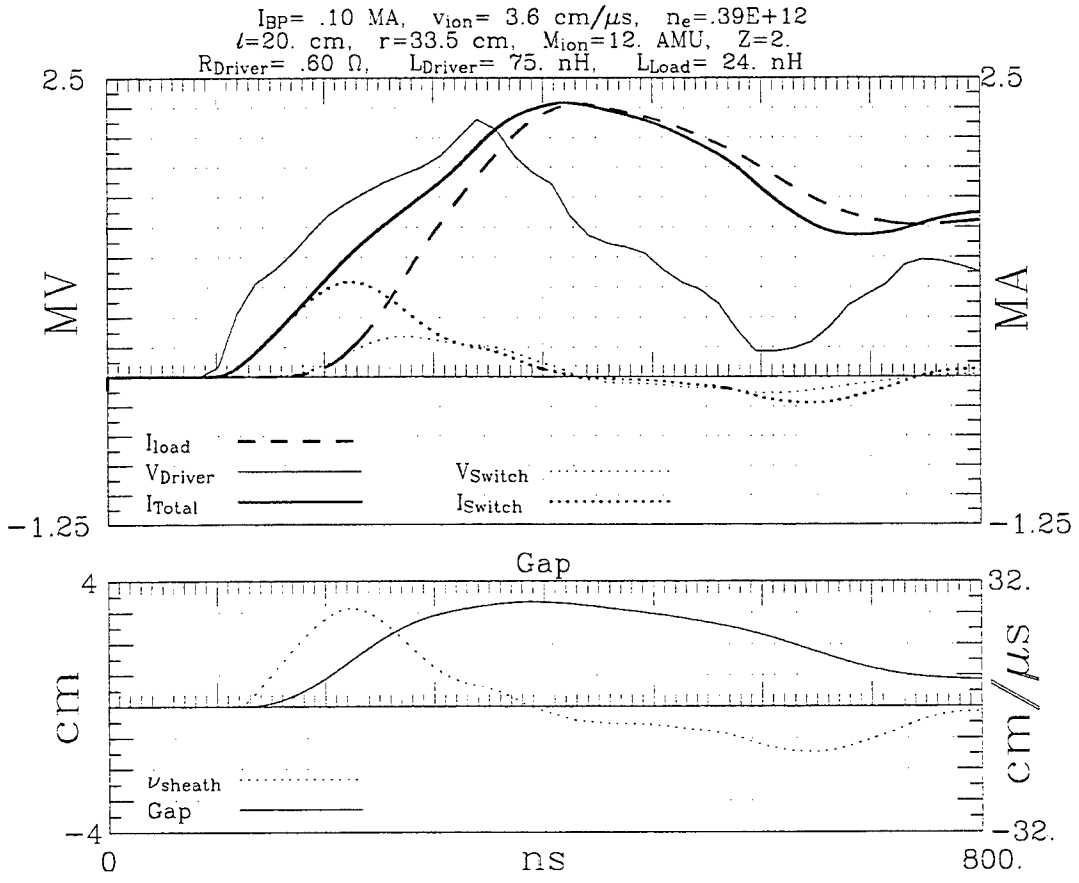

Figure 2-5. Calculated currents and voltages with a bi-polar current limit of 0.1 MA.

2.3 HARDWARE DESCRIPTION.

The hardware design for the POS power flow experiments on DM-2 is shown in Figure 2-6. The switch is mounted on the front end of the DM-2 module, and was designed to be compatible with loads previously fabricated for joint PSI/PI direct drive power flow experiments. To allow the plasma to be injected into the AK gap, the switch anode consisted of 90 rods, evenly spaced in azimuth. This section was ~65% transparent to the injected plasma, and was 30 cm long. By blocking portions of the transparent section with stainless steel foil, the axial length of injected plasma could be varied. The cathode also had a 30 cm long section of 90 rods to reduce plasma stagnation on its surface. The relative orientation of the anode and cathode rods could be varied for optimal performance.

Downstream loads were typically the inductors used on the previous DM-2 power flow experiment. Three inductors were available, giving a choice of 12, 36, or 64 nH downstream of the switch. The inductance of the region from the center of the switch to the downstream inductive loads was ~ 12 nH, so total inductances from switch to

load were 24, 48, and 76 nH. Henceforth we denote these loads by the downstream inductances only. Several shots were taken with an "open circuit" load where the load inductor was removed and the downstream radial feed provided a diode-like load impedance.

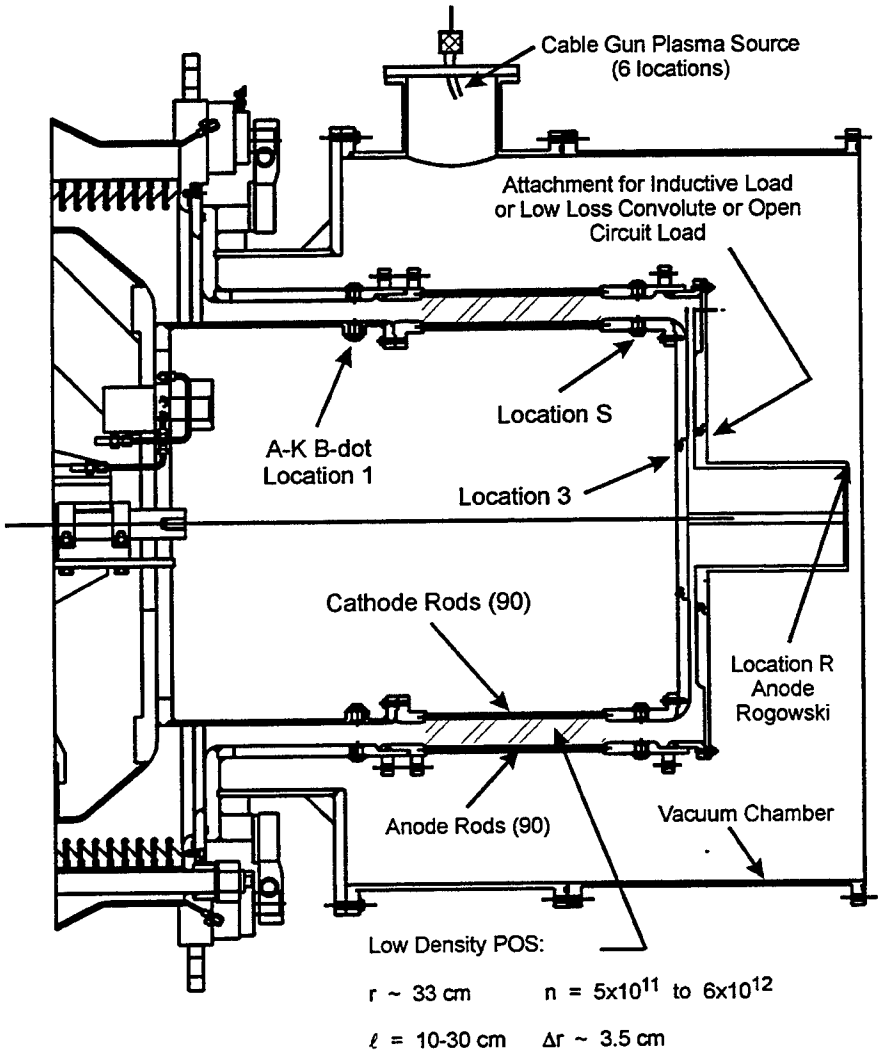

Figure 2-6. PEOS switch hardware on DM-2.

Currents were measured just upstream and downstream of the switch with B-dot current monitors at four azimuthal locations. The azimuthal locations are denoted top, bottom, left and right. Just downstream of the switch there was an additional azimuthal location for a B-dot probe four degrees from the location denoted "left". The additional location has been denoted "extra". Its original purpose was to allow diagnosis of asymmetries in the current flow due to the non-continuous nature of the rod section. There were also B-dot current monitors on the radial feed section at four

azimuthal locations just before the variable inductance load. The final current in the variable inductance load was measured by a self-integrating Rogowski coil.

The plasma source consisted of six cable guns fired radially inward from equally spaced azimuthal locations. The cable guns were made from 0.635 cm diameter semi-rigid coaxial cable, with a 60 degree inverted cone cut into the end. A cross sectional view of the cable gun is shown in Figure 2-7. The chamber allowed radial positioning of the cable guns up to ~37 cm from anode. For the estimated desired density of ~2 x 10^{12} cm^{-3}, we planned to use a single driver bank to fire all six guns. The injected plasma density could be varied by changing the bank charge voltage, the delay time between firing the guns and triggering the main power pulse, and the radial locations of the guns. Several options existed to further increase the range of plasma densities which could be achieved. Holders were made for low transparency meshes to reduce the injected plasma density if desired. If higher densities were desired the number of driver circuits to the guns could be increased, or the inductance of the cables to the guns could be decreased.

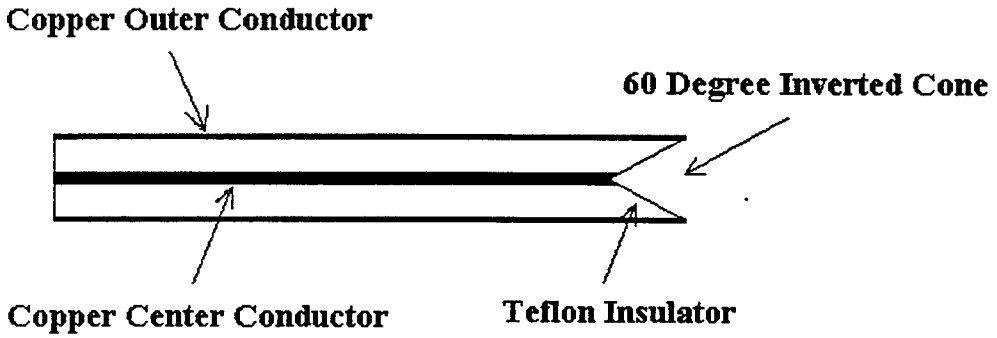

Figure 2-7. Cross-sectional view of the cable gun plasma source.

Prior to the tests we measured the plasma outputs from both single guns and the array of six guns in the DM-2 experiment chamber under a range of conditions. For a single gun, the radial plasma density distribution, as previously measured by Primex/PI, showed a FWHM of approximately 60 degrees. However, this was with a single gun per driver, and at distances within 20 cm of the gun. Tests performed at PSI on the radial distribution of the guns implied that the radial distribution is somewhat more narrow with multiple guns and at greater axial distances. This also appeared to be the case in the DM-2 hardware. To measure the average injected plasma density, eight floating double Langmuir probes were placed inside the switch region. Six of the probes were located midway down the 30 cm long switch, azimuthally aligned with the six cable guns. The remaining two double probes were placed axially 10 cm upstream and downstream of the switch midpoint, still azimuthally aligned with a gun. From the three probes located under one of the cable guns, it is assumed that the distribution of the plasma from all of the guns can be inferred. It is assumed that all of the guns have

the same relative spreads in density, and that the density spreads are the same in both the axial and azimuthal directions.

The floating double probe consists of two tungsten probe tips immersed in the plasma. The tips are biased with respect to each other, while allowed to electrically float as a whole. The probe is designed to collect the ion current incident upon the negative probe tip, and to repel the plasma electrons from that probe tip. Allowing the probe to float to the local plasma potential helps alleviate problems caused by a significant difference in potential between the plasma and experiment ground. The collected ion current is measured, and the local plasma density is inferred using the assumed probe area, and the assumed incident ion velocity. The incident ion current is $J_I = n_i Z e v_i A$, or equivalently by assuming quasi-neutrality, $J_I = n_e e v_i A$, where n_i and n_e are the local ion and electron densities, Z is the average ionization state of the ions, v_i is the incident ion velocity, and A is the effective probe area.

The most significant sources of error in the calculated local densities arise from the assumed area and ion velocity. Scans of the bias voltage of the double probe determined the bias necessary to adequately repel the background electrons. Due to the highly directional average velocities found on the plasmas from the cable gun sources, the assumed effective probe area and the incident velocity are strongly related. At a distance of ~39 cm from the cable gun, the average ion velocity has been found to vary from > 5 cm/μsec down to ~1 cm/μsec as a function of time. Over this time the background electron temperature appears to remain fairly constant and on the order of ~10 eV. If the ion temperature is equivalent to the electron temperature, the ion thermal velocity for carbon is ~0.9 cm/μsec. For most of the time of interest, the plasma ions are supersonic, and the measured ion current must be incident only upon the front face of the double probe. The average ion velocity may be used as the incident ion velocity, and the effective probe area is simply the cross-sectional area of the probe tip. As the average ion velocity becomes comparable to the ion thermal velocity, the full surface area of the probe must be considered. The calculated densities shown in this report include the effects of ions incident upon the full surface area of the probe when the average ion velocity is less than twice the assumed thermal velocity, or for times later than ~22 μsec.

Another potential source of error in the assumed probe area comes from sheath effects around the probe tips. The electron depleted sheath which forms around the negatively biased probe tip can increase the effective collecting area of the probe. For the bias voltage used, the sheath can increase the effective probe area by 4% to 13% when the ions are not supersonic. The sheath was not included in the calculations presented here because it is not clear how to properly include the effects of the sheath in the case of supersonic ions, and the effect is small compared to the uncertainties in extrapolating to the average density for the entire switch.

Due to shot to shot variations in gun output, variations in output from gun to gun, and the extrapolation necessary to compute the average density across the entire switch, there is significantly more uncertainty in the calculated average density than the

calculated local densities. The uncertainty during the early time plasma is not as great as later in time, because there is typically less variation in the output gun to gun. Later in time the standard deviation in the measured densities from the six guns can be as high as 50%, and the extrapolation of the density to locales not actually measured can cause an uncertainty in the average density which exceeds a factor of two. To narrow the uncertainties in the average density, the local density needs to be measured at many more locations.

Initially two driver banks were set up to drive the six guns, although the plan was to use only one driver. Each gun was configured with a single coaxial lead connecting it to the driver bank. The measured densities along the centerlines of the guns' paths were found to compare reasonably well with the values expected from the initial tests, but the FWHM was appreciably more narrow. Since the radial distribution was less than anticipated, the first power shots utilized two driver banks, three guns per bank, one cable per gun. The calculated average densities for the preliminary power shots were 5×10^{11} to 2.4×10^{12} cm^{-3}. The current waveforms for these shots showed that the delivered density was less than the desired density.

To increase the average plasma density, three driver circuits were used to drive the guns, and the inductance of the leads to the guns were reduced. The inductance was reduced by reducing the length of the connecting leads, and by using two coaxial cables per gun. With this configuration average plasma densities ranging from 5×10^{11} to 4.5×10^{12} cm^{-3} were achieved. Shown in Figure 2-8 are the calculated average electron densities as functions of time for switch lengths of 10, 20 and 30 cm with the three banks at 25 kV charge driving the six cable guns. The absolute values are uncertain by a large factor (probably > 2) due to the finite number of measuring points, accuracy of the probes, and the averaging assumptions, but the relative values are more accurate.

2.4 DATA SUMMARIES AND EXPERIMENTAL RESULTS.

Table 2.1 lists the relevant experimental parameters for the thirty-eight shots taken during the DM-2 tests and includes tabulation of: (1) driver charge voltage -- 15 20, and 25 kV; (2) driver banks -- two with 15-ft. cables (one cable each), three with 10-ft. cables (two cables each); (3) delay time [estimated switch plasma densities ranging from 5×10^{11} to 4.5×10^{12} for the 3-driver, 25 kV POS bank voltage shots can be obtained by referencing Figure 2-8; (4) POS length -- 10, 20, and 30 cm; and (4) load inductance or impedance.

For purposes of the data analyses and discussions that follow, the conduction current is defined as the current flowing into the POS at the time current begins to flow in the first downstream cathode B-dot location. The onset of current is determined by measuring when 50 kA and 100 kA flow downstream, and extrapolating linearly back to zero current. This procedure is also used to determine the conduction time. The onset of the conduction phase is defined to begin when 100 kV appears on the DM-2

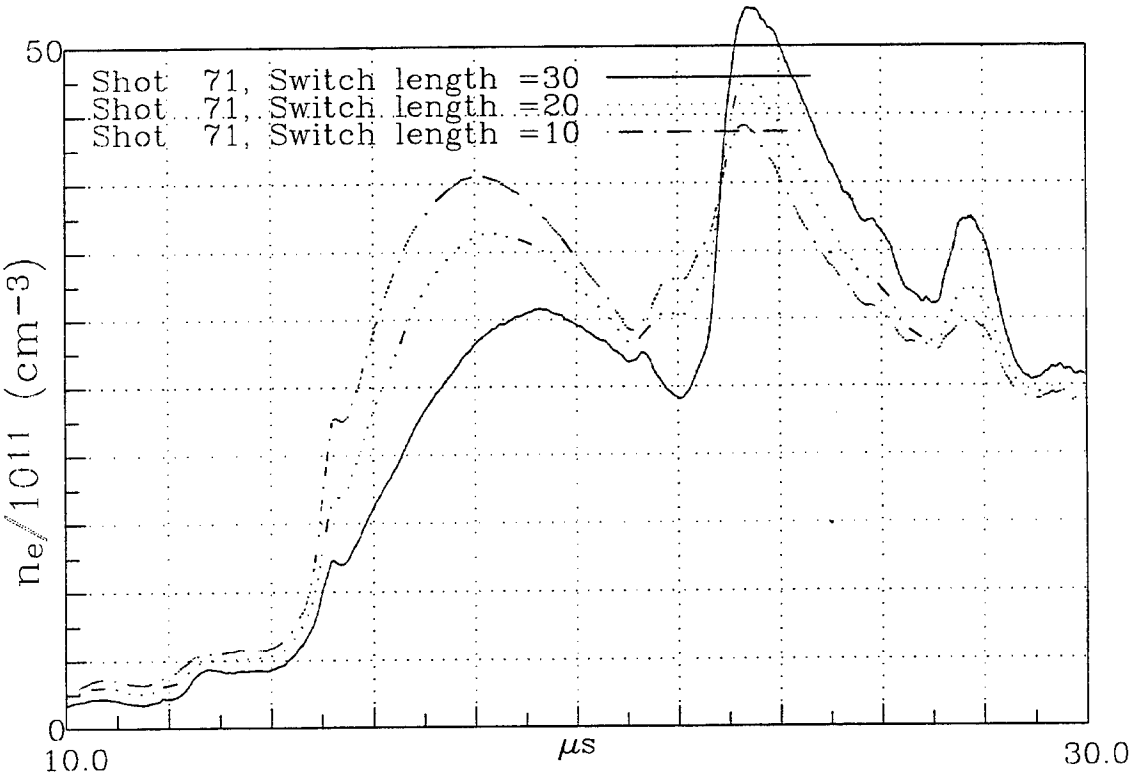

Figure 2-8. Calculated average electron densities for three switch lengths.

Table 2-1. Table of shot parameters.

Shot	POS Vbank	# drivers	Delay (μs)	Est. Average Plasma Density	POS Length	Downstream Inductance (nH)
425	15	2	15	--	30	12
426	25	2	15	--	20	12
427	25	2	15	--	20	12
428	25	2	17	--	20	12
429	25	2	20	--	20	12
430	25	2	24	--	20	12
431	20	3	18	--	20	12
432	25	3	18	3.6×10^{12}	20	12
433	25	3	20	3.3×10^{12}	20	12
434	25	3	20	3.3×10^{12}	20	12
435	25	3	0	--	20	36
436	25	3	20	3.3×10^{12}	20	36
437	25	3	23	3.8×10^{12}	20	36
438	25	3	23	3.8×10^{12}	20	36
439	25	3	26	3.0×10^{12}	20	36
440	25	3	16	2.4×10^{12}	20	36
441	25	3	14	5.0×10^{11}	20	36
442	25	3	14	5.0×10^{11}	20	36
443	15	3	20	--	20	36
444	25	3	23	4.5×10^{12}	30	36
445	25	3	20	3.0×10^{12}	30	36
446	25	3	26	3.6×10^{12}	30	36
447	25	3	23	4.5×10^{12}	10	36
448	25	3	20	3.5×10^{12}	10	36
449	25	3	20	3.5×10^{12}	10	36
450	25	3	20	3.5×10^{12}	10	64
451	25	3	20	3.5×10^{12}	10	64
452	25	3	20	3.5×10^{12}	10	64
453	25	3	0	--	10	64
454	25	3	20	3.5×10^{12}	10	64
455	25	3	14	6.0×10^{11}	10	36
456	25	3	20	3.5×10^{12}	10	36
457	25	3	18	4.0×10^{12}	10	36
458	25	3	24	4.5×10^{12}	10	36
459	25	3	19	3.8×10^{12}	10	36
460	25	3	20	3.5×10^{12}	10	36
461	25	3	20	3.5×10^{12}	10	Open Circuit
462	25	3	16	3.0×10^{12}	10	Open Circuit

vacuum interface. The opening time is the time for the downstream cathode current to go from 10% to 90% of the upstream current.

Before discussing the power transmission characteristics of the opened switch, we first review the observed conduction and opening characteristics of the low density switch under various operating conditions.

Operational Dependence on POS Length. The length of the POS was varied systematically from 10-cm to 30-cm through the use of baffles installed on the anode. Figures 2-9 and 2-10 show the observed dependence of the conduction time and current on the delay time between firing the plasma source driver and firing DM-2 for the range of POS lengths. There is no observable difference caused by the change in length. For reference, a line fit to the 10-cm data, and a line 40% above it are shown. A possible explanation for this lack of length dependence is that the bulk of the data occur in or near the MBP operational mode. This mode is predicted to have no length dependence for the conducted current.

In addition to having no effect on the observed conduction times, the length of the switch also had little influence on the observed opening time, as shown in Figure 2-11. The line through the data implies opening times are a monotonically increasing function of conduction times.

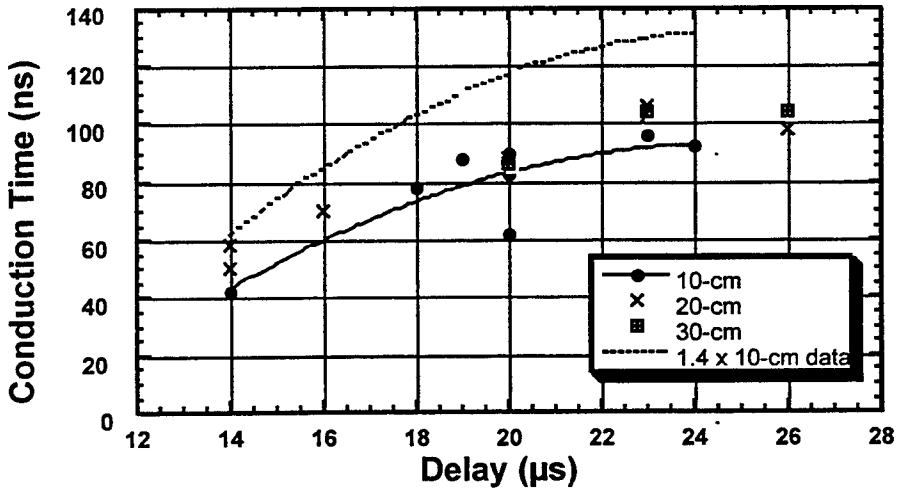

Figure 2-9. Dependence of the POS conduction time on the delay time for various plasma lengths.

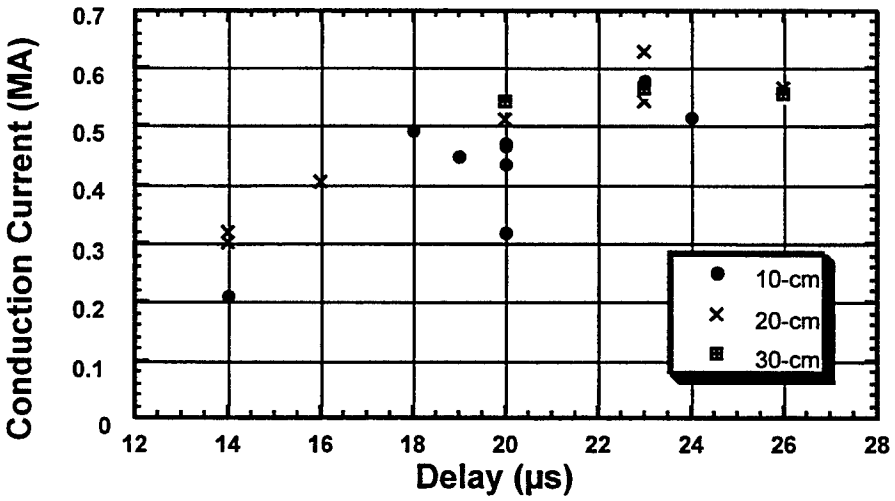

Figure 2-10. Dependence of the POS conduction current on the delay time for various plasma lengths.

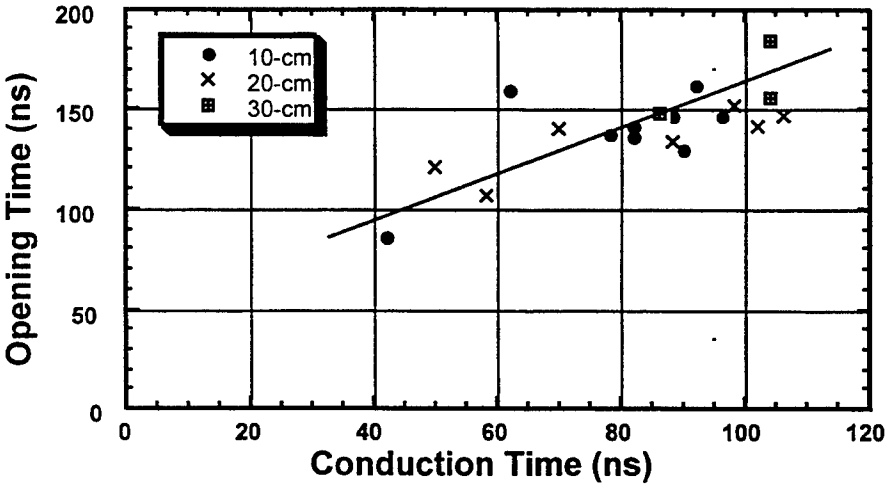

Figure 2-11. Opening time of the POS as a function of conduction time for various tests.

Operational Dependence on POS Driver Bank. The next system variable to examine is the driver bank used to provide plasma to the POS. In Figure 2-12, data obtained into a 12 nH load with a variety of plasma drivers are compared. Figure 2-13 shows similar data for a 36 nH load. In both cases there is no significant difference in

operation due to the different methods of producing the plasma. Next we will look at the operation of the POS into the three loads that were inductors.

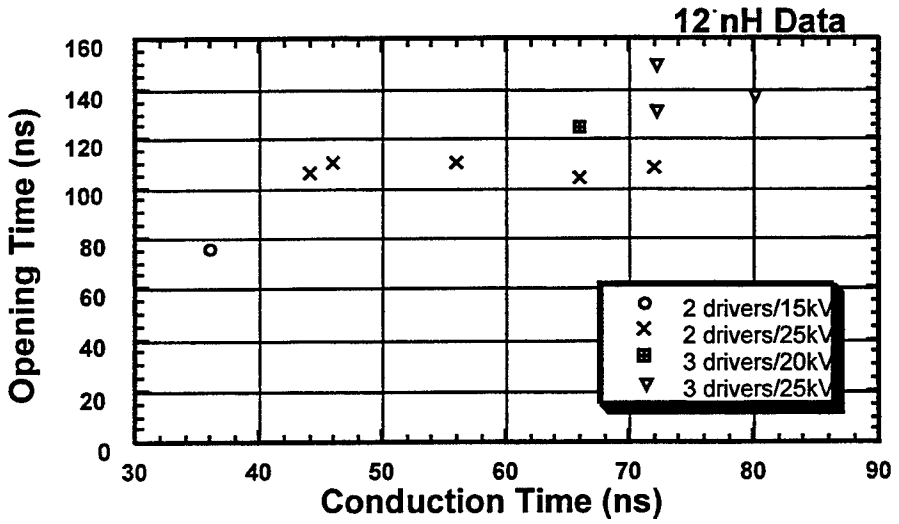

Figure 2-12. Comparison of POS performance with a 12 nH load for a variety of plasma drivers.

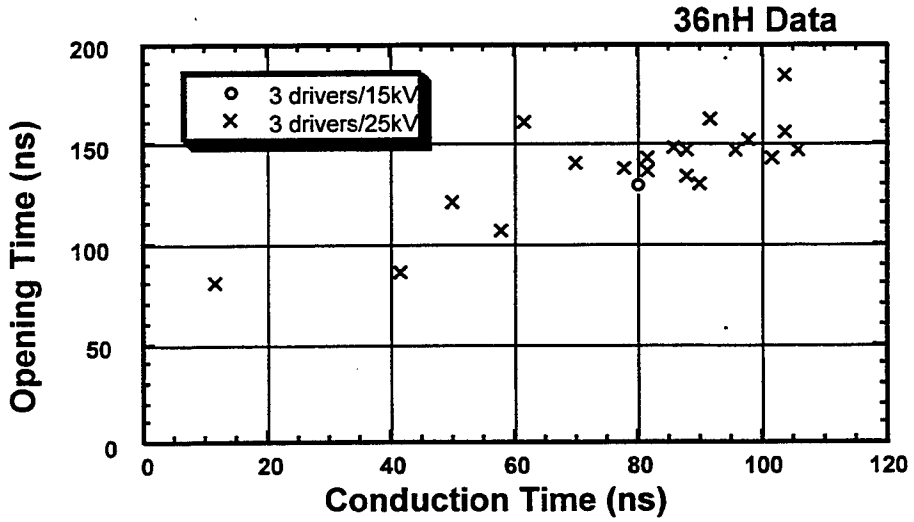

Figure 2-13. Comparison of POS performance with a 36 nH load and two driver configurations.

Dependence on Load Inductance. From consideration of the POS as a simple electrical element, one would expect that as the load inductance increased, the rate of current transfer to the load would decrease. This behavior was not observed however. The current risetime out of the POS is remarkably constant as the load inductance varies from 12 nH to 64 nH. The relation between opening time and conduction time for these various inductances is shown in Figure 2-14. Details of the actual downstream load currents showing similar dI/dt during the opening phase are shown in Figure 2-15. In this last figure, the 12 nH data have been shifted 30ns later in time to allow comparison with the other inductances. [There were no long conduction time shots with the 12 nH load to allow direct comparison.] The observed behavior is consistent with a space-charge limited erosion opening mechanism, where higher load impedances initially increase the voltage at the switch and correspondingly increase the erosion rate to support the higher L dI/dt required to produce the similar current rise rates into the various inductances.

Diagnostics for the Opening Phase of the POS. An attempt was made to measure signals related to the electron and ion fluxes in the switch during the opening event. The objective was mostly to determine signal magnitudes and to see if measurements using Faraday cups were practical on this particular switch. Despite the limited data, it appears clear that both the PIN diodes and the ion Faraday cup are useful for further probing of this POS, and implementation of arrays of these diagnostics could give valuable temporal information on the opening processes of the switch. We briefly summarize the observation of high energy electrons during opening by comparing in Figure 2-16 the measured x-ray output of DM-2 in the far-field to the calculated IV^2 product for the POS. The peaks have been aligned due to questions about the timing of the cables used for this diagnostic.

In the following figure, (Figure 2-17), the Child-Langmuir current calculated from the POS voltage and assuming a critical current gap is compared to the measured ion Faraday cup signal. The time-of-flight of the ions has been taken into account. The measured ion current signal is too noisy to reach any firm conclusions on the magnitude of the ion current during opening of the switch, but the existence of ion current after switch opening suggests that either the switch plasma was not completely eroded, some anode electrode plasma had been generated by electron deposition, or the continued streaming of switch plasma into the opened switch provided a source-limited ion current after opening. Tests with injection of switch plasma through the cathode electrode toward and through the anode electrode (not possible for this particular experiment series) would help clarify the situation.

Power Flow With A POS. In this section data will be presented to show power flow upstream and downstream of the POS for a range of conduction times, and into 36 nH and 64 nH loads. We will begin with an intermediate conduction time shot (shot 436 - 88 nsec conduction time into a 36 nH load). Beginning with monitors at the upstream of the switch, the first point to notice is that there is sometimes launched flow upstream

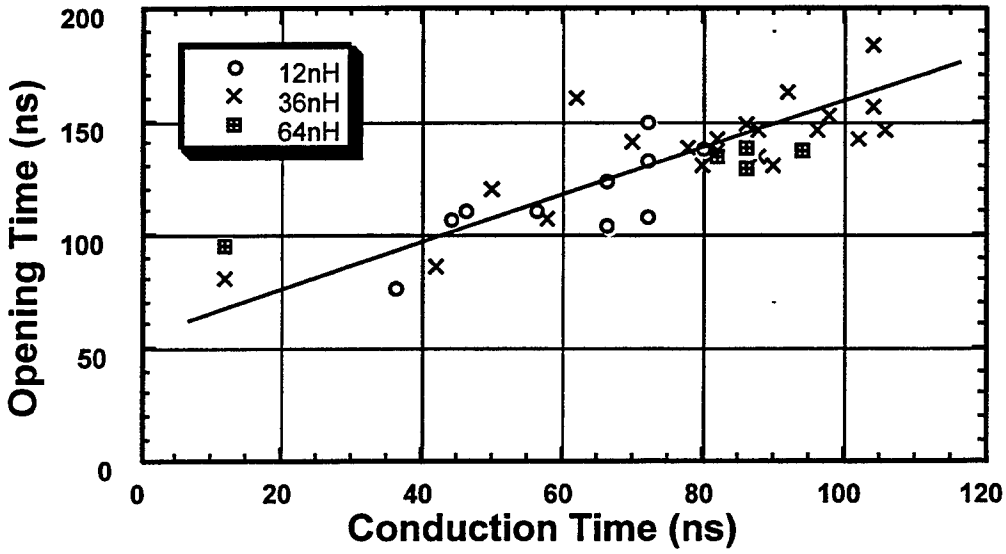

Figure 2-14. Opening time of the POS is independent of the load inductance.

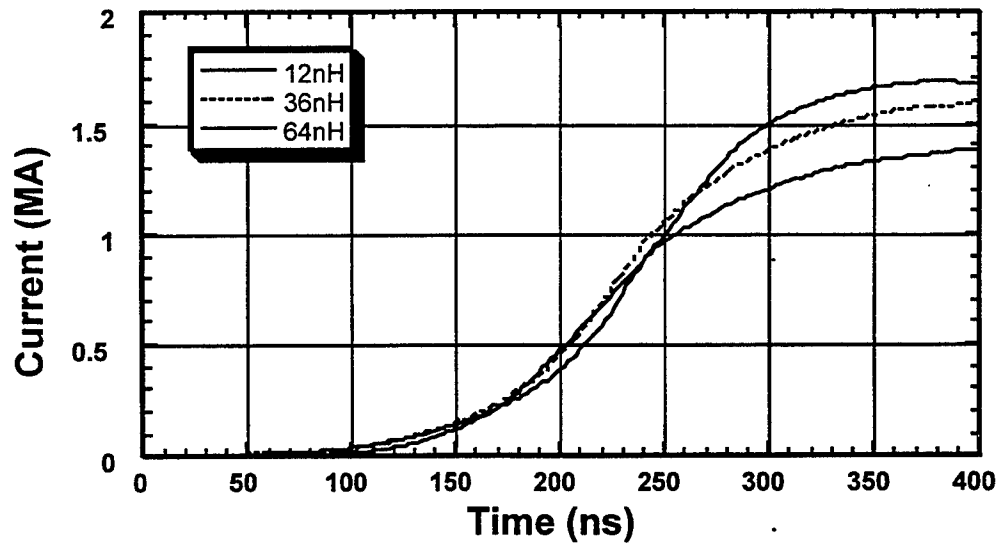

Figure 2-15. Current waveforms into the inductors are very similar despite the change in inductance.

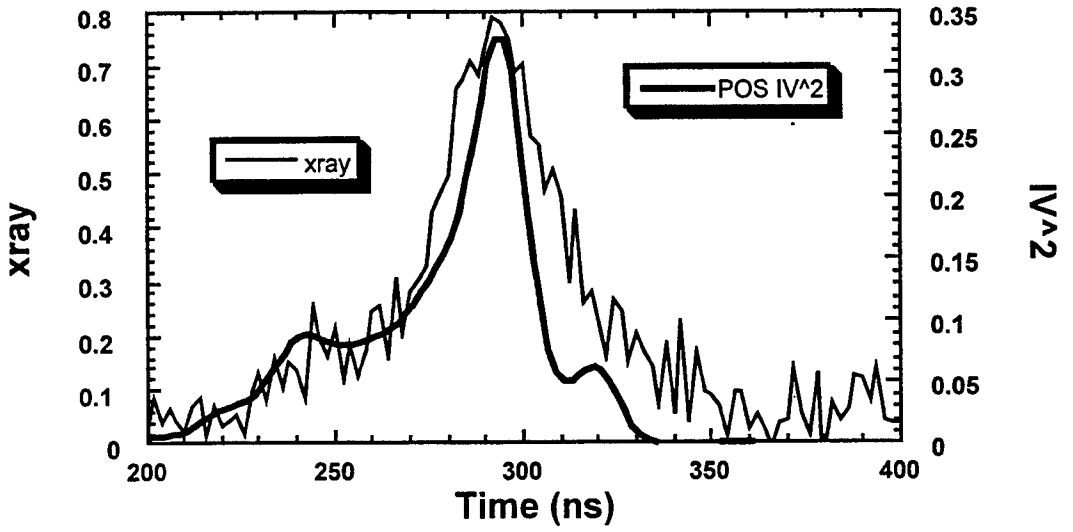

Figure 2-16. Comparison of far field PIN signal and IV^2 in the POS region.

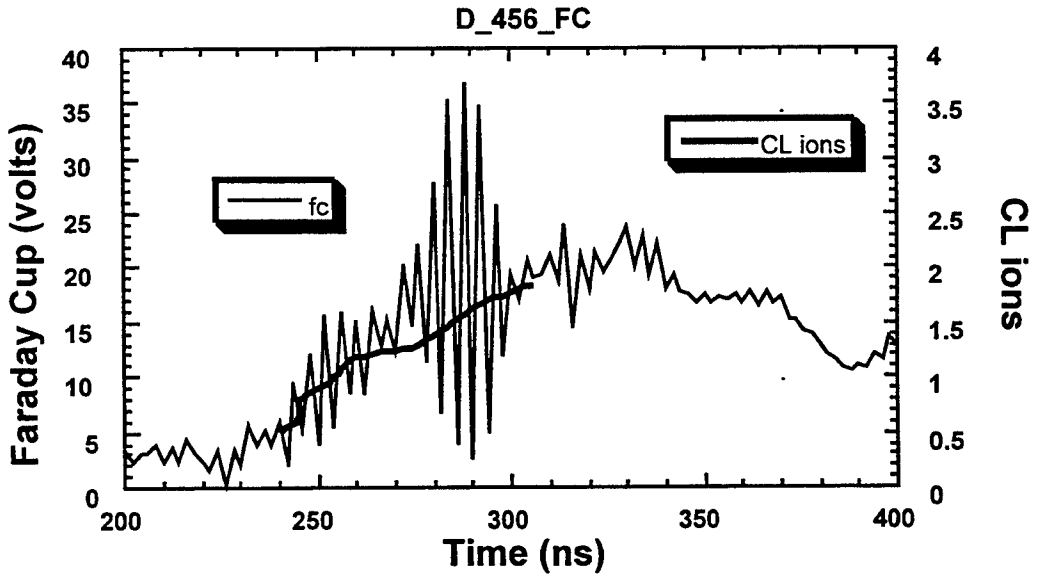

Figure 2-17. Comparison of measured Faraday cup signals in the cathode to predictions of ion current based on POS voltage and gap calculations.

of the switch during the conduction phase. This flow is not seen without plasma injection and could be due to the cathode B-dot being partially shielded initially or to azimuthal variations in current flow through the switch plasma resulting from azimuthal variation in injected plasma density. The magnitude of this current is only about 40-50 kA and the difference observed for shot 436 is shown in Figure 2-18. For reference the upstream and downstream anode currents along with the POS voltage, are shown in Figure 2-19.

Moving downstream of the switch now, the next probes to compare are the anode and cathode B-dots at positions b and e (bottom and extra) for shot 436. At the other positions there were either noise problems on one of the monitors, or damage to the B-dot. Some of these problems were subtle enough, unfortunately, not to be caught until detailed analysis of the data. The two measurements of electron flow immediately downstream of the POS are shown in Figure 2-20.

In analyzing the launched flow, it became clear that it is best to use differences of probes at the same azimuthal location, rather than rely on averages when different azimuthal locations are monitored (as in the case of some probes not working properly), because of the asymmetries observed in the downstream current flow at location "S". These differences are shown for shot 436 in Figure 2-21 and indicate that either the switch is moving downstream slightly in an unstable fashion, or is opening at different times around its circumference which is probable because of the measured azimuthal variations in the injected plasma flux from the six discrete plasma gun geometry. Returning to Figure 2-20, the 100-150 kA launched electron flow increases as the switch is opening and falls to < 50 kA by the time current has been transferred to the load.

Finally, for shot 436, the launched flow observed at location "3" is shown in Figure 2-22 for the two azimuthal positions monitored. The difference currents in this figure are at the limits of being resolved and agree well considering the size of the currents. It appears that of the 100-150 kA launched flow measured immediately downstream of the POS during the opening phase, only a small amount transports to the load region. The remainder must be lost to the anode. After switch opening, from 250 nsec onward, there is no measurable (> 50 kA) difference between drive current and load current.

Next we look at the same traces for a short conduction time shot: shot 455 with a conduction time of 42 nsec. From the waveforms in Figure 2-23 and Figure 2-24, we see that the launched flow is much less than in the previous shot, but the POS voltage is much less also. Again, the launched electron flow measured just downstream of the switch is greatest during the switch opening time period and decreases after opening. The waveforms of the last figure give a good indication of the level of difference current able to be resolved. All these currents have error bars of order 20 kA.

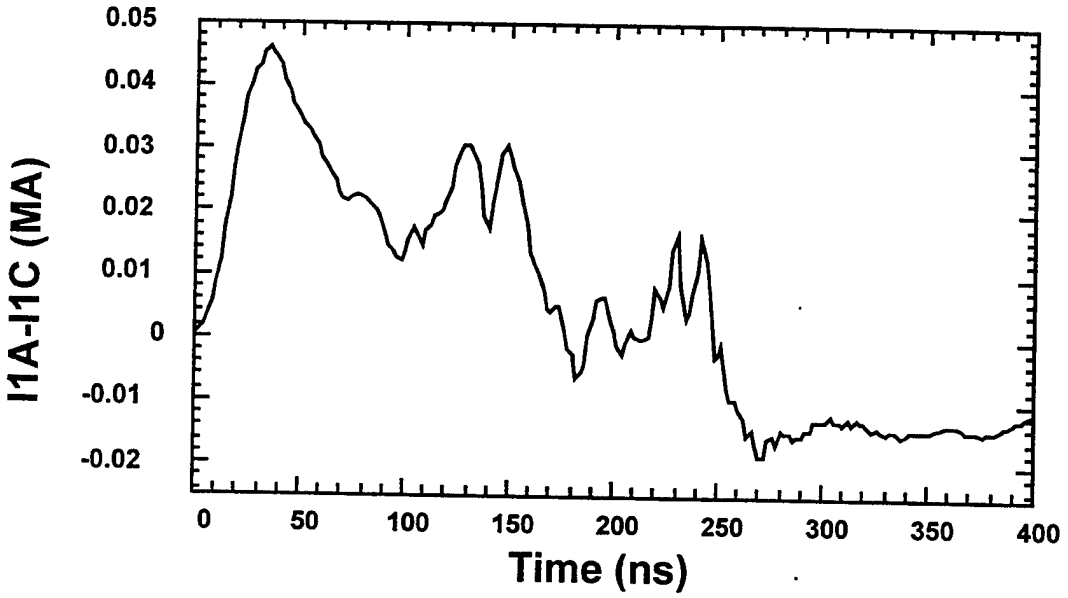

Figure 2-18. Difference between the upstream anode and cathode B-dots for shot 436.

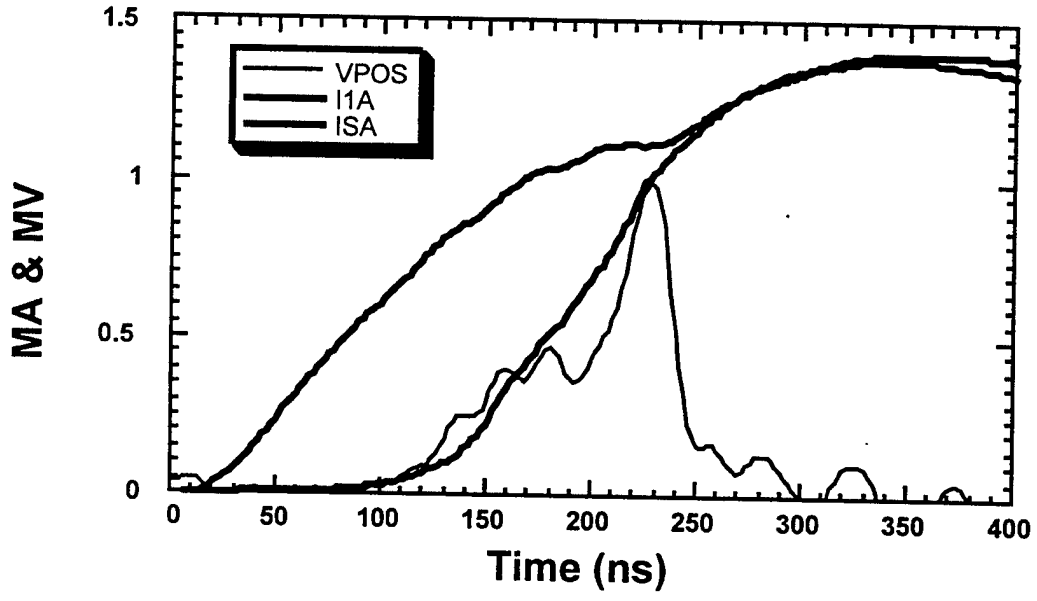

Figure 2-19. Current and voltage waveforms for shot 436.

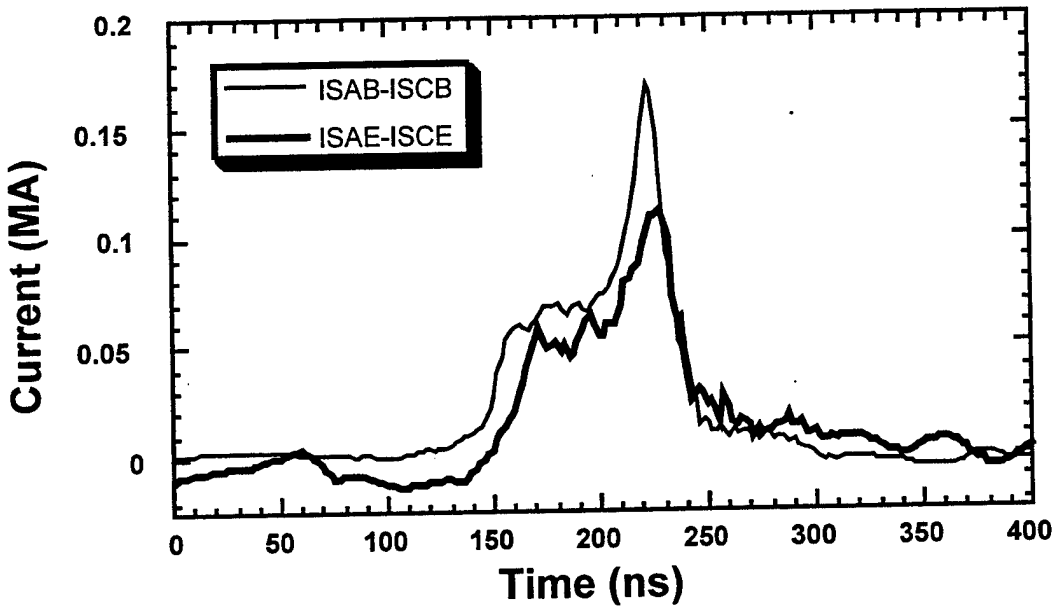

Figure 2-20. Difference between the downstream anode and cathode B-dots at location "S".

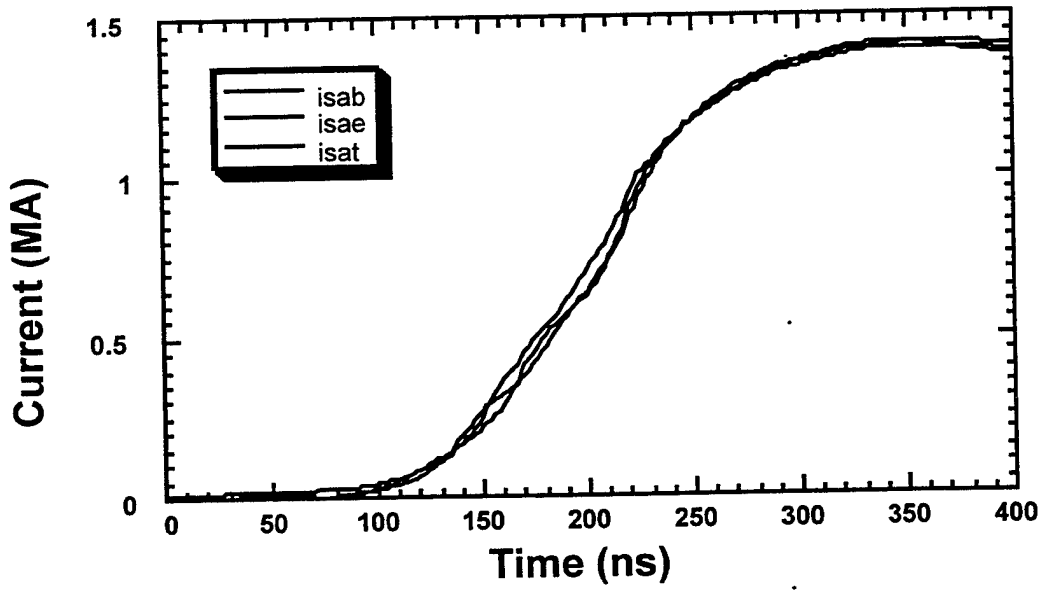

Figure 2-21. Downstream anode currents measured at three different azimuthal locations showing asymmetries in the opening.

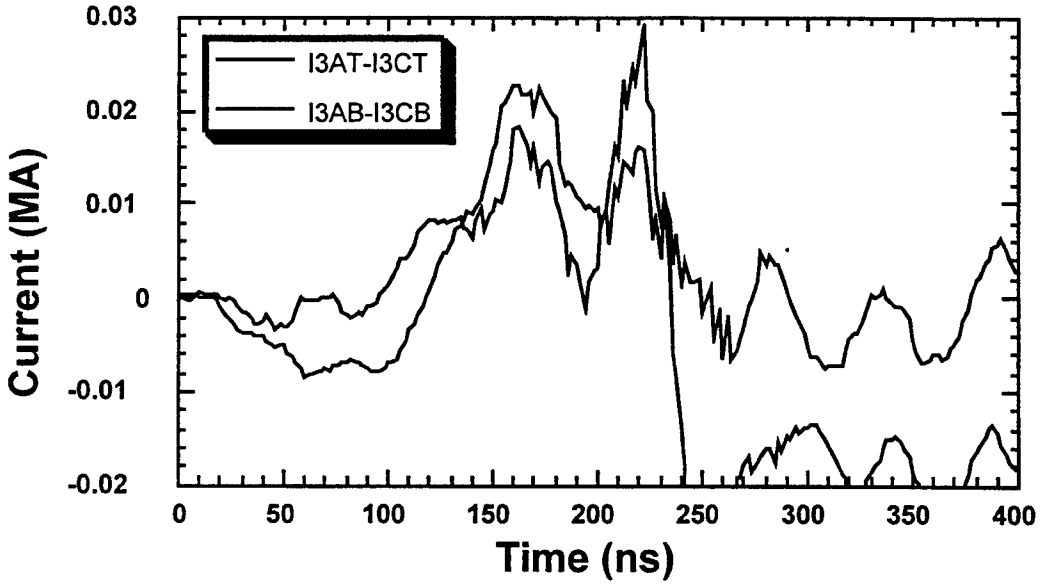

Figure 2-22. Downstream launched flow at position "3" for shot 436.

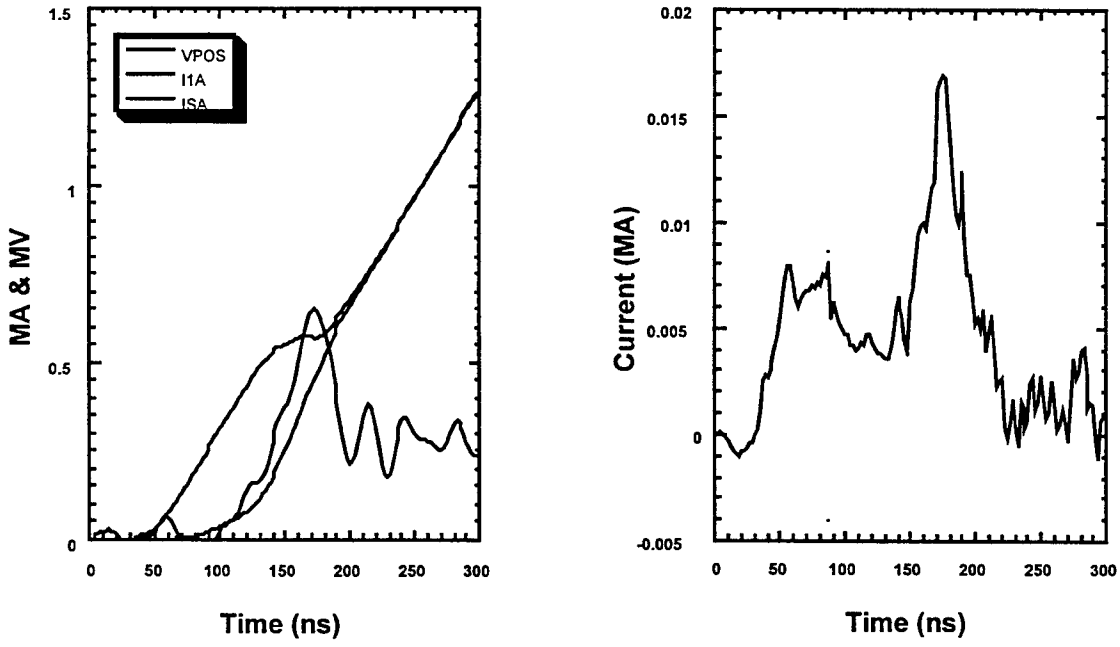

Figure 2-23. Currents, POS voltage, and upstream difference current for a short conduction time shot (shot 455).

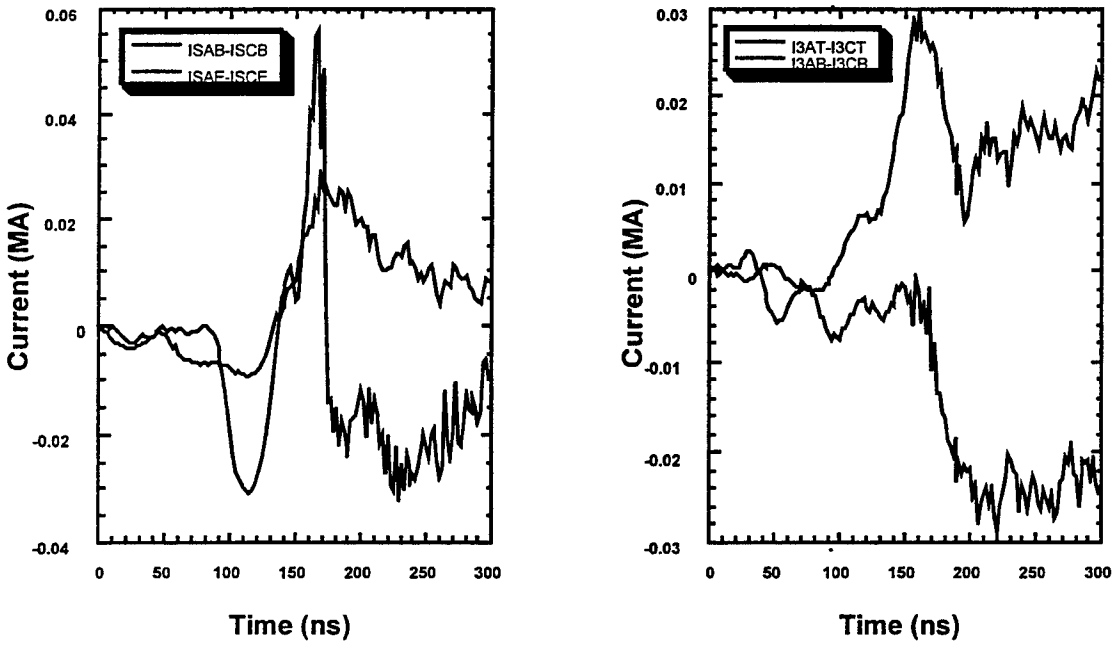

Figure 2-24. Difference currents measured at locations "S" and "3" for shot 455.

Next a shot with a longer conduction time of 104 nsec is examined in Figures 2-25 and 2-26. Despite the lower POS voltage than shot 436, there appears to be more launched flow in shot 444 which may be related to the higher density requirement of the longer conduction time in shot 444.

Finally, we present data in Figures 2-27 and 2-28 from shot 452 which had a higher inductance load and a conduction time of 86 nsec, the same nominal conduction time as shot 436.

Despite the higher POS voltage on shot 452, the launched flow is about the same as in shot 436. This result seems to indicate that the POS opens to a larger gap with the more inductive load or that the ion flux partially controlling the magnitude of the launched electron flow is source-limited. Whether either is true or not has important implications to the use of a large diameter non-hydro POS as a first stage switch in terms of the losses expected when the second stage switch opens.

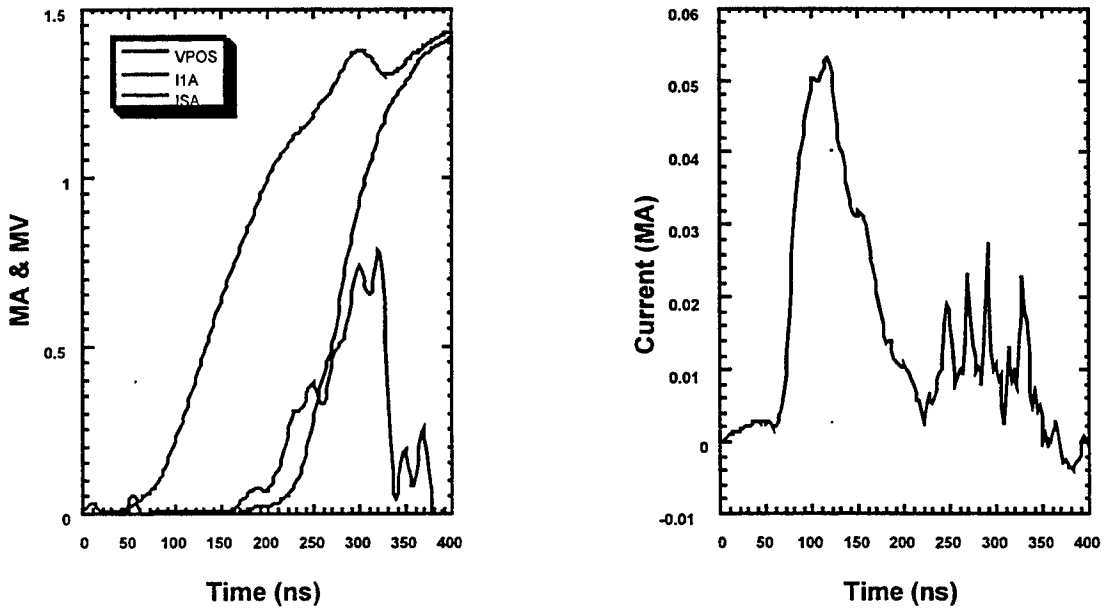

Figure 2-25. Currents, POS voltage, and upstream difference current for a long conduction time shot (shot 444).

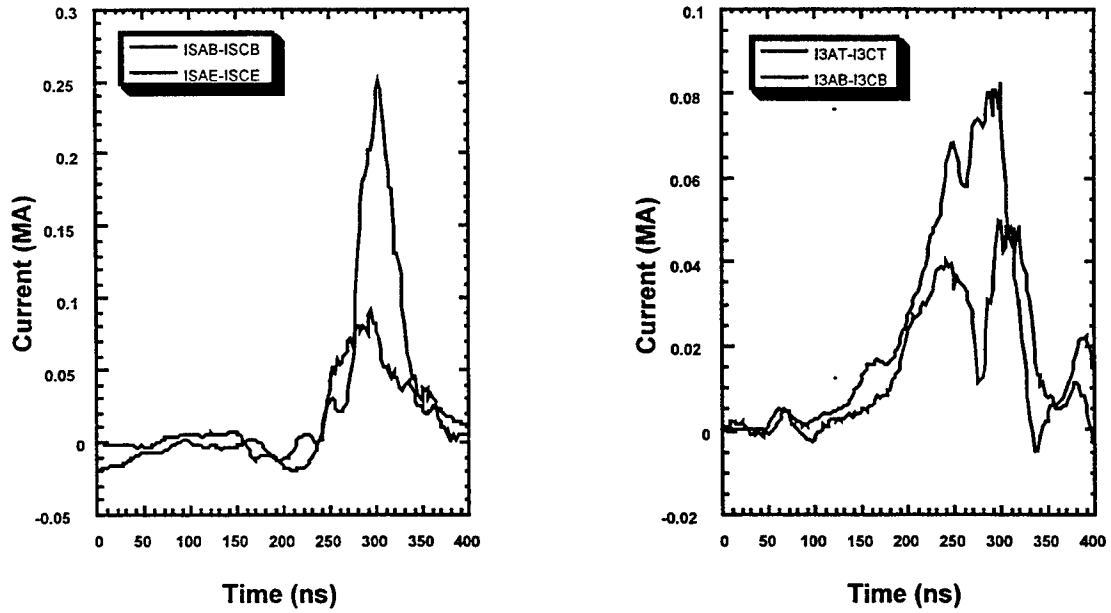

Figure 2-26. Difference currents measured at locations "S" and "3" for shot 444.

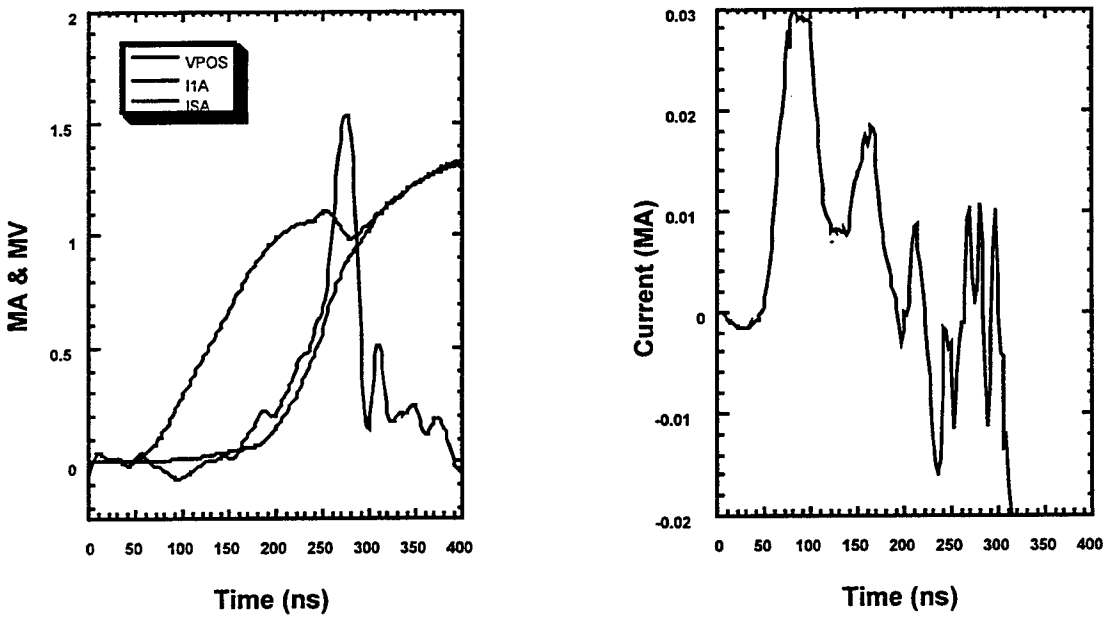

Figure 2-27. Currents, POS voltage, and upstream difference current for a 64 nH load (shot 452).

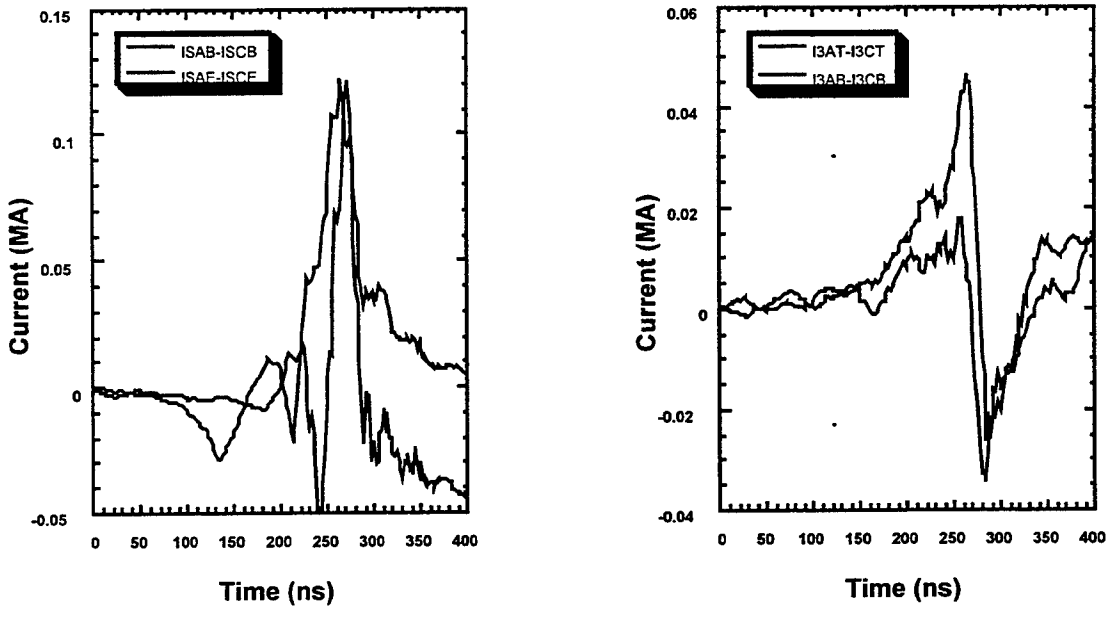

Figure 2-28. Difference currents measured at locations S and 3 for shot 452.

Figure 2-29 shows the currents for a shot into a resistive load. The resistive load was achieved by removing the inductive short, leaving a ~3-ohm (vacuum impedance) MITL that provided a roughly 1.25-1.9 ohm diode load (corresponding to saturated parapotential flow or the minimum current flow solution). In this test the switch opened to about 1.5 MV before significant current was drawn by the down-stream load. At the peak diode load current of 530 kA, the anode current upstream of the switch was 600 kA, indicating about 70 kA loss (12%) in the switch region. The sheath flow downstream of the switch shown on the figure is calculated from average currents at the locations, and as such is not as accurate as the sheath currents shown previously (probably 50 kA resolution vs. 10-20 kA resolution for the single azimuthal location data). The sheath flow downstream of the opened switch persisted well beyond the opening phase of the switch and suggests that either energy deposition in and downstream of the switch region was sufficient to create enough anode plasma to maintain sizeable (~ 17%) launched electron flow, or that the continued injection of plasma from the POS guns provided a source limited ion current that allowed continued electron launching from the switch region.

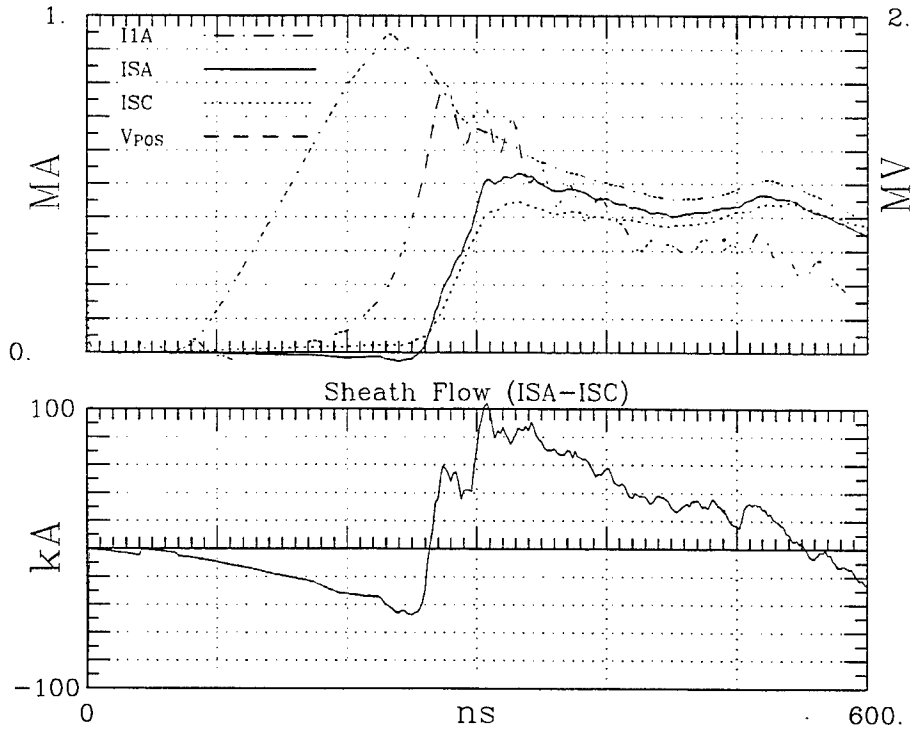

Figure 2-29. Currents, voltage and difference currents for a shot with a resistive load.

More data for a wider range of diode load impedances is needed, particularly for cases where (1) the geometric impedance of all structures downstream of the switch is greater than the geometric impedance of a fully opened switch (in order to

unambiguously determine the full extent of switch plasma erosion), and (2) where an adjustable impedance, fast turn-on, diode load is employed (instead of the smooth radial plate MITL that was the load in the test reported above).

Output Current With and Without POS For Various PRS Drive Times. In cases where the low density switch opened into inductive loads typical of the downstream inductance associated with candidate direct drive Quad PRS circuits, the current transfer efficient was excellent and the load current risetime was sharpened. To quantify the projected benefits of such a sharpening switch approach, we have defined an effective risetime (T_{eff}):

$$T_{eff} = \frac{\int_0^{tf} I(t)dt}{I(tf)} \tag{2.8}$$

This quantity can calculated for shots with and without a POS, and the currents available at various values of T_{eff} can be found. For PRS loads, which may operationally be limited to short implosion times due to Rayleigh-Taylor instability growth, comparing the current available at a fixed time is a good way of judging the efficacy of the POS. These comparisons are made in Figure 2-30, for the three load inductances tested. Once again, the 36 nH load is indicative of a typical Quad PRS design.

As the PRS loads are made stable to longer implosions, the POS plays a diminishing role as can be seen by the convergence of the current levels at longer T_{eff}. However, for PRS designs at present which may be pushed up to 150 nsec, the POS system shows an increase in current level of 1.35 MA/0.8 MA, or nearly a 70% improvement in current.

2.5 CONCLUSIONS.

Efficient power flow through an opened low density POS has been demonstrated for inductive loads typical of PRS driver circuits and for (limited data) high impedance diode loads. The switch was designed (1) to operate in a bi-polar or modified bi-polar (enhanced opening via electron self-magnetic insulation) conduction regime vs. the MHD or EMH regimes typical of the present DECADE POS and (2) to limit electron energy deposition in the anode electrode during switch opening to minimize electrode plasma formation and its effect on power flow.

We have not clearly demonstrated that electrode plasmas have been eliminated, however the measurement of relatively low (~ 100 kA) launched electron flow during switch opening into inductive loads, followed by a decrease to < 50 kA after switch opening suggests that the switch is opening to a large gap (several cm) and that the ion current may be injection-source limited.

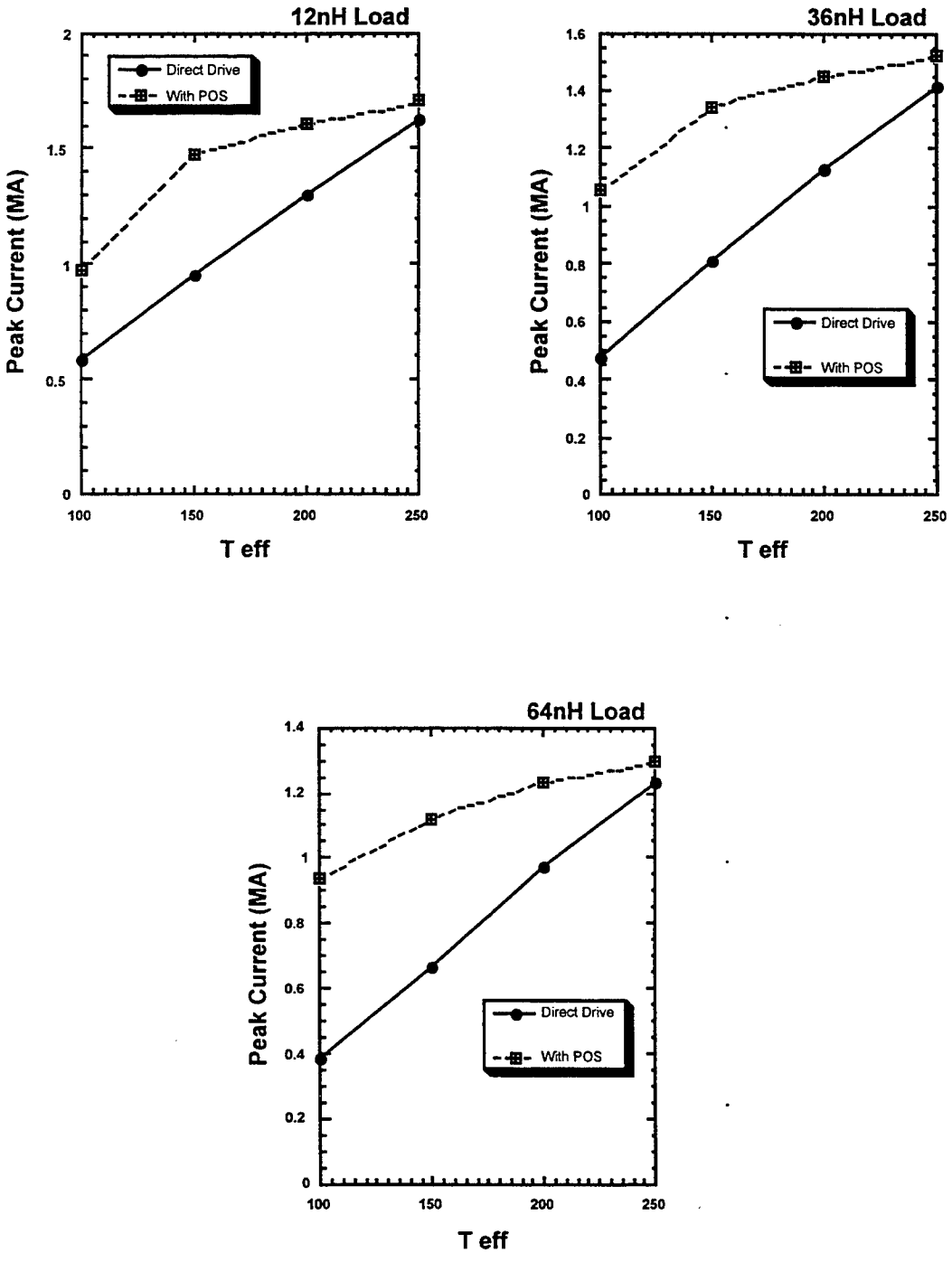

Figure 2-30. Operation with the POS shows higher currents delivered in a fixed time for 12 nH, 36 nH, and 64 nH loads.

Attempts to characterize the opened state of the low density switch by using it as the load were compromised by the diode-like loading of the downstream open-circuit hardware. The resulting tests with a ~1-2-ohm diode load showed that the switch initially opened to greater than 2-ohm impedance but that measurable launched electron current persisted well after switch opening perhaps because the energy absorbed by and just downstream of the switch before the downstream load reached its operating impedance was sufficient to form an anode electrode plasma.

For the inductive load cases where inductances were selected to be representative of candidate Quad PRS direct drive circuits, the low density switch and resulting power flow was demonstrated to allow up to 100 nsec reduction in the 10-90% load current risetime without significant compromise in peak current. The small launched electron flow after switch opening is also compatible with use of downstream vacuum convolute structures for combining currents from multiple lines to a single PRS.

Finally, the good power transmission characteristics of the low density switch opens the potential for its use to amplify power (≤ 2) to a nearby downstream high density MHD or EMH POS to reduce the conduction time requirements on these faster-opening switches.

SECTION 3

EXPERIMENTAL RESULTS OF THE DENSITY CONTROLLED OPENING SWITCH PROGRAM

In this section the experimental results of the program to investigate operation and scaling of the density controlled opening switch (DCOS) are presented. The experimental program was designed to look at switch phenomenology over a wide range of electron (j_e) and ion (j_i) current densities starting at $j_e < 100$ A/cm^2 and $j_I < 10$ A/cm^2. The initial goal was to increase electron current densities to the 1000 A/cm^2 regime for scaling to high current simulator applications. The actual results of the program achieved electron current densities of ~2000 A/cm^2 and total currents in the 100-200 kA range. As mentioned in Section 1, three rather distinct switch operation modes were observed -- two low impedance modes, both of practical interest and a high impedance mode probably of lesser practical interest. The low impedance modes exhibited either a self-opening or a conduction-without-opening behavior where the current increased with the ion current. The latter mode would be relevant to external gating of the ion source for opening. Most of the features of switch operation were observed early in the program at low j_e and j_i levels and persisted to the high current regime. A diagnostic package to obtain voltage across the switch, electron current flow patterns in the gap and ion currents at the cathode was implemented along with a gated camera to infer plasma motion. Using these diagnostics experiments were conducted to elucidate the basic switch phenomenology of these modes and obtain practical design information by varying several key parameters in several current ranges.

Parallel with the experimental work was a theoretical study of switch phenomenology by T. Hughes of MRC, Albuquerque using the simulation code IVORY. Most simulation results were one-dimensional, but some limited two-dimensional simulations were also run. The results of the simulations are given in Section 4, and remarks on relevant simulation results are given along with the data in this section.

This section begins with a description of the experimental hardware followed by results of investigations into basic switch physics issues such as cathode emission limitations and mesh transparency. These studies were first conducted using glass cross vacuum hardware with a 90 degree bend transport section between the flashboard ion source and the switch gap region, and were limited to peak ion current densities of < 10 A/cm^2. The bend was removed to obtain higher ion current densities and the remainder of the experiments were conducted with straight injection geometry using both the glass cross hardware and a coaxial switch geometry in a metal vacuum chamber. Results for the three conduction modes are then summarized, followed by data from ion collectors behind the cathode and arrays of B-dot probes to map current flow. The section concludes with results of scaling of switch operation with key parameters.

3.1 EXPERIMENTAL HARDWARE FOR DCOS EXPERIMENTS.

3.1.1 15 cm Glass Cross Hardware.

The overall experimental plan for the DCOS studies was to first address issues of scaling the electron current density from j_e ~ 10-1000 A/cm^2, and then increase the total current to the level of ~200 kA. This plan allowed diagnosis of the switch behavior, starting in regimes where modifications were simpler and diagnostics were more likely to survive. Following the plan, initial experiments were carried out with the anode-cathode (AK) gap housed in a 15 cm diameter glass cross vacuum chamber. This hardware was suitable for tests of the DCOS at low total currents, from currents a few hundred amperes up to ~20 kA, and had several advantages over a metallic vacuum chamber. The glass cross hardware allowed visible access to the entire AK gap, made insulation between electrodes simpler, and allowed for fast penetration of the applied B-fields. To scale to higher total currents than were practical in the small glass chamber, a larger metallic, coaxial system which had been used in a previous DCOS project was refurbished. This larger hardware was used for currents up to ~200 kA, at charge voltages of up to ~30 kV.

The initial experiments in the glass cross utilized a 90 degree glass bend between the AK gap and a flashboard plasma source. The purpose of the bend was to eliminate possible influence of the switch behavior by neutrals from the flashboard. Shown in Figure 3-1 is a side view of the glass cross hardware with the 90 degree glass bend. There were multiple locations in the cross for electrode hardware. The anode electrode was located at an end flange of the cross, and the cathode electrode was located near the center of the cross 25 cm from the anode. An intermediate location between the anode and the cathode, ~1.7 cm from the cathode could also hold electrode hardware. The anode typically consisted of a 2.54 cm diameter hole in 0.00127 cm thick stainless steel foil held in place by a 3.81 cm ID stainless steel ring. The plasma was fed through the anode towards the cathode. Five types of cathodes were used in this hardware. The types were foil, mesh, carbon velvet, carbon fiber and limited area stainless steel disks. The foil cathode was a ~10 cm x 13 cm rectangular piece of 0.00127 cm thick stainless foil stretched between two ~1.9 cm diameter stainless steel rollers. The mesh cathode had the same dimensions as the foil cathode, except the foil was replaced with a mesh. The carbon velvet and carbon fiber cathodes consisted of 2.54 cm diameter velvet or fiber regions surrounded by flat stainless steel with dimensions similar to the foil cathode. The limited area cathodes were solid stainless steel disks suspended on a stainless steel rod. Magnetic field coils outside the vacuum hardware provided a guiding field for the plasma to travel from the source into the AK gap. Figure 3-2 shows the field strength as a function of the axial location along the glass bend and through the AK gap. The total distance traveled by the plasma from source to cathode was ~100 cm. The field profile of Figure 3-2 was found to transmit the highest ion current from the flashboard to the cathode, even though calculations of the flux tubes showed that less than 20% of the active area of the source was intersected by flux tubes which passed

through the anode aperture. Hence the majority of the field lines from the active area of the plasma source mapped to intersect the solid anode hardware.

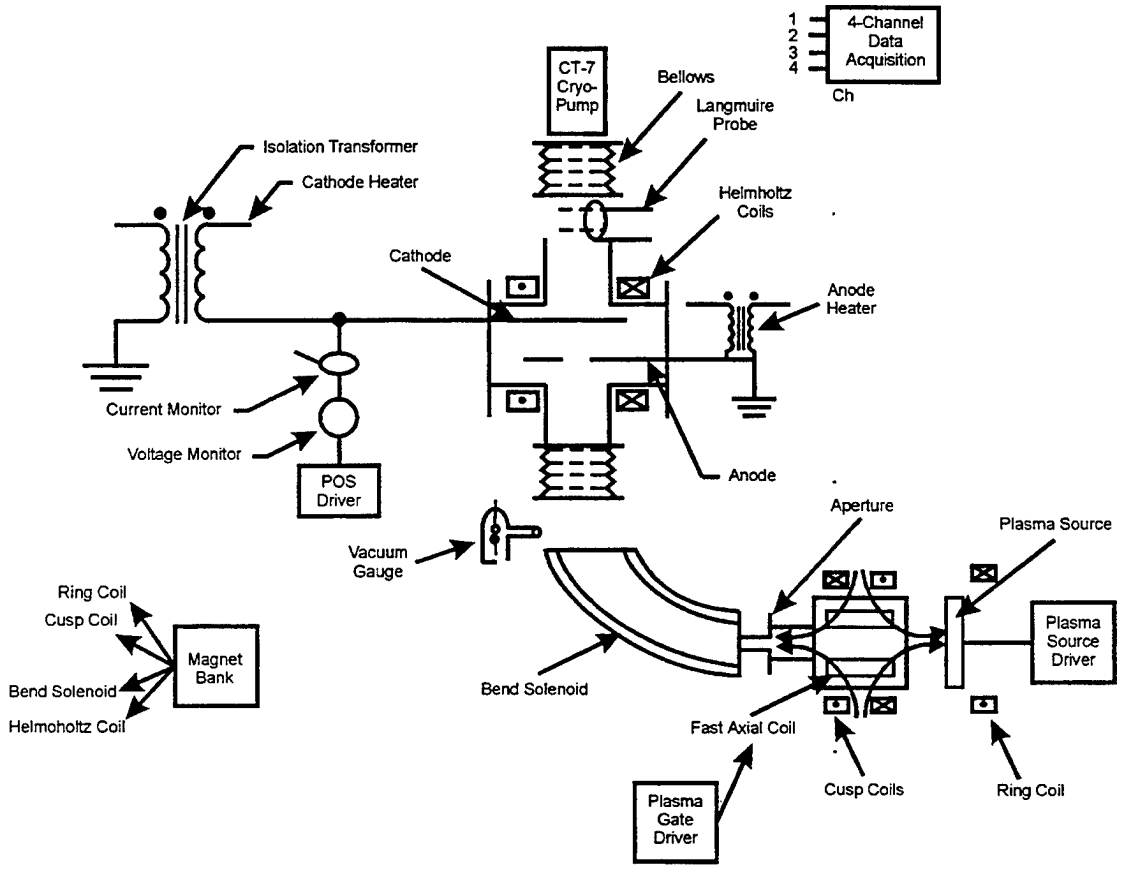

Figure 3-1. Experimental configuration of the glass cross hardware with the 90° bend.

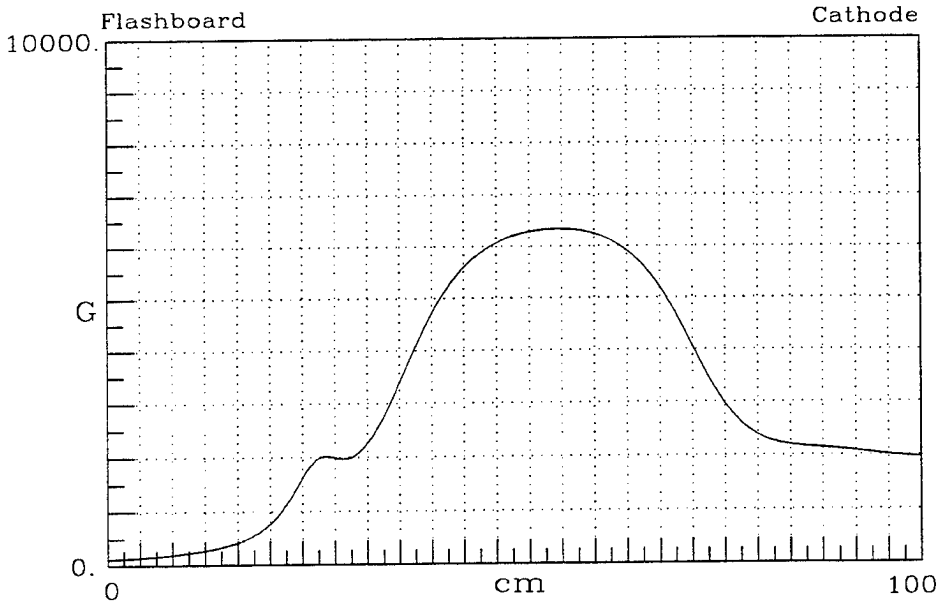

Figure 3-2. Magnetic field profile along the bend and AK gap.

The ion current as a function of time was measured by a heated 0.00127 cm thick stainless steel foil attached in the uppermost electrode location. Heating the foil collector cleaned the surface of adhered gases and allowed for more reliable measurements by reducing emissive behavior. The foil was heatable to over 500°C. Extremely careful conditioning and heating of the foil allowed for measurements with bias voltages ranging from 0 to -20 kV without breakdown of the collector. The current to the collector was measured with a Pearson current transformer. To reduce the plasma incident upon the collector and reduce the measured ion saturation current, a second, slightly larger, stainless steel foil with a 1 cm^2 aperture was placed in front of the collector foil. The measured current was dependent upon the area of the aperture, and the ion density and velocity distribution. For a population of "cold" ions (ion temperature T_i of a few eV or less) with a drift velocity ~10 cm/μsec, the ion current is strictly the area-density-drift velocity product. However, since only ions with a net velocity into the surface of the collector can be collected, if the drift velocity is comparable to or less than the thermal velocity of the ions, only a portion of the total plasma is collected. In the extreme case of zero drift velocity, the ion current into the collector surface is $J_I \cong {}^1/_4 A q_i n_i v_{thermal}$, where A is the effective area of the probe, q_i is the ion charge, n_i is the local ion number density and $v_{thermal}$ is the ion thermal velocity. A 30 eV carbon plasma with zero drift velocity, e.g., would have a collection current ~25 times less than the same plasma with a 10 cm/μsec drift velocity.

The driver bank for the AK current consisted of two 0.7 μF, 100 kV capacitors connected in parallel and switched by a single, mid-plane triggered spark gap. The

inductance of the circuit was 1.4-1.6 μH, and the resistance was typically dominated by the plasma resistance. An external resistance of ~12.7 ohms was added to the circuit during the low current experiments. Figure 3-3 shows the driver circuit and relevant dimensions of the AK gap electrodes.

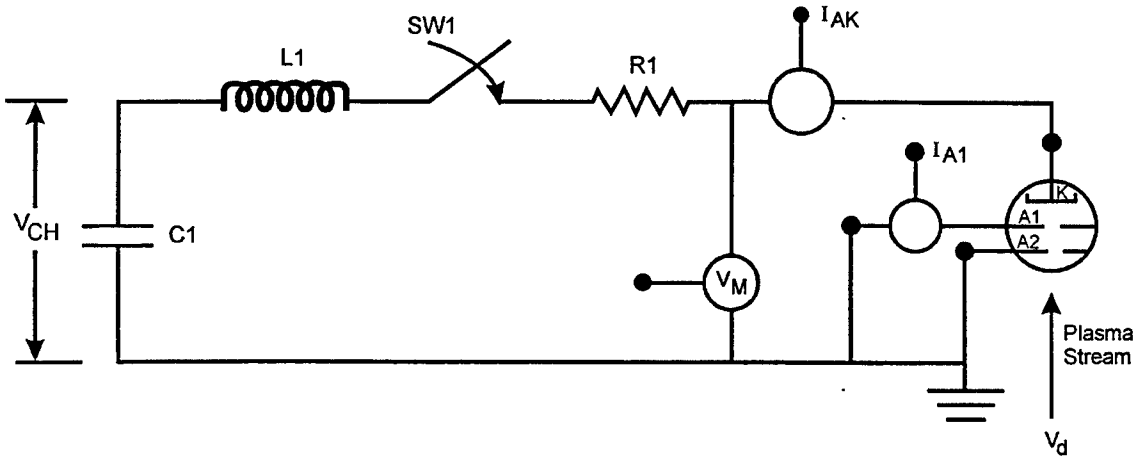

A1-K:	1.73 cm	C1:	1.4×10^{-6} F
A2-K:	25 cm	L1:	1.47×10^{-6} H
Diameter of A1 aperture:	0.44 cm	R1:	0.10 ohms + 12.7 ohms
Diameter of A2 aperture:	2.54 cm		

Figure 3-3. Lumped circuit parameters for glass cross switch apparatus with 90° bend.

The AK current was measured by a pair of Pearson 1411 current monitors. The AK gap voltage was measured by a ~400 ohm PSI vacuum voltage monitor located outside of the vacuum, or by a ~400 MΩ Northstar voltage monitor also outside of the vacuum. The 400 ohm monitor has much better frequency response than the 400 MΩ monitor, but may be more perturbative than the high impedance monitor. Time resolved images of the plasma were acquired using an micro-channel plate (MCP) gated charge-coupled device (CCD) camera. The camera is sensitive to wavelengths from 300 to 800 nm, and can be gated continuously from ~5 nsec to open shutter. The glass cross allowed the camera visual access to the entire switch plasma.

After the tests with the glass cross with the 90 degree bend, the bend was removed to increase the injected ion current. Shown in Figure 3-4 is the glass cross hardware with the 90 degree bend between the flashboard and the AK gap removed. With the bend removed, the flashboard was moved to ~ 44 cm from the cathode. Figure 3-5 shows the field strength as a function of the axial location. This arrangement greatly reduced the mirror field the plasma crossed, and increased the area of the source which mapped along field lines into the AK gap. Correspondingly, the injected ion current in the straight field configuration was much higher than with the bend, up to ~100 A/cm^2. With

the higher ion current, conduction modes not accessible at lower ion currents were explored. The effects on these regimes of a conducting mesh across the anode aperture were tested. Both a ~39x39 line-per-cm woven wire nickel mesh with wire diameters of 0.005 cm, and a ~14x14 line-per-cm woven wire tungsten mesh with wire diameters of 0.009 cm were used. The tungsten mesh, which had a geometric transparency of ~77%, was found to survive better, and was the mesh used in the conduction data presented in this report.

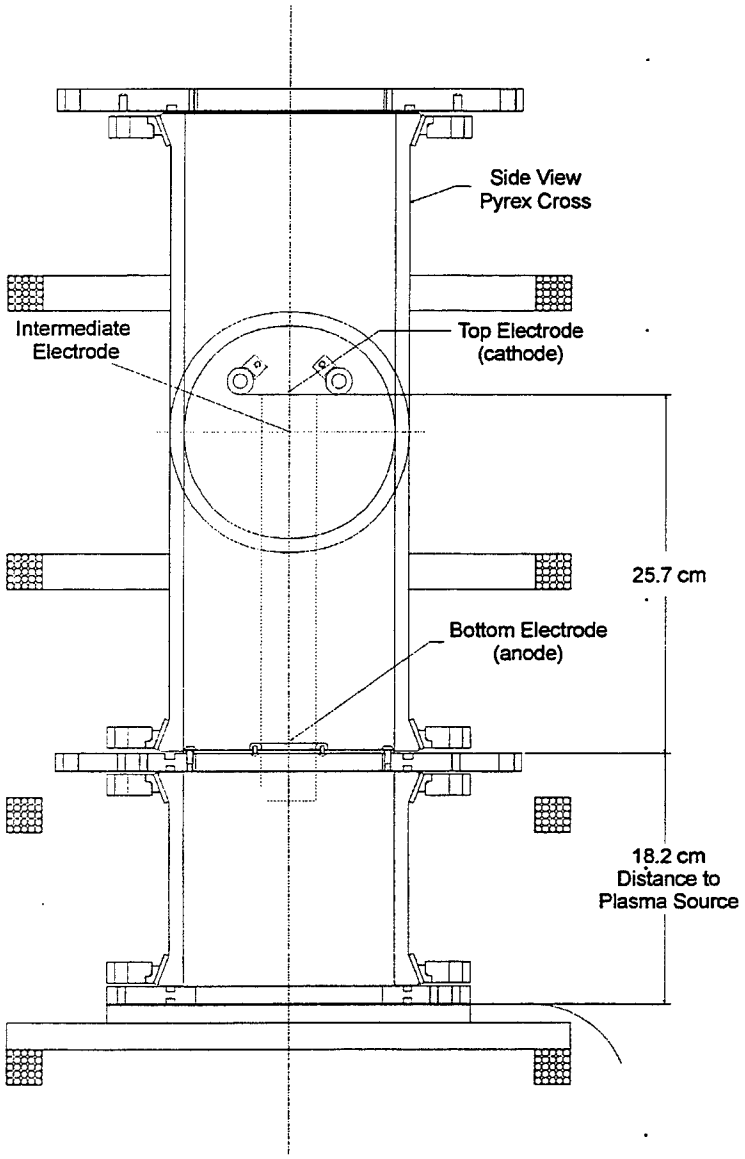

Figure 3-4. Experimental configuration with the 90° bend removed.

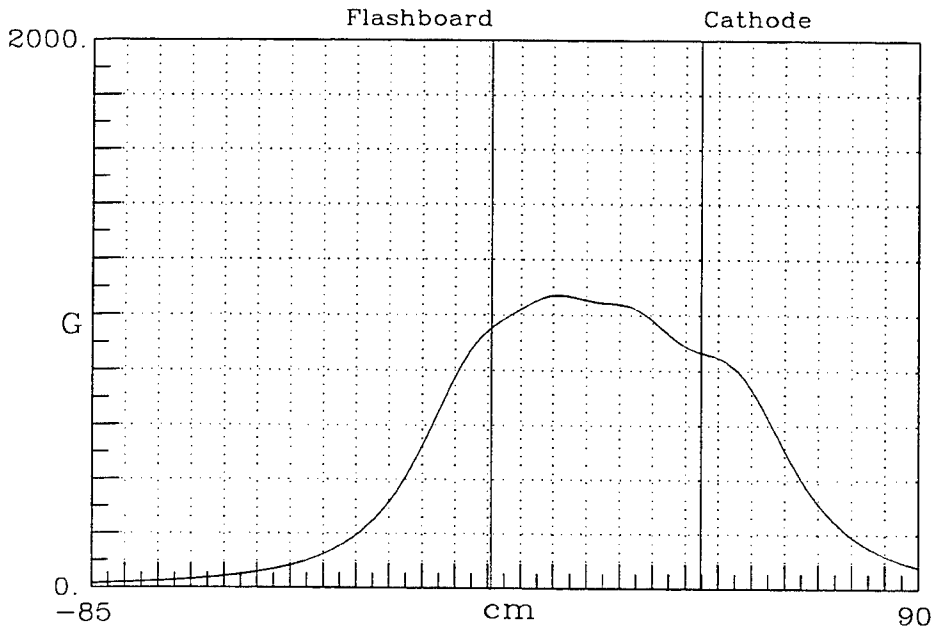

Figure 3-5. Magnetic field profile with the 90 degree bend removed.

3.1.2 Coaxial Hardware.

Following the experiments in the glass cross, experiments in the higher current, coaxial hardware commenced. Besides allowing for higher currents, the coaxial hardware also improved diagnostic access at the cathode potential, and reduced field errors from the non-symmetric current path present in the glass cross. The coaxial electrode and vacuum hardware first used is shown in Figure 3-6. In subsequent experiments, the electrode and magnetic field configurations were changed, and these changes are discussed later. Inside the vacuum, the cathode electrode was a 30.5 cm diameter stalk approximately 1.5 meters in length. The anode for most of the length of the cathode was 39.4 cm in diameter, but the diameter decreased to ~20 cm 6 cm from the cathode mesh. For diagnostic access, the anode was not the vacuum chamber wall in the switch region. This arrangement improved radial access to the switch plasma, both for visual and electrical diagnostics, although it had the drawback that it required the guiding magnetic field coils be placed inside the vacuum. From the vacuum insulator to the switch region, the inductance of the vacuum coaxial section was approximately 70 nH. The vacuum coaxial section was designed to accept up to 36 high voltage coaxial cables (RG217) which fed in directly before the vacuum insulator.

There was a ~29 μH inductive isolator attached at the vacuum insulator end of the cathode stalk. The inductive isolator allowed the placement of diagnostics at the cathode potential, without appreciably shorting out the applied cathode voltage. The inductive isolator had five low voltage coaxial connections, two high voltage coaxial connections, and five high current connections. This combination allowed a variety of

diagnostics and field coils to be at the cathode potential without shorting out the applied voltage on the time scale of interest.

The measured magnetic field profile on-axis for the configuration shown in Figure 3-6 is shown in Figure 3-7. The measured field was in close agreement with the calculated field, even with the electrode hardware present. This field has a magnetic mirror ratio of nearly two (Maximum field/Minimum field), which likely reduced the ion current from the flashboard. The peak field was varied from 0 G to 6 kG in the experiments with this configuration.

The cathode consisted of a mesh stretched in a "drumhead" holder. The anode aperture was a stainless steel foil in a drumhead holder. The aperture holder shown in Figure 3-6 is the same as was used in the glass cross experiments, and apertures from 1 cm to 6.14 cm in diameter were tested. Experiments with and without a conducting mesh across the aperture were also performed. The AK spacing was changed by adjusting the anode mounting hardware. The AK spacing shown in Figure 3-6 is 16 cm.

The voltage was measured with the 400-ohm vacuum voltage monitor connected to the cathode stalk about 10 cm upstream from the cathode mesh. The circuit inductance between the connection points of the voltage monitor was typically around 100 nH, but varied with the geometry of the plasma column. Monitors for the current included Rogowski coils at five locations, including just inside the vacuum insulator, about 30 cm up from the cathode mesh, around the anode aperture holder, and between the anode aperture and the flashboard. Arrays of B-dot coils were also used to monitor the current and determine the displacement of the current centroid. A single B-dot array consisted of four coils located top, bottom, left and right of the plasma column. The calibrations of the B-dot and Rogowski coils were checked with a Pearson current monitor on a shorted load.

For measurements of the ion current, a disk ion collector behind the cathode mesh was used. The collector was biased with respect to the cathode between -40 and -200 V. The bias capacitors were located inside the cathode stalk, at the high voltage end of the isolation inductor. The current was measured by a Pearson current transformer also located at the high voltage side of the inductor. The collector had only one side open to the plasma. The other side was insulated with a ceramic insulator and could not collect ions. The collector was heatable to over 500°C. Even with the heated, cleaned surface emissive behavior was often a problem at the high ion fluences of the experiments.

For comparisons with the glass cross experiments, the experiments with the coaxial hardware were started with an AK bank of two, 0.7 μF capacitors in parallel, switched by a single mid-plane triggered spark gap -- the same as was used with the glass cross. A single high voltage coaxial cable connected the capacitor bank to the vacuum coaxial section. The inductance and resistance of this circuit with a copper shorting strap in lieu of the plasma was ~910 nH, and ~58 mΩ. By changing the inductance of the cable(s) from the spark gap to the vacuum coaxial section, the total inductance of the circuit was varied from ~410 nH to ~2500 nH.

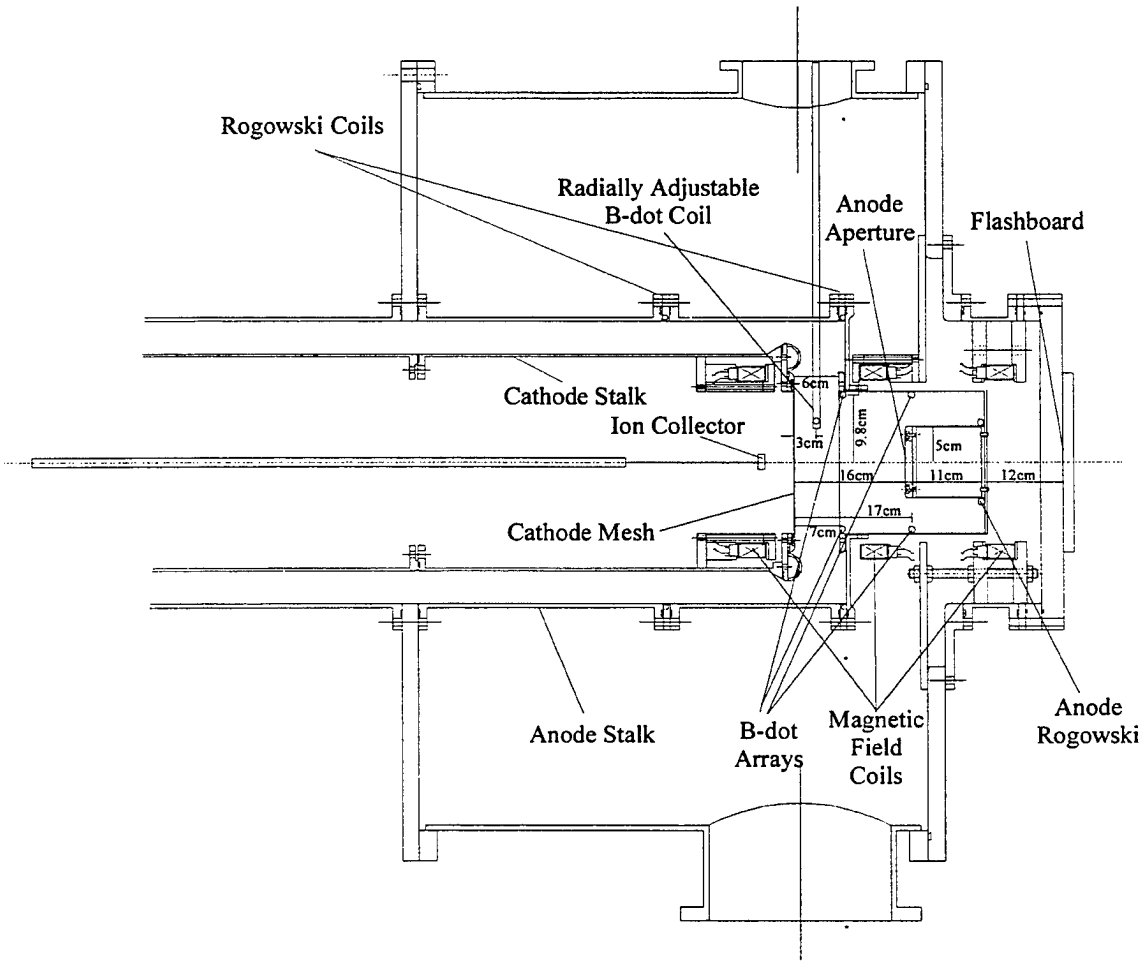

Figure 3-6. Experimental configuration showing the locations of the flashboard, magnetic field coils, electrode hardware and selected diagnostics.

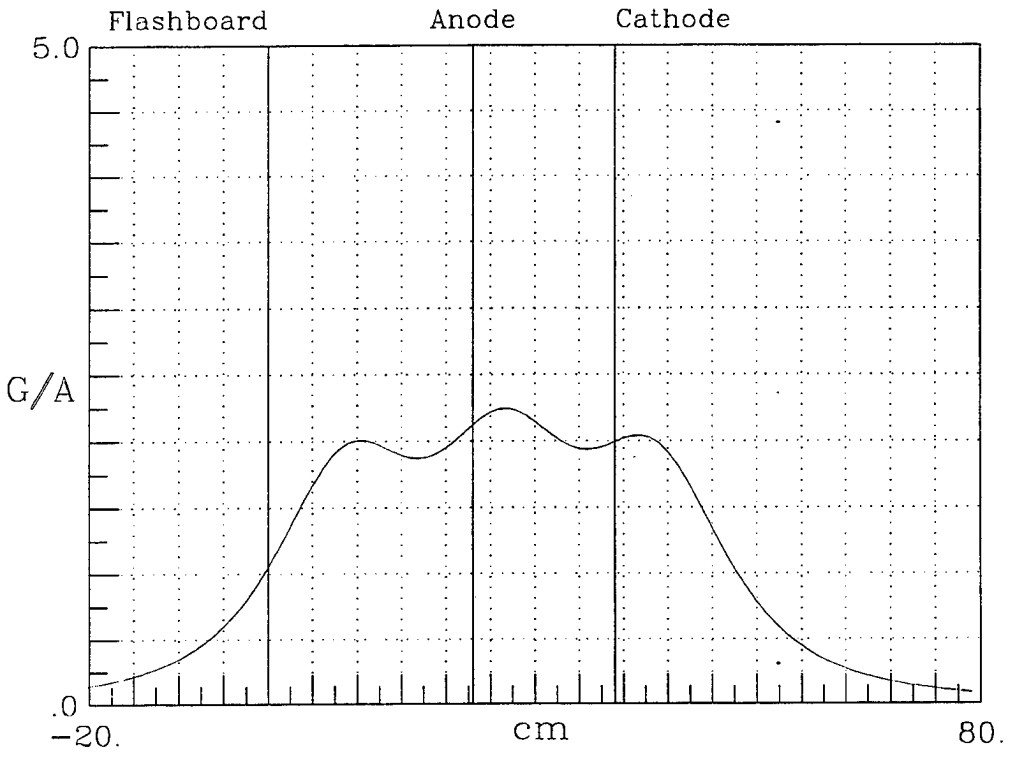

Figure 3-7. On-axis magnetic field profile for the three coil configuration.

To increase the uniformity of the magnetic field across the AK gap, and to increase the separation between the anode and cathode electrodes in areas outside the desired conduction channel, larger diameter magnetic field coils were made and tested along with modifications to the anode hardware. Figure 3-8 shows the modified coil and electrode configuration. In Figure 3-9 the calculated magnetic field on-axis for the configuration of Figure 3-8 is given. In this design the magnetic field was more uniform across the AK gap, and the electrode design changes were intended to reduce current losses at large diameter. With the electrode configuration first used in the coaxial hardware, (Figure 3-6), the minimum axial separation between the anode and the cathode was 6 cm at diameters of 20 cm and greater. This diameter was larger than the injected plasma column diameter, (<5 cm), but it was a concern that break down of the feed at that location would limit the ability to scale the switch parameters. Losses to that section were not severe with a 2.54 cm aperture, but the losses were slightly greater with a 5 cm diameter aperture, and were expected to be worse at even larger diameters. The modified electrode hardware ensured that the minimum axial anode-cathode separation was along the injected plasma column.

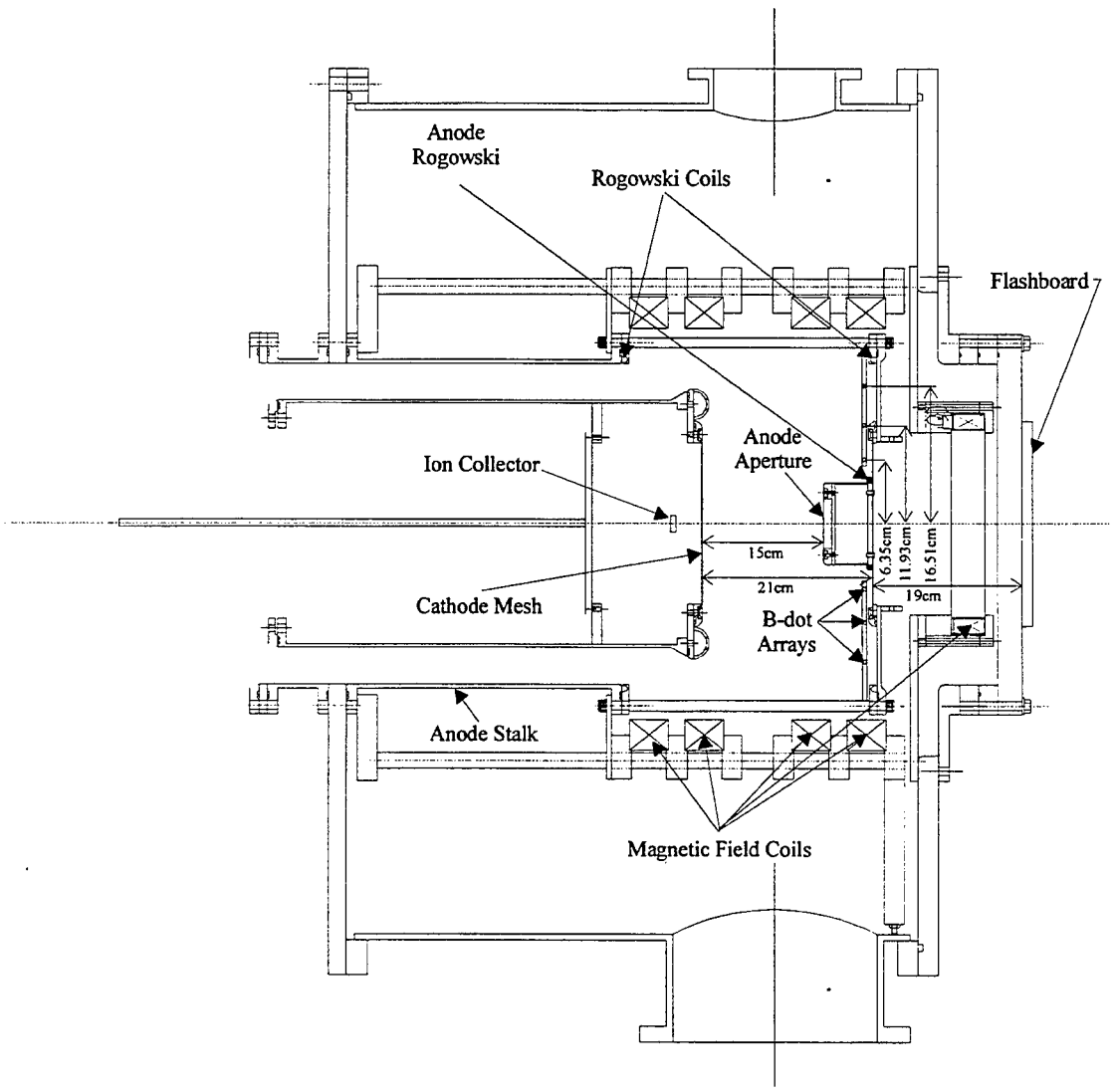

Figure 3-8. Experimental configuration showing the locations of the flashboard, magnetic field coils, electrode hardware and selected diagnostics with the larger magnetic field coils.

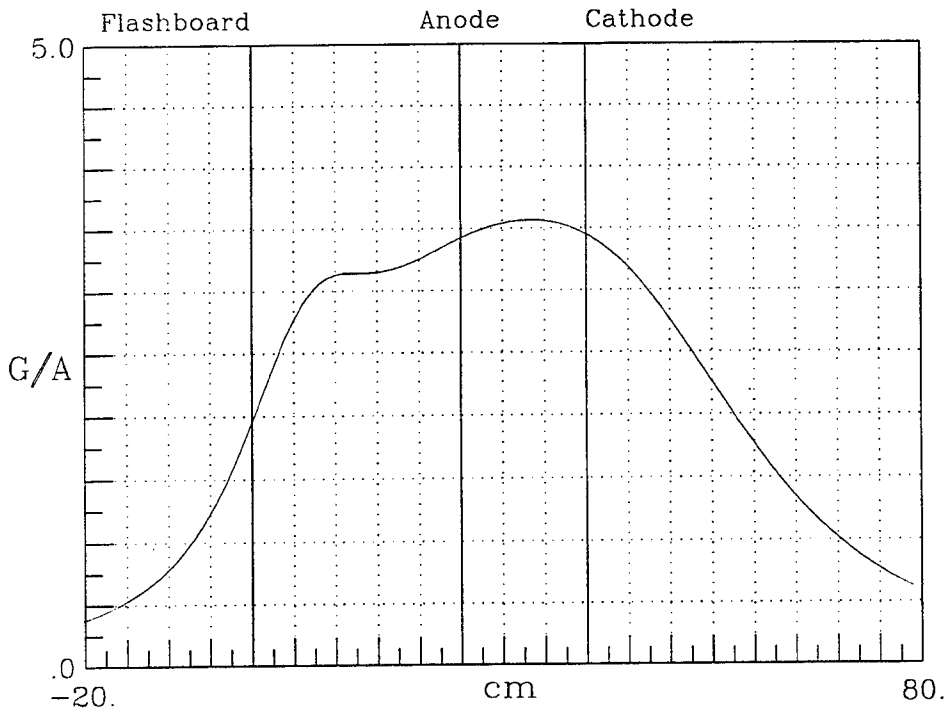

Figure 3-9. On-axis magnetic field profile for the five coil configuration.

3.1.3 High Current Driver Bank.

To achieve currents ~200 kA, a larger AK driver bank was assembled. In the larger bank, fifteen 0.7 μF capacitors replaced the two 0.7 μF capacitors previously used. Each capacitor had 0.2 ohms in series and a mid-plane triggered spark gap. The resistor and spark gap were housed inside of a coaxial "top hat" mounted on the capacitor. With the top hat, both the switch and capacitor header were filled with pressurized SF_6, which allowed for charge voltages up to 100 kV. Each capacitor was connected to the vacuum coaxial section with its own coaxial cable. With a ~26 cm long, 1.6 cm diameter stainless steel short across the AK gap, the circuit inductance was ~300 nH. The total circuit inductance with the plasma was dependent upon the length and diameter of the plasma column, and was typically less than 300 nH. The trigger for all 15 capacitors was a small Marx of two, 0.22 μF capacitors, charged to ±35 kV which, when switched, transferred charge into a 10 nF peaker capacitor. The output of the peaker capacitor was a 15 gap, single envelope, self-break switch, with each gap of the self-break switch triggering a single spark gap. This trigger was found to reliably trigger all 15 spark gaps, with negligible jitter between the spark gaps at charge voltages above ~15 kV.

3.1.4 Plasma Sources.

There were three plasma sources used for the data presented in this report: two flashboards and a cable gun. The driver circuit for all of the sources was a single 0.7 μF capacitor, switched with a pancake spark gap. The circuit was charged to 30 kV for flashboards, and from 15 to 30 kV for the cable gun. A small flashboard with an active area of ~8x8 cm was used for all of the data in the glass cross, and some of the data in the coaxial system. The flashboard is made with a thin copper sheet on one side, copper pads on the other side, and five layers of Kapton insulation laminated in between. The entire arrangement is mounted on a non-conducting G10 backing. The insulating backing allowed for easy magnetic field penetration into the flashboard. Voltage was applied across the pads, and a flashover between the pads creates the plasma. For the small flashboard, there were five chains of pads, and each chain had five flashover points. The copper sheet acted as a low inductance return path for the current. The close spacing of the current in the plasma and the return current was designed to increase the JxB forces in the plasma and enhance the plasma velocity. In order to scale to large aperture areas (100-200 cm^2), a larger flashboard was used. The larger flashboard had an active area of 24x27 cm. The large flashboard had 13 chains of pads, with 18 flash-over locations in each chain on the Kapton insulation. The backing material for the large flashboard was brass instead of G10, which reduced magnetic field penetration into it. The large flashboard was used with the configuration shown in Figure 3-8, but some interesting results were also found with an increased separation of the flashboard to the AK gap. The set-up used is shown in Figure 3-10, and the magnetic field strength on-axis is shown in Figure 3-11.

Similarly to the flashboard, the cable gun plasma source was generated from a flashover across an insulator. In this case the insulator was the Teflon insulation in a 0.635 cm diameter semi-rigid coaxial cable. There were several differences between the cable gun and the flashboard plasma outputs. The cable gun plasma was created at a single location, not at multiple flashover points, and typically had a smaller plasma cross section and a slower average axial velocity than the flashboard. The slower velocity is thought to be due to the differences in the current paths which reduce the JxB acceleration in the cable gun. The higher velocity of the flashboard plasma would be advantageous for a gated plasma source, which is why the flashboard was used for most of the present experiments. Another difference was due to the difference in the insulator. The Teflon in the cable gun had less hydrogen than the Kapton in the flashboard, and had in its place fluorine. This reduced the fraction of the plasma which was hydrogen, and greatly increased the amount of the heavier element fluorine in the plasma.

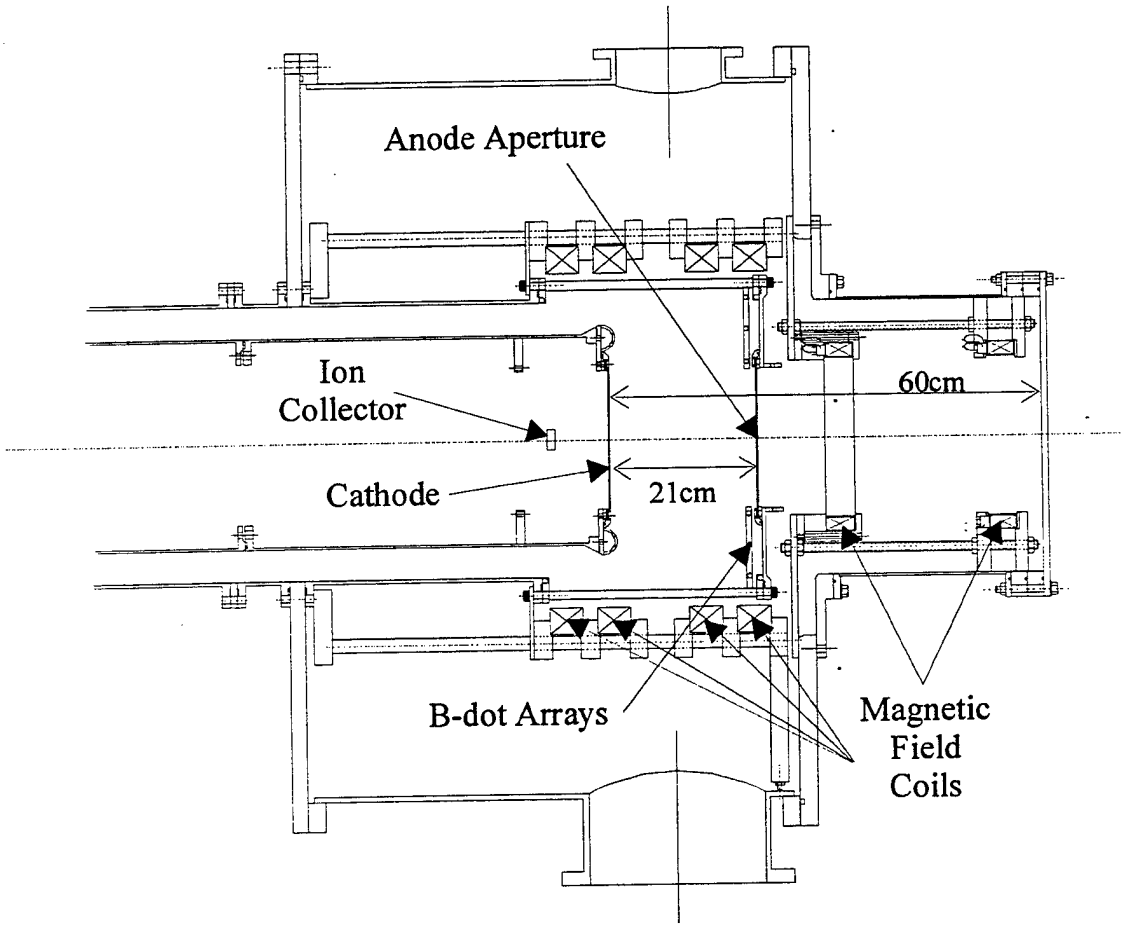

Figure 3-10. Experimental configuration showing the locations of the flashboard, magnetic field coils, electrode hardware and selected diagnostics with the large flashboard 60 cm from the cathode.

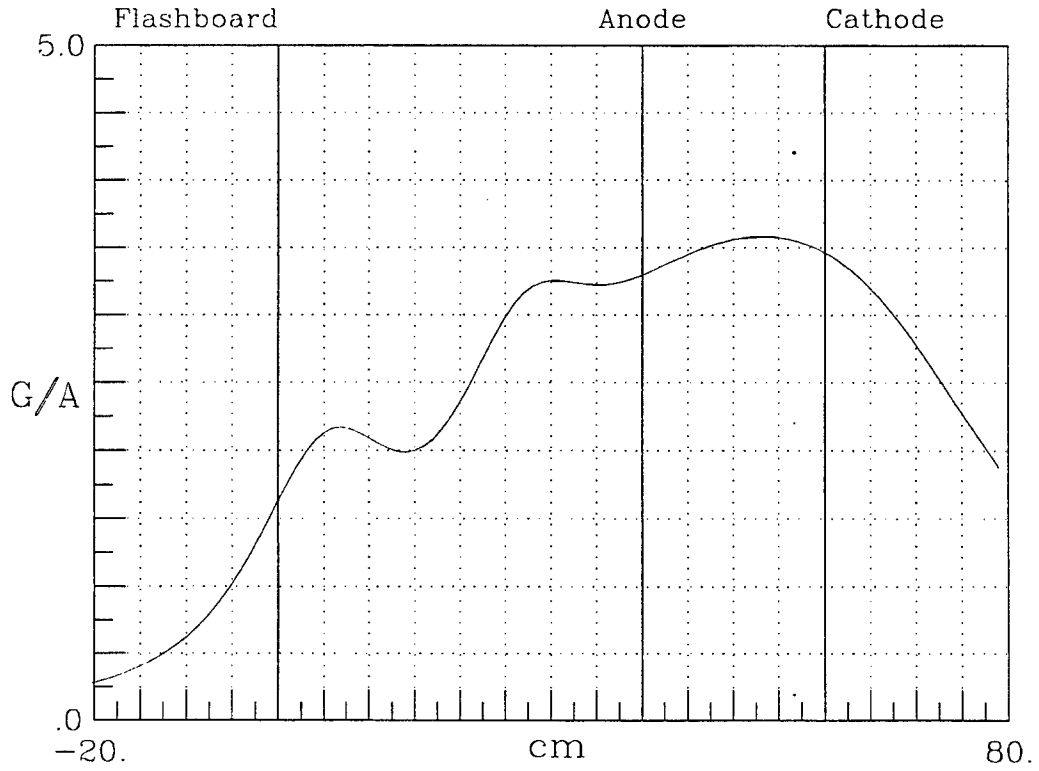

Figure 3-11. On-axis magnetic field profile for the configuration with the large flash-board 60 cm from the cathode.

With the cable gun, only two of the small B-field coils were used for the applied magnetic field, with one inside the cathode stalk and one outside of the reduced diameter anode section, Figure 3-12. In this configuration, the plasma typically traversed a substantial mirror field to enter the AK gap, Figure 3-13. The nominal AK gap was 27 cm long; however, at larger diameters near the cathode the gap was only about 6 cm long. A 39x39 line-per-cm Ni mesh covered the 10.16 cm diameter anode aperture. The cable gun was located along the magnetic axis, with the axial position adjustable from outside vacuum. The large driver bank was used for all conditions tested with the cable gun.

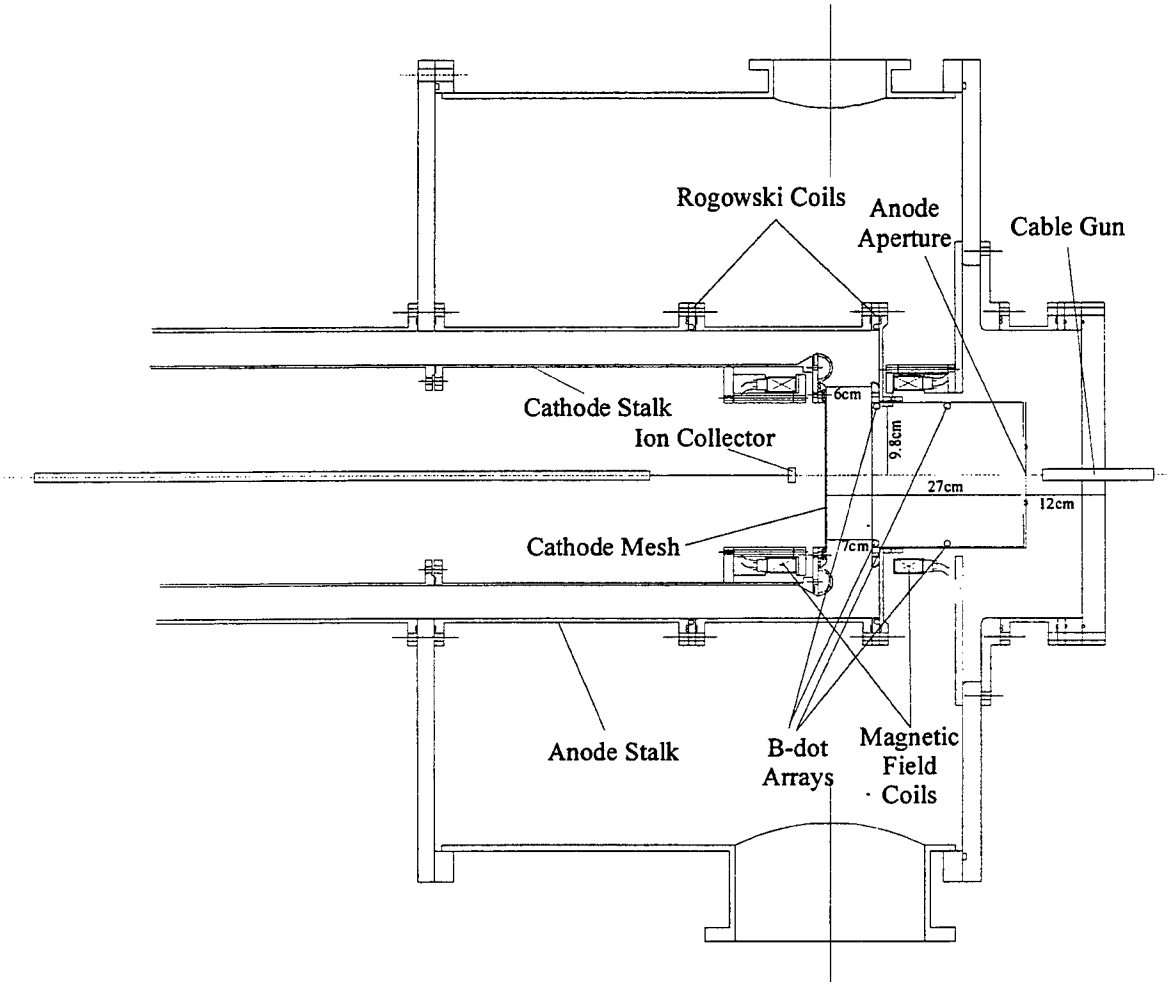

Figure 3-12. Experimental configuration for the cable gun experiments showing the locations of the magnetic field coils and electrode hardware.

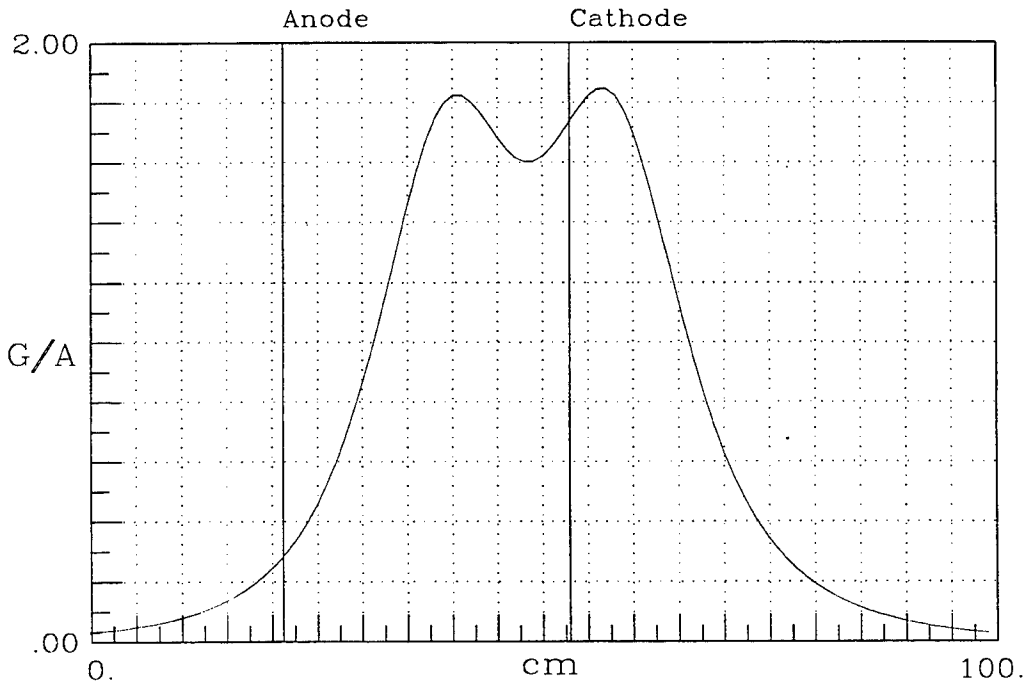

Figure 3-13. On-axis magnetic field profile for the two-coil configuration used with the cable gun source.

3.2 BASIC SWITCH PHENOMENOLOGY.

The glass cross hardware was the first apparatus used in the program. A 90 degree bend with a longitudinal magnetic field transported the flashboard source plasma to the switch gap and was used to insure that neutrals from the source not influence the gap physics. The ion source current density with the bend was limited to about 7 A/cm^2. The apparatus was used to investigate basic issues pertinent to switch operation such as cathode emission, mesh transparency, impedance drop, and control of conduction current by the injected ion current profile. The major new discovery from these experiments was the first association of impedance drop with a radially expanding current channel. Most all the features of the modes of switch operation seen in later high current experiments were apparent in these experiments.

3.2.1 Cathode Limited Emission Effects.

The first results to be discussed were obtained from experiments with the configuration shown in Figure 3-1. Several cathode configurations were tried with this setup, and these experiments led to some understanding of the conditions under which cathode

limited emission occurs. Because of possible formation of potential humps in the anode-cathode gap region and associated changes in the injected ion current and limitation of current flow, it is unfortunately not always possible to distinguish effects of emission limitation from those due to modifications of the ion flow in the gap. Shown in Figure 3-14 are the measured currents on the uppermost electrode, which was a stainless steel foil, at bias voltages of -200 V and -20 kV. An intermediate electrode at anode potential was ~1.7 cm in front of the upper electrode, and had an aperture with an area of ~1 cm^2. The aperture at the entrance to the glass cross was 2.54 cm in diameter, and was not covered by a mesh. At -200 V the uppermost electrode or cathode repelled all of the incident electrons and only collected ion current. There was no formation of a cathode plasma, and the measured current was equal to the incident ion current. At -20 kV, however, the measured current, including the ion current, was nearly three times higher although the conditions on the injected ion current were identical. This change in the measured current was not due to the formation of a cathode plasma, but was due to electron ejection from the cathode by the energetic ions. Hydrogen ions at -20 kV can yield approximately one to two electrons per ion.[1] With a 1 cm^2 area plasma column, and a foil cathode, it appeared that the current could not rise to the Child-Langmuir limit (~200 A) due to cathode emission limitations.

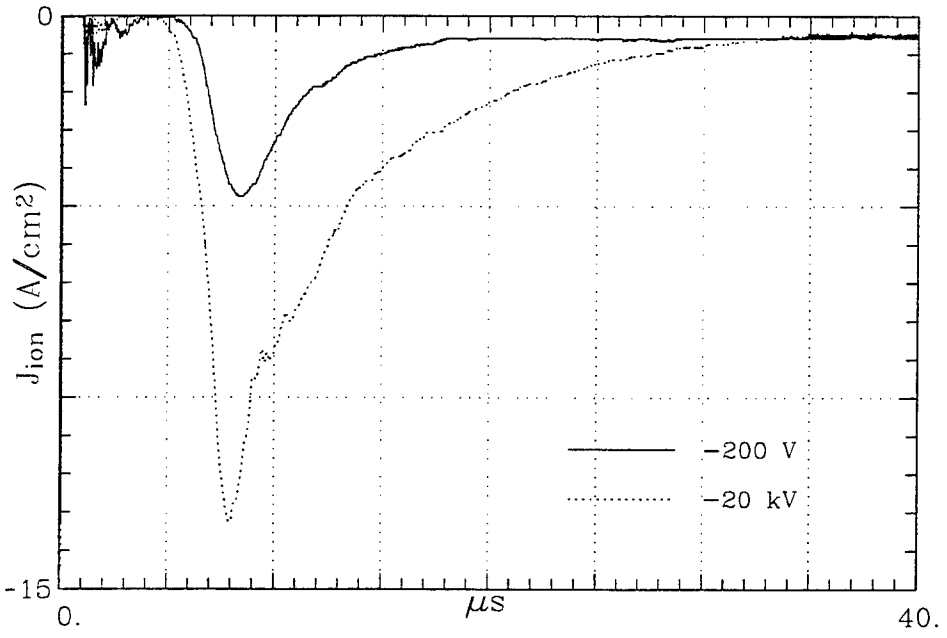

Figure 3-14. Measured currents on the top electrode with two biases.

As a further test of the cathode emission limitation, the intermediate anode was removed, and a similar test was performed with a 25 cm AK gap. Without the inter-

(1) A. vonEngel and M. Steenbeck, Elektrische Gasentladungen, Vol. 1, Springer, Berlin (1932), pg. 116.

mediate electrode, the total ion current incident upon the cathode increased by about a factor of five, (the ratio of the aperture area at the entrance to the glass cross to the area of the intermediate electrode aperture). Shown in Figure 3-15 are the measured ion current on the cathode with a bias of -200 V, the measured current on the cathode with -10 kV applied 5.5 μsec after plasma first arrived at the cathode, and the measured current on the cathode with -10 kV applied before the plasma arrived at the cathode. In both cases with -10 kV, the measured current started at ~100 A or a few times the level of the incident ion current, and then rapidly increased to a peak level substantially above the injected ion current. It appears that initially the current was limited by cathode current limitations, then a cathode plasma was ignited and the current rose, although not to levels given by the Child-Langmuir bipolar current for hydrogen using the ion current at the time of the current increase, as measured without applied high voltage. In fact, in both cases the peak current levels were limited by the voltage drop across the external resistance (12.8 ohms) together with the inductive voltage drop during the rapid current rise. Increasing the diameter of the plasma column incident upon the cathode and increasing the AK gap thus resulted in the formation of a cathode plasma and removed the emission limitation, at least over 100-200 nsec of conduction.

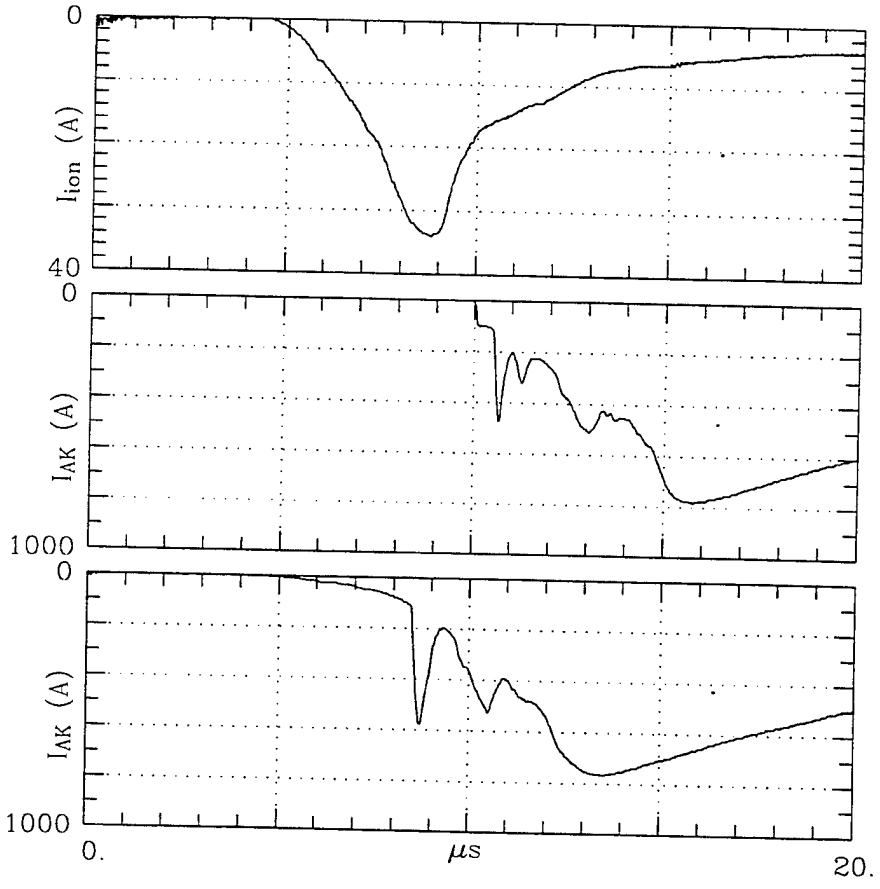

Figure 3-15. Comparison of the injected ion current with cathode currents with voltage applied at two times.

There are two features of the current profiles of Figure 3-15 which are characteristic of much of the data of the program. First of all, after cathode ignition, the current exhibits opening/re-strike type oscillations. Typically with higher ion density sources only a single opening type event is observed and there is little evidence in these cases suggesting cathode emission limitations limit the current initially. In these cases, however, the external circuit resistance is low (~100 mΩ) and the current does not rise to a limit imposed by the driving bank voltage. Using the ion density and velocity from the source current profile of Figure 3-15 and the Kares theory of gap opening due to heating of the background electrons and formation of a potential hump to shut off ion injection, (see Section 4-2, Equation 3), the gap should start opening, e.g. at electron current density levels above j_e~50 A/cm^2 at the ion current density peak (~6.8 A/cm^2). Since the peak electron current density of the bottom curve in Figure 3-15 is >100 A/cm^2, the theory would predict opening. An alternative possibility is that only a limited cathode plasma is formed at ignition and requires high energy (~10 keV) ion bombardment for sustenance (the gap voltage is essentially zero at the first current peaks).

The other noteworthy feature of the current profiles of Figure 3-15 is the general increase of current over time independently of the injected ion current, at least as measured without applied voltage. Both curves rise to near short circuit bank levels after ~5 μsec from ignition, implying effects due to current flow. Though the ion source current at the peak current is adequate to allow the current levels if the plasma is primarily C^+, an obvious explanation is gap closure due to electrode plasma motion reducing the effective gap size. The numbers for high density plasma gap closure rates from typical high current diodes are 1-2 cm/μsec and plasmas from the two electrodes could close the gap at 2.5 cm/μs in about the observed time. Such a picture of gap closure does not fit the data, however, since the effective gap of the plasma column is a very small fraction of the physical gap and the impedance would be roughly constant until near the time when the closure had proceeded to the point where only a millimeter or so opening remained.

Additionally, other data show impedance drop starting at times requiring higher closure velocities (~6 cm/μs/electrode) than the data of Figure 3-15, and in other cases the gap voltage can be high well into the impedance drop phase. A new mechanism has been discovered in the program explaining the impedance drop. It is essentially an expansion of the current channel radially in time, wherein a low current density flow outside the main injected channel is generated as ions move outward, driven in particular by the radial electric field of few kilovolt potential humps. The first evidence of the current channel expansion is given in Section 3.2.3 and it is further documented later in the report with B-dot probe data.

Next a 39x39 line-per-cm stainless steel mesh with 0.00254 cm thick wires (81% transparent) was installed at the intermediate electrode location which was connected to the cathode outside of vacuum and -10 kV was applied before the plasma arrived at the

cathode. Figure 3-16 shows a comparison of the injected ion current with the current from the mesh cathode, indicating that the cathode began to emit 1.5 μsec after the arrival of the first plasma. The cathode also exhibits symptoms of emission limits throughout the current flow since the j_e/j_i ratio is lower than typically observed (20-30) and the current after peak does not rise to the short circuit level. Other data using the mesh cathode but with applied voltage of -20 kV and without the external resistor showed essentially instantaneous ignition and a rapid current rise followed by a single opening when the voltage was applied near the peak of the injected ion current.

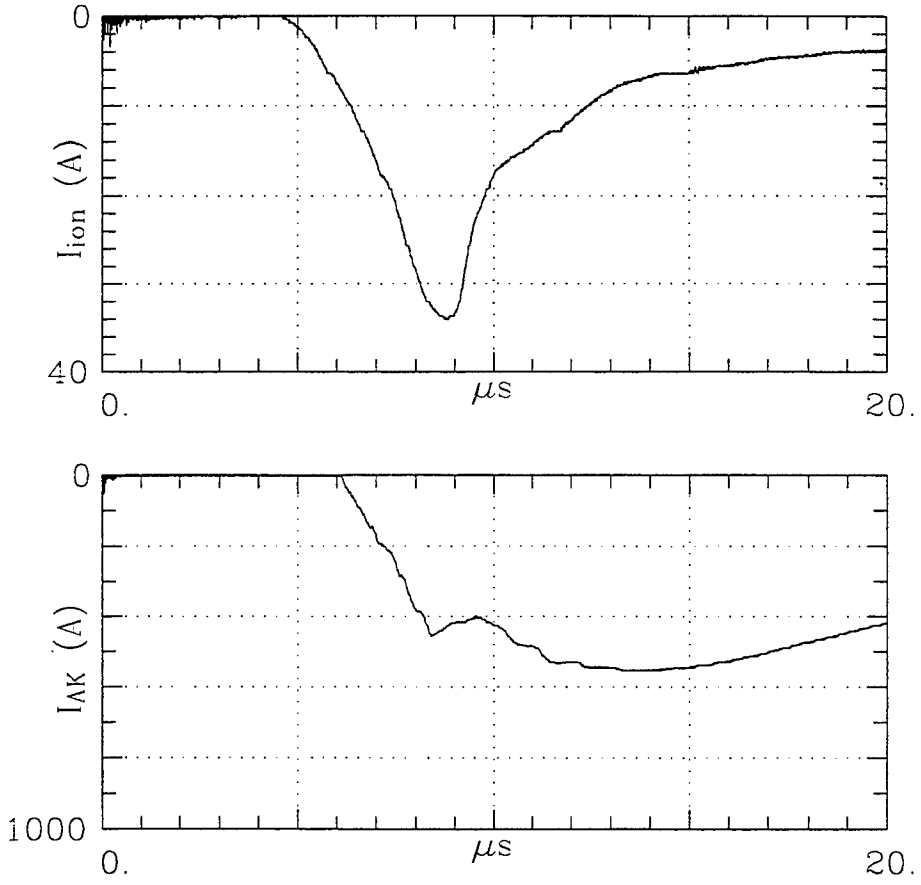

Figure 3-16. Comparison of injected ion current and the current from the biased mesh.

In Figure 3-17 the measured current for -10 kV applied across the AK gap approximately 1.5 μsec after plasma arrival at the cathode is given for a shot with a carbon fiber cathode. The current profile does exhibit a duration of ~500 nsec at the $\lesssim$100 A current level typical of the foil cathode before ignition, followed by a rise to ~200 A lasting about 3.5 μsec. It is interesting to compare the -10 kV carbon fiber cathode date of Figure 3-17 with -30 kV data given in Figure 3-23 of Section 3.2.4 where all other parameters are the same. Voltage is applied at nearly the same time in the ion current profile in the two cases. At -30 kV the current rises smoothly to -200 A over

≤ 50 nsec in contrast to the -10 kV case where ~360 nsec are required to reach about 70 A. The ion dose to the cathode before voltage application is the same in the two cases; the major difference is the higher ion energy at the cathode with -30 kV during the time of current rise. (The peak electron current densities in the two cases up to the time of current clamping in the -10 kV case are of course the same.)

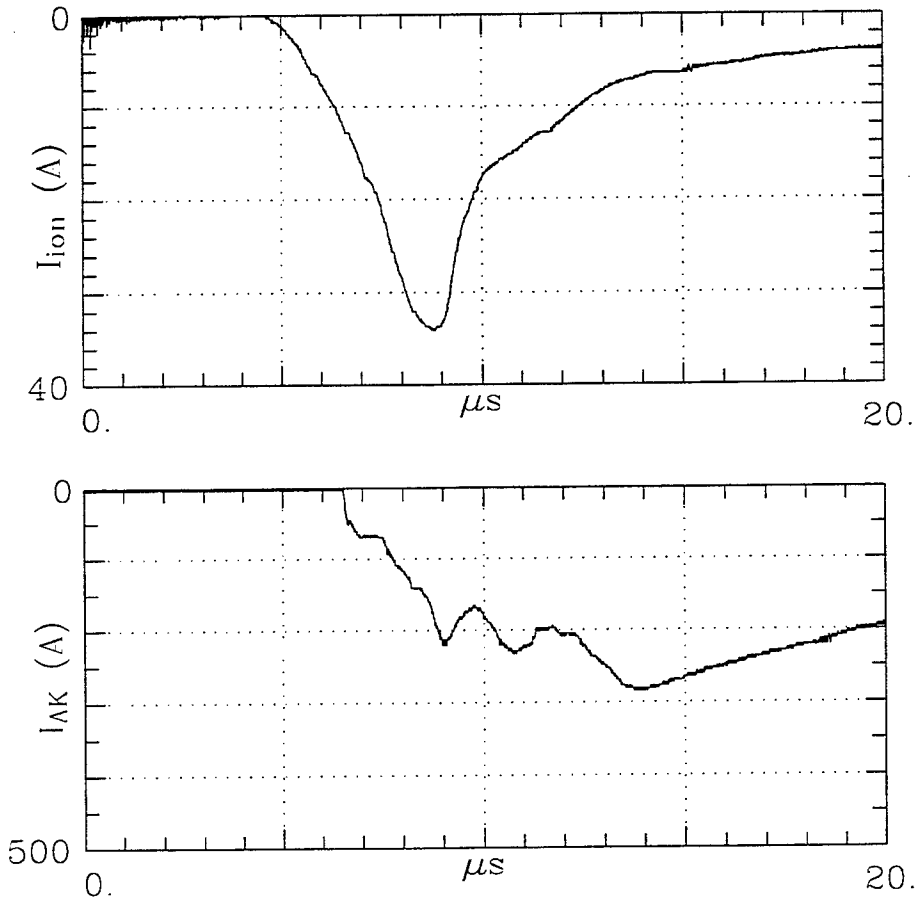

Figure 3-17. Comparison of injected ion current and the current from a carbon fiber cathode.

In summary, there is evidence at -10 kV of at least initial emission limitations with the foil, mesh and carbon fiber cathodes, and their current profiles are significantly different. The foil cathode shows an ignition with very low gap impedance; the others do not. At -20 kV applied near the peak of the ion source current, the mesh cathode also ignites very rapidly with a low impedance phase and an opening type event, and at -30 kV the carbon fiber cathode shows rapid current rise over very short times (≤ 50 nsec) associated with a short-lived lower impedance phase, but high impedance thereafter. In this high impedance mode the carbon fiber cathode gives j_e/j_i ratios of 20-30, similar to those at the peak current with self-opening modes which clearly do not have initial emission limitations. Even with the very low initial ion dose of Figure 3-25 of Section

3.2.4, where the ion current density peak is 0.24 A/cm^2 and electron current density is only ~7 cm^2 (conditions where it is hard not to expect emission limitations), the j_e/j_i ratio of 20-30 still holds.

Simulations with space-charge-limited emission always show a low impedance gap behavior followed by an opening if the plasma fills the gap before application of voltage. In the experiments with the carbon fiber cathode discussed above, there was always source plasma across the entire gap at the time of application of voltage, yet the data shows high impedance behavior.

Experiments described later in this report used all three cathodes discussed above. In the low impedance modes of practical interest, the initial gap impedance is low and therefore likely not limited by cathode emission. These modes were typically obtained after ≥ 2 μsec of cathode irradiation by the ion source and with $j_i \gtrsim 10$ A/cm^2 at the time of voltage application.

3.2.2 Mesh Transparency as a Function of Bias Voltage.

The transparency of an electrode mesh, particularly to ion flow, has practical implications to DCOS and is a key consideration in interpreting experimental results. Experiments were undertaken to study the issue. This set of experiments in the glass cross with the 90 degree bend utilized a 2.54 cm diameter aperture, the ion collector described previously in the upper electrode position, and the biased grid intermediate to the two positions. The biased grid was located ~1.73 cm from the ion collector and the anode aperture was ~25 cm from the collector. The first set of experiments used negatively biased grids. The experiments measured both the ion current collected by the mesh and the ion current transmitted through the mesh. The total current was taken as the sum of the two currents. In some cases secondary electron currents from the grid were included, and were subtracted from the measured grid current to obtain the ion current collected at the grid. This analysis was used to compute the fraction of ion current transmitted through the mesh. The results from measurements with a ~6x6 line-per-cm stainless steel mesh with a geometric transparency of 73% are summarized in Table 3-1. As seen from these results, the transmittance changed from 69.6% to 51.2% as the potential of the mesh was varied from -100 V to -1000 V. The measurements used in the comparison were not all taken at the same time relative to the trigger to the flashboard, but were taken at the time of the peak signal.

A second set of transparency measurements were done with a 81% 39x39 line-per-cm mesh with the same arrangement as the data above. However, the data was analyzed at a fixed time of 7 μsec from the trigger to the flashboard, or 2.3 μsec after the first part of the plasma pulse reaches the cathode. This time was before the peak in the injected ion current, and was chosen due to excessive secondary electron emission from the fine mesh at the peak ion current. It was felt to be less risky to make shot-to-shot comparisons at this earlier time. The results from the 39x39 line-per-cm mesh transmittance experiments are summarized in Table 3-2. As seen in these measurements, the transmittance dropped from 81% to 31% as the mesh potential was varied

Table 3-1. Mesh transparency versus bias voltage.

(73% geometrically transparent, 6.3x6.3 line-per-cm stainless steel mesh)							
SN	F (V)	I_T (A)	I_+	I_-	I_{+top}	I_{+mesh}	Transmittance (%)
888	-100	27	27	0	18.8	8.2	69.6
887	-200	30.4	27	3.4	19.6	7.4	72.6
886	-500	36	27	9	18.8	8.2	69.6
885	-1000	44	27	17	14.8	12.2	54.8
884	-1000	40.8	27	13.8	14.0	13.0	51.2

Table 3-2. Mesh transparency versus bias voltage.

(81% geometrically transparent, 6.3x6.3 line-per-cm stainless steel mesh)							
SN	F (V)	I_T (A)	I_+	I_-	I_{+top}	I_{+mesh}	Transmittance (%)
911	-50	10.4	10.4	0.0	8.4	2.0	81
912	-100	16.4	16.4	0.0	12.8	3.6	78
913	-200	19.2	19.0	0.0	14.0	5.2	73
914	-300	20.0	20.0	0.0	12.4	7.6	62
915	-400	11.2	11.2	0.0	3.6	7.6	32
919	-500	14.4	14.4	0.0	4.4	10.0	31
920	-1000	60.4	16.2	44.2	8.4	7.8	52
923	-2000	56.0	16.2	39.8	16.0	0.2	99

varied from -50 to -500 V. Measurements at higher voltages had too much electron emission to be included. A simple model which roughly agrees with the decreasing transparency with mesh voltage is obtained by assuming the effective ion capture sheath about the mesh wires is given by the Langmuir-Child gap for an ion diode with the mesh voltage and incident ion current density.

In addition to the transmittance changing with mesh potential, a plasma cut-off (transmission delay) was also observed during the first 1.25 μsec of the plasma pulse. Figure 3-18 shows two measurements, one with -50 V on the mesh and the other with -1000 V on the mesh. The time for ion current to be measured was delayed by 1.25 μsec with the -1000 V on the mesh. This delay was continuous as the mesh potential was varied.

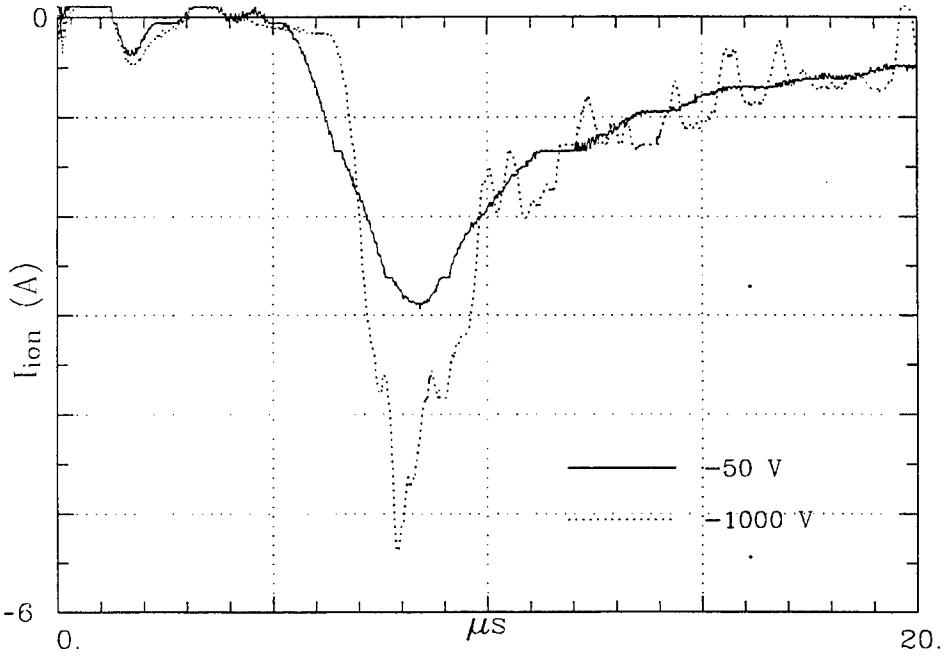

Figure 3-18. Measured ion current with a biased mesh in front of the collector.

The next set of experiments investigated ion transmission through positively biased grids with the ion collector (top electrode) again set at -200 V. Figure 3-19 shows the results for grid voltages of 0 to +10 kV. There is attenuation and some profile distortion as the voltage increased to +1 kV, but the ion flux profile is surprisingly well preserved. Applying a positive bias to the mesh in the middle of the plasma pulse shut off plasma to the cathode. Shown in Figure 3-20 are the measured current on the cathode with a bias of -200 V, and the current and voltage on the intermediate mesh, with +10 kV applied approximately 3 μsec after the first plasma arrived at the cathode.

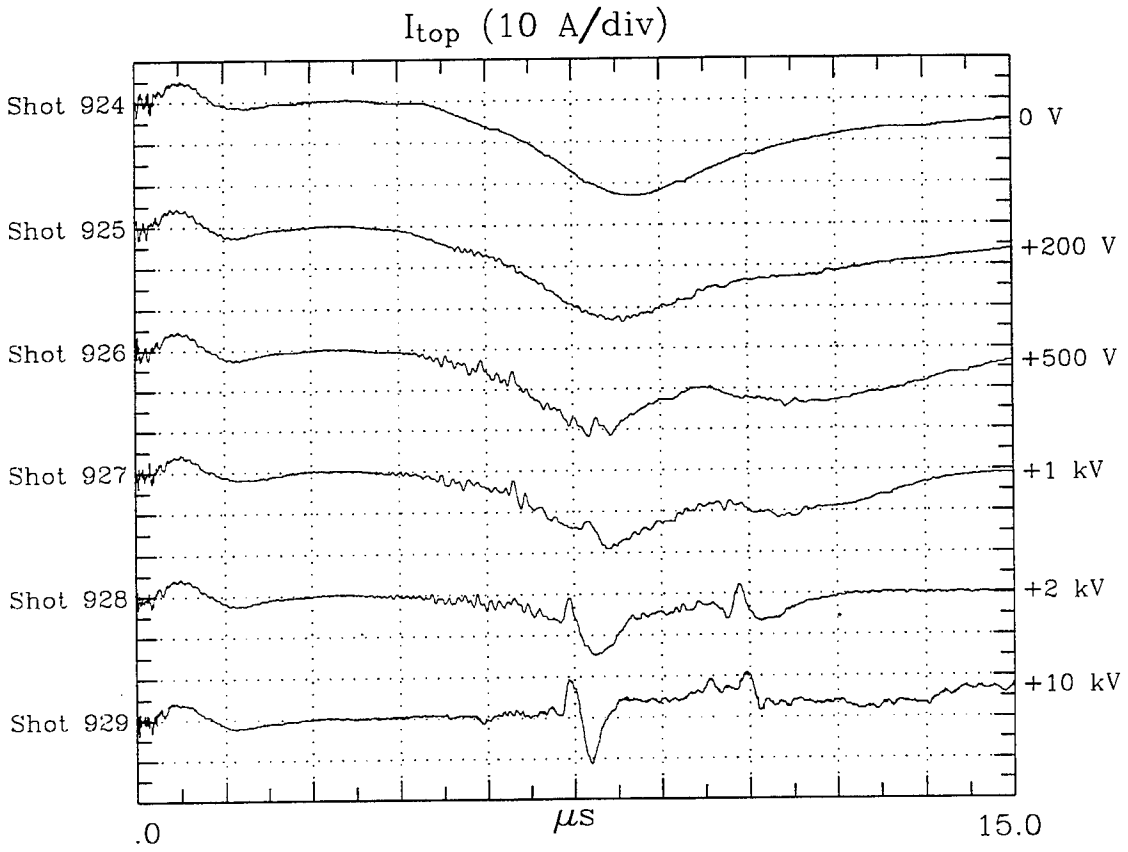

Figure 3-19. Currents collected on the top electrode (-200 V) for various positive biases on the mesh at the intermediate electrode location.

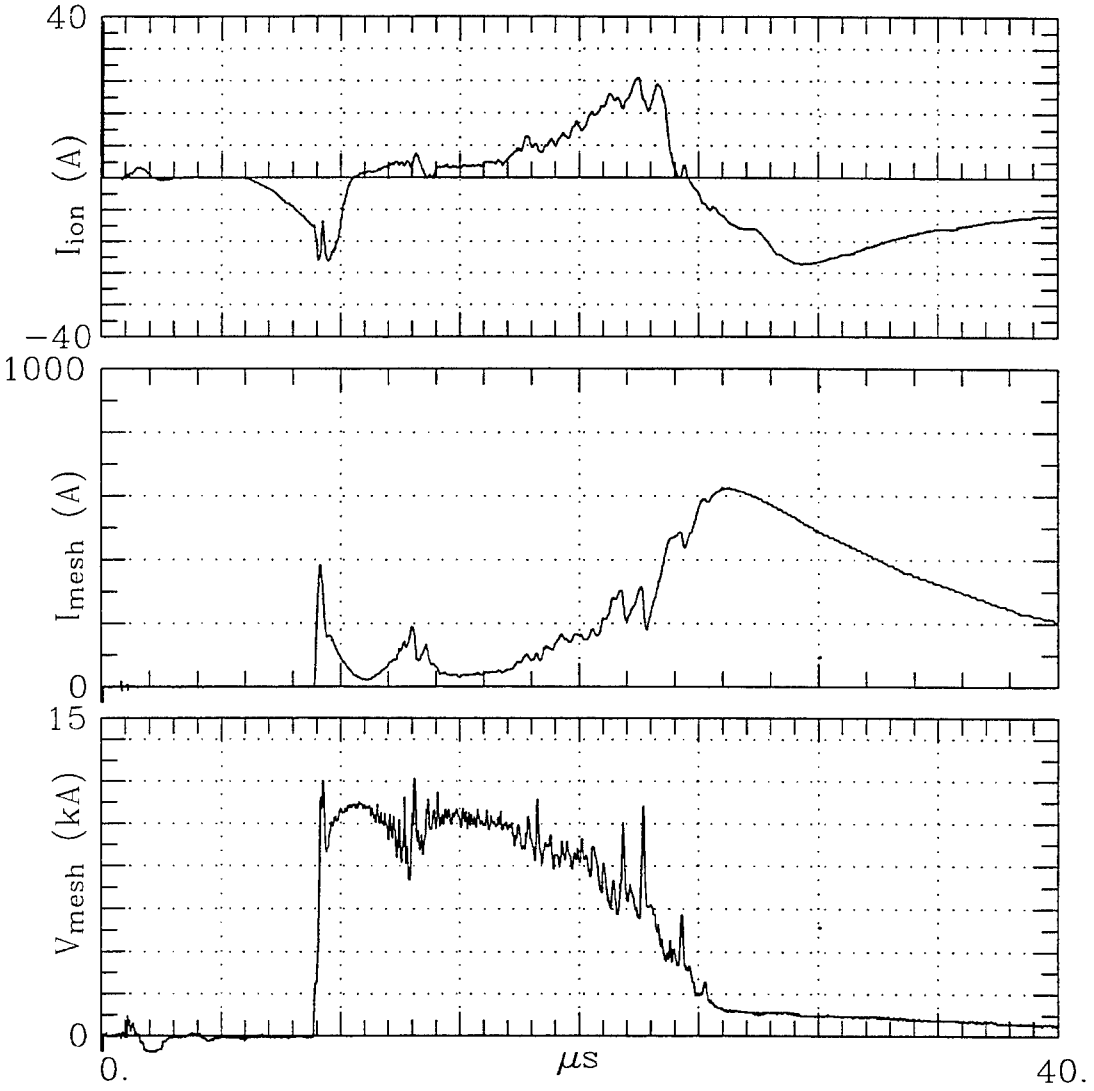

Figure 3-20. Measured current on the top electrode with +10 kV pulsed onto the mesh at the intermediate electrode location.

These data both demonstrate a possible mechanism for gating a plasma with a biased grid and imply that the transparency of a mesh on the anode or cathode may vary during the discharge. Any transparency variation of the anode mesh is very important in influencing plasma injected into the gap after the start of conduction, and for comparing the ion current measurements with the conducted current.

Two meshes were used in experiments discussed in following sections -- one at the cathode and one at the anode. Cathode meshes were used when ion collectors were incorporated behind the cathode to infer ion current density at the cathode with applied voltage, and anode meshes were used to influence total current and radial current density profiles. In measuring the ion current profiles without applied voltage, any attenuation from an anode mesh is, of course, accounted for in measurements made with a solid cathode and no intervening mesh, as was the case for ion source measurements using the glass cross with the 90 degree bend. In this case, the anode mesh gave essentially geometric attenuation. With the bend removed, the anode mesh gave close to geometric attenuation over the time when most experiments were performed; however, later in time the attenuation was greater than geometric.

When voltage is applied, the data above suggest the possibility of both varying anode and cathode mesh transparency. If the potential of these meshes with respect to the surrounding plasma potential is a few hundred volts or less, the data shows the transparency to ion current is not significantly affected by the mesh, aside from the geometric attenuation. The effects of the anode mesh can be significant, as shown later, but are more likely not primarily those of mesh transparency. The presence of the mesh changes the boundary conditions of the anode by allowing an electrical termination of the gap and flashboard currents across the entire current channel cross section and also by providing a source for space-charge-limited emission into the gap to counter formation of potential humps. (According to simulations this anode emission stops the double-sided ion ejection from the potential hump and greatly reduces the hump potential so it never completely shuts off ion injection into the gap.)

The cathode mesh has experimentally been observed to reduce the ion current by as much as a factor of two and alter the profile. Though not a mesh effect, additional uncertainty from ion collector measurements behind the cathode arises from the possibility of collector current increases of a factor of two to three during times when the gap voltage is high (20-30 kV), due simply to electron ejection by ion bombardment of the collector. All in all, ion collector measurements behind the cathode can be uncertain by as much as a factor of three with high voltage, and a factor of two at low gap voltage.

3.2.3 Gated Images of the Plasma at the Cathode Surface.

The gated camera was used to look at the plasma at and near the cathode surface, with the centerline of the camera in-line with the cathode plane. The cathode used was a carbon velvet cathode, and the anode aperture was 2.54 cm in diameter. By changing the light sensitivity of the camera, changing the f-stop and increasing or decreasing the neutral density filtering, observation of the plasma at the cathode both with and without

applied AK voltage was possible. With applied AK voltage it was observed that the visible plasma at the cathode expanded at the same time the impedance dropped. Shown in Figures 3-21 are images of the plasma at the cathode surface at times from 7 μsec to 13 μsec after the trigger to the flashboard. The -30 kV voltage was applied 6.5 μsec after the trigger to the flashboard, τ_{AK} = 6.5 μsec. Representative current and voltage traces for the images in Figure 3-21 are given in Figure 3-22. After 1.5 to 2 μsec of conduction the impedance of the gap started to drop. The current began to increase rapidly and at the same time the voltage across the gap dropped.

The images clearly show a larger region of light emission near the cathode surface as the current increased. If the intensity at the center of the image saturates, or if the camera has a non-linear response with light intensity, an increase in the overall intensity of light emission from the plasma at the cathode may make previously unobservable "wings" of the plasma column become visible to the camera. These "wings" may appear nearly as bright as the plasma on-axis, even if they have a much lower density. Keeping this in mind, the images show that at the time of the impedance drop, there was increased light emission from plasma at radii larger than the column initially injected, implying current flow at larger radii. Further evidence confirming a radially expanding current channel was obtained from B-dot probe data which is given later in this section.

3.2.4 Variation of the Plasma Source.

During the first ~2 μsec, before the impedance drop, experiments to vary the conduction current by changing the injected ion current were performed. These experiments were conducted at relatively low ion current densities, ~0.24 to 5.7 A/cm^2, with an anode aperture of 5.1 cm^2. The cathodes used were velvet and carbon fiber. The ion current was controlled by pulsing the fast cusp coil shown in Figure 3-1. With the appropriate timing and voltages, ion currents which rose, remained nearly flat, or decreased slightly over the time scale of interest were achieved. Shown in Figures 3-23, 3-24, and 3-25 are shots under those three conditions. For the first ~2 μsec of conduction the current approximately followed the shape of the injected ion current. These curves all fall in the high impedance gap regime typically observed early in times after the plasma has crossed the gap, and the ion current density is < 5 A/cm^2. As mentioned previously, the ratio of j_e/j_i is ~20-30 using the j_i values measured without applied voltage. These values should be representative of the ion current density near the cathode early on, but not necessarily later in the current pulse.

A significant effort to model these results was undertaken by T. Hughes using, in particular, source parameters of Figure 3-24. The results are given in Section 4. In order to obtain a high gap impedance, voltage had to be applied just before the plasma filled the gap; otherwise, the gap started at low impedance and typically opened in 30-75 nsec depending on the gap length (2 and 12 cm respectively). When voltage was applied before the gap was filled, a 2 cm gap length gave results roughly agreeing with the data; longer gap lengths showed opening. Hughes observed two-stream heating of

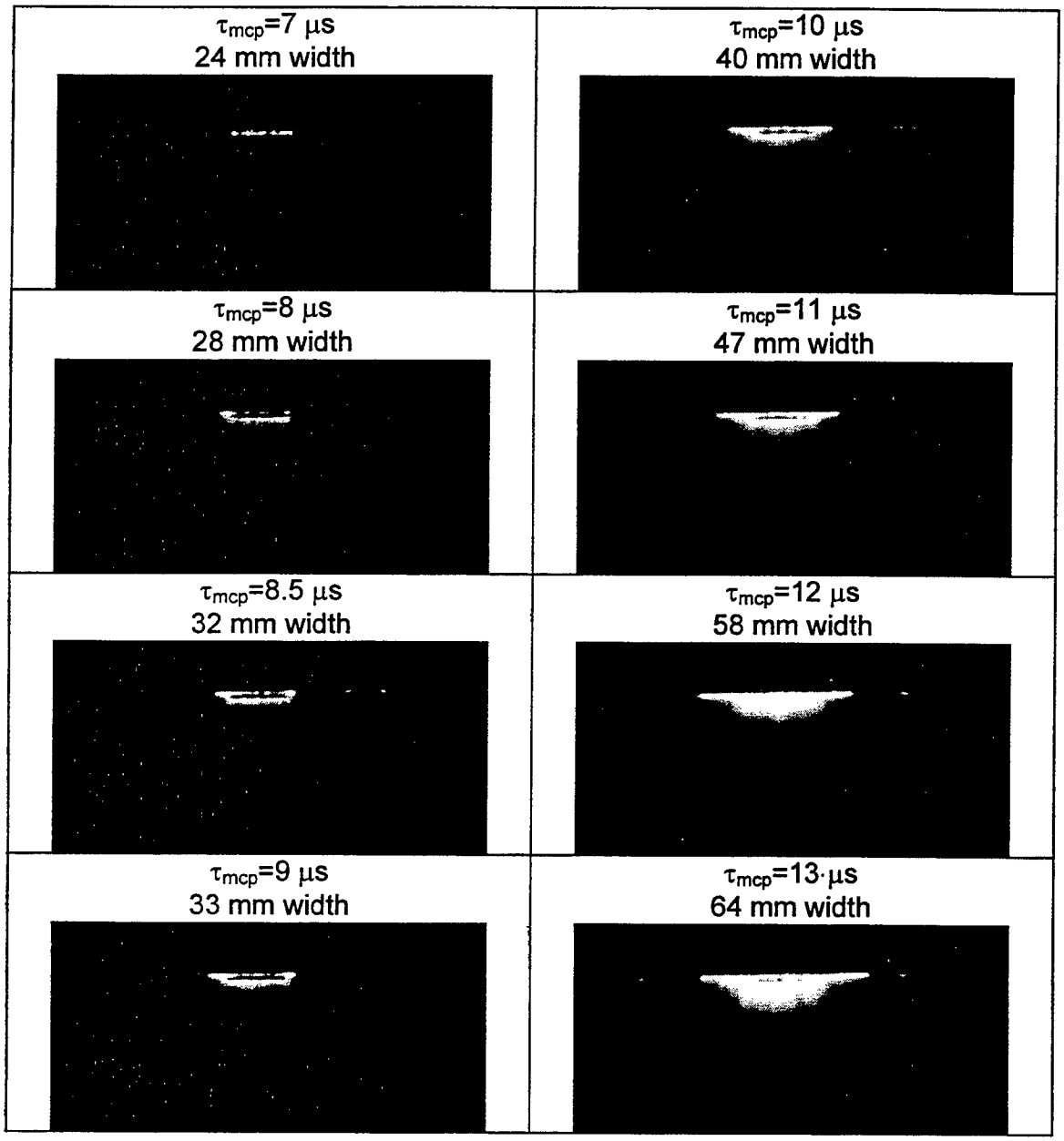

Figure 3-21. Images of the cathode at different times during conduction.

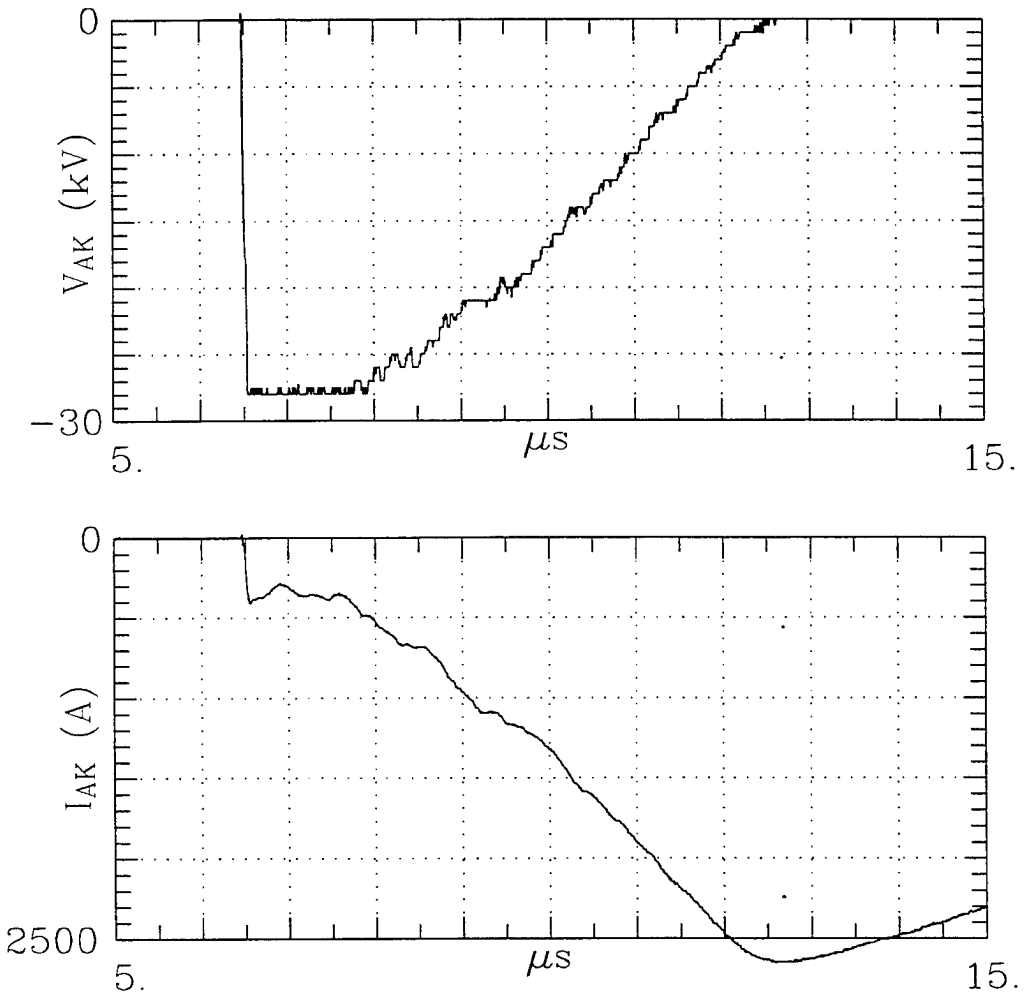

Figure 3-22. Representative current and voltage traces for the images in Figure 3-21.

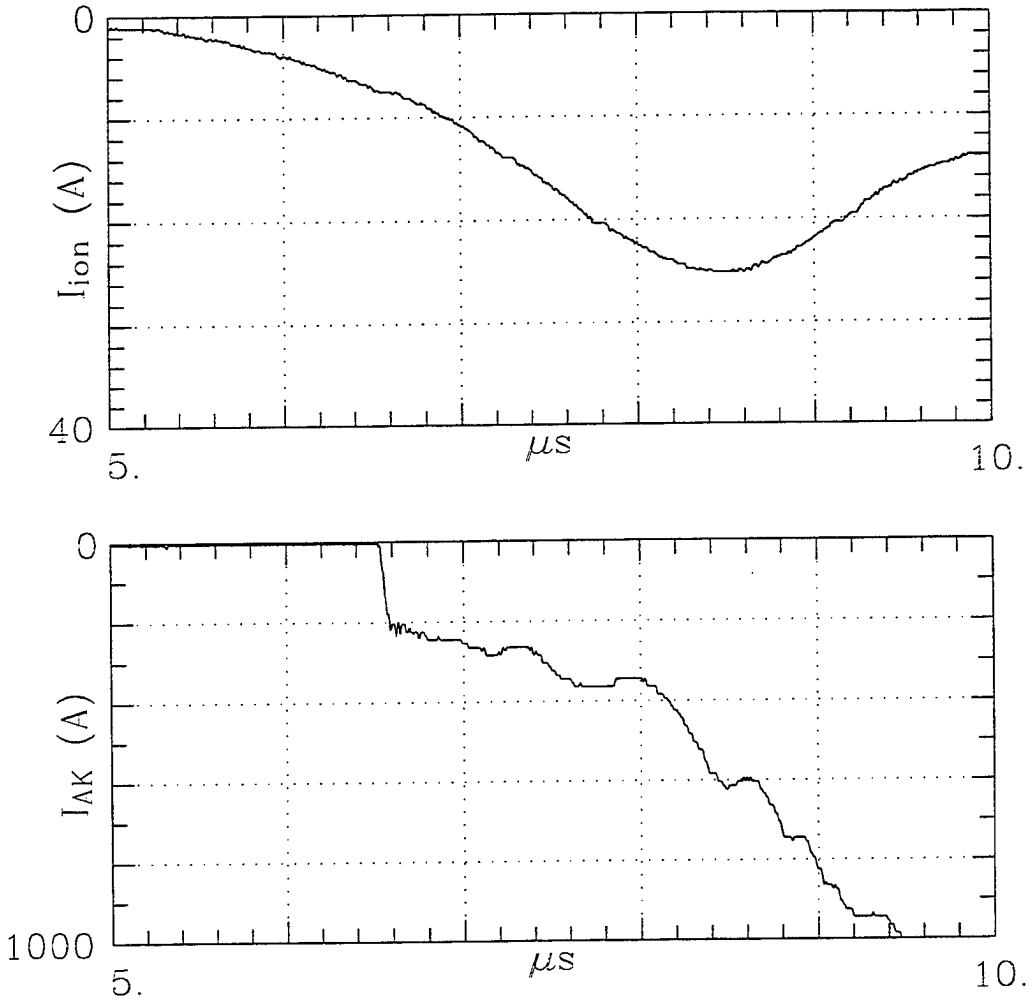

Figure 3-23. Cathode current with injected ion current increasing with time.

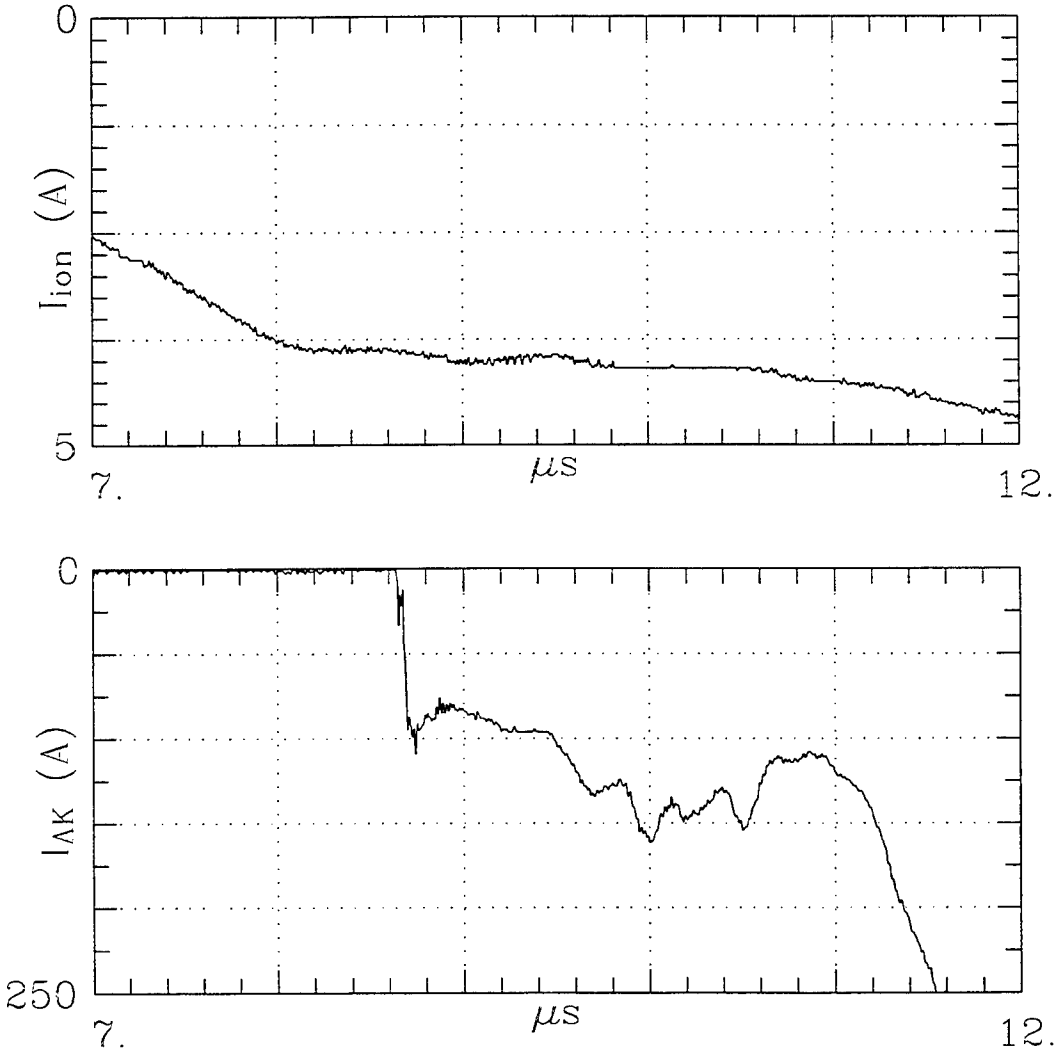

Figure 3-24. Cathode current with injected ion current remaining constant with time.

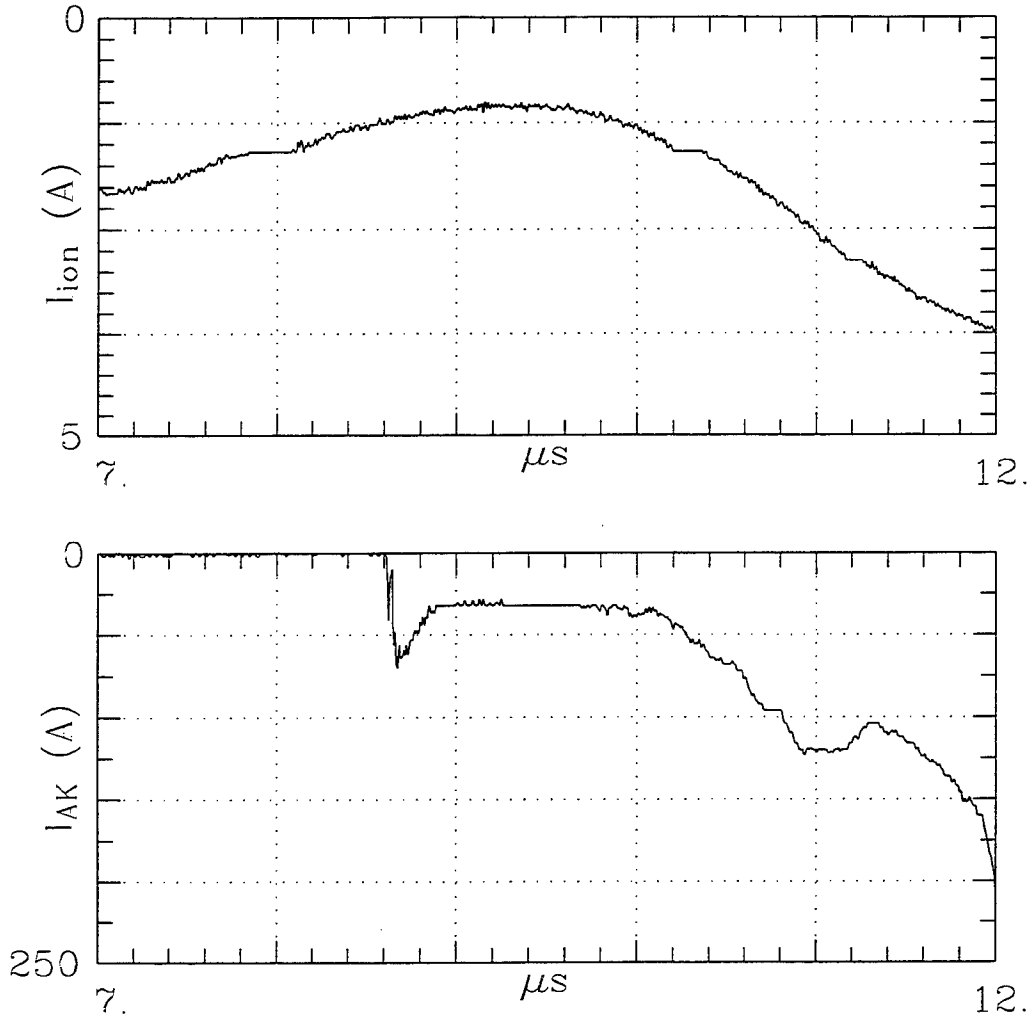

Figure 3-25. Cathode current with injected ion current decreasing with time.

the background electrons with the longer gaps, whereas the 2 cm gap was shorter than the wavelength of fastest growth. The maintenance of current flow in the experiment over the ≥ 2 μsec before start of impedance drop clearly shows that the ion flow from the source is not shut off as predicted by the codes. The lower j_e/j_i ratio than would be expected from Langmuir-Child bipolar flow (43 for hydrogen) does suggest a ~40% reduction in ion current flow, possibly caused by a small potential hump near the anode.

3.2.5 Reverse Bias Experiments.

Experiments were performed with the bias on the electrodes reversed from the standard configuration. These experiments were conducted early in the program and served as the first experiments to compare with simulations. Instead of plasma being injected through a grounded anode toward a negatively biased cathode, the upper-most electrode was biased positive, and the plasma was injected towards it through a 1 cm^2 aperture in a grounded cathode electrode ~1.7 cm from the upper-most electrode or anode. Figure 3-26 compares the measured current on the biased electrode with biases of -200 V and +200 V. With the negative bias the measured current is the injected ion current for the 1 cm^2 aperture, as given previously in Figure 3-14. The measured current with a positive bias showed a strong oscillatory behavior that was not observed with a negative bias. The frequency of the oscillations decreased after ~5 μsec, and it was speculated that the change in frequency might be due to a change in ion species. Particle-in-cell simulations by T. Hughes using the IVORY code show similar oscillations.

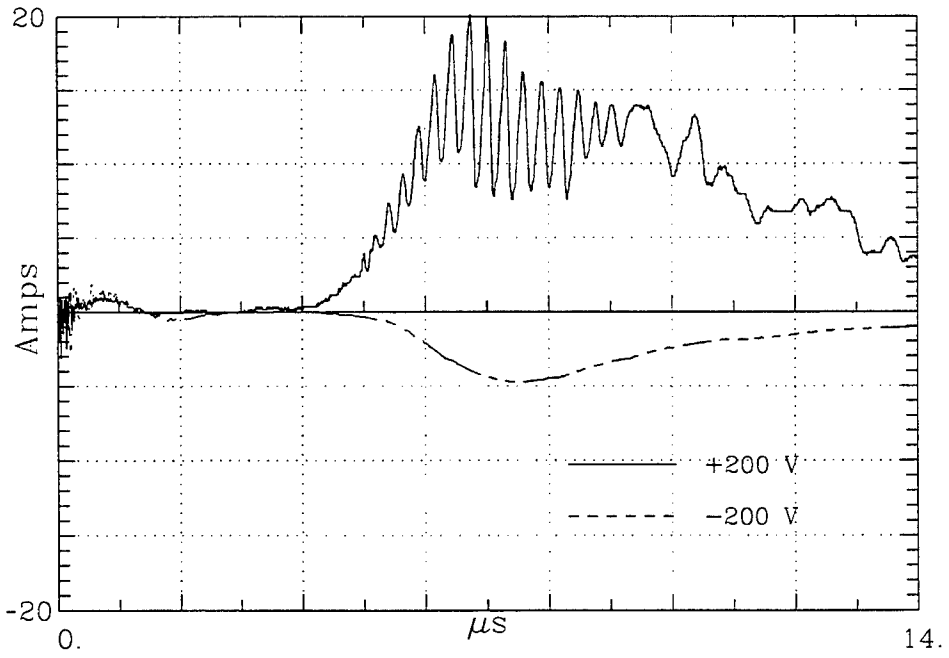

Figure 3-26. Comparison of collected currents with positive and negative biases.

In the simulation shown in Figure 3-27, plasma of density $5x10^{12}$ cm^{-3} is injected at a velocity of 13 cm/μsec into an AK gap of 1.73 cm, giving an injected current of 10 A/cm^2 for both ions and electrons. An applied voltage of 1 kV is such as to accelerate electrons across the gap and decelerate ions. The IVORY simulations exhibit oscillations with a period of ~200 nsec. In the experiment, the period of the oscillations at the peak of the pulse is 200-300 nsec, and gradually lengthens to 400-500 nsec at the tail of the pulse.

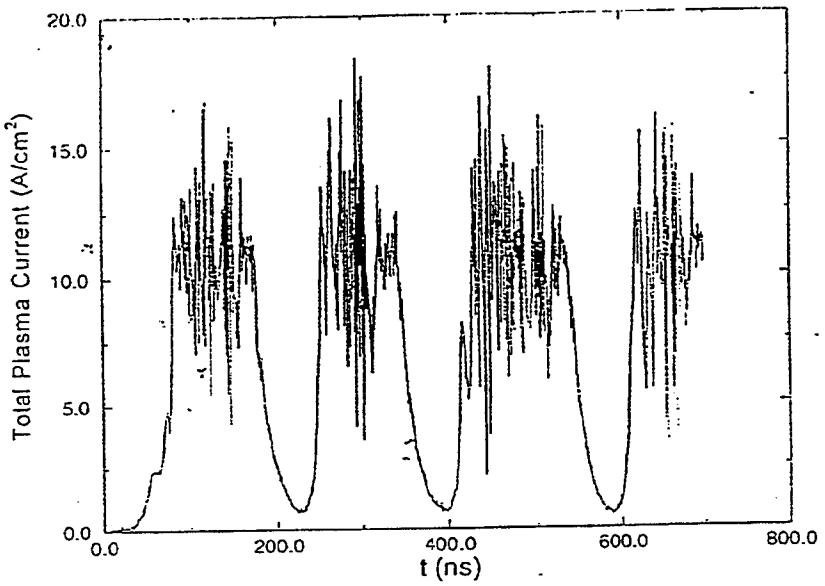

Figure 3-27. Total plasma current vs. time for a 1 kV reverse bias. Ions and electrons are injected at 13 cm/μsec with current density of 10 A/cm^2.

The dynamics of these reverse-bias oscillations are quite interesting. The oscillations are composed of two phases: a "gap-filling" phase and a "plasma-filled diode" phase. In the gap filling phase, electrons and ions travel together across the AK gap as a quasi-neutral plasma at about the ion injection velocity. The vacuum space-charge-limited current for 1 kV and a 1.73 cm gap is 0.025 A/cm^2, much smaller than the injected current of 10 A/cm^2. Therefore, of necessity, there is a virtual cathode at the head of the moving plasma. The plot of the AK potential in Figure 3-28 shows that almost all of the potential difference is between the anode and the head of the moving plasma. The excess charge in the virtual cathode shields the body of the plasma.

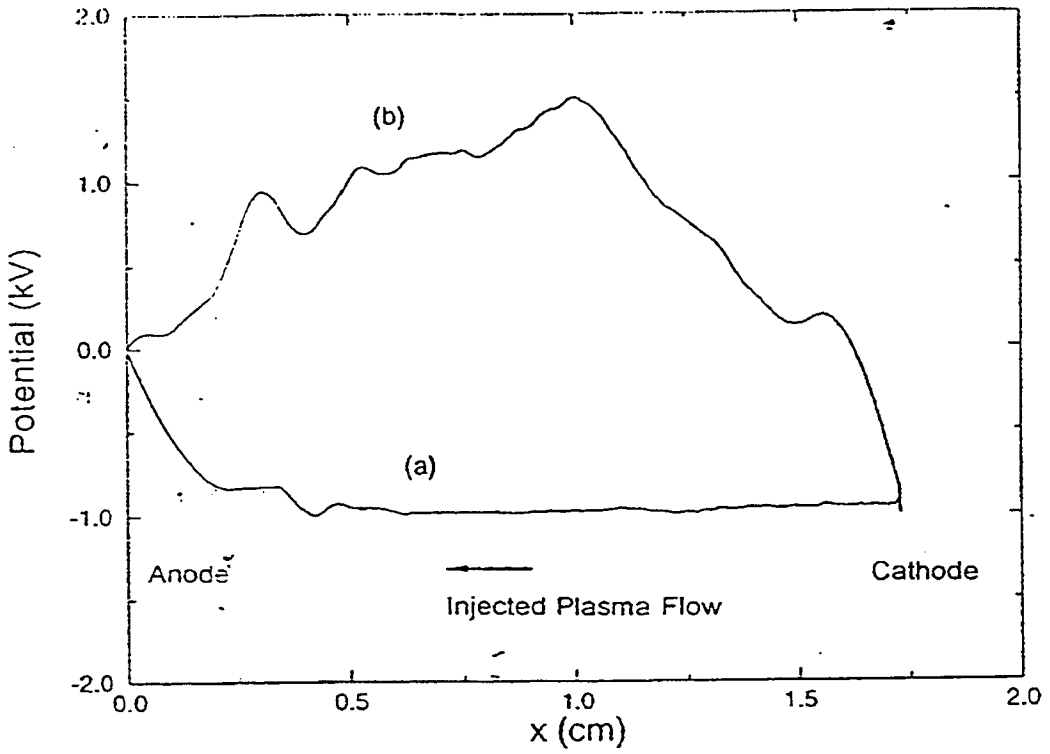

Figure 3-28. Potential across AK gap during the (a) "gap-filling" phase when a quasi-neutral plasma is drifting from the cathode to the anode and (b) during the "plasma-filled-diode" phase. (The anode has arbitrarily been taken to be at zero potential in these simulations.) In (a) the plasma has almost reached the anode (t = 70 ns in Figure 3-27). Most of the potential drop is between the anode and the head of the plasma. In (b) the plasma has developed a net positive charge, which shuts off further ion injection (t = 280 ns in Figure 3-27).

Once the plasma reaches the anode, the behavior changes markedly. A positive potential hump forms in the middle of the plasma as shown in Figure 3-28. The hump develops because electrons are no longer impeded by space-charge from reaching the anode, and so an electron depleted sheath develops at the anode. The positive hump is reminiscent of the ambipolar potential which develops in a hot plasma in contact with a conducting wall. There is a large potential drop at the cathode which shuts off ion injection and draws the maximum electron current of 10 A/cm^2. The region between the cathode and anode has a population of trapped electrons as well as the "beam" electrons which stream from the cathode to the anode. The net positive charge of this region causes the plasma ions to expand to both the anode and cathode. Eventually, the AK gap is essentially emptied of plasma, and the filling process repeats.

Further simulations were carried out to attempt to reproduce the gradual reduction of the oscillation frequency seen in the experiment. It was speculated that the lower frequency might be due to heavier ions such as C^{++} (doubly ionized carbon) reaching the gap. To test the mass dependency, C^{++} was injected with the same velocity as the H^+. It was found that this gave approximately the same frequency as H^+, even though the mass-to-charge ratio was six times larger. This is perhaps not too surprising since, as mentioned above, the injected plasma fills the gap at roughly the injected speed, which is the same for both species. The time scale for the second half of the oscillation (the blow-up phase) is not so obvious, but empirically it is also roughly the same for both species.

Other results of positive bias simulations also showed the oscillation frequency to be roughly proportional to the injected ion velocity, suggesting the observed drop in frequency is associated with slower moving ions. Finally, simulations with different gap voltages show a gradual shortening of the oscillation period from 200 to 150 nsec as the voltage is raised from 500 V to 2 kV.

In Figure 3-26 the current does not go to essentially zero in the oscillation cycle as is shown in the simulation, probably due to electron emission from the cathode electrode.

3.2.6 Ion Current and Species Evolution with Removal of the Bend.

To increase the injected ion flux, the 90 degree bend was removed from the system, as shown in Figure 3-4. Bandpass filters were utilized with the gated CCD camera to gain information about the time histories of the ion species in the plasma. The images can be compared with the measured ion current, and inferences about the relative proportions of the species in the plasma can be made. These experiments were performed in the glass cross with its easy visual access. Similar to the images shown earlier, Figure 3-21, the centerline of the camera was in-line with the cathode plane.

The bandpass filter experiments compared images using two different bandpass filters and a neutral density filter. The bandpass filters used were a filter centered at 486.1 nm to look at the neutral hydrogen line H_β at 486.1 nm, and a filter centered at 589.3 nm to

look at spectral lines of singly ionized carbon, C+, at 588.9 and 589.1 nm. These filters have 10 nm FWHM spectral ranges, and very low transmittance over the rest of the visual range. The only strong spectral lines transmitted by these filters are from the desired species. However, there is always a transmitted component of background continuum which can complicate the interpretation of the data. The neutral density filters have flat transmission characteristics over most of the visible spectrum, so the images with the neutral density filter are sensitive to all visible wavelengths. The transparency of the material of the glass cross, Pyrex, drops off sharply in the UV portion of the spectrum, below ~300 nm, as also do the light collecting optics and the sensitivity of the photo-cathode on the gated MCP. This limits these measurements to light from the visual range, and hot plasmas which may radiate strongly in the UV will not be observed.

Due to the nature of this type of measurement, care must be taken in comparing the absolute intensities of the images of one filter with another. The relative line strengths depend upon more than just the density of the species. However, comparisons of the intensity of one image may be made with another image with the same filter with some confidence in the interpretation.

The camera gate used in these experiments was a microsecond wide and no voltage was applied to the AK gap. To demonstrate the MCP gate time in relation to the plasma pulse, gate pulses at 2, 2.5, 3 and 4 μsec are shown along with the measured ion current in Figure 3-29. The anode aperture was 2.54 cm in diameter without a mesh. Shown in Figure 3-30 are gated images of the plasma at the cathode with a 0.9 neutral density filter and an f-stop of f5.6. The standard nomenclature for neutral density filters is logarithmic base 10, so a 0.9 neutral density filter attenuates the transmitted light by a factor of x8. To better demonstrate the differences early in time, when the intensity is low, the images are artificially brightened and the contrast increased. At MCP gate times of 2 μsec and earlier, there was no light visible at this sensitivity. Light from the flashboard surface was reflected off of the curved edge of the cathode, so a baseline shot with only reflected light has been subtracted from these images. The location of the subtracted light can be seen in some images late in time as a dark strip above the bright plasma. There is no subtraction where the plasma is located. Shown in Figures 3-31 and 3-32 are equivalent series of images with the C+ and H_β bandpass filters instead of the neutral density filters. Due to the narrow band of the filters, the f-stop for these images is f1.8.

After about 4 μsec, there do not appear to be any significant differences in the light emitted from any of the bands. The differences in absolute intensity between one filter and another cannot be fully interpreted without knowing more details about the plasma conditions and the relative line strengths. Before 4 μsec there do appear to be differences in the images from the different filters.

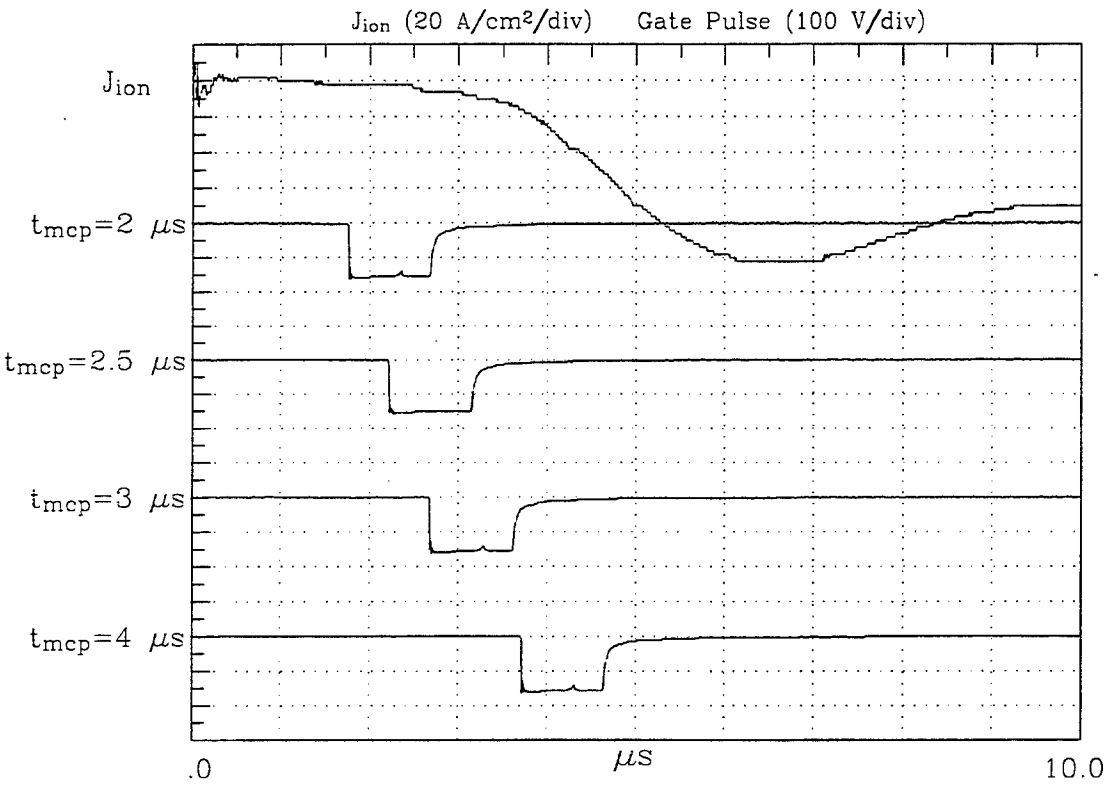

Figure 3-29. Relative timing of measured ion current and MCP gate pulses.

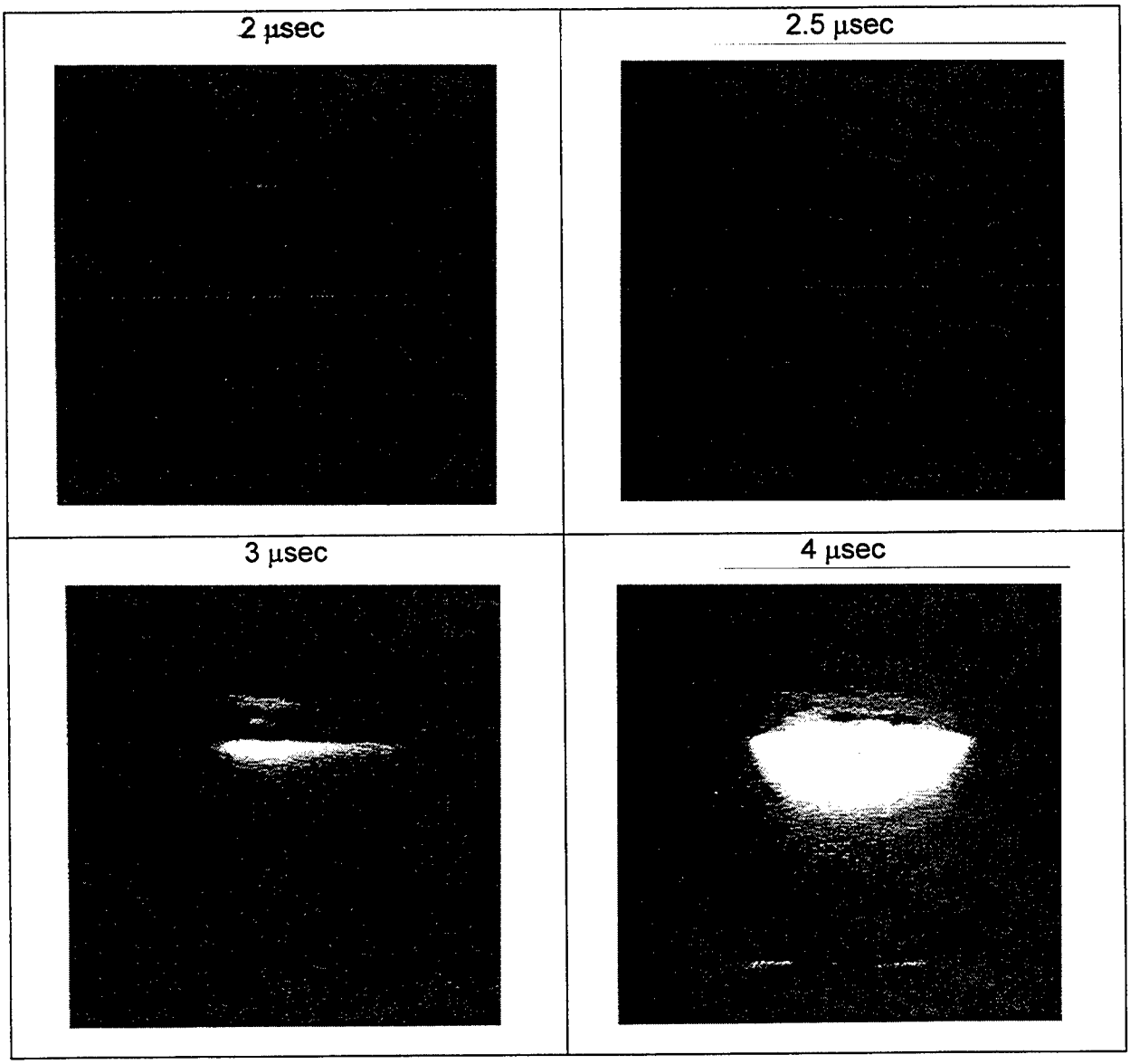

Figure 3-30. Enhanced images of all visible light at the cathode.

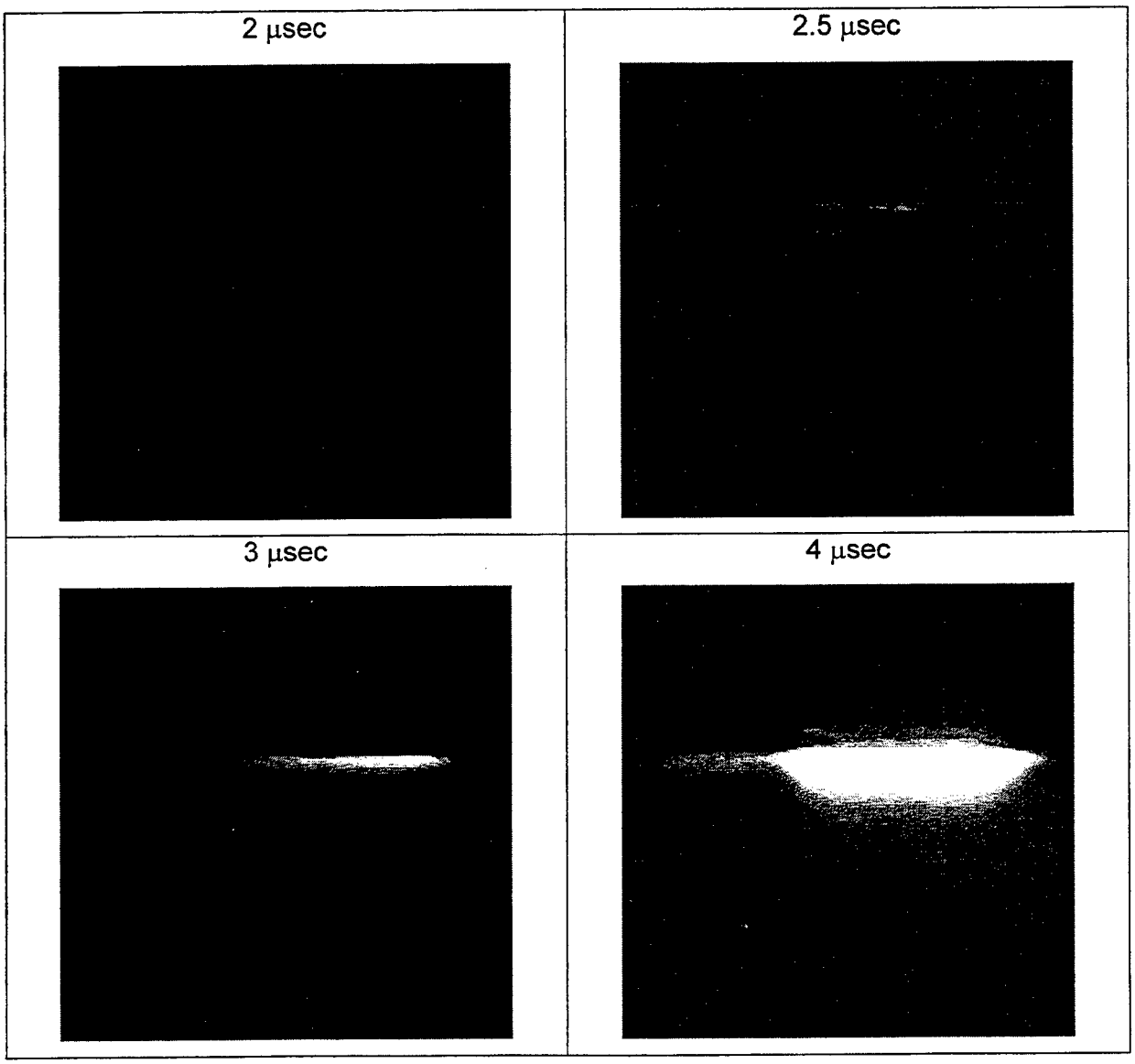

Figure 3-31. Enhanced images of the light in the C^+ band at the cathode.

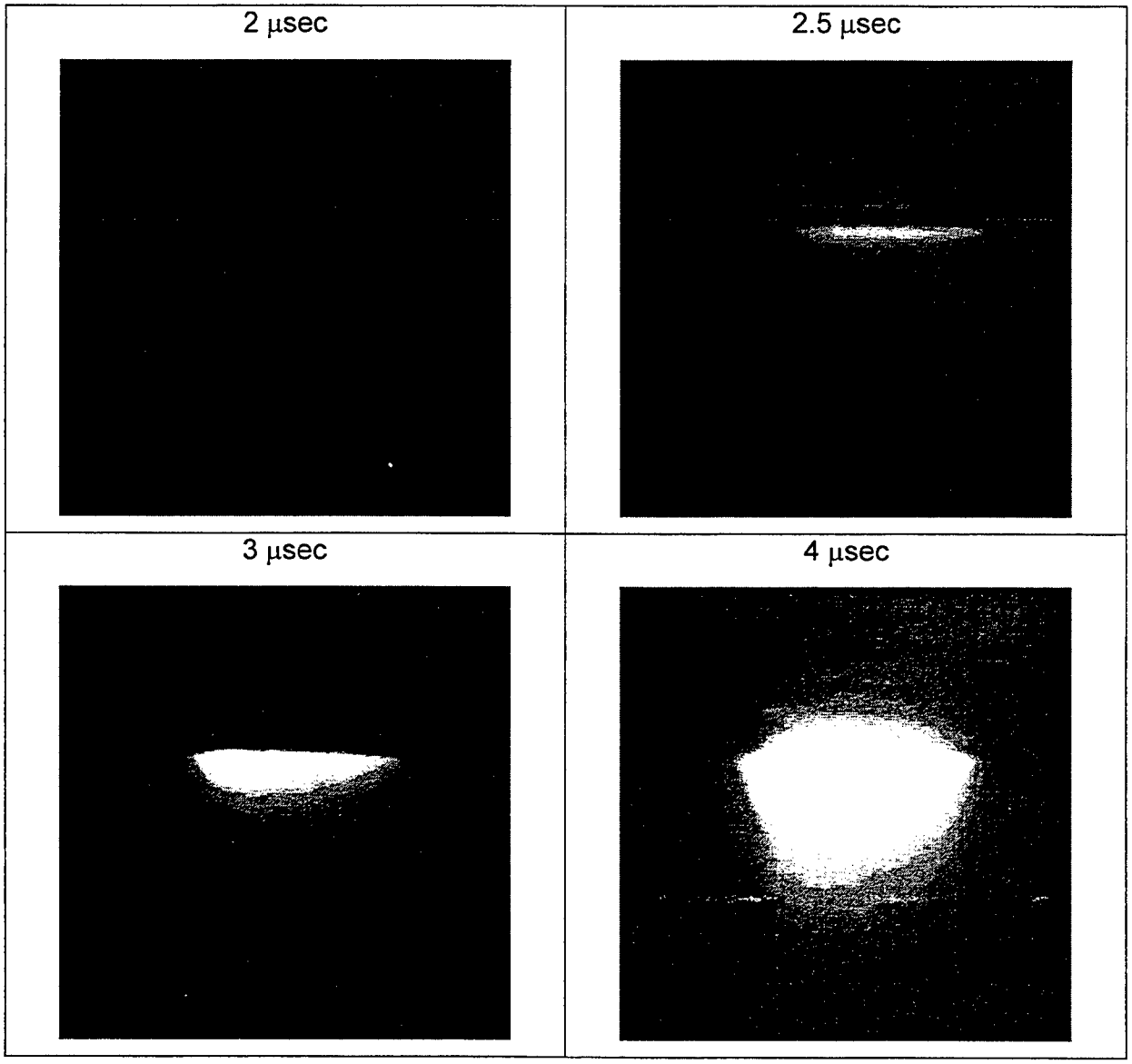

Figure 3-32. Enhanced images of the light in the H_β band at the cathode.

At 2 μsec, none of the images showed appreciable signal from the plasma, although there was some reflected light for which the subtraction routine did not account. The most noticeable differences were at 2.5 and 3.0 μsec when there was clearly much more light coming in the H_β band than through the other filters. There may still be relatively more light in the H_β images at 4 μsec, but all of the images showed a strong increase in light at that time.

From the bandpass filter results, it appears that for the first ~1 μsec of the plasma arriving at the cathode, the light came almost solely from hydrogen, and that was probably the dominant species in the plasma. From ~1.5 to 2 μsec after the first plasma reaches the cathode the images still show a greater proportion of the light coming in the spectral band that includes H_β than in the spectral band that includes the singly ionized carbon line, implying that the plasma was still predominately hydrogen, but there was likely more of a carbon component. Approximately 2 μsec after the first arrival of the plasma, there was a dramatic increase in the total light emitted and an increase in the light emitted in each of the bands measured. The strong increase in overall intensity along with the relative increase of the light in the C^+ spectral band implies that there was a fairly large mount of carbon present in the plasma at that time. As the proportion of carbon increases, the total light emitted should increase drastically because carbon has many more radiative channels than hydrogen.

If the plasma is highly collisional, time-of-flight separation of the ion species might not be expected. In the relatively low density leading edge of the plasma pulse more separation of species may occur, but in the later bulk of the plasma collisions may limit separation of the species. During most of the time intervals of the conduction experiments there was likely a mix of species in the plasma.

3.2.7 Flashboard Erosion.

During experiments in the glass cross at the higher ion currents after removal of the 90 degree bend, increased shot-to-shot variation in the conduction currents was noted, and it was noted that the flashboard had sustained considerable damage. The flashboard was made with a copper sheet on one side, copper pads on the other side, and five layers of Kapton insulation laminated in between. Voltage was applied across the pads, and the flashover between the pads created the plasma. The copper sheet acted as a low inductance return path for the current, and increased the magnetic field at the flashboard surface to increase JxB acceleration of the plasma. The damage to the flashboard appeared as a circular image of the anode aperture. Inside the damage circle some or all of the layers of Kapton insulation between the pads and the copper sheet were eroded away. This situation obviously can change the current paths in the flashboard, and can change the flashboard's net output, spatial uniformity, and reproducibility.

The measured ion current waveforms from the damaged flashboard were very similar in general waveform shape to the previous measurements from the flashboard before the damage was evident, but were down in net ion current by about a factor of two from the undamaged flashboard, and the shot-to-shot variation was significant. It is not clear whether the shot-to-shot variations in the measured signals were due to spatial non-uniformities in the plasma column, or due to global variations from differences in the current paths at the flashboard.

The damage to the flashboard was most likely caused by "energetic" particles from the AK gap streaming down and striking the surface. Since the flashboard was inductively isolated from the rest of the system, it was not expected that large currents from the applied AK voltage could flow through the flashboard ground. Measurements of the flashboard current during a discharge confirmed this expectation. Most likely the net current to the flashboard was reduced by a return current from the surface of the flashboard back to the anode. This return current could flow through the fairly dense plasma between them, along field lines which intersect portions of the anode hardware. The damage to the flashboard explains the shot-to-shot variation seen in the data.

If the erosion of the flashboard insulator was caused by energetic electrons, it is reasonable to assume that there would be some Bremsstrahlung radiation from electrons striking the copper in the flashboard. To test this hypothesis, a dosimeter was placed 2.4 cm from the copper strip in the flashboard and another was placed 9.0 cm away. No measurable radiation above background was observed after numerous shots when only the flashboard was fired, but the dose on the closer dosimeter was measurable after a single shot with -30 kV applied to the AK gap. After a short data run with -30 kV voltage on the AK gap, the dosimeter at 2.4 cm measured ~17 mR, and the dosimeter at 9.0 cm measured ~3 mR. Assuming a point source for the radiation, these numbers imply a source located ~2.4 cm in front of the flashboard. These numbers are also consistent with a distributed source at the surface of the flashboard. Lead shielding ~0.16 cm thick was found to completely block the radiation.

Flashboard erosion was substantially reduced by injecting the plasma into a mirror field which reduced the higher energy electron flux from the switch on the flashboard as the electrons followed the diverging field lines.

3.3 CONDUCTION MODES AND SCALING.

3.3.1 Conduction Modes with the Straight Magnetic Field Configuration.

When the bend transport was removed from the glass cross system and the plasma source located closer to the AK gap, higher ion current densities were obtained ($\leq$ 100 A/cm^2) and new conduction modes were observed. Conduction modes can be broadly categorized into the two main divisions of high and low impedance. The low impedance

conduction can be broken down into cases with and without self-opening behavior. Near instantaneous ignition of the cathode upon application of voltage and very low gap "resistive" impedance are necessary for the low impedance modes. They typically occurred when voltage was applied after the gap was well filled with plasma, and are characterized by a rapidly rising current limited mostly by the inductance of the circuit. The self-opening mode is obviously of practical interest, and has demonstrated conduction times from a few hundred nsec or so up to over a microsecond at current levels in the 100 kA range. The low impedance mode without self-opening is needed for a switch triggered by external gating of the ion source. The externally gated switch requires a small but finite gap impedance (not shorted gap) at near peak current which exists over durations adequate for external gating. The high impedance mode was typically observed when the injected ion current density is low (≤ 5 A/cm^2) at early times after the injected plasma has reached the cathode. During these times it is likely that the cathode has not fully ignited initially and most of the voltage across the gap is effectively resistive. The mode is characterized by low currents, relatively flat or slowly rising over 1.5 - 2 μsec times, followed by the impedance drop which occurred for all modes at some point.

Simulations by T. Hughes with space charge limited cathode emission show high impedance modes only when voltage is applied before the plasma fills the gap, and the gap always opens. Otherwise the codes show low impedance initially with a very low gap resistance followed by self-opening as potential humps are formed in the gap as a result of heating of the background electrons. The hump shuts off incoming ion flow from the source and the gap opens as ions in the gap are emptied by acceleration to the electrodes. The simulations typically show a j_e/j_i ratio at opening of 25-30 for H^+ plasma densities experimentally associated with good opening events. Experimental ratios are in agreement with these simulation results.

The first regime to be discussed below is the low impedance mode with self-opening which is followed by results for the low impedance mode suitable for external gating. Some additional results for conduction at high impedance (>> few ohms) beyond those of Section 3.2.4 are then given. The remainder of this section gives more detailed diagnoses of characteristics of the self-opening and high impedance modes.

3.3.2 Low Impedance Conduction with Self-Opening.

The self-opening behavior was evident to some extent in nearly all of the configurations tested with the gap well filled with plasma, both with flashboard and cable gun sources. When present, the opening event occurred under conditions without an appreciable gradient in the ion current across the gap, and with gradients in either direction across the gap. During the initial current rise the measured voltage across the gap was approximately equal to the inductive voltage drop, and the resistive voltage drop was small. Depending on circuit parameters and ion source, the current rose at the inductively limited rate for ~200-900 nsec before the self-opening occurred. The rate at which the current dropped during the opening was 2 - 4.5 times faster than the initial

rate of rise for good openings, and the opening voltage was on the order of twice the charge voltage with the bank voltage and magnetic field parameters of the experiments.

Shown in Figure 3-33 is a small aperture shot in the glass cross hardware with the bend removed which demonstrates the self-opening. A voltage of -30 kV was applied to the gap 5.0 μsec after the trigger to the small flashboard, τ_{AK} = 5.0 μsec.

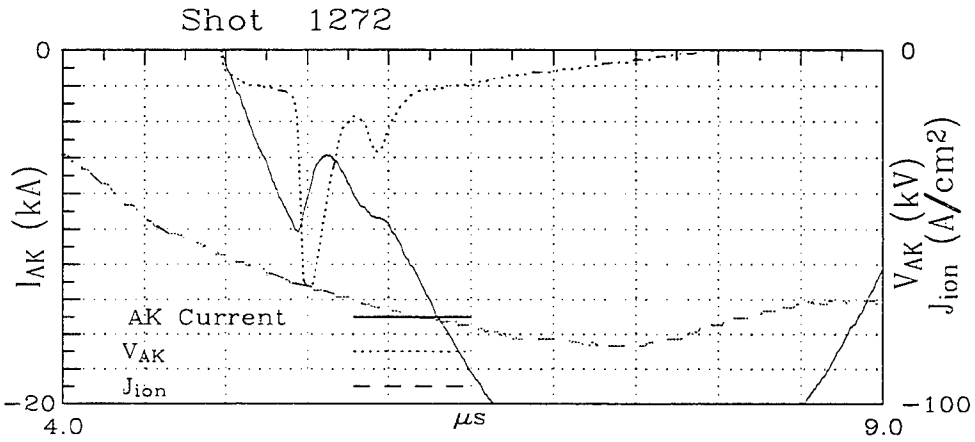

Figure 3-33. Discharge with τ_{AK} = 5.0 μsec demonstrating the self-opening mode. Ion current measured on a shot without voltage.

The flashboard was 44 cm from the cathode; the configuration is shown in Figure 3-5. There was no mesh across the 2.54 cm diameter anode aperture, and the AK gap was 13.6 cm, with an applied magnetic field of 2.1 kG in the gap. The driver bank had C = 1.4 μF, and L ≤ 1400 nH.

The voltage across the switch during the current risetime is ~10 kV and, assuming the voltage is entirely inductive during the risetime of the current, the inductance of the switch is ~555 nH and the actual bank inductance is 1115 nH. During the current bite, the voltage across the switch rises to 65 kV giving a peak voltage multiplication for an external load connected as the voltage monitor of 2.2 over the driver voltage, or a factor of >2 over 100 nsec. The resistive voltage drop across the switch during opening is ~86 kV. The j_e/j_i ratio at peak current is ~2000/60 or 33.

Figure 3-34 shows an opening event at higher current levels (80 kA) using a cable gun ion source located 12 cm from the 10.16 cm diameter anode mesh with a gun charge voltage of 15 kV. The AK voltage was applied 9 μsec after the trigger to the gun and the external field was 6.4 kG. The experimental configuration for this shot is shown in Figure 3-12, and the large ~150 nH driver bank was used. The peak rate of change of current during the bite was ~4.4 times the rate during the conduction, implying a resistive voltage during the fall of ~132 kV, and the switch remained open for >0.5 μsec.

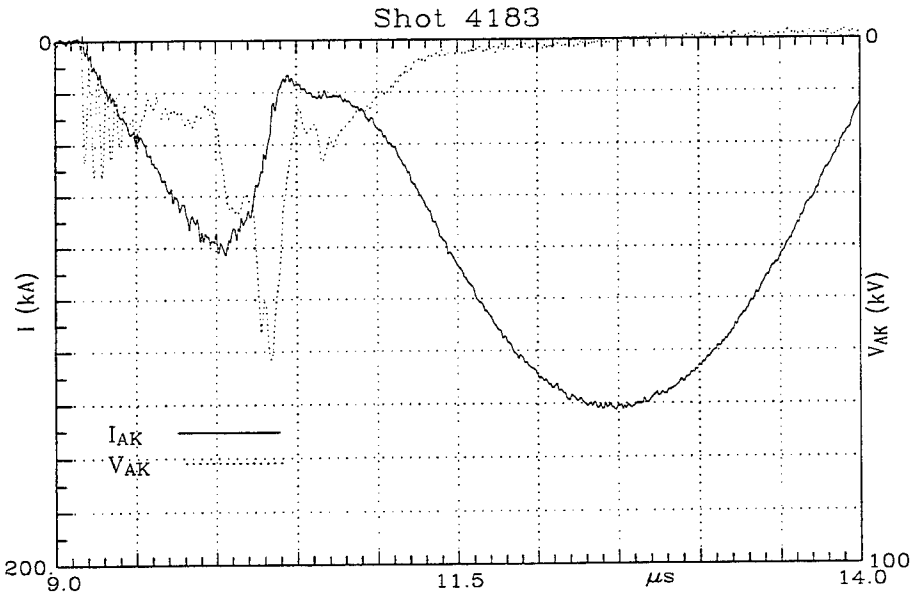

Figure 3-34. Discharge with the cable gun 12 cm from the anode mesh and a guiding magnetic field of 6.4 kG.

A model can be developed for scaling of the self-opening mode which incorporates results from both simulations and experiments. The model assumes the basic phenomenology of the simulations in which a potential hump is formed by heating of the background electron population. The potential hump then restricts or shuts off the ion flow, leading to an opening event as the ion "reservoir" of the gap is depleted.

Simulations with the gap initially filled with plasma all show very low impedance when the voltage is applied, consistent with experimental results in the self-opening mode. Experimentally, though, voltage does appear across the gap during the conduction phase due to the inductance of the switch. [This inductance is not included in a one-dimensional simulation or was negligible in the limited two-dimensional simulations.] The voltage across the gap remains low until the magnitude of the potential hump is of the order of the injected ion kinetic energy.

A model of Kares, et al.[(2)] gives an upper limit on the magnitude of the potential hump. Using this model and setting the hump potential equal to the injected ion kinetic energy gives a limit on the j_e/j_i ratio around which ion flow is restricted:

$$\frac{j_e}{j_i} < \frac{1}{2}\sqrt{\frac{M}{Zm}}\left(\frac{1}{1+\gamma}\right) \qquad (3.1)$$

(2) R. Kares, et al., J. App. Phys., 71, 2168 (1992).

where M is the ion mass, Z the ion charge number, m the electron mass, and γ a parameter which accounts for the effects of trapped electrons in the potential hump ($\gamma \leq 1$). Taking $\gamma = 0.3$ from simulations, the formula gives j_e/j_i ratios of 17, 57, and 41 for H^+, C^+, and C^{++} respectively. Simulations with low driver bank voltages (1 kV) and "long" current risetimes ($\gtrsim$ 200 nsec), or $dj_e/dt \lesssim 0.6 \times 10^9$ A/cm^2/sec, generally agree with the model and show current "clamping" at $j_e/j_i \sim 15$ for H^+ or an opening. The injected ion current is relatively unimpeded until the j_e/j_i ratio approaches that of the above formula.

Simulations with higher voltage ($\geq$ 5 kV) and shorter risetimes (~ 100 nsec), or $dj_e/dt > 3 \times 10^9$ A/cm^2/sec, show openings with a higher j_e/j_i ratio at opening than the Kares formula values, i.e., $j_e/j_i \sim$ 25-30 for cases with injected H^+ ion current density relevant to experimental self-opening conditions ($j_i \gtrsim 10$ A/cm^2).

Experiments with self-opening modes also show $j_e/j_i \sim$ 25-30 at the time of opening in cases where the ion current density is reasonably uniform over the channel cross-section and with no evidence of appreciable channel expansion. The ion current density used in the experimental ratio is that around the time of application of voltage, but measured without applied voltage, and pertains to cases where the injected ion current is nearly constant or increases over the time of conduction. (See, e.g., Figure 3-33). With good openings, the experimental values of dj_e/dt exceed 10^9 A/cm^2/sec, i.e,, are in the fast risetime range of the simulations.

With the above discussion in mind, simple formulas for scaling the peak current, I_p, and conduction time, t_c, of the self-opening mode can be given:

$$I_p \sim j_i(0)\, \eta\, A \qquad (3.2)$$
$$t_c = [j_i(0)\, \eta\, A\, L_T]/V_c$$

where $j_i(0)$ is the ion current density of the time of application of the voltage, A is the channel cross-sectional area, L_T the total system inductance (bank and switch), V_c is the charging voltage, and η the peak j_e/j_i ratio. From experiments and hydrogen plasma simulations $\eta \sim$ 25-30. The above formulas assume that the ion current density is uniform in radius and nearly constant over the conduction time, $dj_e/dt \gtrsim 10^9$ A/cm^2/sec, the bank external resistance is negligible, and that the cathode is fully ignited at the on-set of conduction. The latter condition was typically realized experimentally when the ion current was collected by the cathode for a duration of $\gtrsim 2$ μsec and $j_i(0) \gtrsim 10$ A/cm^2 at the time the voltage was applied.

There are two points worthy of note regarding the scaling formulas above. First, the parameters used in simulations show conduction times before opening of 50-100 nsec; i.e., nearly an order of magnitude shorter than experimental results. The discrepancy is due to the small channel area of the simulations (~ 1 cm^2) and, in the inductively-limited

conduction time formula above, it is of course the total current which determines the time. The other remark is that simulations do show higher η values than 25-30 in certain cases which may be practically exploitable. For example, a C^+ simulation with the same injected ion velocity as the H^+ simulations (13 cm/μsec) reaches the Langmuir-Child bi-polar value of ~ 150 at opening.

3.3.3 Low Impedance Conduction Without Opening.

The low impedance mode without opening must of course not be simply that of a shorted gap to be useful. The current should rise to near peak levels and the gap should have a residual impedance as the current reaches near peak levels in order to control an opening with external gating. With short AK gaps (< 5 cm) a low impedance mode without opening was observed when voltage was applied near peak injected ion currents; the gap however did not typically have significant impedance near peak current. Very near the end of the program the mode was obtained with a larger (20.5 cm) AK gap when the large flashboard was moved closer to the anode mesh.

In order to achieve high total currents a 15.24 cm diameter anode aperture with a ~14x14 line-per-cm mesh was used, and the large flashboard was 38 cm from the cathode. This configuration is shown in Figure 3-8. The switch was driven by the large 150 nH driver bank charged to -30 kV. The AK gap spacing was 20.5 cm, with a 2.5 kG applied field. In this configuration, it was possible to achieve one of the major goals of the program; namely, low impedance gap behavior over microsecond time scales. The switch data given in Figure 3-35 shows basically an inductance dominated current rise without opening, a non-shorted gap over nearly 2 μsec and conduction current correlating with ion current for as long as the ion collector signal is believable. After ~1.5 μsec of conduction, when the current rise flattened at ~95% of peak current, the gap still had ~10 kV residual voltage which lasted nearly 0.5 μsec.

Figure 3-35 shows the data from three ion collectors behind the cathode mesh, the total current, and the voltage across the gap for a shot with the voltage applied 5 μsec after the trigger to the flashboard. With no voltage applied to the AK gap, the collectors behind the cathode, at radii of 0 cm and ±4 cm, showed fairly good agreement with each other, but with some shot-to-shot variation. When the AK voltage was applied, all of the collectors showed similar behavior, but there was a fairly large spread in the amplitudes of the signals. For comparison, the measured ion current on-axis without applied voltage is also plotted. The early time oscillations on the voltage across the gap are due to an impedance mismatch in the driver circuit, and are not an artifact of the diagnostic. For the first ~200 nsec, the measured ion current from each collector remained approximately the same as before the voltage was applied. After that time the collector signals increased, with all three collectors tracking each other for 500 nsec. All of the collectors tracked the general shape of the AK current, although typically with more structure than the AK current. Around 6 μsec it was clear the collectors were no longer responding properly. The signals increased rapidly, at a much higher rate than earlier in the discharge. This behavior was most likely caused by the

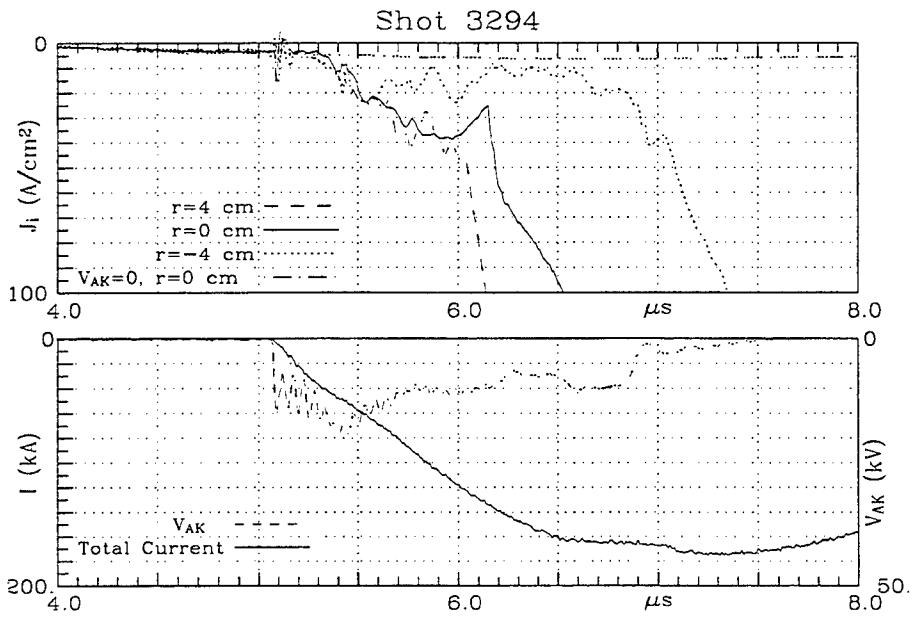

Figure 3-35. Measured current, voltage and ion currents at three radii with the large flashboard 38 cm from the cathode, and τ_{AK} = 5.0 μsec.

formation of plasmas on the collectors' surfaces. The plasma allows electron emission from the collector and may expand and increase the effective collecting areas of the 1 cm^2 collectors. The earlier increase in the collector signals did not show the same characteristic, and probably represented an increase in the ion current from the gap. Although the collectors showed similar waveforms, their amplitudes frequently differed by up to a factor of two or more. This strong variation in the amplitudes implies that when the AK voltage was applied, there were large density gradients and variations in the ion current in both the radial and azimuthal directions were generated. At the time of departure of the r = -4 cm collector current from the other two, the discharge should have been MHD stable to kink motions according to the Kruskal-Schafranov criterion.

The sustained increase in ion current shown by the ion collectors was only observed when the flashboard or cable gun was "close" to the anode mesh (18.5 cm for the flashboard in the case of Figure 3-35). With all other parameters the same, increasing the flashboard to anode distance to ~40 cm, e.g., gave an opening type current profile as shown for comparison in Figure 3-36.

In the two cases the on-axis ion current densities measured without voltage were not significantly different. On-axis ion collector measurements with opening events show an increase by a factor of 2-3 in the ion current density over those measured without voltage during the current rise, followed by a drop in the j_i to below or near the no

voltage level. (See Section 3.3.5) Simulation results show an increase in ion current density by a factor of ~1.5 for H^+ injected at ~88 eV and up to a factor of ~4-5 for ~1 keV C^+ ions. The ion current density is increased by the electric field of the potential

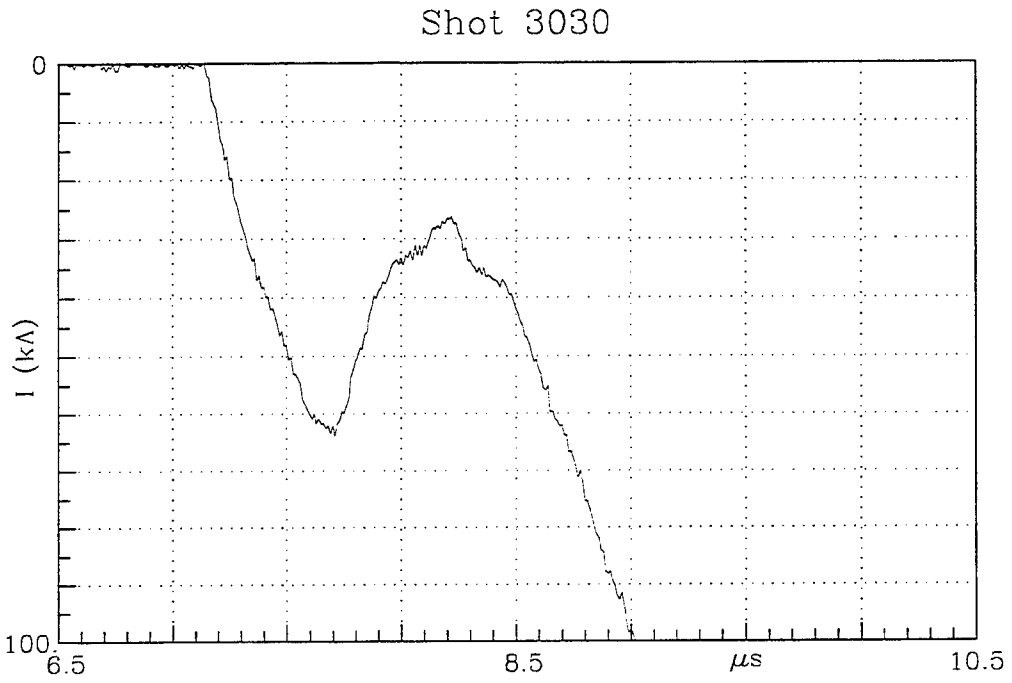

Figure 3-36. Shot with a 15.24 cm diameter anode aperture and the large area flashboard.

hump accelerating ions out of the gap before opening. A sustained increase in ion current density implies that the ion current density injected into the gap from the source or from the anode mesh plasma increases and that a potential hump does not exist to shut off or restrict the ion flow as with a self-opening behavior. The ~5 kV increase in V_{AK} in Figure 3-35 when the ion current density rises over 0.5 μsec or so suggests an anode sheath is formed accelerating ions from the source or anode mesh plasma into the gap, possibly caused by electrons reflexing through the anode or by injection of low energy electrons from the source region. In any case, simulations including the anode to source region and more extensive measurements of the time dependence of the radial ion density distribution of the source are needed to better understand this important conduction mode.

The simulations and analytic models of conduction discussed in Section 3.3.2 suggest a method for realizing a mode suitable for external gating. To be conservative, the limit on the j_e/j_i ratio from the Kares model is assumed. We use doubly-ionized carbon, the most practically advantageous ion with $j_e/j_i \lesssim 40$, and the main output component of

DSWA gun sources used in the DECADE program. [The experimental observation that this mode was obtained when the flashboard source was moved closer to the anode may be in part due to a dominant carbon output at time of voltage application.] As long as $j_e/j_i \lesssim 40$ the ion flow should then be relatively unimpeded and the current should follow the ion source current. The peak current and time to reach it are obtainable from the same formulas as used for the opening mode scaling, but with $\eta \sim 40$ and C^{++}. Near the time of peak current, the ion source needs to be gated to reduce the ion current density by only a factor of ~2 to achieve opening if H^+ results can be scaled to C^{++}.

3.3.4 High Impedance Conduction Mode.

The high impedance conduction mode typically occurred when the voltage was applied early in time, from before to ≤1.5 μsec after the first plasma had crossed the AK gap. In this condition the ion current was fairly low, the plasma probably had a greater proportion of hydrogen than later in time, and there was a gradient in the ion flux from the cathode to the anode. The gradient in ion flux varied from a factor of 1.5 times to 4 times greater ion flux at the anode than at the cathode. In this mode the voltage across the gap was approximately the charging voltage and the current roughly followed the ion current as measured without voltage with $j_e/j_i \leq 30$ until the start of the impedance drop. With the relatively low ion dose at the cathode at the time of application of the voltage, cathode emission appeared to be limited initially and the impedance of the gap was effectively resistive. During the 2 μsec or so conduction before the start of the impedance drop, the injected ion current was not entirely shut off.

Figure 3-37 shows two high impedance shots taken with the glass cross hardware with the bend removed, as shown in Figure 3-4. The voltage was applied to the gap 2.0 μsec after the trigger to the flashboard, $\tau_{AK} = 2.0$ μsec. The charge voltage in Figure 3-37(a) was -30 kV, and the charge voltage in Figure 3-37(b) was -15 kV. The driver bank consisted of the two, 0.7 μF capacitors with a total inductance of ~1400 nH. These shots were taken with a 13.6 cm AK gap, a ~14x14 line-per-cm tungsten mesh across the 2.54 cm diameter anode aperture, and guiding magnetic field of ~2.1 kG. The ion current shown is representative of the shape of the injected ion current. However, as the shots with voltage were taken near the time the flashboard erosion became a serious problem, and when frequent measurements were not yet being made of the ion current, there may have been changes in the flashboard output between the time the ion current was measured and the shots with voltage were taken.

These shots demonstrate that the current was limited by the injected ion current and was relatively independent of the charge voltage. There was some correspondence between the conducted current and the injected ion current measured without applied voltage for times up to ~2 μsec, dependent upon the conditions. However, after a conduction time of ~2 μsec the conducted current started to increase, with a corresponding decrease in the measured voltage across the gap. The conducted current for the first part of the discharge was clearly not limited by the driving circuit, so

it must have been limited by either cathode emission, or by the ion source in the gap. Varying the cathode conditions from a foil cathode, to a mesh cathode, to a carbon velvet cathode and even a solid, limited area cathode did not change the discharge characteristics. A possible explanation of these observations is that the cathode is initially emission limited in all cases, leading to the formation of a nearly full voltage sheath. Once formed, the sheath persists with the current largely controlled by the ion source. The increase in the current, accompanied by the drop in voltage across the gap, was probably due to an expansion of the current channels described in Section 3.3.8.

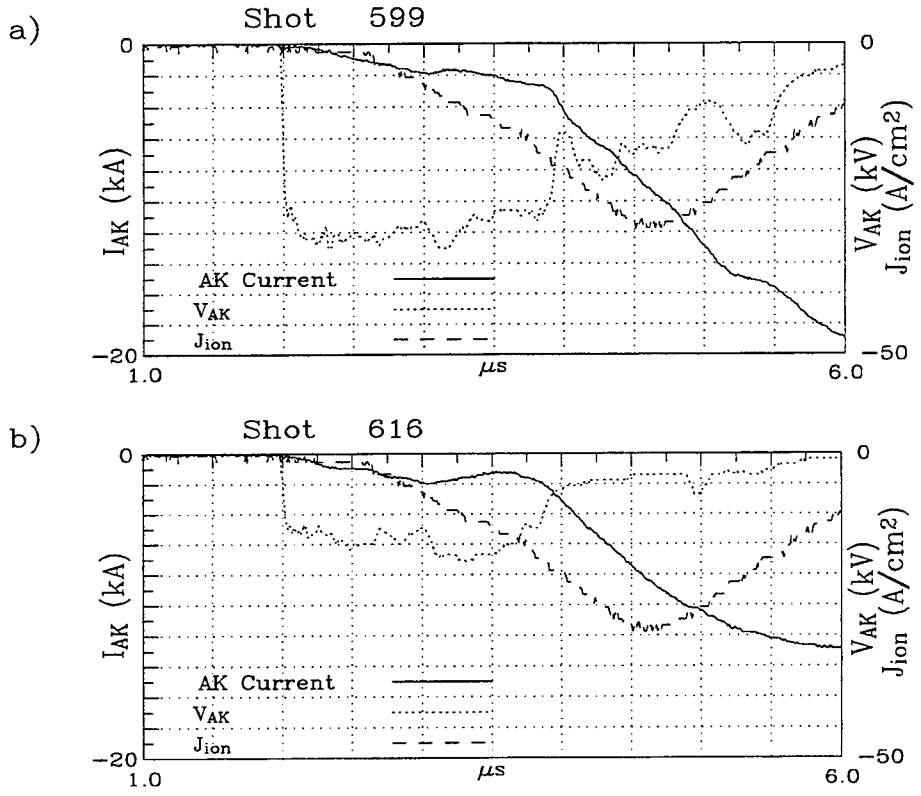

Figure 3-37. Two high impedance shots.

Shown in Figure 3-38 for comparison with Figure 3-35 is a high impedance conduction shot with the same hardware set-up as was used for Figure 3-35 (flashboard "close"), but with the voltage applied just as the injected plasma reaches the cathode. At this time the measured ion current density is very low. With this initial condition on the ion current, nearly the full charge voltage was measured across the AK gap, and the AK current was fairly small for ~1.25 μsec. Similarly to the data in Figure 3-35, the total current and the measured ion currents roughly track in shape, but there are significant variations between collectors and the collectors are suspect after a microsecond or so. After about 1.25 μsec the voltage across the gap drops, and the current begins to rise at

a more rapid rate. This drop in impedance is always seen, and some correlation with the gap length will be shown for the high impedance modes in a later section of this report.

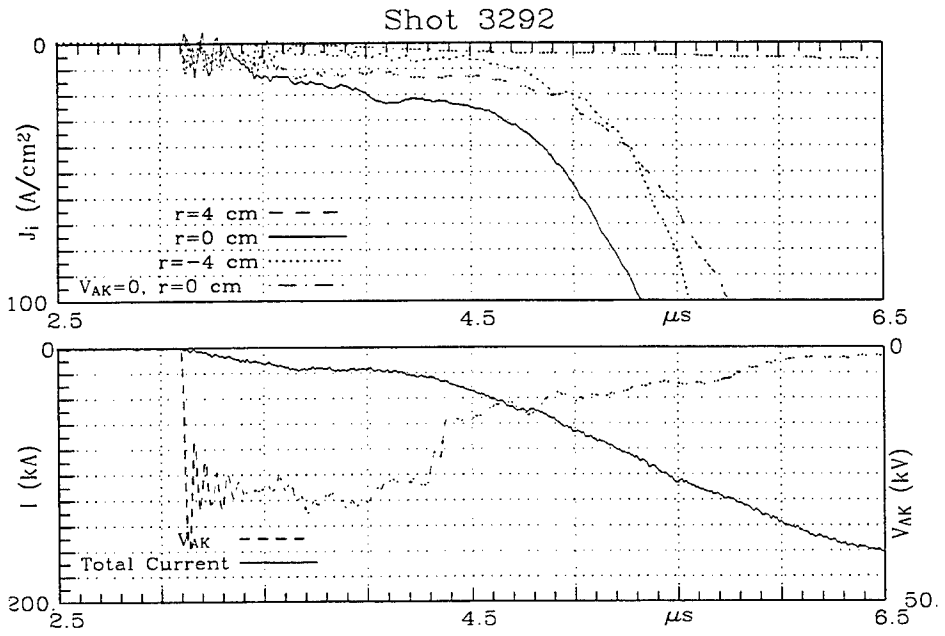

Figure 3-38. Measured current, voltage and ion currents at three radii with the large flashboard 38 cm from the cathode, and τ_{AK} = 3.0 μsec.

3.3.5 Ion Current Measurements.

Measurements of the ion current during the discharge were made in the coaxial system with the heatable collector behind the cathode. The collector was typically located 4 cm behind the cathode. This displacement caused a small temporal shift between the ion current it measured and the actual ion current near the cathode in the gap. The duration of the shift was dependent upon the drift velocity of the ions. Without applied AK voltage, the ion drift velocity typically ranged from ~20 cm/μsec early in time to ~6 cm/μsec later in time, so the ion current measured by the collector was indicative of the ion current in the gap 200 to 700 nsec earlier. The time shift with applied AK voltage was reduced, depending upon the velocity gained by the ions in crossing the cathode sheath. Shown in Figure 3-39 are "mixed-mode" traces of the total current, voltage and measured ion current with the AK voltage applied ~1 μsec after the first plasma had crossed the gap. For comparison, the measured ion current without applied voltage is also shown. The driver bank for this shot had C = 1.4 μF and L = 910 nH, and the guiding magnetic field was ~2.5 kG. The small flashboard was 38 cm from the cathode, the AK gap was 16 cm, and there was a 14x14 line-per-cm mesh across the 2.54 cm diameter anode aperture. The collector was 4 cm behind the cathode mesh.

The ion collector signals always showed a sharp transient when the bank was triggered and this transient spike is evident in the figure. The signal then showed an increase in the collector signal which rose to a factor of ~x3 above the pre-voltage ion current

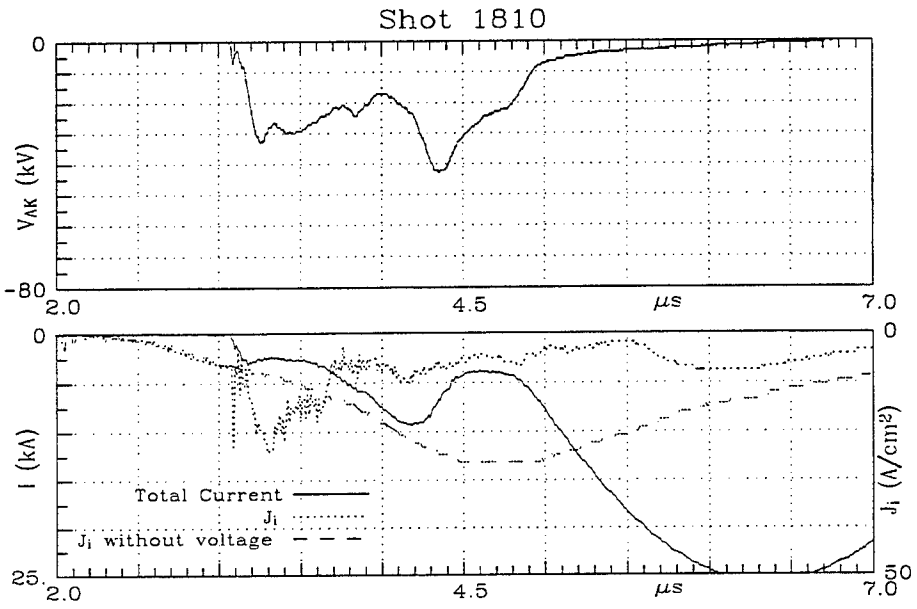

Figure 3-39. Comparison of measured ion current with and without applied AK voltage, with τ_{AK} = 3.0 μsec.

density. The peak of the ion current density occurred ~136 nsec after the current peak both in Figure 3-39 and the following figure. If this delay is due to the transit time from cathode to collector, the ion velocity is ~29 cm/μsec corresponding to an effective accelerating potential of ~450 Volts in the gap during the current rise. Furthermore, if the delay is due to transit time, the ion signal increases once voltage is applied and peaks at peak current as is evidenced in the simulation runs. On the other hand, if the transit delay is less, the peak ion current density shifts more towards the peak voltage across the gap. There are unfortunately two other ambiguities in the ion signal. Once the gap voltage becomes >20 kV, the ions can generate 2-3 ejection electrons from the collector which appear as an additional ion current. The other uncertainty is the cathode mesh transparency, as previously discussed. With no initial cathode emission limitation, the simulations show an ion current density enhancement of a factor of ~1.5 for H^+ ions injected at ~90 eV, and a factor of ~5 for C^+ ions with energy of ~1 keV.

After the peak j_i, the signal drops significantly below the level measured without voltage and stays roughly constant even as the impedance of the gap drops. If the ion signal is believable, there is thus likely some initial depletion of ions near the axis in the gap near the cathode, followed by a sustained injection into the gap at a low level (~5 A/cm^2). One of the significant new results of the simulations of the program showed that if anode space charge emission of electrons is allowed, an opening event does not

entirely shut off the current flow, but reduces it by roughly a factor of two. This effect may be relevant to the data of Figures 3-39 and 3-40. A consistent explanation of the impedance drop with flat on-axis ion current density is the radial expansion of the current channel associated with outward ion transport and diffusion from the original channel.

Figure 3-40 shows a shot with the same experimental parameters as with Figure 3-39, but with voltage applied on the downward slope of the ion source profile. Again, there is a ~136 nsec delay between the peak of the current and the peak j_i. Also, a factor of ~3 enhancement in the j_i over the source without voltage is observed.

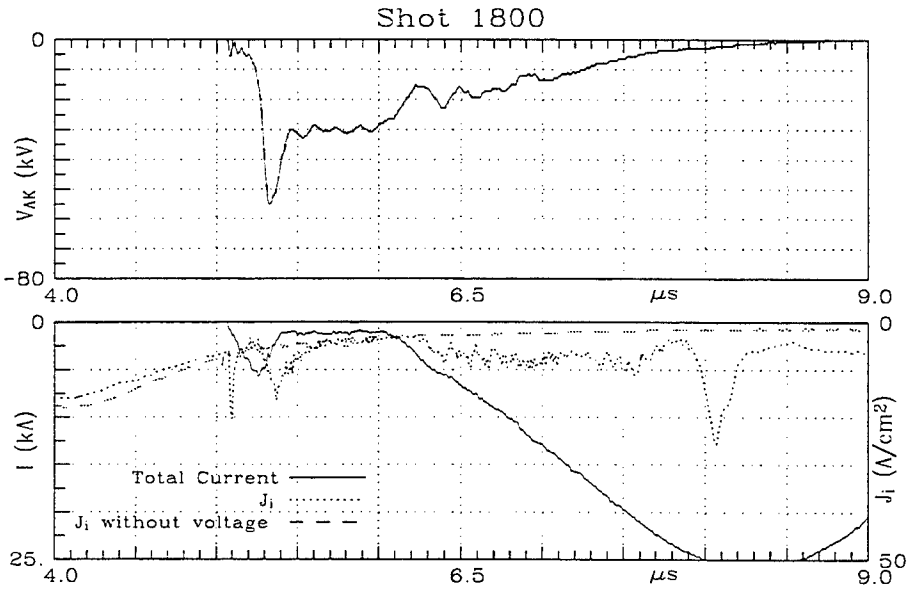

Figure 3-40. Comparison of measured ion current with and without applied AK voltage, with τ_{AK} = 5.0 μsec.

Shown Figure 3-41 is the scaling of the conduction current with the measured ion current density on-axis. The conduction current is defined as the current level to which the current rises and maintains a nearly constant value in the case of a high impedance mode, or the level at which the self-opening occurs. These data were taken with the same electrode and magnetic field configurations as the data in Figures 3-39 and 3-40, but the driver bank inductance was reduced to 480 nH, from 910 nH. The data displayed in Figure 3-41 is from shots both with and without a mesh across the 2.54 cm diameter anode aperture. The scaling of conduction current and charge transfer is unfortunately beclouded by the shot-to-shot variation in the flashboard output and by effects of current channel expansion which occurred with the 2.5 kG magnetic field level of the experiments, particularly in the case of the high impedance modes. (See Section

3.3.8). The data does show an approximate scaling of conduction current with on-axis ion current density.

With the cable gun source the conduction current was also found to vary with the injected ion current density. However, the behavior of the opening was observed to change with increasing ion current density on-axis, and discharge conditions were found

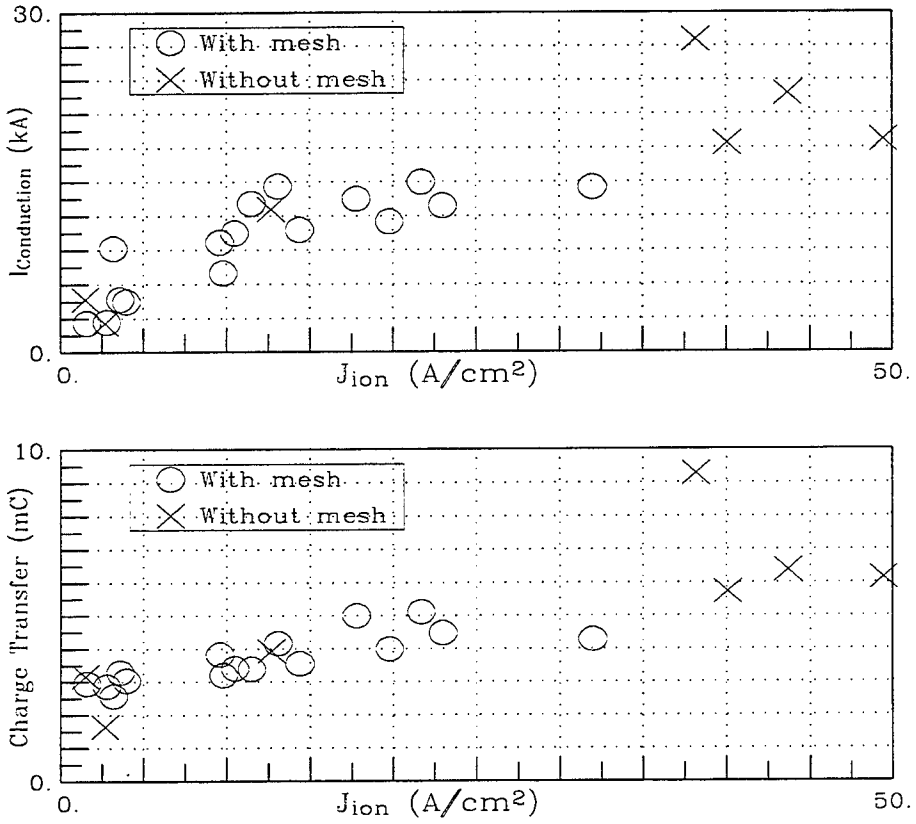

Figure 3-41. Discharges with 480 nH of total inductance. The charge voltage was -30 kV in all cases.

to vary with the gun location and applied magnetic field. An effort was made to diagnose the plasma density and distribution as the gun location and magnetic field were changed. Ion collectors were placed on-axis and 2 cm above and below the axis to measure the incident ion current density while the gun location, magnetic field strength, and charge voltage on the plasma driver were varied. In general, it was found that there were some variations in the radial distribution of the plasma as the gun parameters were varied, but these were not as significant as the variations in the total injected ion current. By varying several of the parameters, nearly equivalent net ion currents could be achieved with fairly different gun to AK gap spacings. Discharges with similar net ion currents show that it was the amount of injected ion current that dominated switch behavior rather than its radial distribution, at least within the limited

information on the radial distribution of ion current density available from the two off-axis collectors.

Shown in Figure 3-42 are two discharges with the cable gun source. The configuration is shown in Figure 3-12, with the cable gun 12 cm from the anode mesh, and an applied field of 6.4 kG. At the time voltage was applied, the ion current density on-axis was ~65 A/cm^2 with 15 kV on the cable gun and ~100 A/cm^2 with 30 kV on the cable gun. At the higher ion current density, the switch "tried" to self-open at higher current, but the opening was not as good.

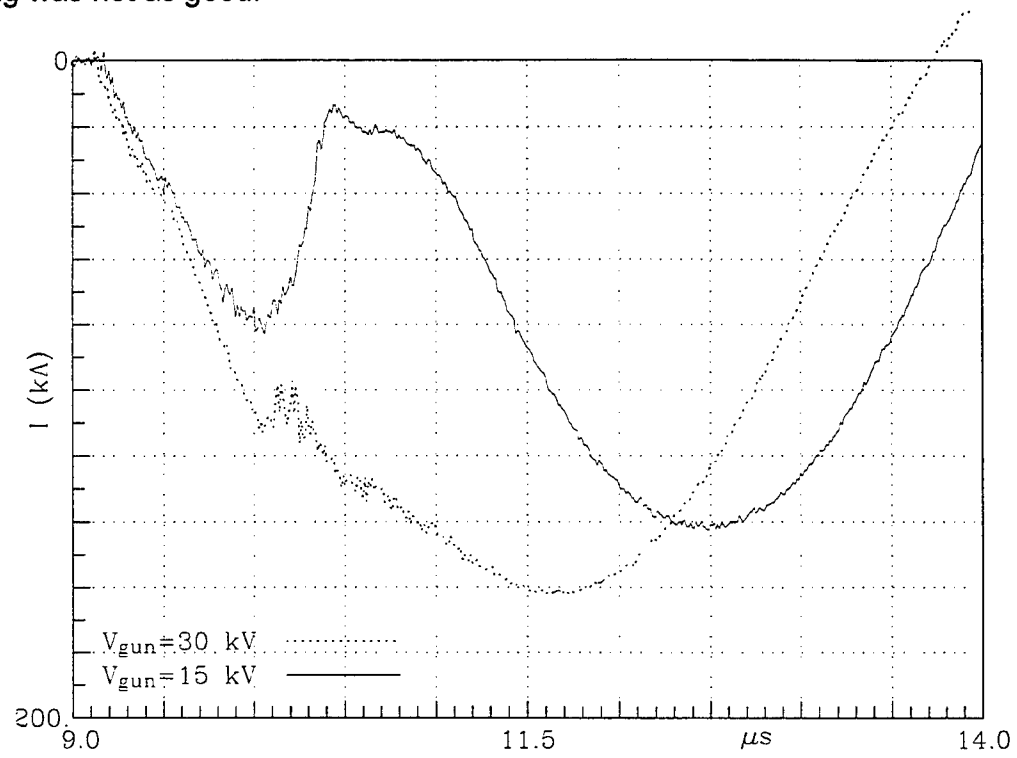

Figure 3-42. Discharges with two different charge voltages on the cable gun.

3.3.6 Gated Images of the Plasma Column.

In the glass cross hardware with the 90 degree bend, gated images of the plasma were acquired showing radial expansion of the light emitting region at the cathode correlating with the impedance drop (Figure 3-21). Images were later taken of the AK gap region with the straight magnetic field configuration shown in Figure 3-4, at a field strength of 2.1 kG. The C=1.4 μF and L=1400 nH driver bank was used. The AK gap was 8.6 cm and there was a ~14x14 line-per-cm mesh across the 2.54 cm diameter anode aperture. The ion source profile for these experiments (measured without applied voltage) is given in Figure 3-29. Shown in Figure 3-43 are four high impedance discharges with

τ_{AK} = 3.0 μsec, and with MCP gate pulses at four times during the discharges. For this set of discharges, the gate pulse to the MCP was 100 nsec long. In Figures 3-44 and 3-45 the images of the plasma column at the four times are shown. The "positive" images have both the intensity and contrast enhanced to better display the light emitting regions, but the "negative" images have not been altered. The same camera set-up of Figure 3-21 was used here, except that the electrode images were blocked because the plasma at the surface of the electrodes was much brighter than the plasma column. Approximately 3.5 cm of the plasma column was visible. The cathode was near the top of the image, approximately 1 cm above the visible portion of the plasma column, and the anode was approximately 4 cm below the camera's field of view. In general, luminous regions of the gap indicate the presence of partially ionized plasma excited mostly by electrons, either background or accelerated. Highly ionized or low density plasmas, or regions with low electron current density or temperature give little or no visible light.

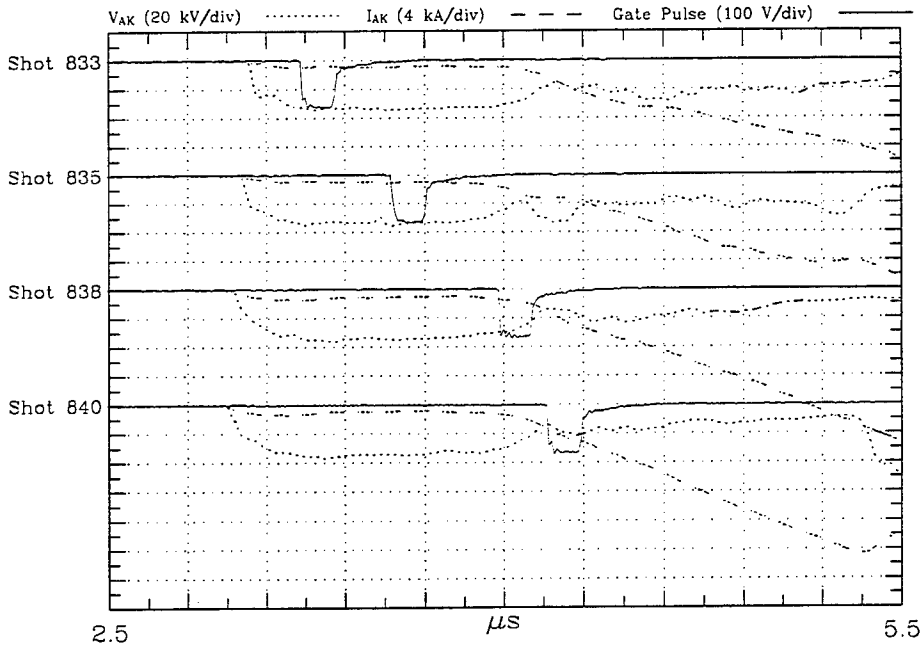

Figure 3-43. Relative timings of MCP gate pulses and the measured current and voltage for high conduction impedance discharges.

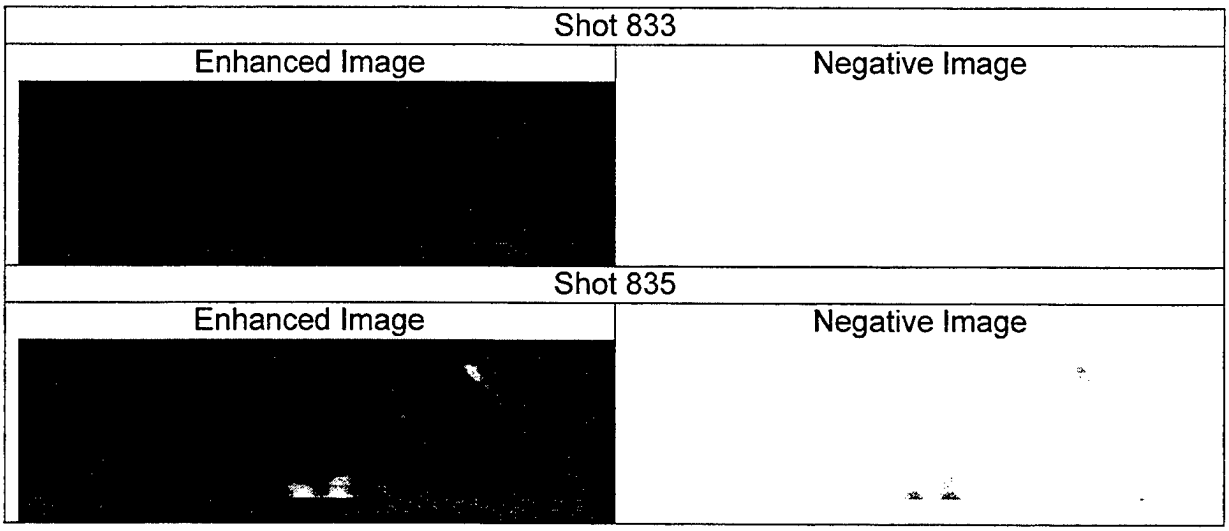

Figure 3-44. Images of the plasma in the AK gap before the impedance drop.

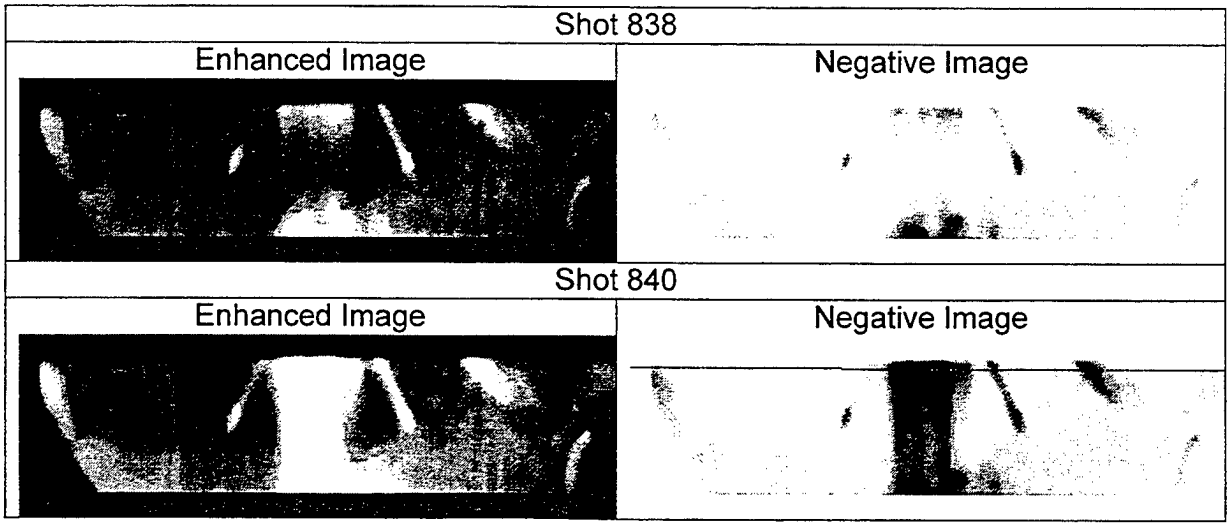

Figure 3-45. Images of the plasma in the AK gap at the start of the impedance drop.

This sequence of shots shows that the plasma column was not visible across the entire gap until the start of the impedance drop which in this case corresponded with increasing injected ion current density, but there was a bright region near the anode before the impedance drop. In shot 835 the two bright regions on the anode side of the gap were visible about 0.64 cm into the visible gap, but there was no evidence of light emission from the cathode yet, even though the cathode was nearer the field of view. If the bright spots in Shot 835 were due to anode plasma, their average velocity from the time of application of the voltage was ~7 cm/μsec - much higher than can be argued from dose estimates for the anode mesh. From Shot 838 to 840 the negative images suggest the anode spots have moved at ~1 cm/μsec, a more typical thermally driven velocity for high current density diodes. However, since the spots extend ~4.6 cm from the anode mesh, the ~1 μsec duration of current flow at the time of the Shot 840 image suggests the electrode plasma velocity was much higher earlier, as remarked for Shot 835, and then slowed down - an unlikely scenario. The dose arguments are based on electron energy deposition in the anode mesh; ion dose was not likely important given the absence of the bright spots in Figure 3-47 wherein the ion dose was much higher than in Shots 835 and 838 and the field of view extended closer to the anode. The image in shot 840 was approximately 540 nsec later in the discharge, and there was a clear bright column across the entire visible gap. For electrode plasmas to close the 2.8 cm gap from the bright region in shot 838 over the ~160 nsec rise time in between Shots 838 and 840, the average closure velocity for plasmas from both sides would need to be ~8.8 cm/μsec. This gap effective closure velocity was in the velocity range of the injected plasma and the ion current density was rapidly rising at these times.

Although these images might be similar to those of electrode plasmas expanding across and shorting the gap, the current and voltage traces for these discharges clearly demonstrate that the gap was not shorted even at 5.5 μsec. If plasmas from the electrodes were forming and crossing the gap in this time, their densities were low enough that the ~20 kA current was able to erode the plasma. In addition, the region of luminescence at the center of the gap did not grow to be as wide as the luminescent regions near the electrodes, as seen in Figure 3-21, and the luminescent regions near the electrodes are indicative of the width of the electrode plasma region.

At the time the current started to rise, there appeared to be light from the surfaces of the glass cross. This light may have been caused by the cross flashing over when it was exposed to the UV from the plasma. There was also some reflected light that appeared as diagonal streaks due to the curvature of the glass cross where the horizontal sections met the vertical sections. The diagonal streaks are unrelated to the switch behavior.

The absence of luminescence in the center of the gap at larger diameters than the initial plasma column diameter implies that any plasma there was fairly low density and/or highly ionized. Since the area increases rapidly with the radius, it is not necessary to have a high current density at larger radii to account for growth in the current.

The MCP gated CCD camera was also used to diagnose the location and relative density of the plasma in the AK gap before an opening event. The same configuration of the glass cross was used as above, except the camera's position was changed slightly. The camera was raised up and angled down slightly to allow viewing of the plasma closer to the anode surface; hence, nearly the entire 8.6 cm gap was visible. However, since light emission from the column was much dimmer than emission near the electrodes, the light from the electrodes and a small portion of the column near each electrode was still blocked to avoid saturating the signal on the CCD array.

Four discharges are shown in Figure 3-46 with the AK voltage applied 6.0 μsec after triggering the flashboard. The data in Figure 3-46 compare the timing of the gate to the MCP with the measured current and voltage across the gap. Since the time scale of interest is relatively short, the gate pulse to the MCP was only 40 nsec. The τ_{AK} = 6.0 μsec triggering time was chosen instead of the 5.0 μsec time shown in some of the previous data because at that time the plasma column was more visible early in the conduction phase, which made observation of the changes in light emission easier. This increased luminosity may have been an indication of smaller amounts of hydrogen and larger amounts of carbon or other high Z elements in the plasma at the later time. In Figures 3-47 through 3-50 the images of the plasma column at the four times are shown.

Early in the conduction phase, the plasma column was surrounded by bright regions at its edges, which is evidence of a "hollow" region of light emission. For an optically thin medium, a hollow, annular emitting region viewed from the side appears brightest at the edges where the line of sight intercepts more emitters. If the bright, emitting regions were caused by excitation of the plasma ions by conduction electrons, then a current sheath flowing on the outside of the column may be inferred. As the plasma continued to conduct, the hollow sheath appeared to move radially inward until there was a more narrow, central column from which most of the light was emitted. At the start of the opening event, when the voltage began its rapid rise above the inductive voltage, the plasma column became dimmer, and showed signs of a gap in emitted light.

The diameters of the luminous plasma columns in Shots 886, 888 and 890 were all smaller than that of the injected plasma and decrease as time increases from shot-to-shot. Keeping in mind that the outer regions may be more highly ionized in time as the current builds up and therefore of lower luminosity, the question nevertheless arises about beam pinching from self field forces as the current increases. If the actual conduction channel remains at or larger than the initial diameter, the B_θ field is always smaller than the applied longitudinal field (peak value of B_θ~1.7 kG) and the column is at worst marginally stable through opening to MHD kink growth. If the longitudinal field flux is preserved as the channel pinched, no significant pinching would have occurred. The longitudinal field in the current channel would, e.g., increase to ~7 kG with the radius of the luminous channel of Shot 888. A plasma conductivity of ~10 mho/cm would give a current diffusion rate comparable to that of Shot 886, and rough estimates

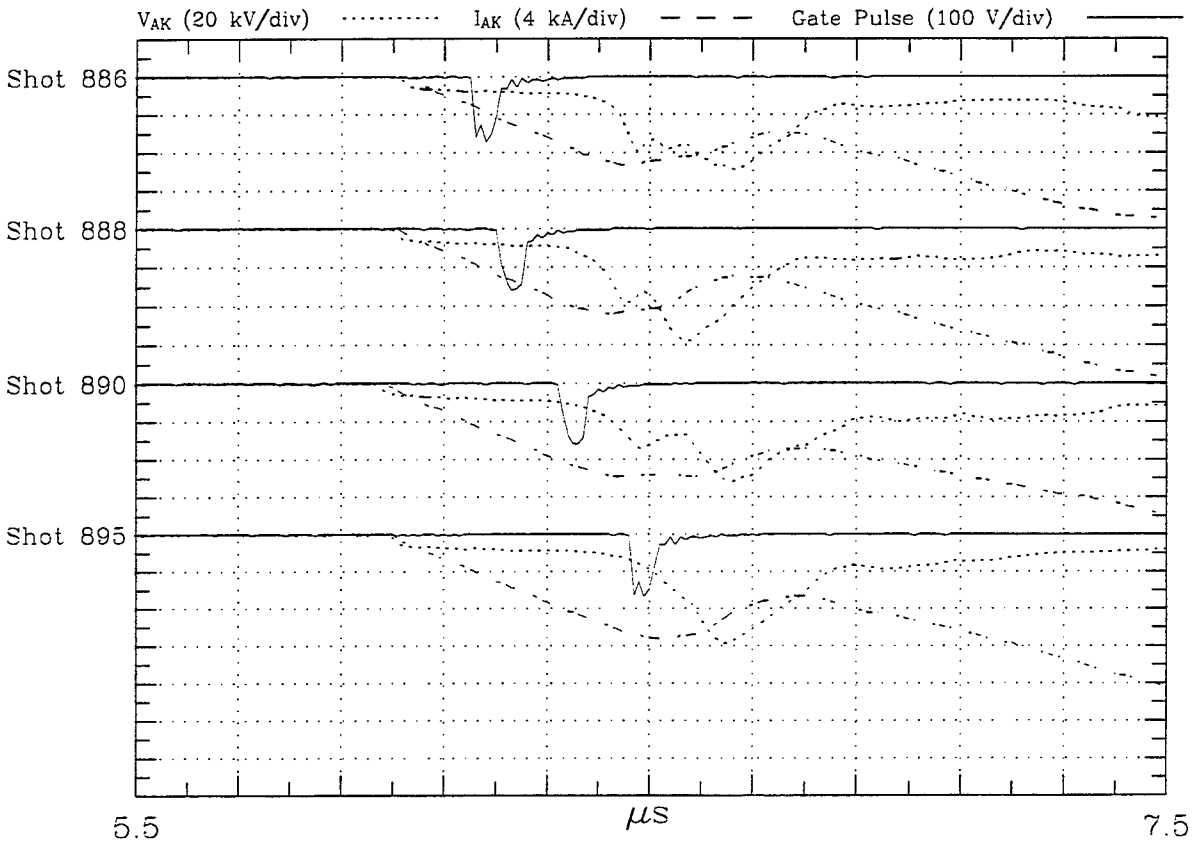

Figure 3-46. Relative timings of MCP gate pulses and measured currents and voltages for discharges with self-opening events.

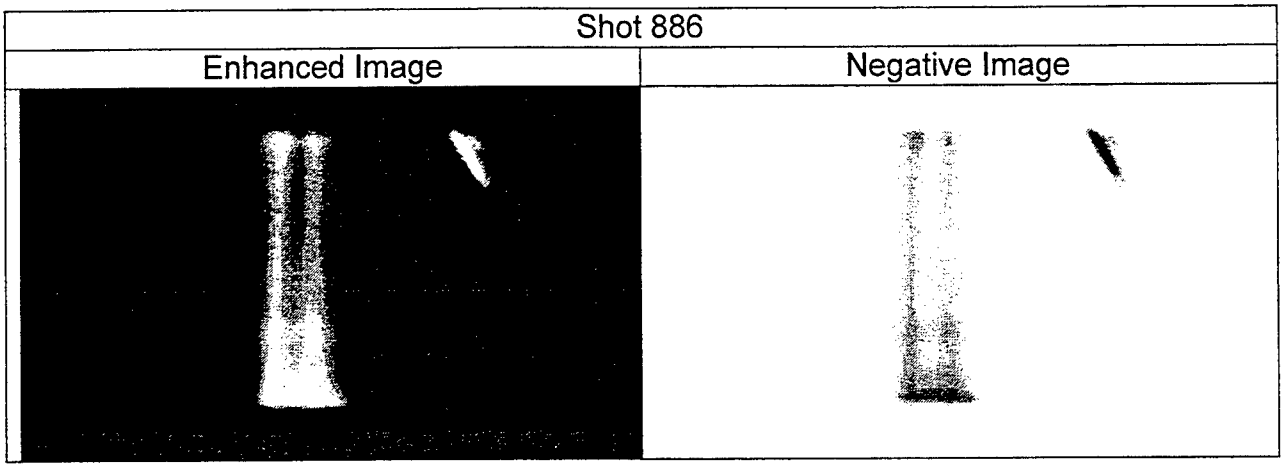

Figure 3-47. Image of the plasma column at the start of current conduction.

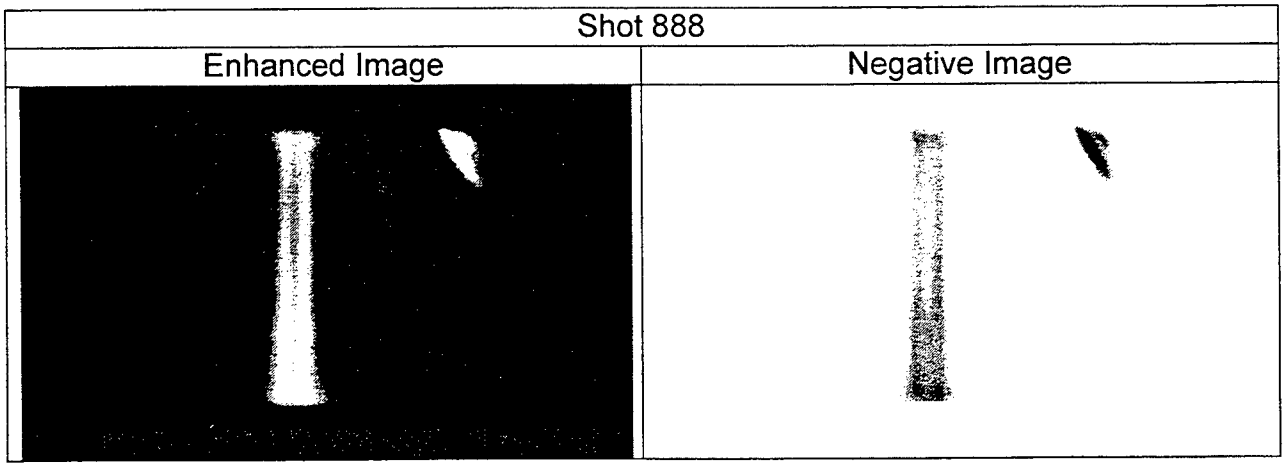

Figure 3-48. Image of the plasma column during the inductively limited current rise.

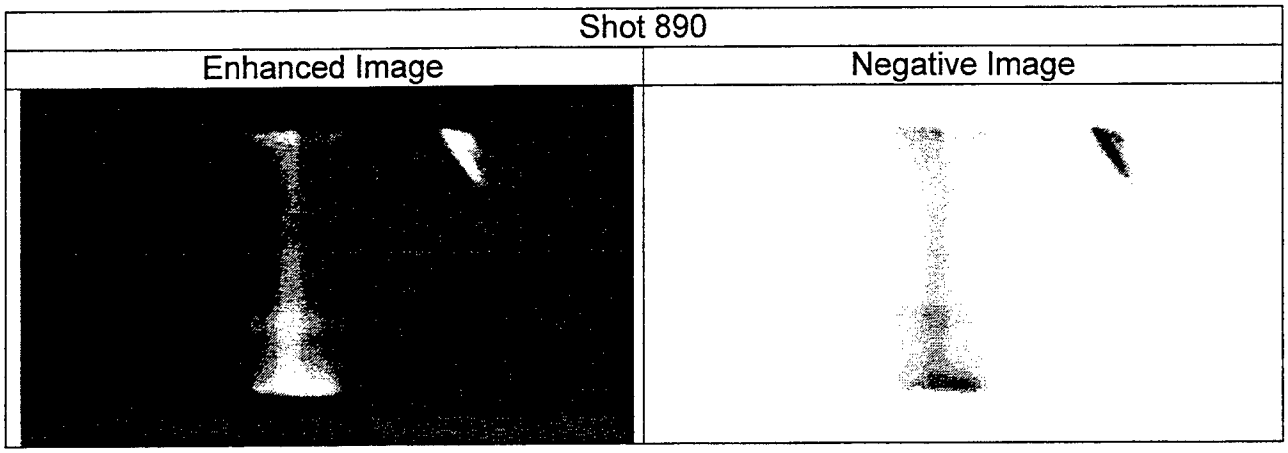

Figure 3-49. Image of the plasma column just before the start of the opening event.

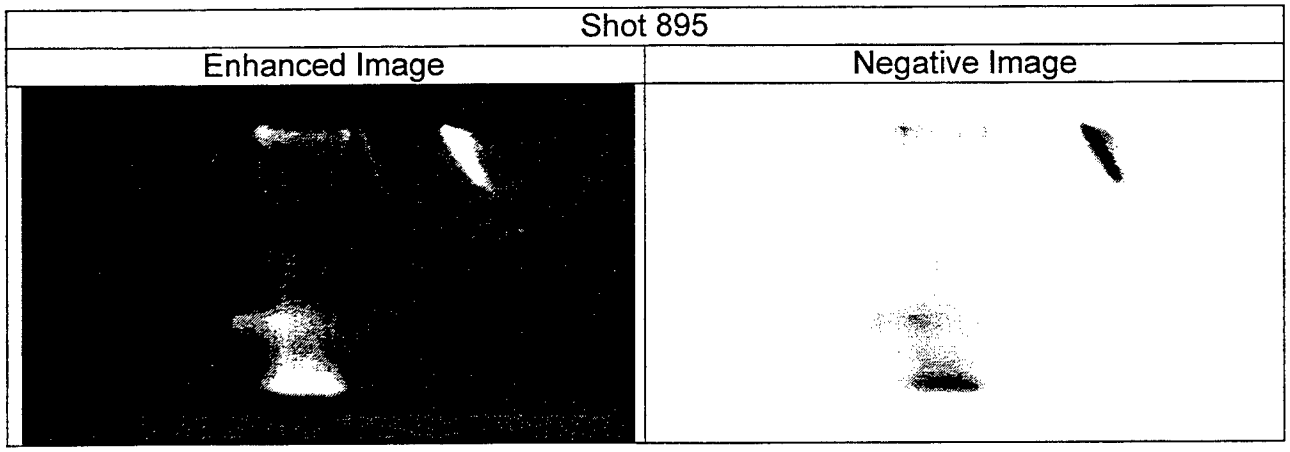

Figure 3-50. Image of the plasma column at the start of the opening event.

of the Magnetic Reynolds number using this conductivity suggest weak field line tying to the plasma. All in all, the data is consistent with mostly current diffusion, a small amount of beam pinching and enhanced ionization of outer channel regions as the current rises.

At low average electron current density (~80 A/cm^2) and ion current density of ~8 A/cm^2, a two-dimensional simulation run by T. Hughes showed a sheathed radial current density profile - the cathode emits all across its surface, but the plasma channel has a non-uniform current density profile at early times, (4.5 nsec in the simulation example with lower conductivity than likely in the experiment).

The other noteworthy feature of the gated images of shots 890 and 895 is a disk-like luminous region ~2.6 cm into the gap from the anode side. This feature appears in many of the gated images in the series and was always at the same location. It is likely that this region is a reflection from some component of the apparatus, but such a component has not been identified.

In summary, the gated camera images for both τ_{AK} = 3.0 and 6.0 μsec, pertaining to a high impedance and self-opening mode respectively, show no evidence of high density electrode plasmas playing a role in the discharge behavior over the time scales of the images.

3.3.7 Effects of a Mesh Across the Anode Aperture.

The mesh across the anode aperture made significant changes in the behavior of the switch. In general, the mesh provides an electrical termination for the current flow in the switch gap over the current channel cross-section and can electrically isolate the current flow in the gap from that in the anode-to-ion source region. Accelerated or current carrying electrons in the gap are collected by the mesh, depending on the effective transparency of the mesh, as are return current electrons in the anode-source region which are driven by the inductive fields of the changing transmitted current. Additionally, the mesh is a source of plasma across the channel cross-section for space charge accelerated electrons or ions depending on the shape of the potential near the anode. A potential hump, e.g., can be largely shorted out by space charge emitted electrons from the mesh or source plasma, thereby preventing total current shut-off during an opening. On the other hand, a potential drop on the gap side of the mesh can accelerate ions into the gap. The current flow and electrostatic potential distributions in the anode-to-source region and the role of the mesh are complicated physics problems and ultimately need to be included in simulations to obtain a complete picture of switch operation. Experimentally, the presence of a mesh across the anode aperture had the following effects on switch operation:

i. The on-axis ion current density was reduced, typically by more than the geometrical attenuation, and the ion current density time profile changed, particularly at late times.

ii. A low impedance mode showing little current bite in the metallic coaxial hardware changed to one with a current bite and an increased open time with the mesh present.

iii. The rate of radial growth of the current channel was reduced with the mesh, accounting for the observation of (ii) above.

iv. The net current in the anode-source region was reduced to negligible levels with the mesh, implying an effective electrical termination of the switch current by the mesh. (See Section 3.3.10)

The following three figures illustrate some of these effects.

Figure 3-51 compares the measured ion current density on-axis in the coaxial system of Figure 3-6, both with and without a 14x14 line-per-cm tungsten mesh across the 2.54 cm diameter anode aperture. Shown in Figure 3-52 is a high impedance shot with the glass cross hardware without a mesh across the anode aperture, but with all other conditions held the same as in Figure 3-37(a). The lower ion current with the mesh led to the initial current being slightly lower. The current stayed at the lower level for nearly a microsecond longer with the mesh than in Figure 3-52.

The mesh across the aperture also had an effect on the self-opening mode. In the glass cross, discharges with a mesh had a current bite of longer duration than those without a mesh, but there were little other apparent changes. The presence of the mesh across the anode aperture made a more striking change in the discharge characteristics in the coaxial system. Shown in Figures 3-53 (a) and (b) are discharges in the coaxial configuration shown in Figure 3-6, under identical conditions except with and without a ~14x14 line-per-cm tungsten mesh across the 2.54 cm diameter anode aperture. The magnetic field was 2.5 kG in the 16 cm AK gap, and the small flashboard was 38 cm from the cathode. The small driver bank of C = 1.4 μF, L = 480 nH was used. Without the mesh, the self-opening event was not apparent on the total current, although a small current bite similar to an opening event occurred on the current to the anode aperture holder which was instrumented with a Rogowski coil at a radius of 5.4 cm. In the glass cross hardware, where commutation of current to larger diameters was limited by the insulating nature of the glass chamber, the effect of the mesh was not quite as dramatic.

There was a small difference between the anode current and total current with the mesh and the anode Rogowski was noisy during the opening in this particular shot. After the current bite, the anode and total currents again tracked for ~0.5 μsec. Without the mesh, the two currents diverged after ~300 nsec and the current outside the anode Rogowski increased to >12 kA. Both curves show late time "current loops" between the anode Rogowski and the total current monitor; the reverse current occurs nearly a microsecond later with the mesh. Further data and discussion on expansion of the current channel is given in the next section.

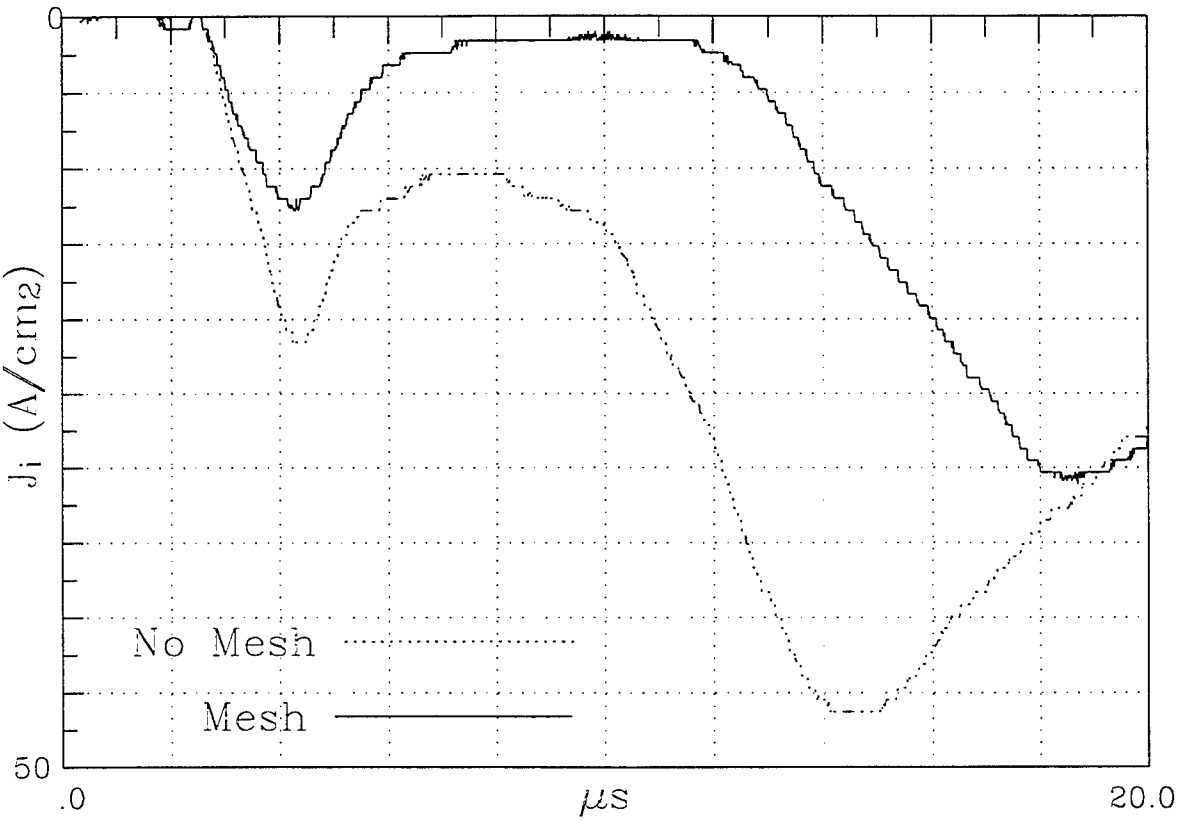

Figure 3-51. Measured ion current density on-axis behind the cathode with and without a mesh on the anode aperture.

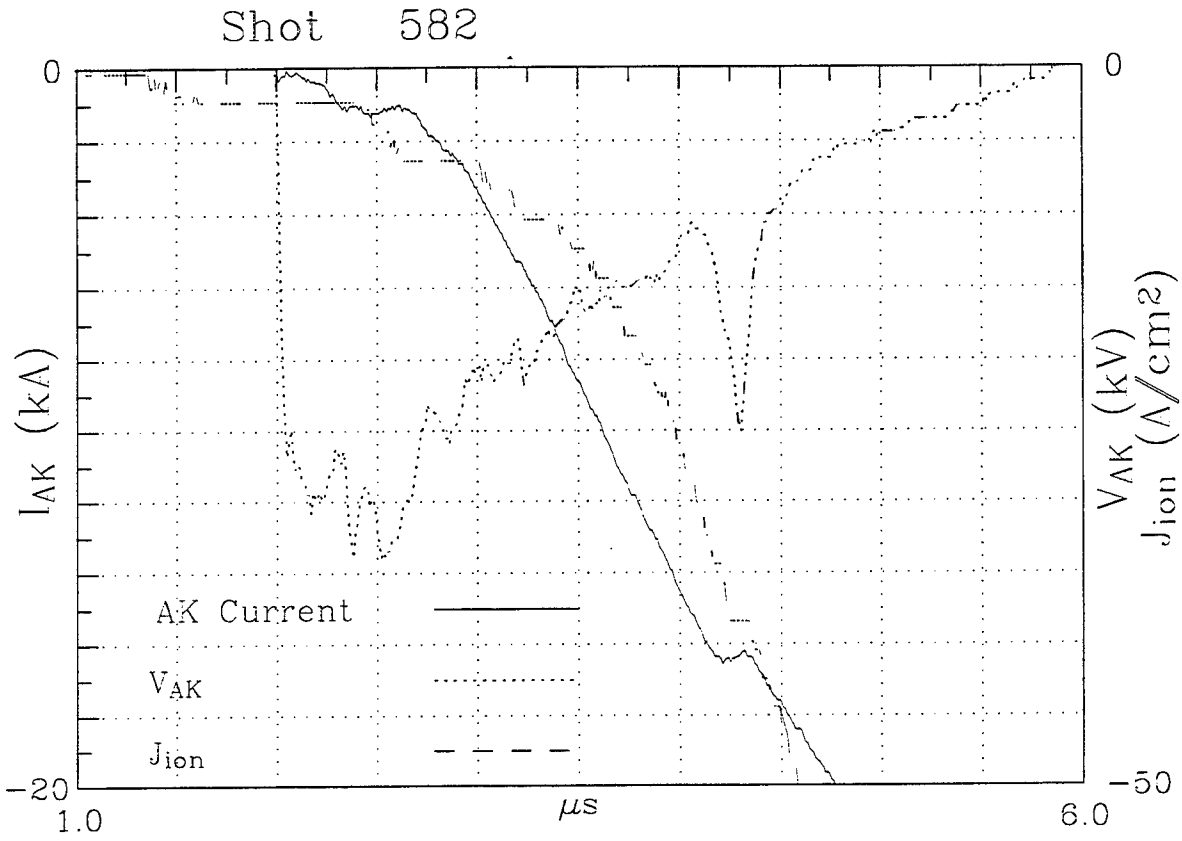

Figure 3-52. Discharge with a -30 kV charge voltage and no mesh on the anode. Ion current measured on a shot without voltage.

(a) Discharge with a mesh across the anode aperture.

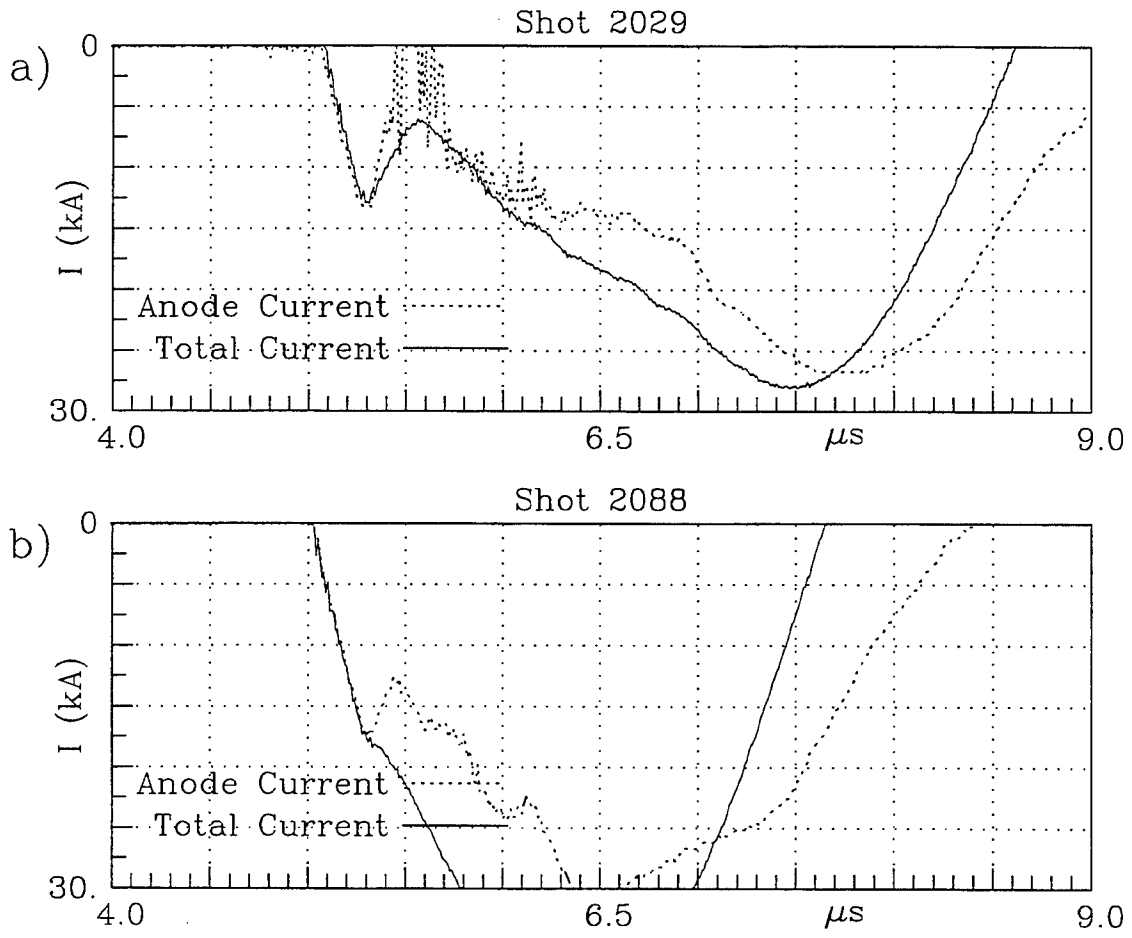

(b) Discharge with no mesh across the anode aperture.

Figure 3-53. Discharges in the coaxial configuration shown in Figure 3-6.

3.3.8 Current Paths in the Coaxial Hardware.

Determination of the time dependence of the current flow as a function of radius and gap position was a major technical objective of the program and is central to understanding the switch operation, particularly with regard to the nature of the impedance drop observed in all modes at some point in the current profile. A substantial effort was devoted to the task, starting with the gated images of cathode plasma formation given in Section 3.3.6 where the first evidence was obtained of a radially increasing current channel correlating with the start of the impedance drop. Experiments were performed with and without anode meshes, with small and large aperture ion sources, and with high impedance and self-opening modes. Additionally, beam centroid motion was inferred from B-dot probes to determine the role, if any, of growth of MHD kink instabilities in the switch opening. The results of the experiments confirm the early evidence in the glass cross hardware of radial current channel expansion and suggest that the impedance drop is largely due to current flowing outside the original channel at relatively low current densities ($\leq$ few 10s A/cm^2) over large areas. Indeed, the current near the axis remains relatively clamped in larger aperture experiments as the impedance continues to drop.

The nature of the evolution of expanded current channels is not clear. It is clear that an ion background must exist throughout the gap at the annulus of current flow, except for sheaths, in order to have electron current densities $\geq$ 10 A/cm^2; a vacuum gap would have much lower current densities. Also, a simple expansion of an ion current channel without additional sources would not increase the total current. A two-dimensional simulation of a gap with an initial injected ion channel of fixed radius, but with electron/ion space charge limited emission allowed at the electrodes outside the channel, gives a clue to a possible mechanism. A low density injected plasma with a radius of 1.25 cm and space charge emission at the electrodes allowed up to a radius of 2 cm showed a 40% increase in current over the case with no emission allowed outside the injected channel radius. The simulation had a 6 cm gap and showed radial ion transport across the 2 kG longitudinal field with effective radial velocities up to an equivalent of a few keV energy and an electron current density outside the injected channel radius of ~7 A/cm^2. The ions were accelerated outward radially by a potential hump. In other words, the potential hump acts like an ion "pump" accelerating ions from the channel out radially, and the hump fields and applied field accelerate the ion longitudinally allowing the ions to fill the annulus and electron current to flow. This pumping action tends to reduce the amplitude of the hump which in turn allows additional injected ions to enter the gap from the source. In the simulation the 6 cm gap opened after ~100 nsec, whereas experimentally the conduction times were significantly longer, as previously mentioned.

The rate of channel expansion is influenced or controlled by the magnetic field, the presence of a mesh, and probably by the radius of an injected ion channel with fixed charge/length (the ion kinetic energy gained from the accelerating radial electric field near the edge of a uniform charge density channel varies as Δ/a, where Δ is a small displacement from the channel radius and a is the channel radius).

In the coaxial hardware with the small field coils, the current diagnostics used were a total current Rogowski, a Rogowski around the anode aperture holder, a radially adjustable B-dot probe ~3 cm from the cathode, and arrays of B-dot probes along the ID of the current return which surrounds the anode aperture holder. The radially adjustable B-dot probe was shielded from the plasma by an alumina insulating sleeve. Only a relatively small number of shots were possible in this location because of insulator survival problems. Each of the arrays of B-dots consisted of four coils at radii of 9.8 cm, located top, bottom, left and right of the plasma column. There were arrays at three axial distances from the cathode. The configuration of the 16 cm AK gap is shown in Figure 3-6. Shown in Figure 3-54 are three discharges at τ_{AK} = 3.0 μsec without a mesh on the 2.54 cm diameter anode aperture. A different current monitor was fielded in each discharge. The driver bank for these shots had C = 1.4 μF and L = 910 nH, and the guiding magnetic field was ~2.5 kG. The flashboard was 38 cm from the cathode. Evidence of expansion of the current channel appeared almost immediately after conduction started, when the radially movable B-dot probe at 3.0 cm radius located 3 cm from the cathode began to show a divergence from the total current. The B-dot probe when at 4.2 cm showed a similar divergence later in time, after 1-1.5 μsec of conduction. The divergence is interpreted as a portion of the total current flowing at larger diameters than the probe radius, but it could be due in part to motion of the plasma column relative to the B-dot probe. The fact that the time at which the divergence occurred changed with the probe radius, is evidence in support of the interpretation that the divergence was caused by expansion of the current channel. Up to and through the times that the B-dot probes showed all of the current within 4.2 cm, nearly all of the current attached to the aperture holder. After ~1.5 μsec there was current flow at larger diameter than the ~5.4 cm radius anode Rogowski. All of the these data together imply that there was an expansion of the current channel at both the cathode and the anode. The very early evidence of expansion on the B-dot probe at r = 3.0 cm implies that the expansion likely occurred first at the cathode.

Discharges at τ_{AK} = 3.0 μsec in the same configuration as above, except with driver bank inductance lowered to 480 nH are shown in Figure 3-55 (a) and (b). Arrays of B-dot coils at a radius of 9.8 cm located 7 cm and 17.2 cm from the cathode were fielded. The B-dot probes showed that most of the discrepancy between the anode Rogowski and the total current was due to current attaching at or near the back plate, and it was only near the peak in current that there was any appreciable current flow across the 6 cm gap. The current across the 6 cm gap was always less than 10% of the total current.

All of these data show that there was some radial expansion of the current channel, and hence plasma present in the gap at larger radii than initially injected, although the gated camera images imply that the density of that plasma was low.

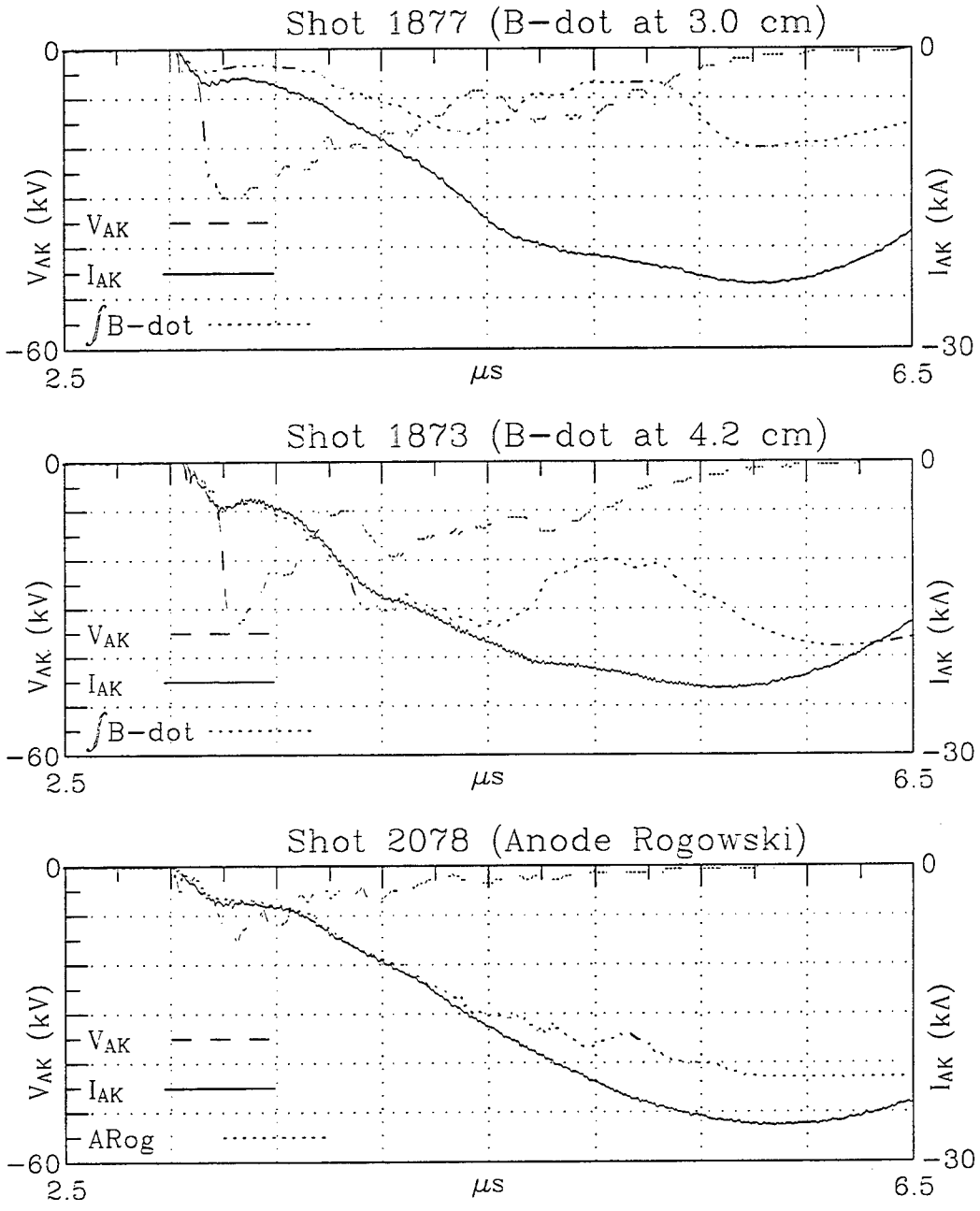

Figure 3-54. Current measurements with a B-dot probe at two different radii, and a Rogowski coil around the anode aperture holder for high impedance conduction.

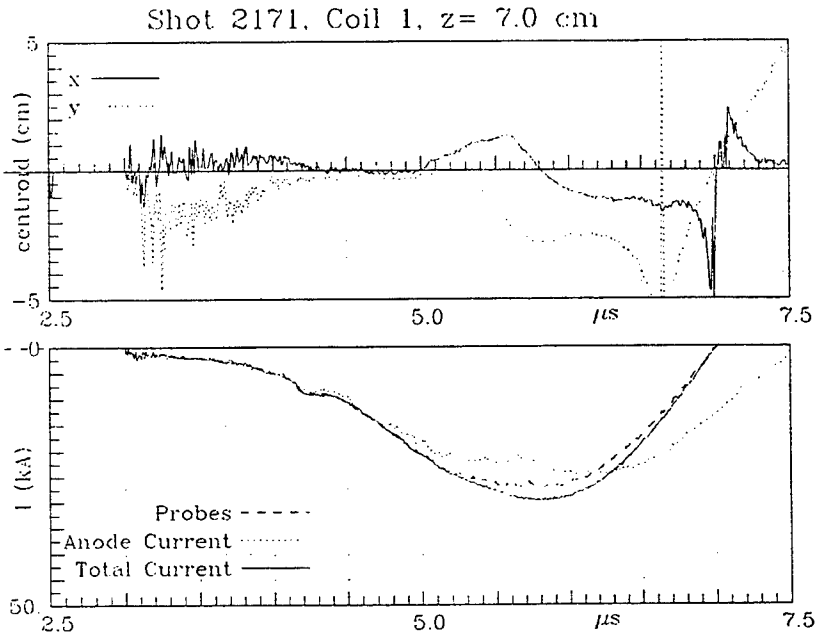

(a) Measured currents with B-dot probes 7 cm from the cathode.

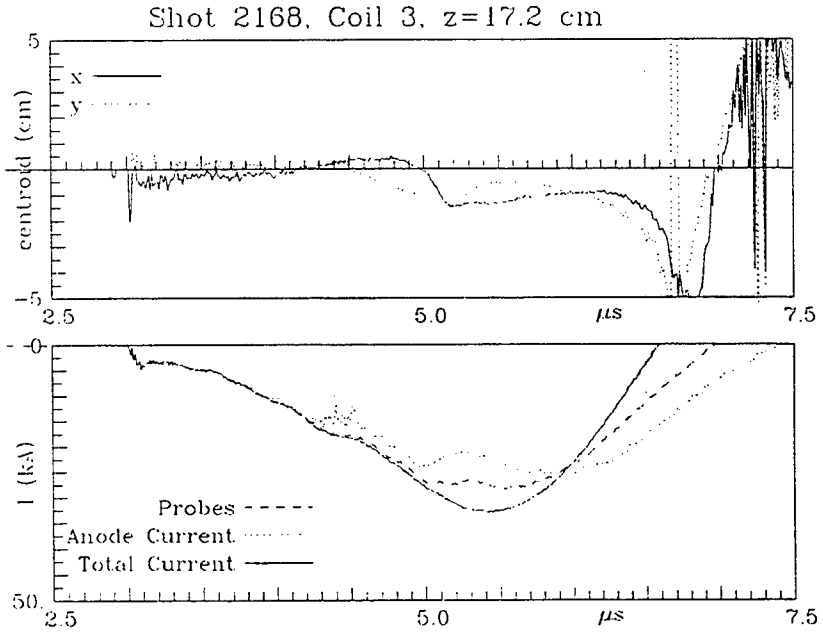

(b) Measured currents with B-dot probes 17.2 cm from the cathode.

Figure 3-55. Current measurements with B-dot probes.

The calculated x and y displacements of the current centroid for these data were always less than the radius of the anode aperture holder (5 cm) during the times of interest, supporting the conclusion that m=1 kinks were not the primary cause of the differences in the measured currents at the different locations. Shots at higher applied fields showed smaller x and y centroid motion, but at all fields from ~0.8 kG to ~4 kG, the current channel expansion was present. The high frequency oscillations during the first μsec or so shown in the centroid plot for probes at 7.0 cm are probably not reflective of actual centroid motion but rather are likely due to electrostatic pickup.

In Figure 3-56 three discharges at τ_{AK} = 5.0 μsec without a mesh on the anode are shown. The discharges used the same configuration as was used for Figure 3-55. Clearly the current at the cathode was initially inside r = 4.2 cm, but near the time of the current interruption to the anode, the current started to flow at larger radii. The discrepancy between the current inferred from the B-dot probe at r = 3 cm and the total current started very early on, implying that the current expanded radially outwards at the cathode at the start of conduction. The data from the r = 4.2 cm B-dot and the anode Rogowski show that the current expansion occurred across the entire gap and was not limited to one side.

With the small B-field coils in the coaxial hardware, (Figure 3-6), arrays of B-dot probes along the ID of the current return which surrounded the anode aperture holder were used to map the current attachment to the anode as well as calculate the displacement of the mean current channel in both the x and y directions. The probes were located very close to the conducting boundary of the anode hardware, so it was assumed that there would be non-symmetric image currents in the hardware when the mean current channel moves off axis. This assumption is only correct if the penetration time of the hardware is long compared to the time scale of the motions in the current channel. The estimated penetration time was ~15 μsec, which is much longer than the time scale of any expected current channel motions. If the data were to be analyzed ignoring the effects of non-symmetric image currents in the wall, the calculated displacements would be approximately twice the displacements calculated with the image currents taken into account.

Shown in Figures 3-57 (a) and (b) are the measured total currents, currents which attach to the anode aperture holder, and the currents measured by sets of B-dot coils at two axial locations for typical discharges at τ_{AK} = 5.0 μsec. The same configuration as was used for Figure 3-55 was used, with no mesh across the 2.54 cm diameter anode aperture and with a B-dot probe radius of 9.8 cm. Also shown are the calculated x and y displacements of the current channel centroids. The differences between the measured currents from the different locations show that there was current attachment between the diagnostics. The Rogowski on the anode aperture holder showed an identical signal to the total current for ~250 nsec, at which time the anode Rogowski showed a signal characteristic of an opening event, while the total current had only a small inflection. Current which was attached to the anode aperture holder was commutated to other sections of the anode hardware. The data from the B-dot probes at 7 cm shows similar agreement with the total current until the current was commutated

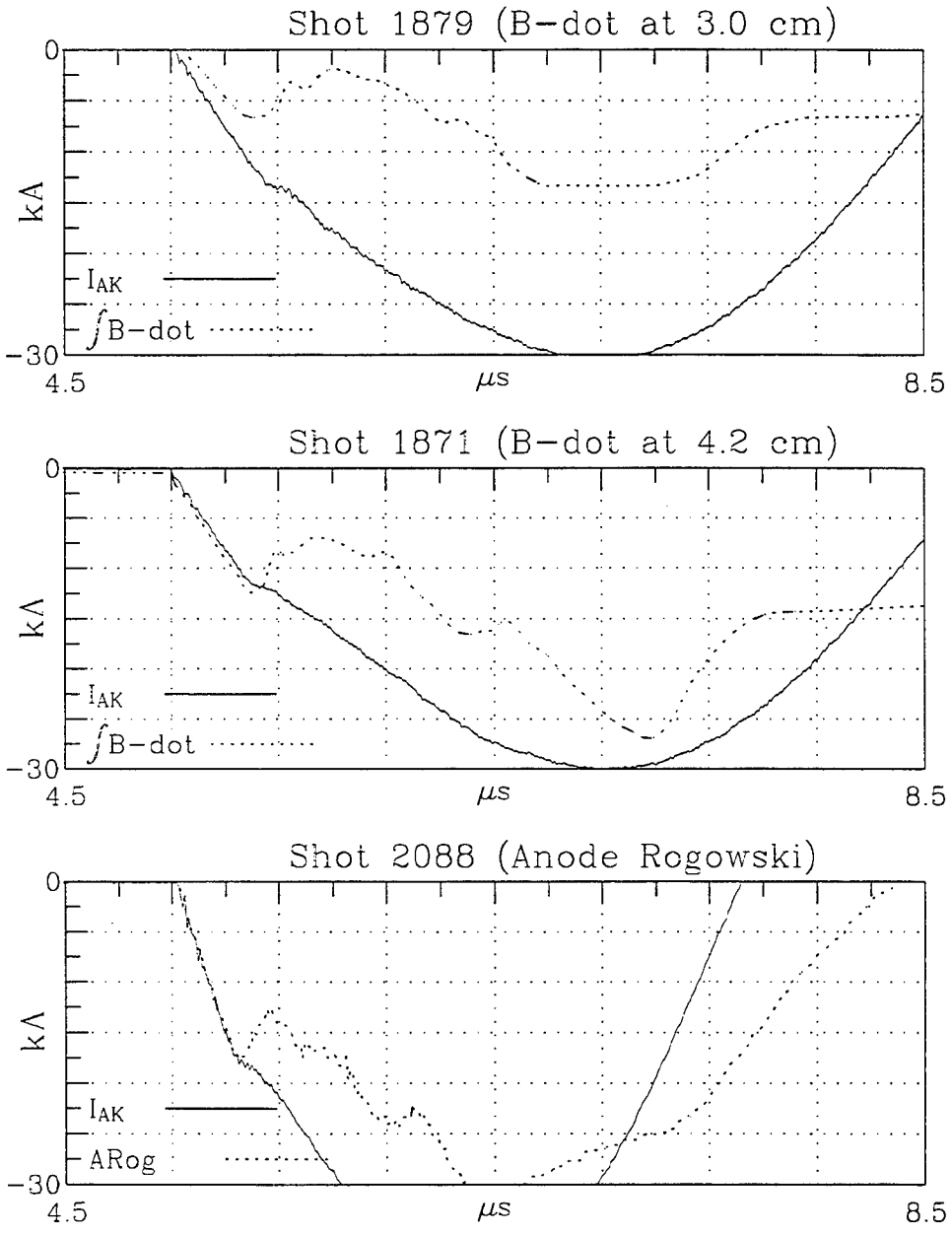

Figure 3-56. Current measurements with a B-dot probe at two different radii, and a Rogowski coil around the anode aperture holder.

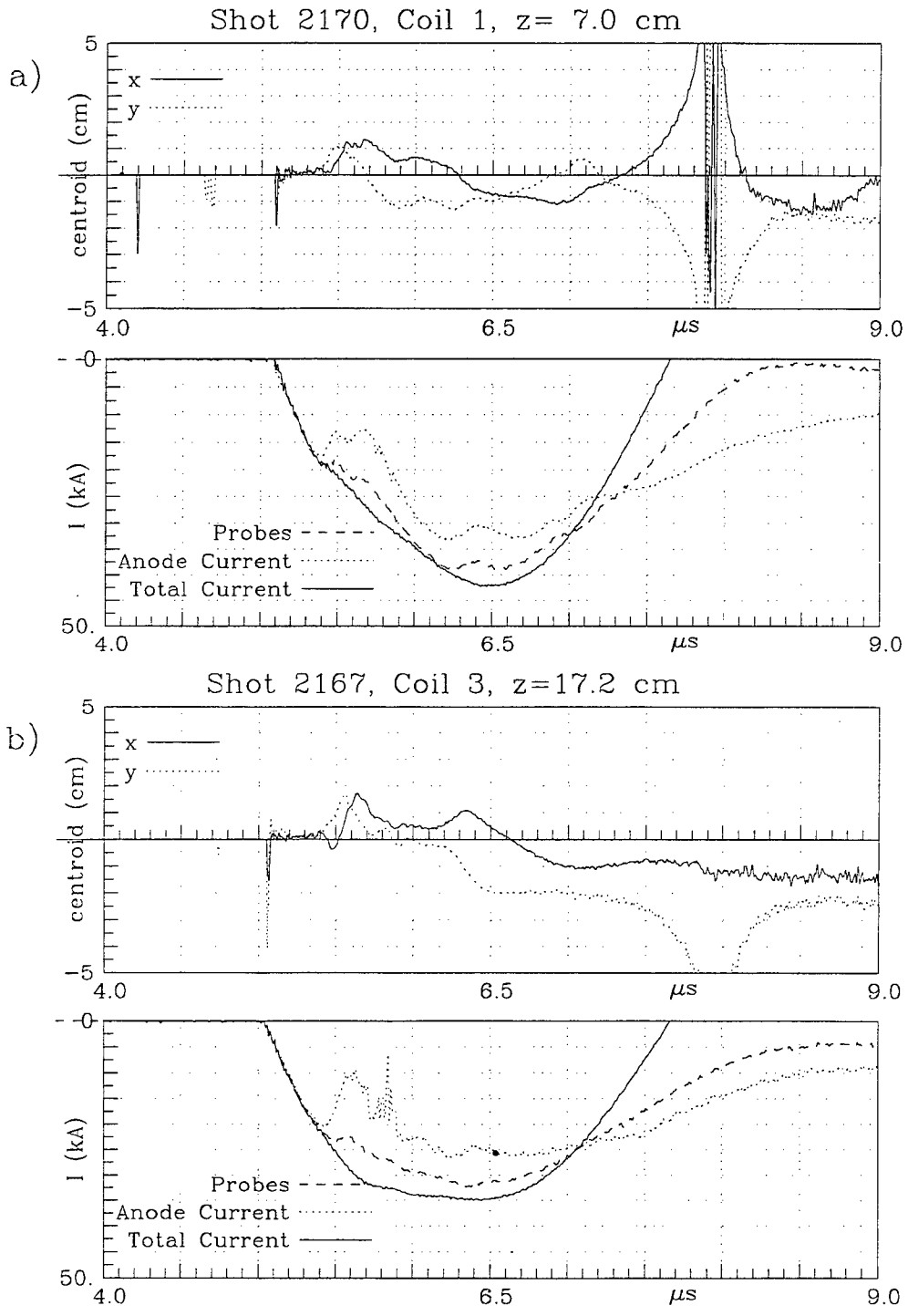

Figure 3-57. Current measurements with B-dot probes 7 cm and 17.2 cm from cathode.

away from the anode aperture holder. The current inferred from the B-dot probes showed closer agreement to the total current than the anode Rogowski, and it diverged from the total current 50 to 100 nsec later than the anode current signal did. The discrepancy between the B-dot signals and the total current was current attaching somewhere across the short gap which was present at large diameter in this configuration. Clearly this difference only accounted for a small portion of the current which was commutated. In addition, the timing of when the signals diverged from the total current implies that the current channel was expanding radially outward, with the first difference appearing on the anode Rogowski and later appearing on the B-dot probes. The probes 17.2 cm from the cathode were located just beyond the location of the anode aperture, and any difference between them and the anode Rogowski must have been due to current flowing along side the anode aperture holder and attaching to the back plate. The difference between the B-dot probe signals and the total current was slightly greater at this location than at the B-dot coils 7 cm from the cathode, implying that there was some current attaching along the walls between the two sets of probes, although most of the current was commutated to the back plate. The current flowing across the short 6 cm gap was typically less than 10% of the total current, and didn't flow in that location until after current began to flow to the back plate. The currents measured by the two sets of B-dot probes diverged from the total current at nearly the same time. If the plasma column was expanding radially, it would be expected that these signals would diverge near the same time, as they were at the same radius.

The centroid motion in both positions of the B-dot arrays was very small until current bites appeared on the anode Rogowski monitor. The current channel should have been stable to MHD kink motion at the times of the current bites if the channel radius was >2 cm according to the Kruskal-Schafranov (K-S) criterion. Since the total current diverged from the anode monitor at the time of the bites, the channel radius was ~5 cm, although the current density within the channel was not necessarily uniform as assumed in K-S calculations. The anode Rogowski current bites in these figures are largely consistent with a ~5 cm channel radius moving transversely with amplitudes of ~1 cm in the x and y directions, as indicated by the centroid plots.

Data from discharges with a ~14x14 line-per-cm tungsten mesh across the anode aperture, but otherwise identical conditions to the discharges in Figures 3-57 are given in Figure 3-58. The B-dot coils 7 cm from the cathode showed that there was basically no current flowing across the 6 cm gap up to and slightly past the first 1/4 period of the bank current, so all of the difference between the anode Rogowski and the total current was due to current flowing to the back plate. The B-dots 17.2 cm from the cathode showed similar traces. It is clear from the B-dot probes that nearly all of the difference between the anode Rogowski and the total current was due to current flowing to the back plate, and that less than 10% of the difference was flowing to the side walls. Almost no current was flowing in the 6 cm gap, even after 4 μsec and the full peak in the current.

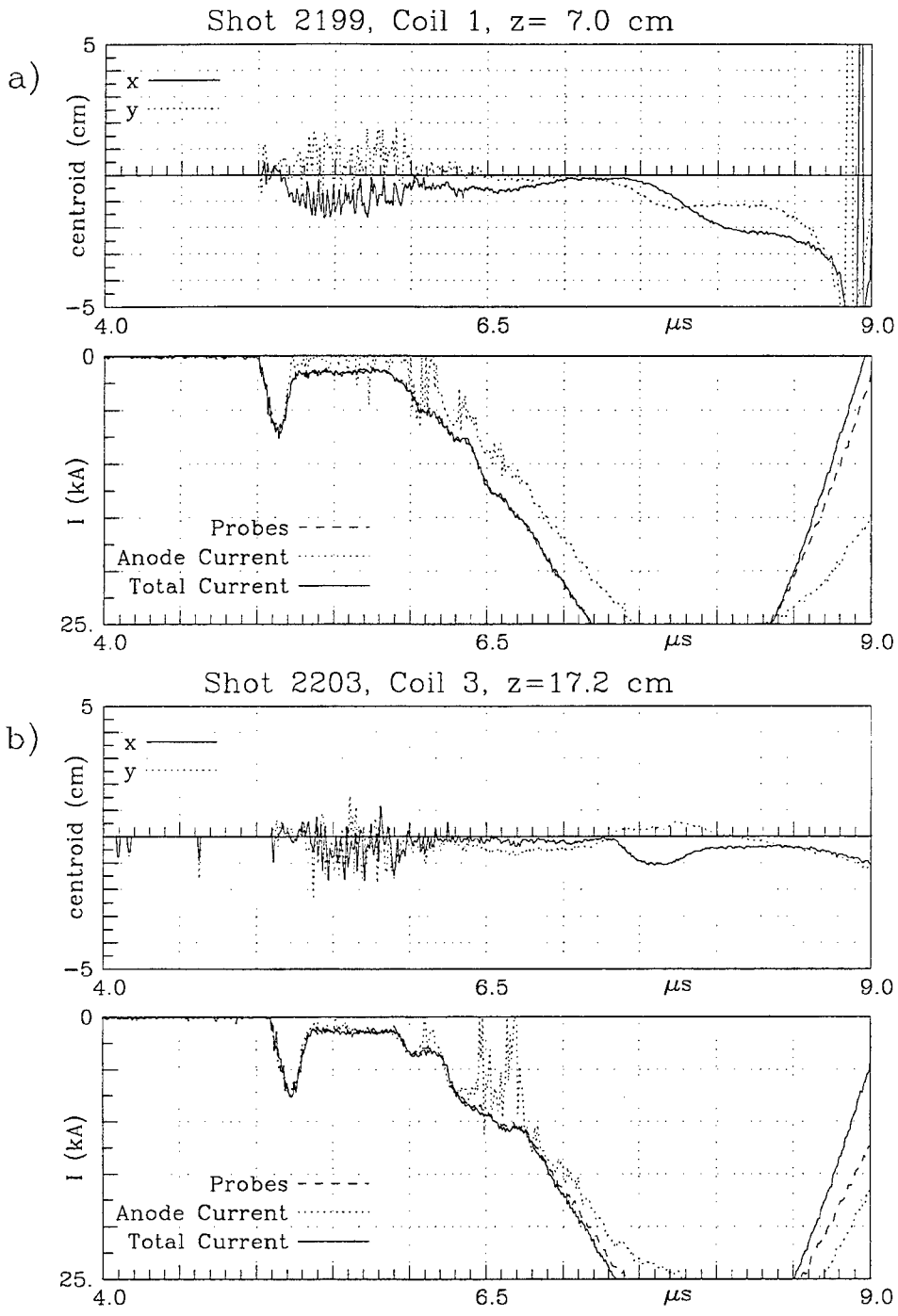

Figure 3-58. Current measurements with B-dot probes 7 cm and 17.2 cm from cathode (with mesh).

The discharges were stable to kink growth during the current rise and opening according to the K-S criterion. During the opened times of nearly 1.0 μsec the centroid motion plots were noisy and unreliable probably due to fluctuating electrostatic field/charge pickup. During the conduction and actual opening with the anode mesh present the current bite appears as a drop in current at the radius of the anode Rogowski without appreciable centroid motion, whereas without the mesh, transverse oscillation cannot be ruled out as the source of the anode current bite.

A more detailed diagnosis of the current distribution was made in the coaxial system with the large bank and flashboard and a 20.5 cm AK gap. The large flashboard was 40 cm from the anode mesh and the applied field was 2.5 kG. Of particular interest in this configuration were the B-dot probe arrays 19.5 cm from the cathode at radii of 6.35 cm, 11.43 cm and 16.51 cm. With the large 7.62 cm radius aperture, the inner-most set of B-dot probes was 1.27 cm inside the edge of the plasma column. With these sets of B-dot arrays, the radial distribution of the current to the anode was mapped throughout the discharge. Shown in Figure 3-59 are B-dot probe data from three shots, each shot using a B-dot array at a different radius. For the data presented in Figure 3-59 there was little shot-to-shot variation in the total current. The total current shown is the measured total current from the shot with the B-dot probe array at r = 16.5 cm. The calculated average current densities in the annular areas between the B-dot probes are shown, and compared with the calculated average current density assuming the total current was confined to the original aperture area. The probes at r = 6.4 cm showed that most of the current started inside that radius, with a very small amount outside for ~400 nsec, indicating that the ion source current did not fill the anode aperture initially. The probe data at the several radii clearly showed expansion of the current channel before the opening event was apparent on the total current. The expansion was rapid, but the average current density of the expanded portion of the current channel was not large, ≤ 50 A/cm^2 as compared to a peak of ~350 A/cm^2 calculated for the on-axis current density before the impedance drop.

The current in the annulus with inner radius of 6.4 cm and outer radius 16.5 cm continued to grow over ~300 nsec from the start of the current bite observed at a radius of 6.3 cm. At the peak of the total current 10-15 kA was flowing in both the $6.4 < r < 11.4$ cm and $11.4 < r < 16.5$ cm annuli, and the total current bite started with nearly all the current drop occurring within the 6.4 cm radius. Near the current minimum however, the current flow in the $6.4 < r < 11.4$ cm annulus dropped to nearly zero as did the current flow in the $11.4<r<16.5$ cm annulus, although at a slightly earlier time. After the current minimum the bulk of the current increase as the impedance decreased was due to current flowing in the $6.4 < r < 11.4$ cm annulus; the $r<6.4$ cm current stayed roughly flat at about the value (40 kA) at the time of the start of the current bite.

The current bite of the shots of Figure 3-59 was too slow for a good opening, and the current density profiles show that the time delays in shutting off current in the outer current channel annuli was the cause of the relatively slow opening. Comparing this data with the opening of Figure 3-34, which had a fast opening, shows the likely effect of the higher B_Z field (6.4 kG vs. 2.5 kG) in retarding current channel expansion. It is

also noteworthy that the bulk of the increase in current in Figure 3-59 during the impedance drop occurred in the annulus 6.4 < r < 11.4 cm which included a 1.27 cm wide annulus within the anode aperture.

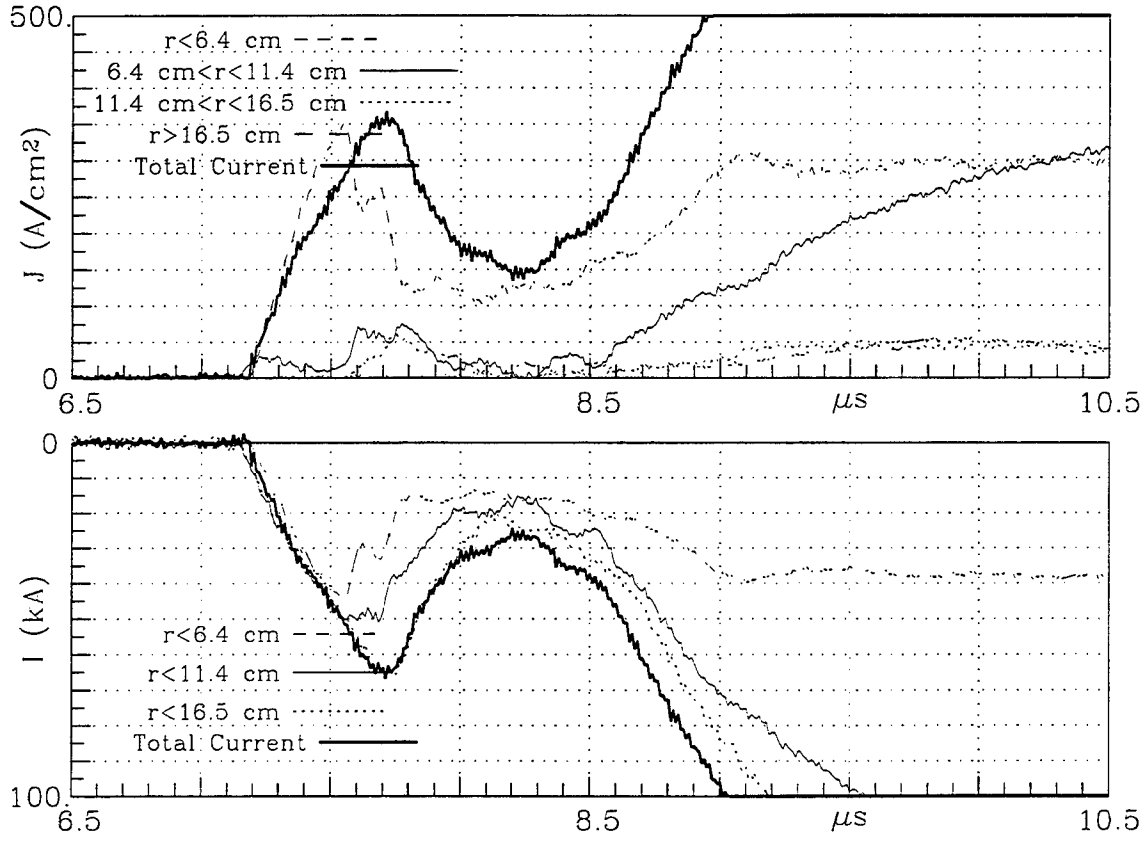

Figure 3-59. Measured currents and inferred average current densities from three shots with the 15.24 cm diameter anode aperture and the large area flashboard.

3.3.9 Scaling with the Applied Magnetic Field.

The magnetic field amplitude for a given spatial profile affected the on-axis ion source time profiles and the expansion of the current channel. The latter effect in turn influenced the opening time and rate of current decrease in an opening current bite. In this section some data are given showing the effect of magnetic field level on the ion source time profiles for both the small flashboard and cable gun in the coaxial system. Data with the small flashboard and small anode aperture is also included illustrating the differences in enclosed currents at the anode Rogowski monitor and B-dot probes at radius of 9.8 cm as the magnetic field increased from 1 to 6 kG.

The ion source data was taken in the configuration shown in Figure 3-6, with a 16 cm AK gap. The flashboard was 38 cm from the cathode, and there was a 14x14 line-per-cm mesh across the 2.54 cm diameter anode aperture. Figure 3-60 shows the measured ion current behind the cathode mesh at 1, 2, 4 and 6 kG applied fields. The ion current for the 6 kG data was reduced because of damage to the flashboard insulator.

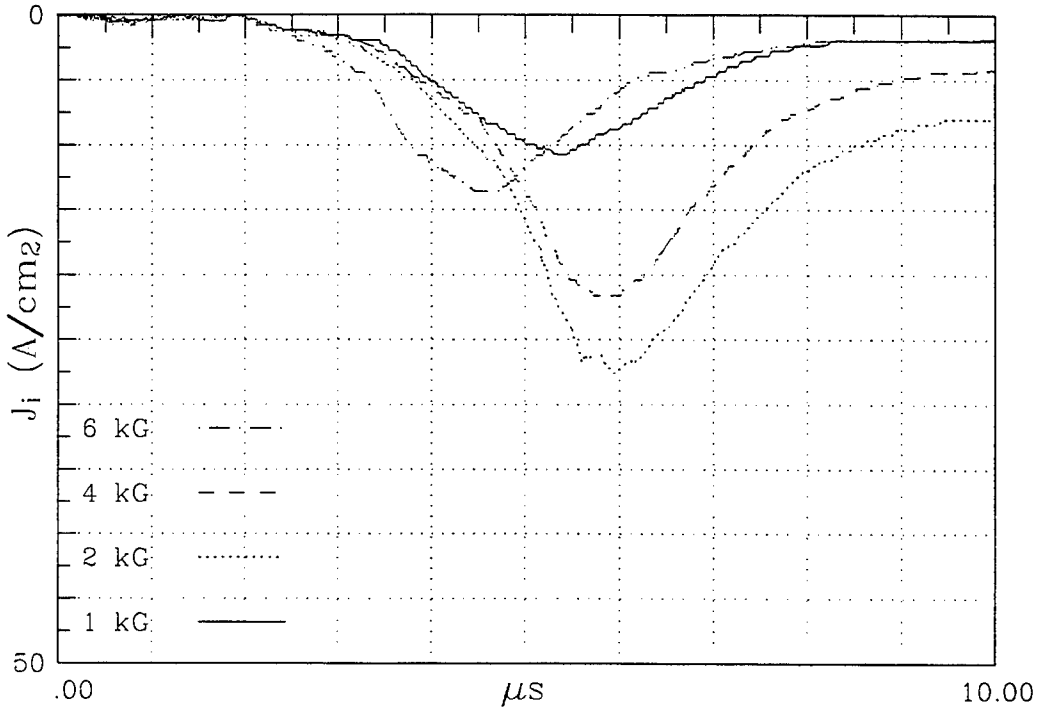

Figure 3-60. Measured ion current behind the cathode mesh at four applied fields.

With the cable gun source there were also changes in the ion current as the applied magnetic field was increased. Shown in Figure 3-61 is the measured on-axis ion current density with the cable gun 15 cm from the anode mesh, a gun charge voltage of 17.5 kV, and applied magnetic fields of 6.4 kG, 2.6 kG, and 1.3 kG. The electrode configuration is shown in Figure 3-12. Increasing the field both increased the peak ion current density on-axis and changed the waveform so that there was proportionately more plasma later in time.

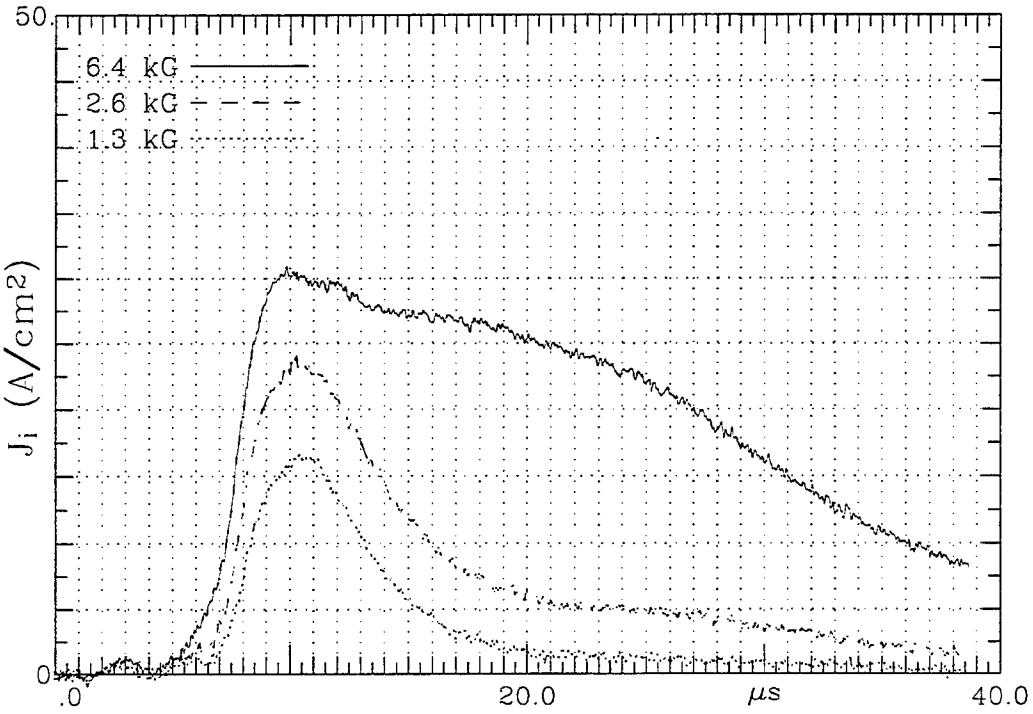

Figure 3-61. Measured ion current from the cable guns at three guiding magnetic field strengths.

In Figures 3-62 (a) through (d) are shown discharges with the mesh on the anode at applied fields of 1, 2, 4, and 6 kG respectively with τ_{AK} = 5.0 μsec. The driver bank inductance was 480 nH, the capacitance was 1.4 μF, and the other parameters were as for Figure 3-60. The time until the opening increased from ~100 to ~200 nsec with field increasing from 1 to 4 kG. The reduced ion current due to the damaged insulator was likely the reason the time to opening did not continue to increase at 6 kG. The increase in the time to the opening from 1 to 4 kG correlate with the higher opening current at 4 kG due to the higher ion current density. Increasing the field improved agreement between the diagnostics, particularly near the time of current decrease. In the 2 kG case the total current after peak current decreased before the current measured by the anode Rogowski or the B-dot probes. This data implies that there was a region with trapped B_θ flux which decayed over time. For B_θ flux to be trapped between the anode Rogowski and the total current Rogowski, there must have been plasmas at large radii connecting the different sections of the anode hardware. At 6 kG this trapped flux was practically absent, implying that the increased field hindered the plasmas from forming at or expanding to larger radii.

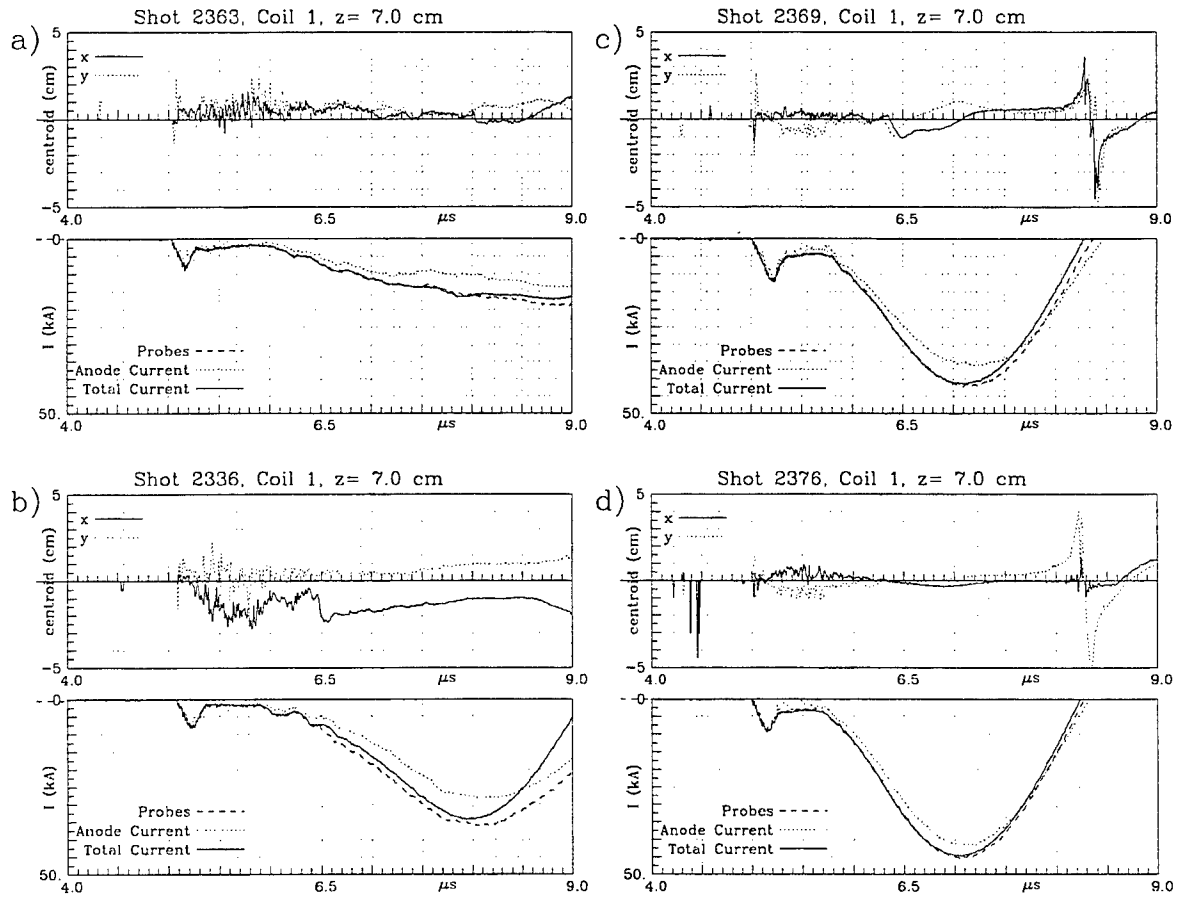

Figure 3-62. Shots with a mesh on the anode and an applied field of (a) 1 kG, (b) 2 kG, (c) 4 kG, and (d) 6 kG.

The probe data at 2 kG evidenced anomalous centroid motion. The centroid plots are initially noisy and after the opening the current inferred from the probe signals showed a sudden "jump" corresponding with a change in the x centroid of the current channel. The degree of the "jump" varied on a shot-to-shot basis. The current channels of these shots were unstable to kink motion at the peak current before opening for field levels below 3 kG, assuming the channel radius of the anode aperture.

3.3.10 Current Flow Through the Anode Aperture.

The experiments discussed so far showed measurements of the current inside the AK gap. The erosion of the flashboard and other evidence implied that appreciable currents were flowing through the anode aperture into the anode to source region. To measure that current, a Rogowski was placed inside the anode aperture holder. The surface of the Rogowski was protected from the plasma by an insulating ring. The ring also limited the possible current paths for return currents. Measurements were taken

with anode apertures of 2.54 cm and 5.08 cm in diameter, and both with and without a ~14x14 line-per-cm tungsten mesh across the aperture. The inner diameter of the annular insulator used to shield the Rogowski was the same as the diameter of the aperture used.

Without a mesh, electron current from the AK gap can flow through the aperture without making direct electrical contact except at the edge of the aperture, and the measured current can be reduced by a coexisting return current. This return current can be provided by electrons from the background plasma in the anode to source region driven by the inductive field of the rising current from the AK gap if the aperture effectively shields the plasma from the applied electric field of the AK gap. With the anode mesh present, the plasma return currents can flow inside the current channel downstream of the aperture and terminate at ground on the mesh. Without a mesh, the plasma return currents can flow to ground outside the channel in the larger diameter plasma from the flashboard, and any plasma electron return current within the channel proper must either diffuse radially outward to ground in the AK gap region or flow back into the gap along field lines until reflected by the external electric field. These "injected" plasma electrons can delay the formation of a potential hump or reduce its amplitude and may be related to the observation that the aperture without a mesh typically conducted ~30% longer than with a mesh before opening.

Shown in Figures 3-63 (a) and (b) are high impedance shots at τ_{AK} = 3.0 μsec with a 5 cm diameter aperture without and with a mesh. The large driver bank with C = 10.5 μF, and L = 300 nH was used. The plasma source used was the small flashboard, 38 cm from the cathode. The ~2.5 kG guiding field across the 15 cm AK gap was provided by the large field coils. The experimental configuration is shown in Figure 3-8. The radius of the B-dot array was 11.4 cm. Without the mesh the measured current inside the anode was ≤50% of the anode aperture current for the first several hundred nsec and less thereafter. Occlusion of A-K current at larger diameters than the anode aperture may have contributed to a reduction in the percentage of the total current measured inside the anode as the total current rose.

The addition of the mesh clearly reduced the measured current inside the anode to negligible levels over the first 0.5 μsec and the reduction was particularly noticeable during times of increasing total current. The mesh acted to collect a greater portion of the current during the rise than was collected without the mesh, and it also supplied a path to ground for any induced return current in the plasma on the flashboard side of the aperture.

In Figures 3-64 (a) and (b) are shown shots at τ_{AK} = 5.0 μsec with 2.54 cm and 5.08 cm diameter apertures with a mesh. The other conditions are the same as in Figure 3-63. The diagnostics shown are the total current, the current which attaches to the aperture holder, the current inside a B-dot probe array at a radius of 11.4 cm, and the measured current inside the anode aperture holder. Again the mesh essentially resulted in nearly complete current neutralization throughout the discharge, indicating that the mesh was a good electrical termination for the current flow in the AK gap.

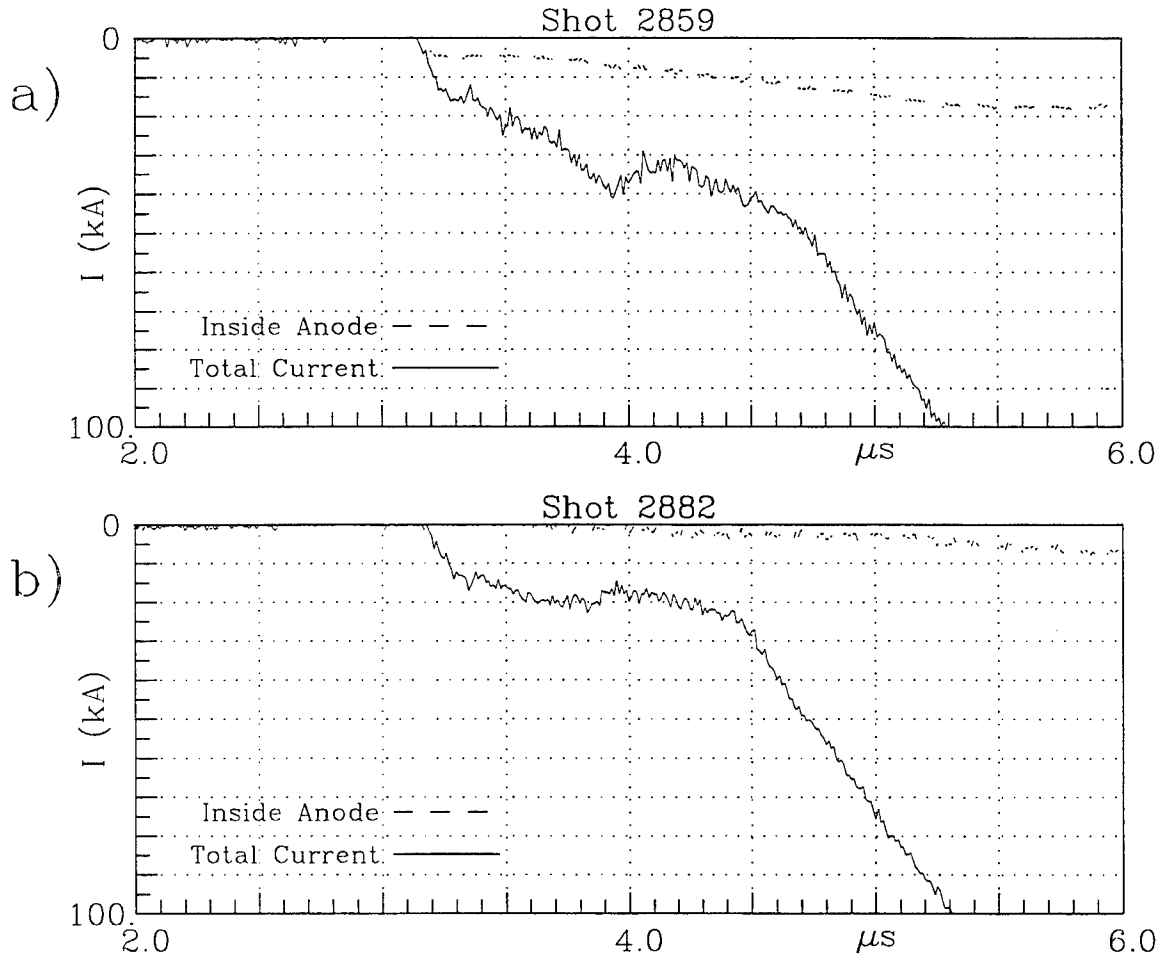

Figure 3-63. High impedance shots at τ_{AK} = 3.0 μs with a 5 cm diameter aperture with and without a mesh.

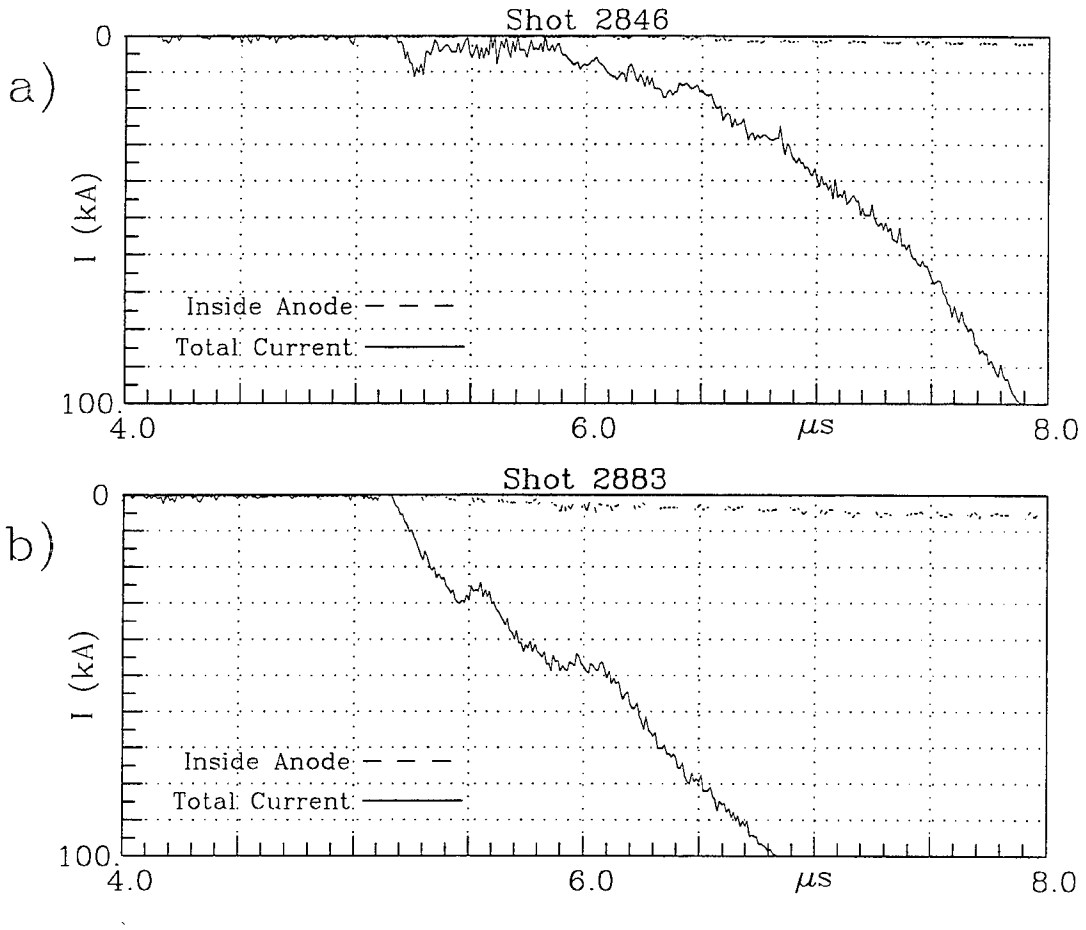

Figure 3-64. Shots at τ_{AK} = 5.0 μs with a 2.54 and 5.08 cm diameter apertures with a mesh.

3.3.11 Scaling with Aperture Area.

In this section the scaling of total current with area of injected ion current is presented. The scaling with aperture area was tested in both the high and low impedance modes. Area scaling experiments were performed with anode apertures of 1.6 cm and 2.54 cm in diameter, for areas of injected ion current of 2.0 and 5.1 cm^2, respectively, and a seven hole anode aperture with circular holes in a hexagonal-close-pack arrangement and an open area of 11.2 cm^2. The experiments which increased the anode aperture up to 15.24 cm in diameter found increases in the total current at opening, but the current scaling was not found to scale proportionally with the aperture area with areas over ~5 cm in diameter. The differences from the expected area scaling were due to source non-uniformities over the large areas (see Figure 3-59 , Section 3.3.8). For the

tests with the three anode apertures there were no meshes on the apertures. The small flashboard was 38 cm from the cathode, and the electrode configuration is shown in Figure 3-6. The guiding magnetic field in the 16 cm AK gap was ~2.5 kG.

The measured ion current densities on-axis for the three anode conditions are shown in Figure 3-65. The ion current was measured behind the cathode mesh, which reduced the signal by approximately a factor of two. In all of the conditions the measured ion current rose to between 30 and 40 A/cm^2 about 6 μsec after the flashboard trigger.

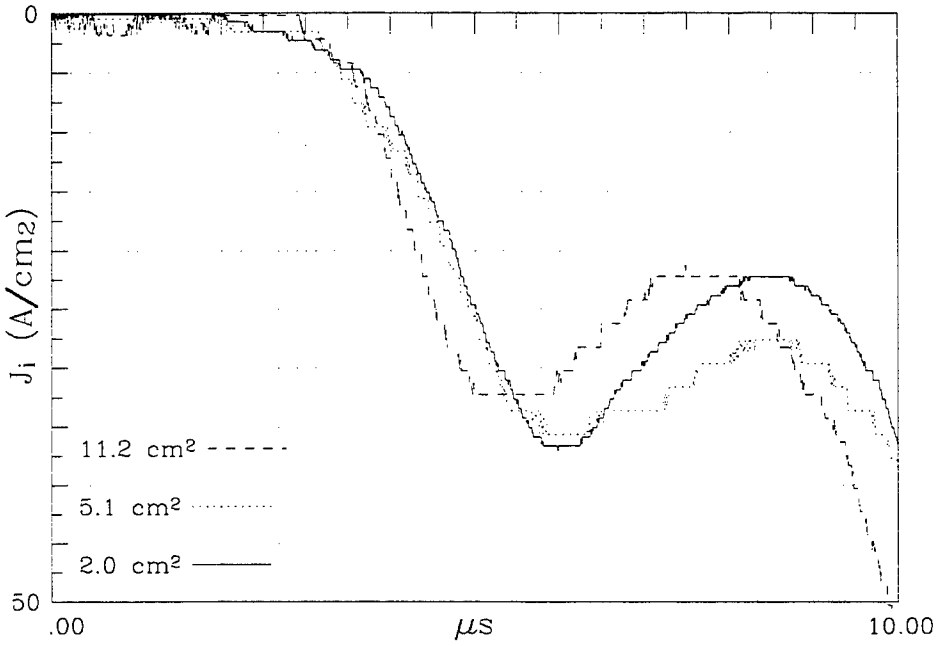

Figure 3-65. Measured ion current densities for three anode apertures.

In Figures 3-66 (a) through (c) high impedance shots with -30 kV applied to the AK gap 3.0 μsec after the trigger to the flashboard are shown for the three anode apertures tested. The driver bank consisted of two 0.7 μF capacitors with a total inductance of 480 nH. In all three cases, analyses of the current from the B-dot probe data showed the centroid to be less than 2 cm off axis up to the peak in current. During the first ~500 nsec of conduction, the voltage across the gap was approximately the full -30 kV charge voltage in all three conditions. The current during this time clearly increased with larger aperture area. Shown in Table 3-3 are the measured ion current densities without applied AK voltage as measured without correction for cathode mesh transparency, and the measured currents at two times with the voltage applied. The currents after 250 nsec of conduction were 0.6, 1.3 and 5.0 kA for the 2.0, 5.1 and 11.2 cm^2 apertures, respectively. The increase in current from the 5.1 cm^2 to the 11.2 cm^2 aperture was more than the increase in area. After 1.5 μsec from turn-on of the voltage, the currents

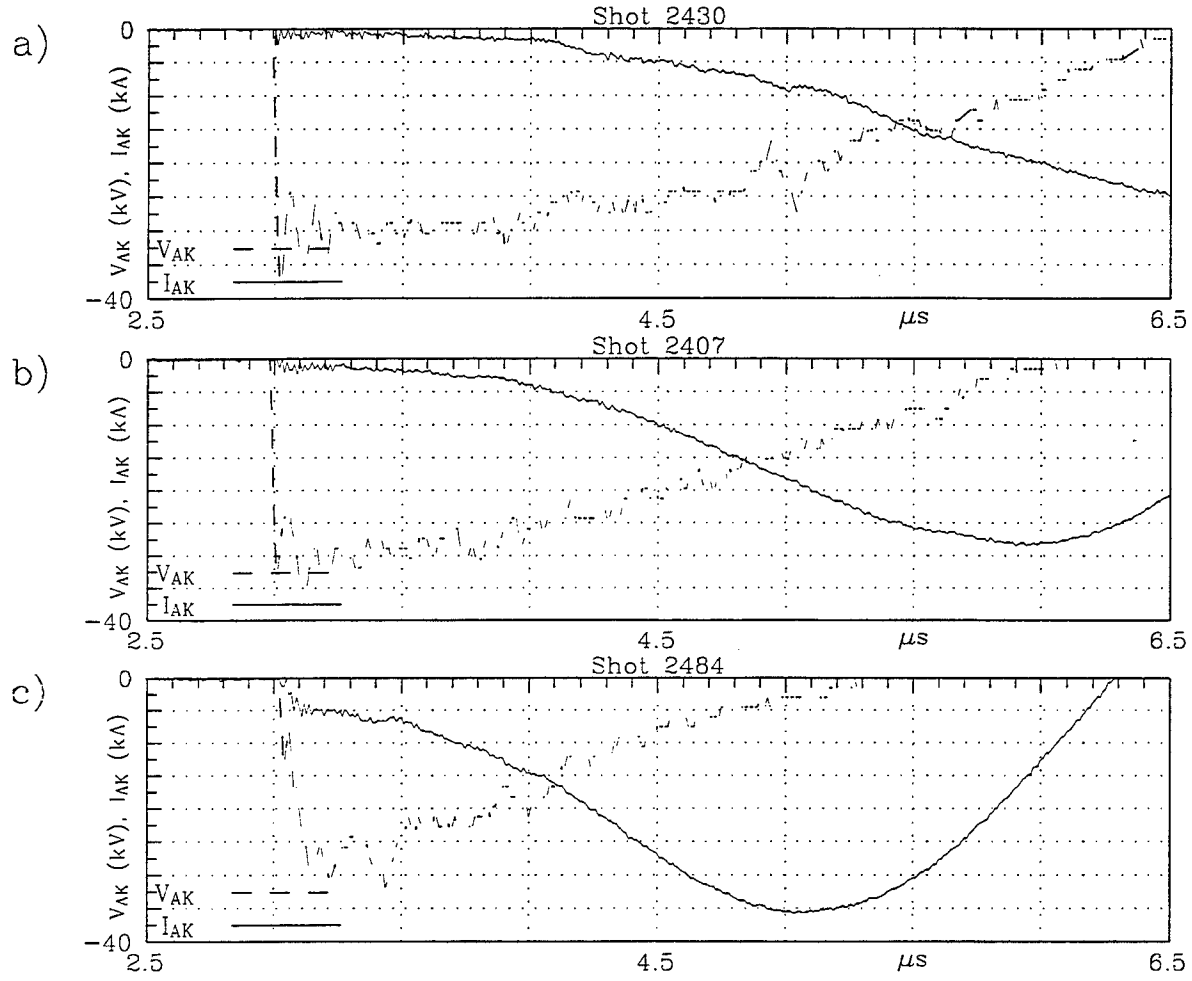

Figure 3-66. (a) Discharge with a 2.0 cm^2 aperture, (b) with a 5.1 cm^2 aperture, and (c) with a 7 hole aperture, with an open area of 11.2 cm^2.

Table 3-3. Measured ion current densities without applied AK voltage for three anode apertures.

	2.0 cm^2	5.1 cm^2	11.2 cm^2
J_i without voltage at τ = 3.25 μsec	3 A/cm^2	3 A/cm^2	3 A/cm^2
J_i without voltage at τ = 4.50 μsec	16 A/cm^2	16 A/cm^2	24 A/cm^2
Total current at τ = 3.25 μsec	0.6 kA	1.3 kA	5.0 kA
Total current at τ = 4.50 μsec	5 kA	10 kA	28 kA

were 5, 10 and 28 kA for the 2.0, 5.1 and 11.2 cm^2 apertures, reflecting an area scaling between the 2 and 11 cm^2 apertures within 14% and an area scaling between the 2 and 5 cm^2 apertures within ~28%. These are reasonable area scalings considering non-uniformities of ion current in radius, flashboard variation, and current channel expansion due to the low magnetic field and absence of a mesh across the anode aperture.

Similar results hold for the low impedance mode. In Figures 3-67 (a) through (c) shots with -30 kV applied to the AK gap 5.0 μsec after the trigger to the flashboard are shown for the three anode apertures. There was good agreement between the three current diagnostics during the initial rise in current until there was an abrupt change in the total current rate of rise and a current commutation typical of behavior without an anode mesh. At the time of this event, the anode Rogowski and the B-dot probes showed a rapid reduction in measured current, while the total current Rogowski showed only a change in the rate of rise in the total current. Table 3-4 summarizes the time τ_c, at which the total current slope changes, and currents for the three apertures. The current commutation occurred when the total currents were at 9, 15 and 30 kA for the 2.0, 5.1 and 11.2 cm^2 apertures respectively, showing that the total current conducted until the current commutation scaled fairly well with the aperture area up to apertures of 11 cm^2.

Again, the data was unfortunately compromised by non-uniformities in the ion source, flashboard variation, and current channel expansion.

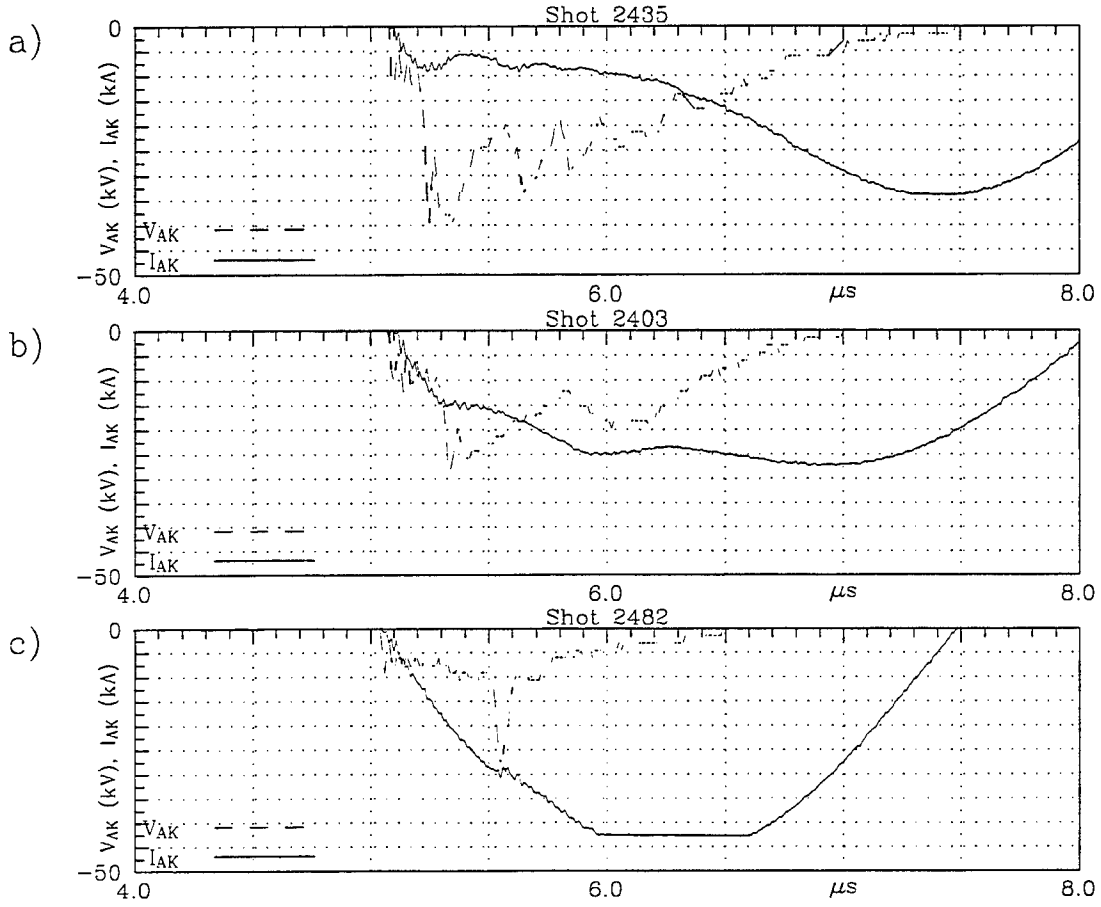

Figure 3-67. (a) Discharge with a 2.0 cm^2 aperture, (b) with a 5.1 cm^2 aperture, and (c) with a 7 hole aperture with an open area of 11.2 cm^2.

Table 3-4. Summary of time (τ_c) at which the total current slope changes.

	2.0 cm^2	5.1 cm^2	11.2 cm^2
J_i without voltage at τ = 5.0 μsec	28 A/cm^2	28 A/cm^2	33 A/cm^2
τ_c	185 nsec	250 nsec	510 nsec
Total current $\tau = \tau_c$	9 kA	15 kA	30 kA

3.3.12 Scaling with AK Gap Length.

The effect of the AK gap length on the conduction time for an opening mode and on the time of the start of the impedance drop are important issues for scaling of switch operation. One-dimensional simulations were carried out to investigate the length scaling of peak current before opening with a low density plasma ($3.8x10^{11}/cm^3$) and an injected ion current density of ~0.8 A/cm^2 (see Section 4). Gap lengths of 2, 6 and 12 cm were used with the gaps initially filled with plasma; i.e. with conduction giving a low initial impedance, and with space charge limited electron emission from the anode not allowed. The conduction times were approximately 30, 40 and 60 nsec, respectively, for the three gaps and the peak current were ~450, ~550 and ~525 A. The conduction times and peak current clearly did not scale with length, nor with the square root of the length. The total electron charge transferred before opening did however scale roughly with the square root of the length.

Experimentally it was observed that the conduction time for opening and the time to the start of the impedance drop did not scale with the length of the gap for the low impedance modes, but the time to the start of the drop in impedance did roughly scale with length in the case of the high impedance modes. A length scaling for the time to the start of impedance drop can be interpreted in two ways. Electrode plasma motion at nearly constant velocity would of course give a linear length dependence. Impedance drop due to current channel expansion can also scale with length since the ion background density must build up essentially across the whole gap to allow the observed electron current densities. If channel expansion is due to ion pumping from an interior channel caused by the radial electric field associated with a potential hump, as suggested by simulations, the pumping will occur around localized potential humps or preferentially near the center of the gap if the hump extends symmetrically across the

gap because of the effects of the conducting boundaries. The ions are then longitudinally accelerated towards the electrodes.

The first high impedance data presented was obtained from the coaxial system with the large magnetic field coils, large flashboard, and the large driver bank. The large flashboard was 38 cm from the cathode and AK gap lengths were 5.5, 10.5, 15.5 and 20.5 cm. The external magnetic field was 3.3 kG and a 5.08 cm diameter anode aperture was used without a mesh. Figure 3-68 shows the current profiles for the different gap lengths. There is no correlation between the switch length and the conduction current before the start of the impedance drop. The times from the start of conduction to the start of the impedance drop were 1.7, 1.4, 1.0 and 0.7 μsec for the 20.5, 15.5, 10.5 and 5.5 cm gaps respectively. These times correspond to effective closure speeds of 4 to 6 cm/μsec/electrode - very large values for any thermally driven electrode plasma motion.

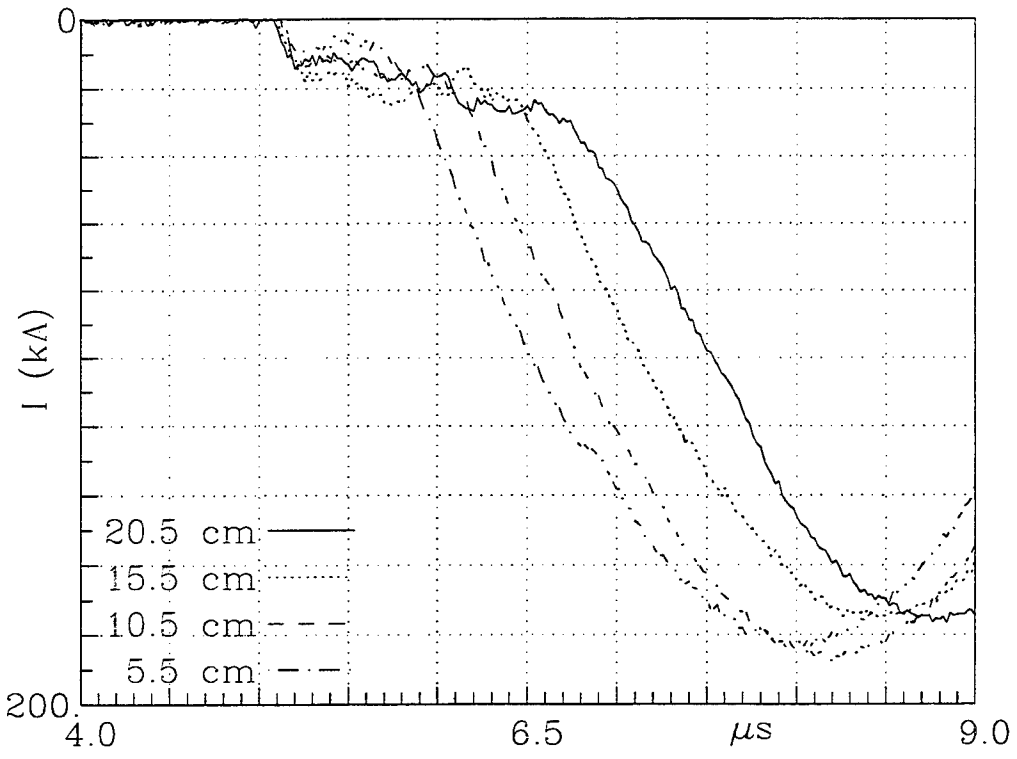

Figure 3-68. Shots at 3300 G applied field and four gap lengths with τ_{AK} = 5 μsec.

A second set of data for the high impedance mode was taken with the glass cross hardware and small flashboard without the bend using a 2.54 cm diameter anode aperture with a mesh. AK gap lengths were 13.6, 8.6 and 3.6 cm and τ_{AK} was 3.5 μsec. An effective closure velocity of ~4 cm/μsec/electrode was observed.

Figure 3-69 shows two current profiles for low impedance opening modes obtained with the same glass cross hardware as above at τ_{AK} = 5.0 μsec. Current and voltage traces are shown for AK gap lengths of 8.6 and 13.6 cm; a 3.6 cm gap length showed no opening and a low impedance behavior throughout the current profile. The conduction time for the 8.6 cm gap was ~400 nsec which was ~15% longer than with the 13.6 cm gap, a variation within the reproducibility of the flashboard. The time to start of the impedance drop was essentially the same for both lengths (~675 nsec). It is noteworthy that the 8.6 cm gap was not shorted after ~1.75 μsec of conduction as a "resistive" voltage of 20 kV appeared across the gap when the current rise flattened.

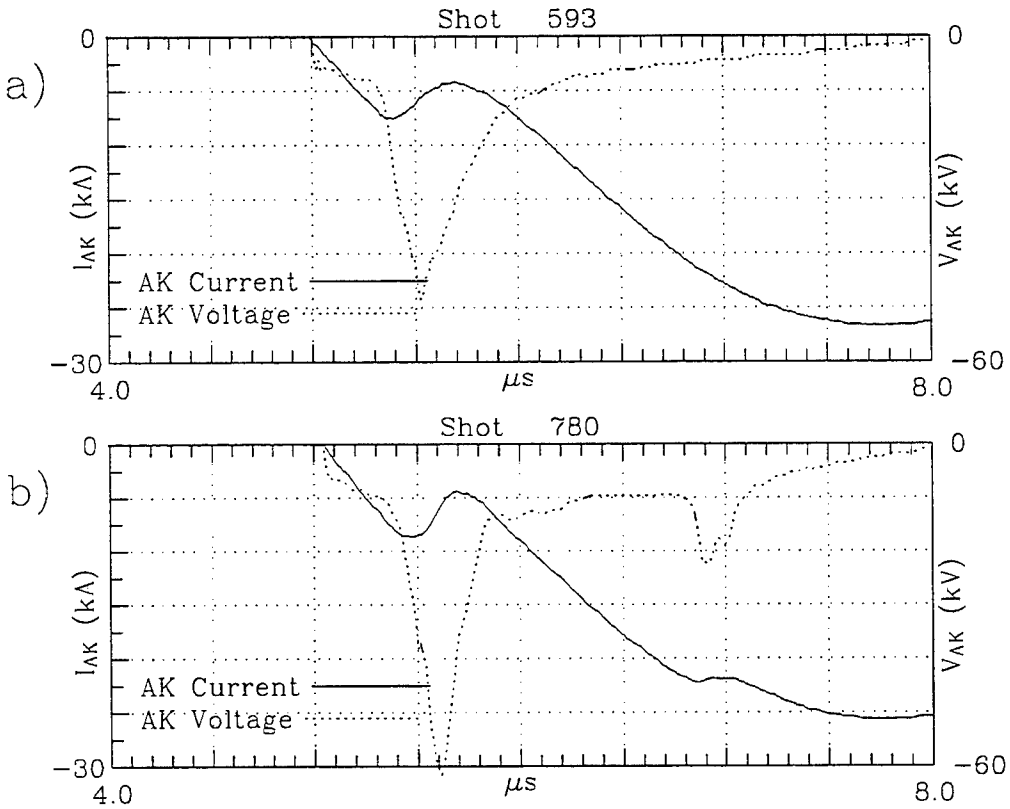

Figure 3-69. (a) Shot in the glass cross with a mesh and an AK gap of 13.6 cm; (b) with an AK gap of 8.6 cm.

3.3.13 Scaling with Charge Voltage and External Inductance.

The scaling of the conduction current with the bank charge voltage and the external inductance was checked in the coaxial hardware with the small driver bank, C = 1.4 μF. The electrode configuration for the 16 cm AK gap is shown in Figure 3-6, and the anode aperture used was 2.54 cm in diameter. The applied magnetic field was 2.5 kG. With the small bank it was possible to vary the external inductance, and a range of the total inductance from 480 nH to 2500 nH was tested. Figure 3-70 shows the conduction

current, conduction time, and charge transfer for discharges with 480, 1400 and 2500 nH of inductance and driver bank voltage of -30 kV. Increasing the external inductance decreased the conduction current somewhat, but had a stronger effect on the conduction time. The decrease in conduction current can be attributed to the drop in the ion source current over the longer conduction times of the higher inductance cases. [The ion source current profile measured without applied voltage for these experiments is given in Figure 3-39.] The injected ion current, e.g., dropped by ~33% as the conduction time increased from the 480 nH value to the value for 2500 nH. The increase in the conduction time was large enough that the charge transfer increased slightly with the external inductance. The charge transfer would show a larger increase with inductance if the conduction current is adjusted for the drop-off in ion source current.

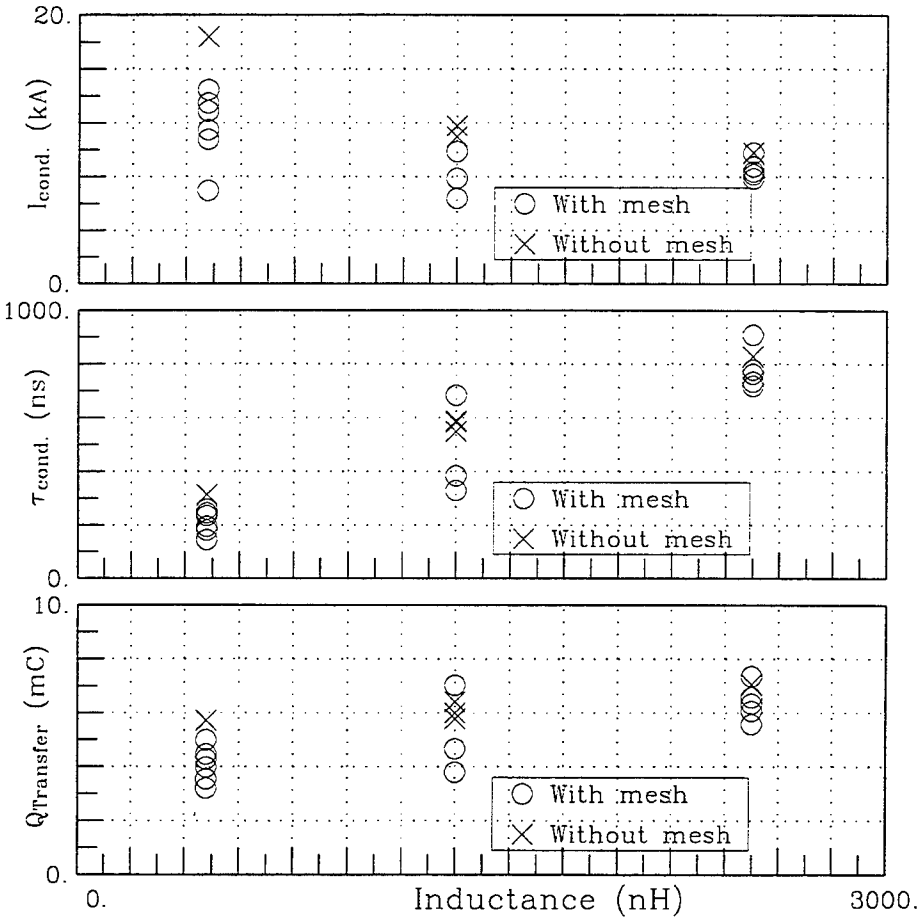

Figure 3-70. Discharges with 480, 1400, and 2500 nH of total inductance with and without mesh across the anode aperture. The voltage was applied 5 μsec after the trigger to the flashboard.

As with increased inductance, reduction of the charge voltage decreased the conduction current, as can be seen in Figure 3-71. The decrease in conduction current is again attributable to the drop in the ion source current over the longer conduction times of the cases with lower charging voltage. There was an expected increase in the conduction time as the voltage was reduced. However, in this case, the charge transfer appeared to decrease as the charge voltage was reduced. Scaling the conduction current for nearly constant ion source current would give an increased charge transfer with decreasing voltage.

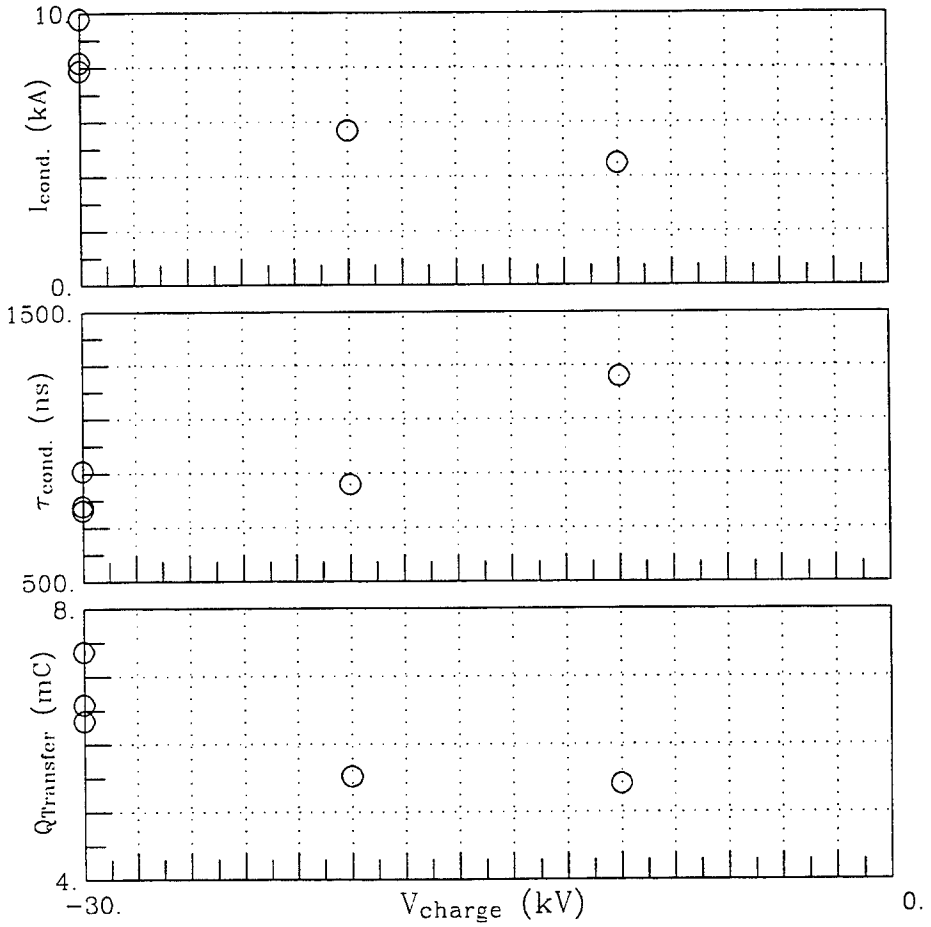

Figure 3-71. Discharges with 2500 nH of total inductance at three charge voltages. The voltage was applied 5 μsec after the trigger to the flashboard.

The results of these experiments are in agreement with the conduction time scaling of Section 3.3.2 if the conduction current levels are adjusted to account for the decrease in ion source current as the conduction time is increased.

SECTION 4

SIMULATION AND THEORY OF DENSITY CONTROLLED OPENING SWITCH

4.1 INTRODUCTION.

To obtain some insight into the behavior of the Density-Controlled Opening Switch (DCOS) experiments, we have used numerical simulations and analytic models. The 2½D (2 spatial coordinates + 3 velocity coordinates) simulation code **IVORY** is used in the numerical work. Most of the experiments were carried out with long (16-25 cm) AK gaps and simulation of such long gaps is impractical for us even in one dimension because the Debye length determines the spatial resolution required. The longest gap we attempt to simulate is a 12 cm gap in 1-D.

In general, we observe that the electrons emitted from the cathode cause substantial heating of the injected plasma. Since the heated plasma is (in most of the simulations) in contact with the grounded anode electrode, the plasma rises to a positive potential relative to ground. If the plasma is sufficiently hot, this potential shuts off the inflow of ions, so that the gap "self-opens" when the existing ion population becomes depleted.

Two types of heating mechanisms can be distinguished in the simulations. If the gap is initially filled, there is a low-impedance phase during which the current rises linearly. Strongly nonlinear bunching of the beam and plasma electrons heats the plasma. Behavior of this type was previously investigated by Kares[1]. On the other hand, if the gap is partially or completely empty when voltage is applied, then the AK voltage *starts out* large. In this regime, which we call the "high impedance" regime, the beam-plasma (two-stream) instability is observed to heat the plasma. (Two-stream heating may be involved in the low-impedance regime also, but it is difficult to separate it from other nonlinear phenomena.)

In the experiments two types of behavior are observed depending on the relative timing of the applied voltage and the injected plasma pulse. When the capacitor is fired soon after the first plasma reaches the cathode electrode ("early voltage"), then the AK voltage rises to approximately the capacitor voltage, and an almost flat current pulse lasting for 1 μsec or longer is produced. When the capacitor is fired later in the plasma pulse ("delayed voltage"), the AK voltage is significantly lower than the bank voltage for a period. During this time the current rises to a higher level than the "early voltage" case, and then drops sharply to a lower value which persists for about 1 μsec. In either case, the current rises gradually after 1 μsec to short-circuit levels due, presumably, to gap closure.

It is natural to attempt to relate the two simulation regimes to the two regimes seen in the experiment. We believe that the opening seen in the "delayed voltage" case is in fact due to the same mechanism that produces opening in the filled-gap simulations.

We have not, however, been able to reproduce the quasi steady-state experimental results for the "early voltage" case. At the experimentally measured current levels, the simulations invariably show periodic behavior of conduction followed by opening (cf. Fig. 4-10). The experiment behaves as though there were no interruption of the injected ion flow. This basic discrepancy is disturbing. It may be due to the expanding electrode plasmas which eventually short the gap.

Several effects aimed at stabilizing the two-stream instability, or reducing its effects, were investigated, including density gradients, energy spread on the beam, and changing the particle boundary conditions at the anode. The latter, which involves reflecting some particles instead of allowing them to freely pass to ground, had the most significant impact on the system, but did not result in the desired behavior.

Two-dimensional simulations show the same qualitative features as those in one dimension for both completely and partially filled gaps. Some intrinsically 2-D effects are observed. With a partially filled gap and low density, the cathode sheath is wide and there is significant radial spreading of the ions as they stream across it. In two-dimensional
simulations of a dense plasma, we see substantial hollowing of the radial current density. Some of the experimental data show a hollow light intensity profile which may be related to this effect.

We were able to find simulation parameters for which the plasma does not self-open. If the potentials which develop in the plasma are smaller than the injected ion energy, then the ion flow is not interrupted. This requires that the current ratio j_b/j_i be substantially lower than the bipolar ratio $\sqrt{M/m}$, making it less attractive for controlling large electron currents. We have obtained criteria for keeping the potentials sufficiently small in both the low-impedance and high-impedance regimes. Additionally, if the AK gap is sufficiently short in the high-impedance regime, the two-stream instability cannot grow and a quiescent bipolar sheath forms.

We have re-examined the analytic model of Kares in connection with the low-impedance regime, and that of Creedon in connection with electron reflexing at the anode. The two models are closely related. Using a modification of the Kares theory, we find improved agreement between the model and 1-D simulations. We have generalized the Creedon model for bipolar flow by including non-zero initial ion energy. The model shows that trapped electrons result in an electron-to-ion current density ratio smaller than the bipolar ratio of $\sqrt{M/m}$, and that the ratio decreases with increasing temperature of the trapped electrons.

In Section 4.2, we describe one-dimensional electrostatic simulations, including the effects of density gradients, velocity spread, and modified anode boundary conditions. In Section 4.3 we show the results of 2-D electromagnetic simulations. Analytic theory supporting the simulations is given in Section 4.4.

4.2. 1-D ELECTROSTATIC SIMULATIONS.

One-dimensional electrostatic simulations have commonly been used to model plasma-filled diodes and similar devices[1-3]. Until the plasma density increases to the point where the collisionless skin depth c/ω_p (where ω_p is the plasma frequency) becomes small compared to the plasma radius, the electrostatic approximation is justified in treating the entire system. For experiments where the plasma radius α is about 1.27 cm, and the plasma flow velocity is on the order of 10 cm/μsec, a (singly charged) ion current density of 1 A/cm^2 has a c/ω_p value of about half the beam radius. Most of our simulations are near this regime. Note that even if c/ω_p is small compared to the dimensions of the plasma, the electrostatic approximation still applies to the small-scale physics of the plasma heating, even though inductive effects are important on a larger scale.

The simulation configuration is shown in Figure 4-1. The gridded region constitutes the AK gap. Plasma ions and electrons are injected at the right and the cathode at the left can emit space-charge-limited electrons. The simulation region is attached to an external RLC circuit in the manner described by Lawson[2]. At the start of the simulation, the capacitor is charged to the desired voltage and the simulation region may or may not be preloaded with moving plasma. The capacitor then proceeds to discharge through the inductor, resistor, and the plasma.

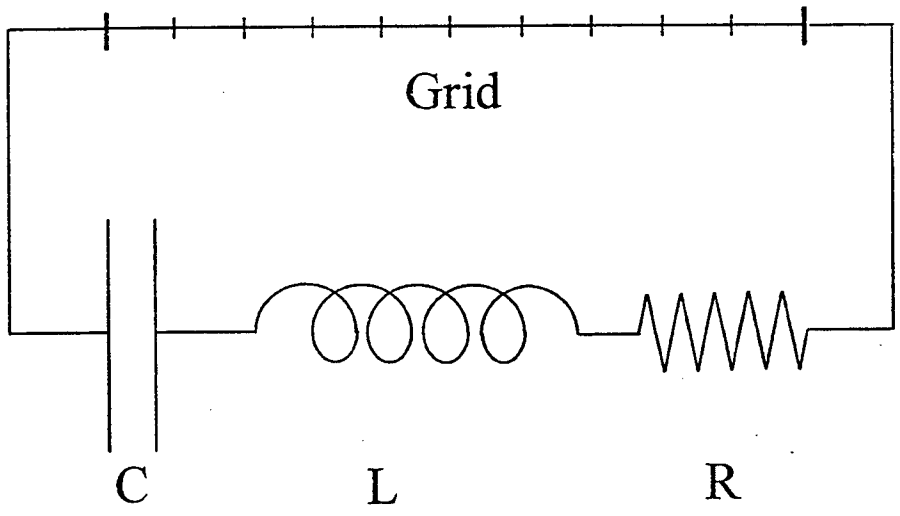

Figure 4-1. Schematic of setup for 1-D simulations.

4.2.1 Low Impedance Regime.

The simulations show different behavior depending on whether plasma initially fills the gap or not. When the gap is prefilled, the plasma initially behaves like a short circuit. The gap has low-impedance for a period during which the plasma heats rapidly. This is followed by an opening during which the voltage spikes up. A typical example of this is shown in Figure 4-2. The parameters for this simulation, given in Table 4-1, correspond to a low-density injected plasma used in initial DCOS experiments[4]. The initial linear current rise in Figure 4-2 is determined by the external inductor; the plasma resistance is low. The longitudinal phase-space near the peak of the current is shown in Figure 4-3. At the time shown, the plasma has heated strongly and ions are being accelerated towards both the cathode and anode. Injection of new plasma is continuing, but the ions are immediately turned around and leave the simulation. This is essentially the same behavior observed by Kares[1] in 1-D simulations for a much shorter (1 mm) AK gap. The mechanism for heating the plasma involves strongly nonlinear beam bunching associated with virtual cathode formation[1]. The theory of this regime is discussed in more detail in Section 4.1.

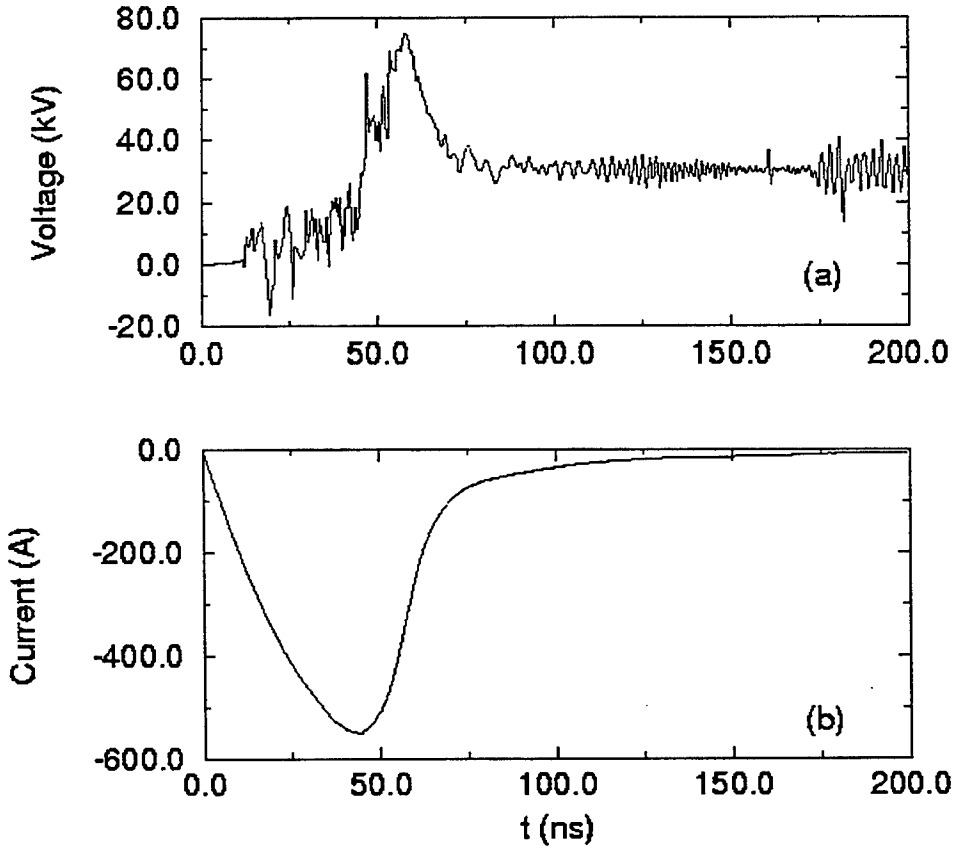

Figure 4-2. Voltage and current vs. time for initially filled AK gap. Parameters are given in Table 4-1 (IVORY run 53).

Table 4-1. Parameters for low-density simulation in Figures 4-2 and 4-3.

Circuit:		**Simulation:**	
External inductance	1.47 μH	Number of cells	800
Bank capacitance	1.4 μF	Cell size	0.0075 cm
Initial bank voltage	30 kV	Timestep/c	0.05 cm
External resistance	12.8 Ω	Initial no. of particles	20,000 (per species)

Plasma:	
Injection area	5 cm^2
AK gap length	6 cm
Injected plasma density	3.8 x 10^{11} cm^{-3} (H^+ + e)
Injected ion velocity	13 cm/μsec
Injected ion current density	0.8 A/cm^2
Cathode SCL emission	On
Anode SCL emission	Off

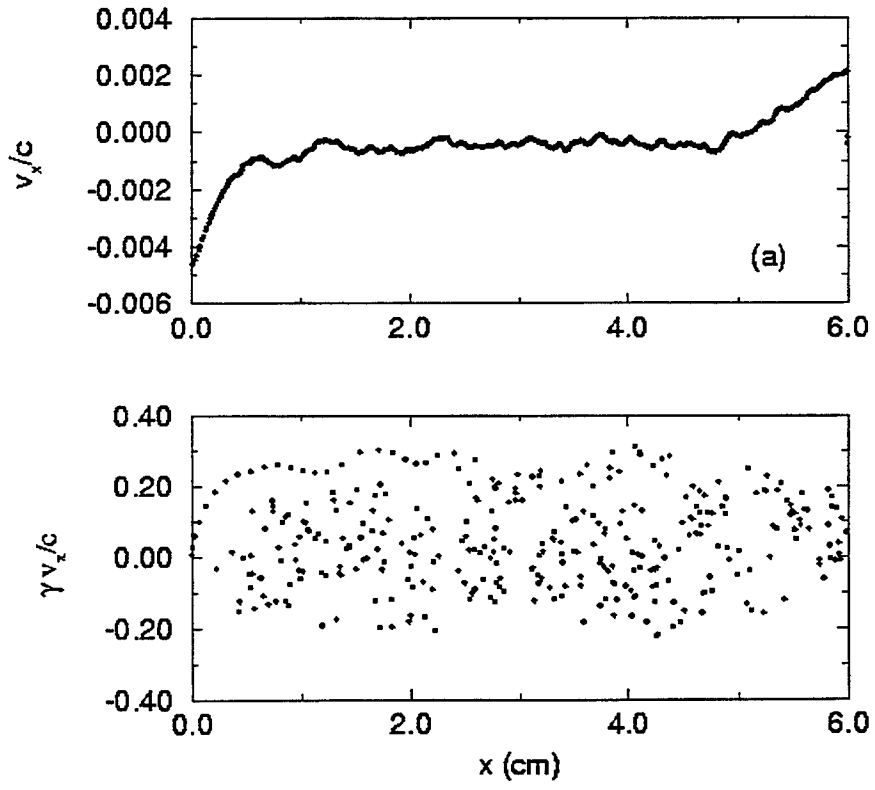

Figure 4-3. Plots of (a) longitudinal phase-space for ions and (b) cathode-emitted electrons near peak current in Figure 4-2 (IVORY run 53).

Carrying out simulations with shorter (2 cm) and longer (12 cm) gaps gives the current traces shown in Figure 4-4. The main difference between these and the 6 cm case is in the time for which the gap can supply high current. In each case, the gap is almost completely depleted of ions after the conduction phase. The gap then slowly refills with plasma.

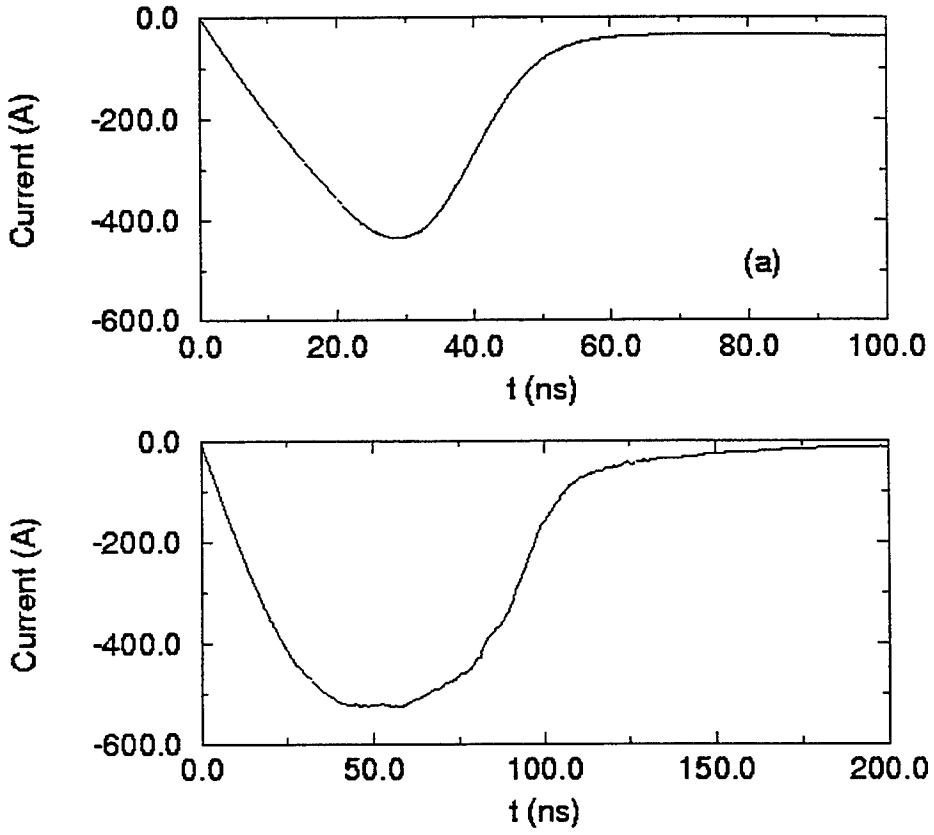

Figure 4-4. Current versus time for initially filled (a) 2 cm gap and (b) 12 cm gap. Other parameters as in Table 4-1 (IVORY runs 56, 54).

4.2.2 High Impedance Regime.

The behavior of the gaps as they refill is not the same as for an initially completely filled gap. The electrons emitted from the cathode are accelerated to essentially the full AK voltage (30 kV in these examples) in the space between the cathode and the advancing plasma. Thus their density inside the plasma is considerably lower, and velocity higher, than during the initial low-impedance phase. We call this the "high-impedance" regime. The mechanism for heating the plasma in this regime is the beam-plasma two-stream instability[5]. The wavelength of this instability is approx. $v_b/w_p \approx 2.5$ cm, where v_b is the beam velocity. For the 2 cm gap, the instability is

unable to develop, and a quiescent bipolar sheath develops, as shown in Figure 4-5. For the 6 and 12 cm gaps, however, the two-stream instability develops strongly as the current rises, and the gap opens, as shown in Figure 4-6. (For this simulation, the AK gap was initially empty;

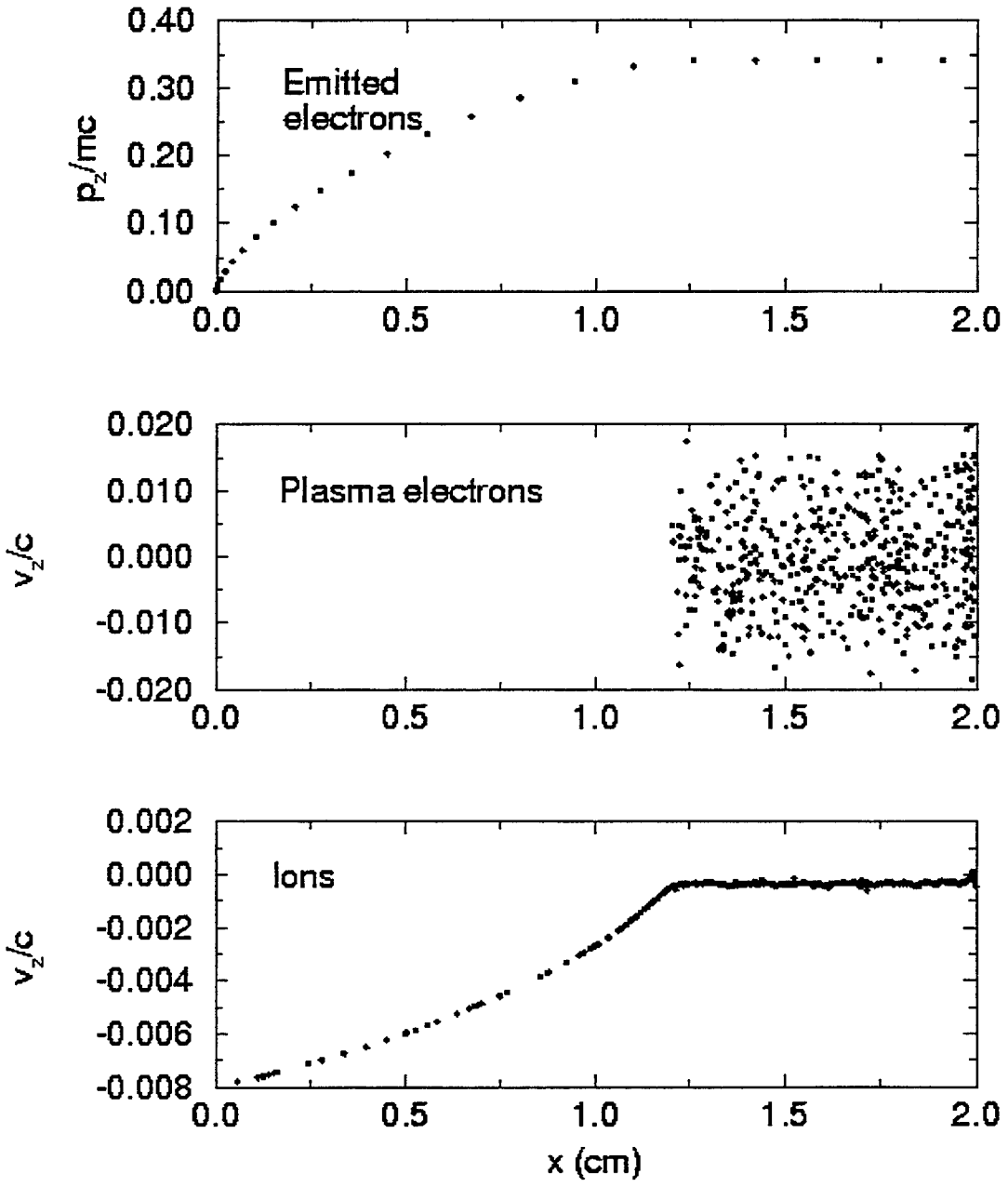

Figure 4-5. Longitudinal phase space when quiescent bipolar sheath has developed in 2 cm gap. Other parameters as in Table 4-1 (IVORY run 37).

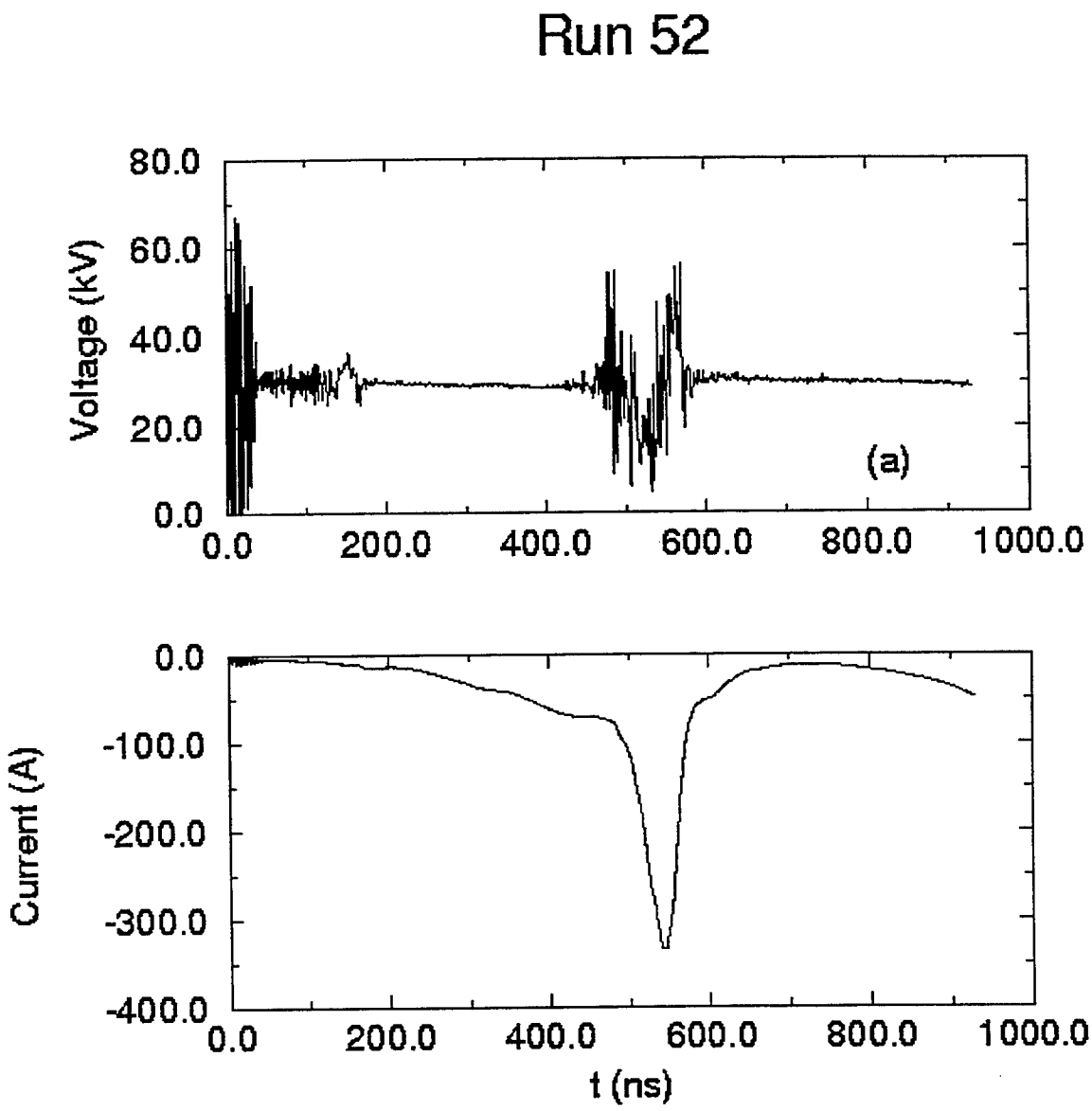

Figure 4-6. Voltage and current versus time for initially empty 6 cm gap. Other parameters as in Table 4-1 (IVORY run 52).

simulations where the gap was initially full and subsequently refilled show similar behavior during refill.) In the experiment which these simulations were attempting to model[4], the current rose to about 100 A and stayed at about that level for about 1 μsec. This current is considerably less than the peak current shown in Figures 4-2, 4-4 and Figure 4-6. We considered the possibility that the experimental current was source-limited to around 20 A/cm^2 (100 A total) and that this low value might reduce the plasma heating. The simulation in Figure 4-6 was rerun with a 20 A/cm^2 emission limit. The result in Figure 4-7 shows that opening still occurs. The phase-space plot in Figure 4-8 shows the beam-trapping which is typical at nonlinear levels of the two-stream instability.

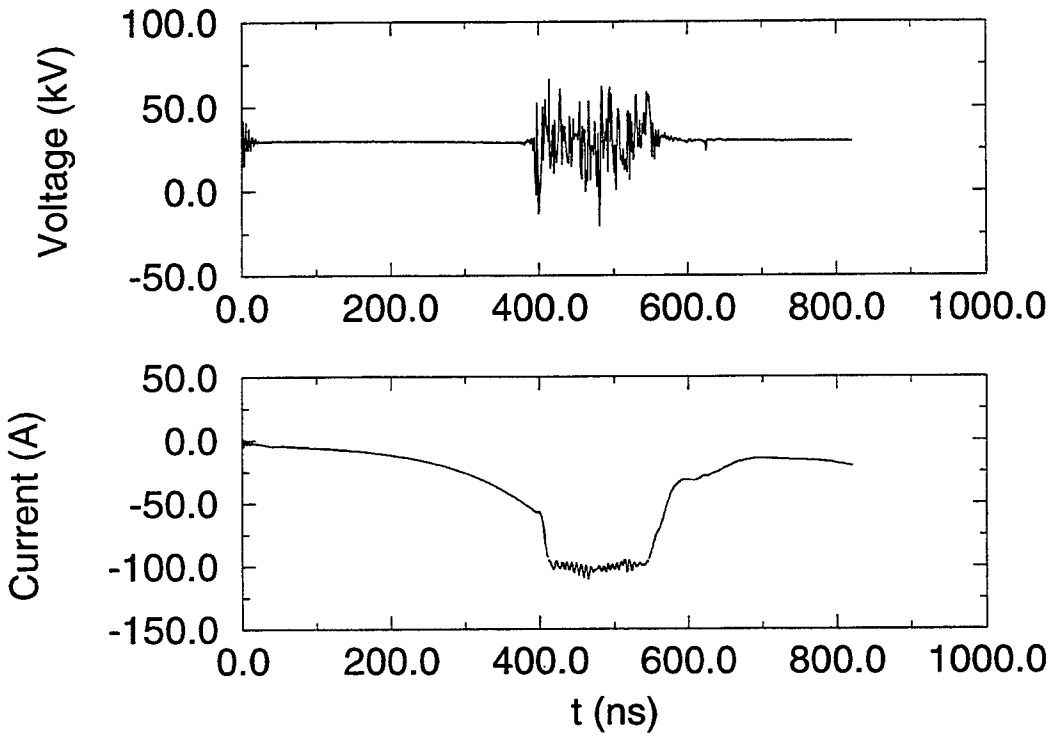

Figure 4-7. Current and voltage for initially empty 6 cm AK gap and current limit of 100 A. (IVORY run 60).

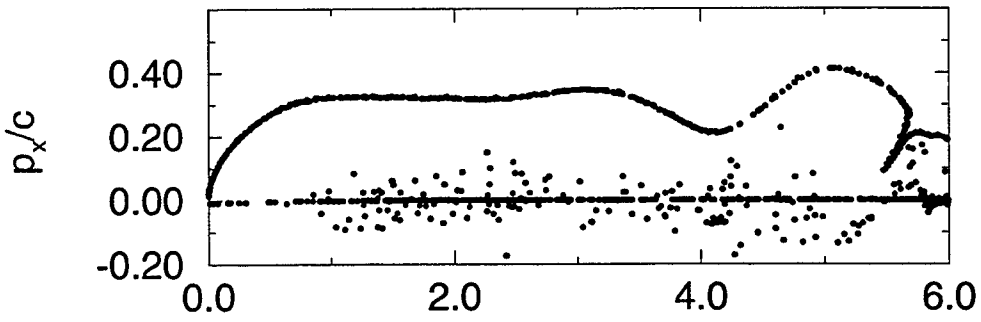

Figure 4-8. Longitudinal phase-space for cathode-emitted electrons, anode-emitted electrons, and ions at t = 500 nsec in Figure 7 (IVORY run 60).

4.2.3 Similarity To Experimentally Observed Opening.

Experimental data for the "delayed voltage" case typically shows opening events similar to those in Figures 4-2 and 4-4. In shot 2336, for example, which has a 16 cm AK gap, the current rises linearly for about 130 nsec, reaching a peak of 7.5 kA. The current flattens out and then begins to fall. At 300 nsec, the current has dropped to about 2 kA. The ion flux, which is measured on a separate shot with no applied AK voltage, is about 10 A/cm^2. This includes an estimated 50% attenuation due to the anode mesh present in shot 2336.

A simulation with a 6 cm AK gap and 6 A/cm^2 of injected C^+ ions is shown in Figure 4-9 (parameters are given in Table 4-2). The peak current reached is about 4.6 kA, and the impedance starts to climb after 100 nsec.

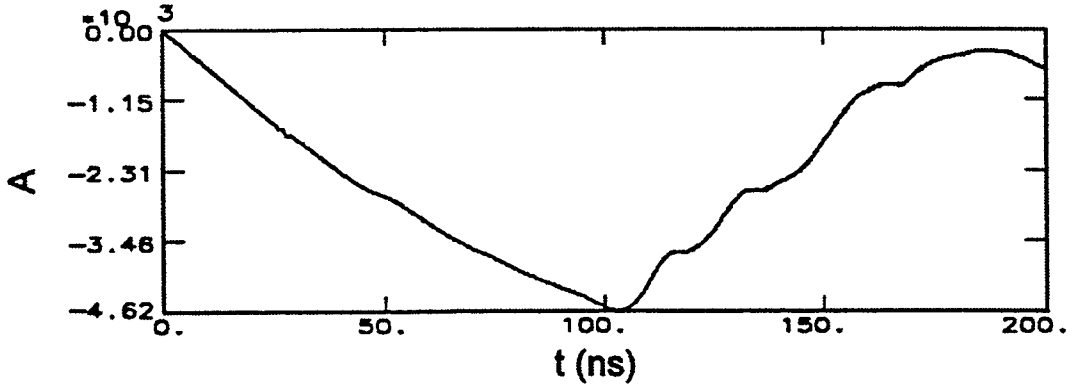

Figure 4-9. Current vs. time for filled-gap simulation of 6 A/cm^2 C^+ ions. (IVORY run 73k)

Table 4-2. Parameters for simulation in Figure 4-9.

Circuit:		**Simulation:**	
External inductance	0.48 μH	Number of cells	1600
Bank capacitance	1.4 μF	Cell size	0.00375 cm
Initial bank voltage	30 kV	Timestep/c	0.02 cm
External resistance	35 milliΩ	Initial no. of particles	20,000 (per species)
Plasma:			
Injection area	5 cm^2		
AK gap length	6 cm		
Injected plasma density	3.8×10^{12} cm^{-3} (C^+ + e)		
Injected ion velocity	13 cm/μsec		
Injected ion current density	6.3 A/cm^2		
Debye length	0.0017 cm (for 15 eV plasma		
Cathode SCL emission	On		
Anode SCL emission	Off		

From the simulations in Figures 4-2 and 4-4, we see that the main effect of a longer AK gap is to increase the time for which high current is conducted. This, together with the fact that the peak electron current is roughly proportional to the plasma density, makes it plausible that the simulation and the experiment are exhibiting the same phenomenon. To increase one's confidence that this is the case, it would be desirable to identify the dominant plasma ion species, and to measure the rise in plasma temperature, which in the simulation reaches several kV.

4.2.4 Two-stream Instability Stabilizing Effects.

4.2.4.1 *Beam Velocity Spread*. In the "high-impedance" simulations above, the two-stream instability is in the hydrodynamic regime, in which the phase velocities of the unstable waves lie outside the beam velocity distribution. When this is not the case, the instability becomes kinetic and growth is considerably weakened[6]. This requires

$$\frac{v_{thb}}{v_b} >> \left(\frac{n_b}{n_p}\right)^{1/3} \tag{4.1}$$

where v_{thb} is the beam velocity spread and n_b, n_p are the beam and plasma densities, respectively. For the case in Figure 4-8, this requires $v_{thb} >> 0.3\ v_b \sim 0.1c$. A thermal velocity of 0.1c corresponds to a temperature of 5 kV. We carried out a simulation with this temperature, obtaining the results shown in Figure 4-10. Comparing this figure with Figures 4-7, 4-8 shows that marginally satisfying the inequality in Equation 4.1 does not have much effect on the instability. A large longitudinal velocity spread could develop if the emitting surface had bumps comparable in scale to the bipolar

cathode sheath thickness, which is about 0.85 cm for the parameters here. This might occur if a dense, non-uniform, expanding plasma formed on the cathode.

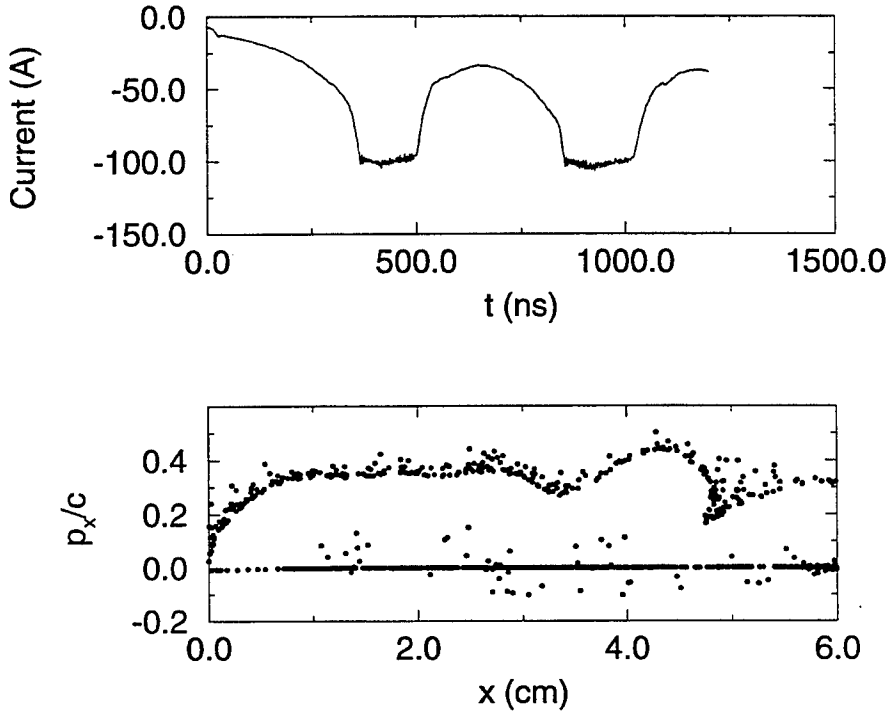

Figure 4-10. Simulation with 5 kV beam temperature showing (a) current versus time and (b) longitudinal phase-space at t = 400 ns. Otherwise parameters are the same as for Figure 4-8 (IVORY run 61).

4.2.4.2 *Electron-Neutral Collisions*. In the simulations, it is assumed that the plasma electrons which are injected with ions into the AK gap are collisionless. It is well known that two-stream instability is reduced when collective plasma oscillations are damped by electron-neutral collisions. The condition for a significant effect is[6]

$$\frac{\upsilon_c}{\omega_p} > \left(\frac{n_b}{n_p}\right)^{1/3} \tag{4.2}$$

where v_c is the collision frequency and ω_p is the electron plasma frequency. For electron energies in the range of 1 - 10 eV, the collision frequency is of order 5×10^{12} sec^{-1} atm^{-1} (Ref. 7). Applying Equation 4.2 to low-density parameters ($\omega_p \approx 3.5 \times 10^{10}$, $(n_b/n_p)^{1/3} \approx 0.32$), yields an estimate of about 2 Torr for the required neutral pressure. This is orders of magnitude larger than the measured experimental

pressure of 1.5 x 10^{-6} Torr (Ref. 5). Therefore, the collisions are not expected to have any significant effect on the instability.

4.2.4.3 *Density Gradients*. Longitudinal gradients have been shown to have a stabilizing effect on the two-stream instabilitiy[8-10]. Based on ion time-of-flight velocities and ion current measurements, we estimate that the plasma density can vary by a factor of two or more over a 6 cm AK gap.

In Figure 4-11 we compare a case with a flat plasma density profile to a case where the density increases by a factor of two from the anode to the cathode. To initialize these simulations, we filled the AK gap with plasma almost to the cathode.

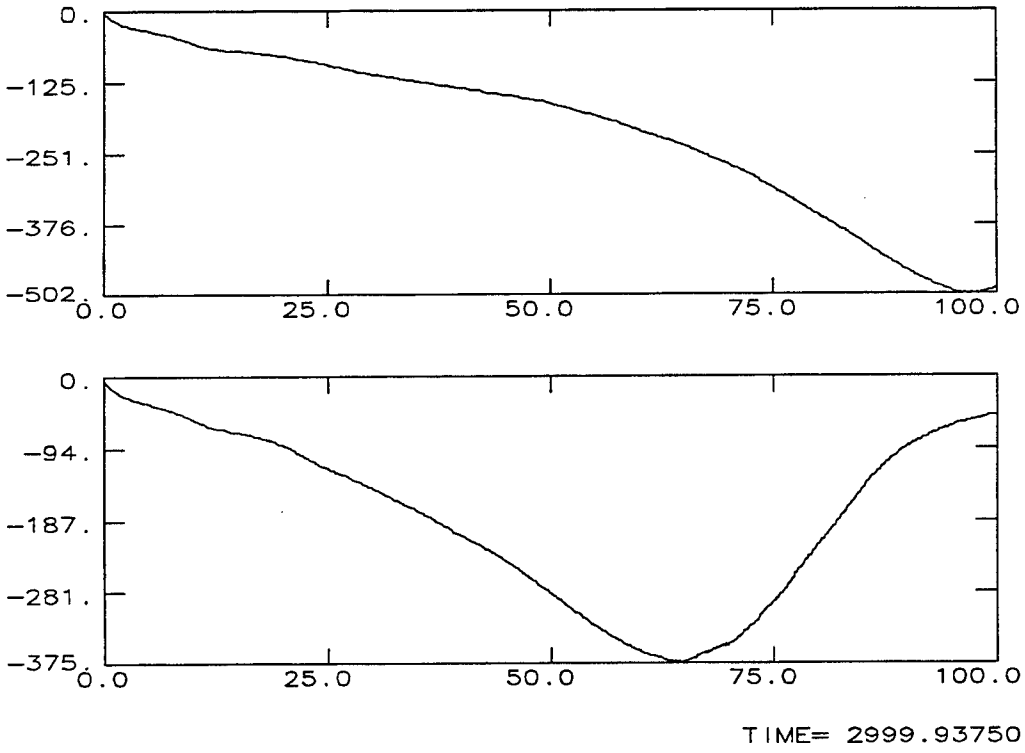

Figure 4-11. Current vs. time comparing case with (a) density gradient (density doubles from cathode to anode across 6 cm gap) and (b) case with no density gradient. Ion current density at cathode is same (0.8 A/cm^2 H^+) in each case. (IVORY run 73b and 73c).

A gap approximately equal to the bipolar gap width (about 1.25 cm) was left empty. This allows us to get into the two-stream unstable ("high-impedance") regime without first going through the low-impedance phase followed by plasma blow-out followed by refill which occurs when the gap is completely filled initially (see e.g. Figure 4-2). The

results show that the case with the density gradient takes longer to open than the flat case, and that the peak current is higher. At comparable electron currents, the case with a gradient appears to be less unstable than the case without. However, the gradient does not quench the instability sufficiently to prevent heating. At the end of the density gradient simulation, the ion phase-space resembles that in Figure 4-3: ions are accelerating towards both the cathode and anode and opening is inevitable.

A simulation with a factor of three density gradient also opened in the same manner.

4.2.4.4 *Anode Reflexing of Electrons*. From the 1-D simulations described above, and the 2-D simulations in the Section 4.3, it is difficult to see how strong heating of the plasma can be avoided. This led us to consider conditions under which this heating does not prevent ions from entering the plasma. Schematically, if the shape of the AK potential can be changed from that in Figure 4-12(a) to that in Figure 4-12b), then ions can continue to be drawn in. Figure 4-12(b) is typical of the potentials in the reflex triode[11-12] (see Section 4.2). The essential feature is that hot electrons cannot immediately leave the plasma, creating a layer of ions. Indeed, there is a net excess of electrons in the sheath which forms at the anode. To be consistent, we must assume that the ion source is space-charge-emission from the anode surface, rather than injected plasma. In the experiment, this situation might develop if the plasma source were not electrically connected to the anode. In that case electrons would be reflected from the source as the source potential became depressed. This would also prevent ions from leaving the source.

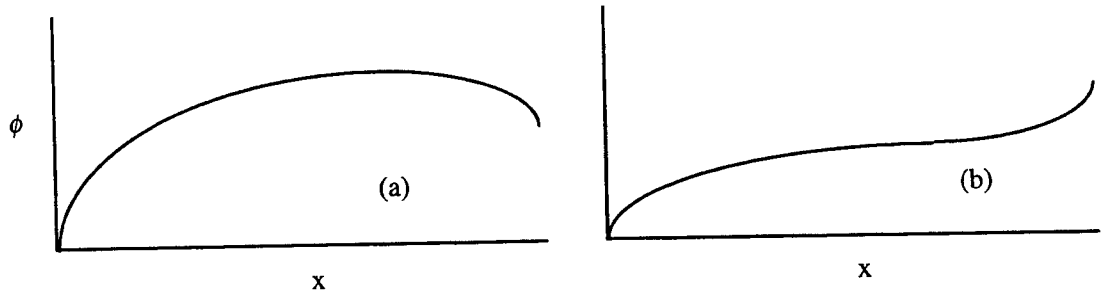

(a) Absorbing Anode (b) Reflexing Anode

Figure 4-12. Schematic of potential for hot plasma contact.

In order to draw current, some electron have to get to the anode. To simulate this, we set the boundary condition at the anode to absorb some fraction of the electrons striking it, and reflect others (such as might happen with an anode grid). Results for 5% absorption are shown in Figure 4-13. Simulation parameters are given in Table 4-

Table 4-3. The simulations are started with a plasma filling the AK gap, leaving a 0.3 cm gap (the estimated bipolar gap) at the cathode. As the current rises, the plasma heats strongly. The ion current at the cathode rises to 15-20 A/cm^2, and the cathode sheath widens since this ion current is larger than the supplied current. The ion loss is essentially one-sided, to the cathode. The ion and electron phase spaces near the end of the run, shown in Figure 4-14, show a wide sheath at the anode which is drawing in

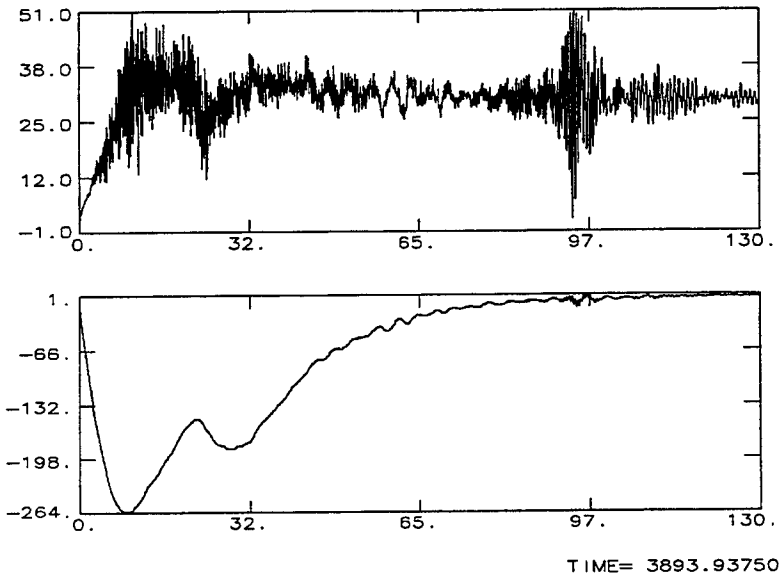

Figure 4-13. Voltage and current vs. time for reflexing simulation with 5% absorption at anode. Parameters are given in Table 4-3 (IVORY run 77).

Table 4-3. Parameters for simulation in Figure 4-13.

Circuit:	
External inductance	0.48 μH
Bank capacitance	1.4 μF
Initial bank voltage	30 kV
External resistance	35 milliΩ
Plasma:	
Injection area	5 cm^2
AK gap length	3 cm
Injected plasma density	1.5 x 10^{12} cm^{-3} (H^+ + e)
Initial ion velocity	13 cm/μsec
Initial ion current density	3.1 A/cm^2
Debye length	0.0024 cm (for 15 eV plasma
Cathode SCL emission	On
Anode SCL emission	On

Simulation:	
Number of cells	800
Cell size	0.00375 cm
Timestep/c	0.01 cm
Initial no. of particles	20,000 (per species)

a space-charge-limited ion (H^+) current. However, the cathode sheath is too wide to generate significant electron current in steady state.

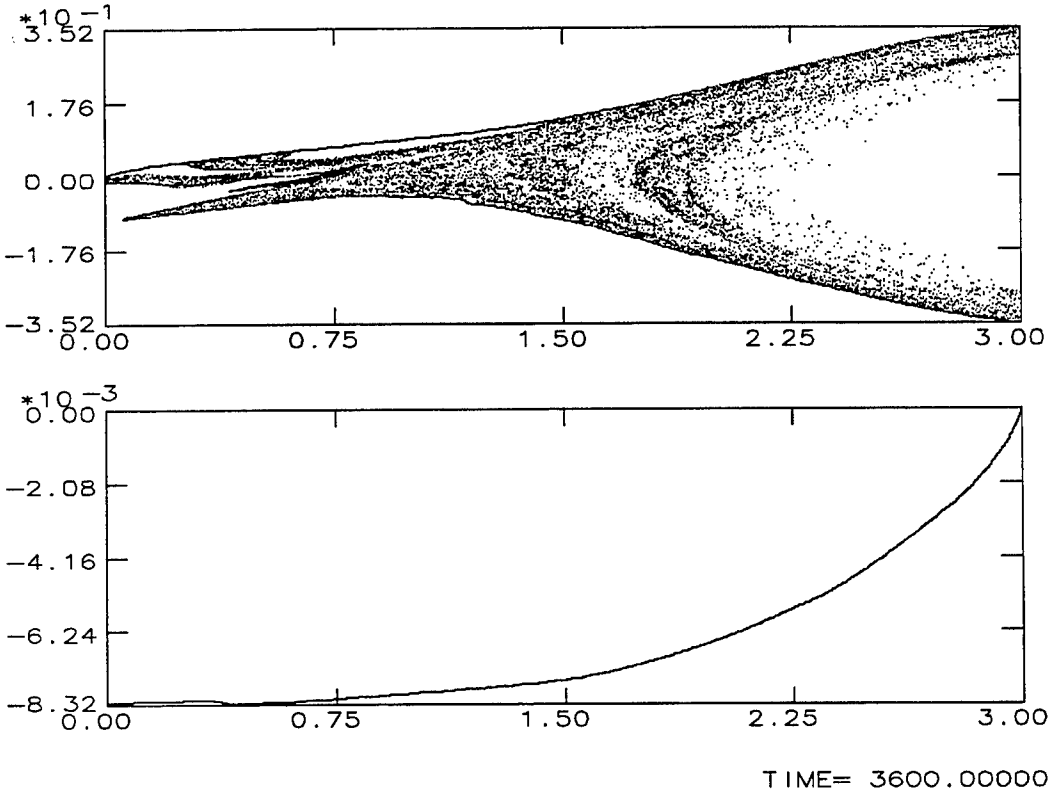

Figure 4-14. Longitudinal phase-space for (a) electrons and (b) ions at t = 120 ns for reflexing simulation in Figure 13 (IVORY run 77).

4.2.5 Regimes Where Plasma Injection Is Not Shut Off.

4.2.5.1 *Low Impedance Regime.* In their model of a plasma-filled diode with an immobile ion background[13], Kares et al. give an expression for the maximum amplitude of a stationary potential well in an AK gap with a uniform ion background and space-charge-limited emission of electrons from the cathode (see Section 4.1):

$$\phi_{\max} = \frac{2m}{e}\left(\frac{j_b}{en_i}\right)^2 (1+\gamma)^2 \qquad (4.3)$$

where j_b is the electron current density, n_i is the ion density, and γ is a parameter which takes account of the effect of trapped electrons. For the flat energy distribution assumed by Kares et al., γ ranges between 0 and 1 ($\gamma = 0$ means there are no trapped electrons). We can plausibly use ϕ_{max} as an upper bound for the positive potential the plasma can float to as a result of beam heating mechanisms. If the ion kinetic energy is such that for the "worst case" of $\gamma = 1$ we have

$$e\phi_{\max} =<< \frac{1}{2} M v_i^2 \tag{4.4}$$

where M is the ion mass and v_i is the ion injection velocity, then plasma injection should not be shut off, regardless of how unstable the plasma is. Note that application of Equation 4.4 is self-consistent in that when it is satisfied, the velocity (and therefore the density) of the injected plasma will be approximately uniform, which is one of the assumptions used to

$$\frac{j_b}{j_i} << \frac{1}{2(\gamma+1)} \sqrt{\frac{M}{m}} \tag{4.5}$$

For $\gamma = 1$, this $j_b/j_i \ll \sqrt{M/m}$ gives which is a considerable reduction from the classical bipolar ratio of $\sqrt{M/m}$.

We ran some simulations to test how far the inequality in Equation 4.5 can be pushed to increase j_b/j_i. Based on this limited set of results, it appears that one can have j_b/j_i which approximately satisfies equality, i.e.,

$$\frac{j_b}{j_i} \approx \frac{1}{4} \sqrt{\frac{M}{m}} \tag{4.6}$$

We find that under this condition, the ion flow is strongly affected by the plasma potential, but injection is not shut off. These results are for a short AK gap of 1 cm, and the gap is completely filled at the start of the simulation. Other parameters are given in Table 4-4. Figure 4-15, for which the injected ion current density is 10 A/cm^2, shows that the current initially follows the short-circuit current density and then levels off at a level given roughly by Equation 4.6. In Figure 4-16, the ion velocity is doubled to give an injection current density of 20 A/cm^2, and the level-off current density rises correspondingly.

The phase-space plots in Figure 4-17 show that the ions are strongly perturbed by the plasma potentials. Thus, the calculation which leads to Equation 4.6 is not fully self-consistent, since it assumes a uniform ion density. The actual average ion density is larger, due to the slowing down of the ions in the turbulent potentials.

Table 4-4. Parameters for runs in Figures 4-15 to 4-17.

External inductance	1.47 μH
Bank capacitance	1.4 μF
Initial bank voltage	1 kV
External resistance	0.1 Ω
Injected plasma density	5×10^{12} cm^{-3} ($H^+ + e$)
Injected electron temperature	15 eV
Injected ion temperature	0
Injection area	1 cm^2
AK gap length	1 cm
Cathode SCL emission	On
Anode SCL emission	On

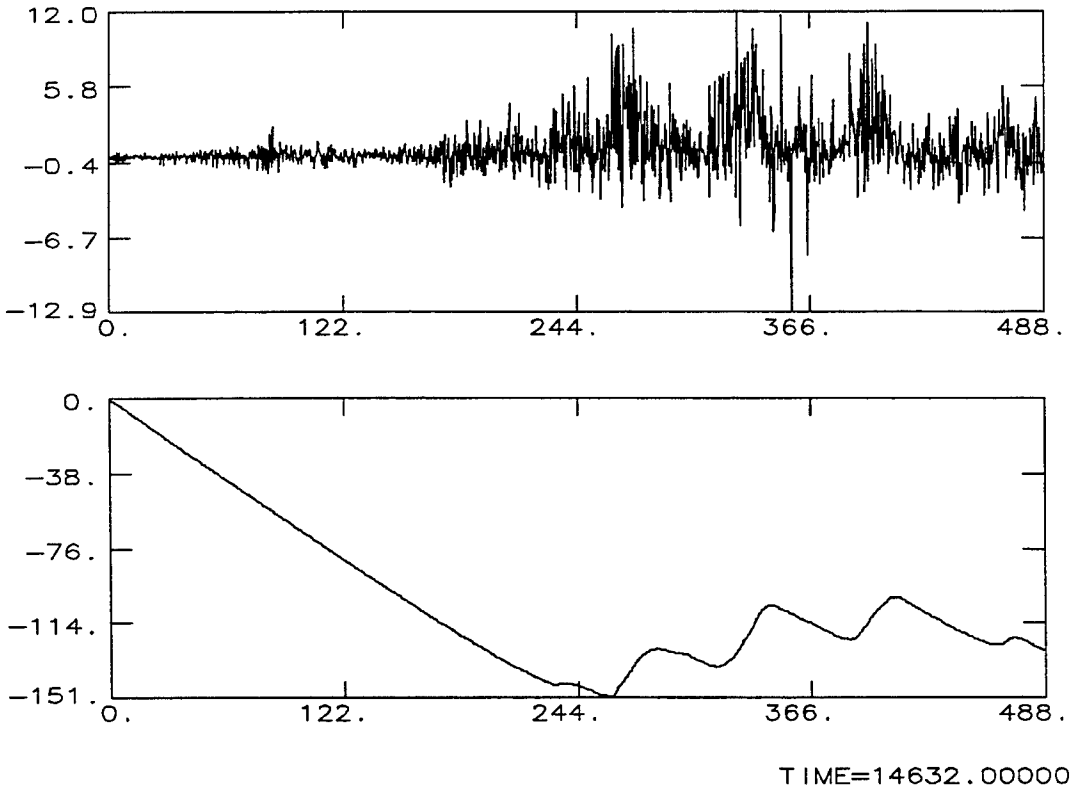

Figure 4-15. Plots of (a) voltage and (b) current vs. time for parameters in Table 4-4 and ion (H^+) energy of 88 eV (IVORY run 42).

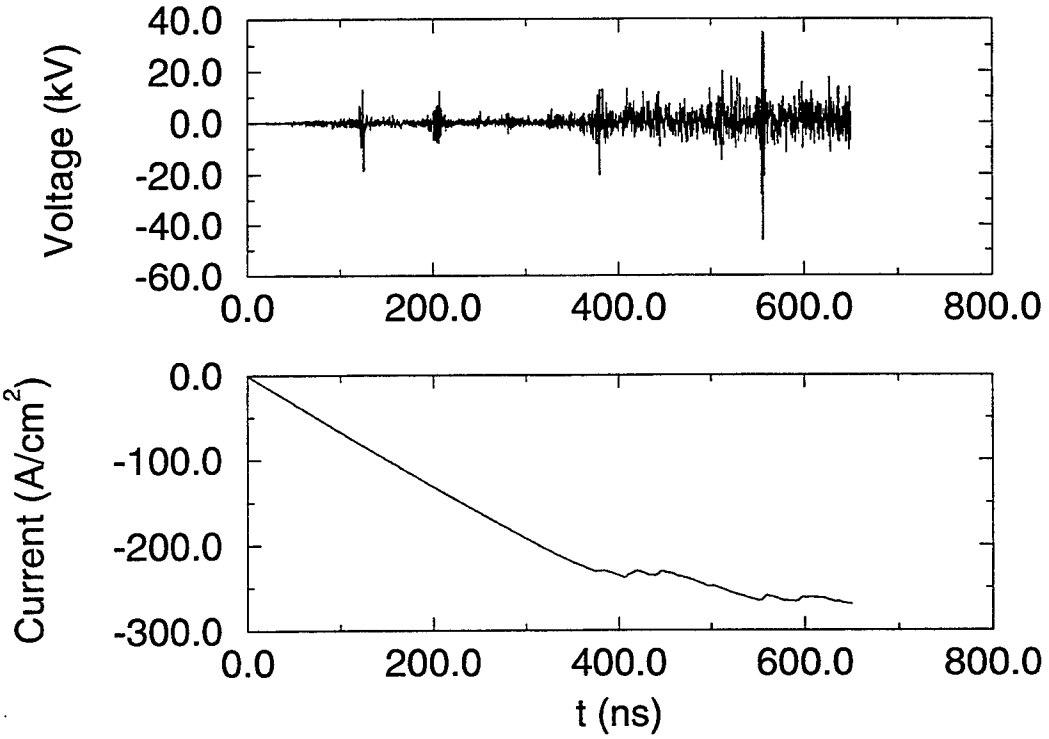

Figure 4-16. Voltage and current vs. time for parameters in Table 4-4 and ion (H^+) energy of 352 eV (IVORY run 39).

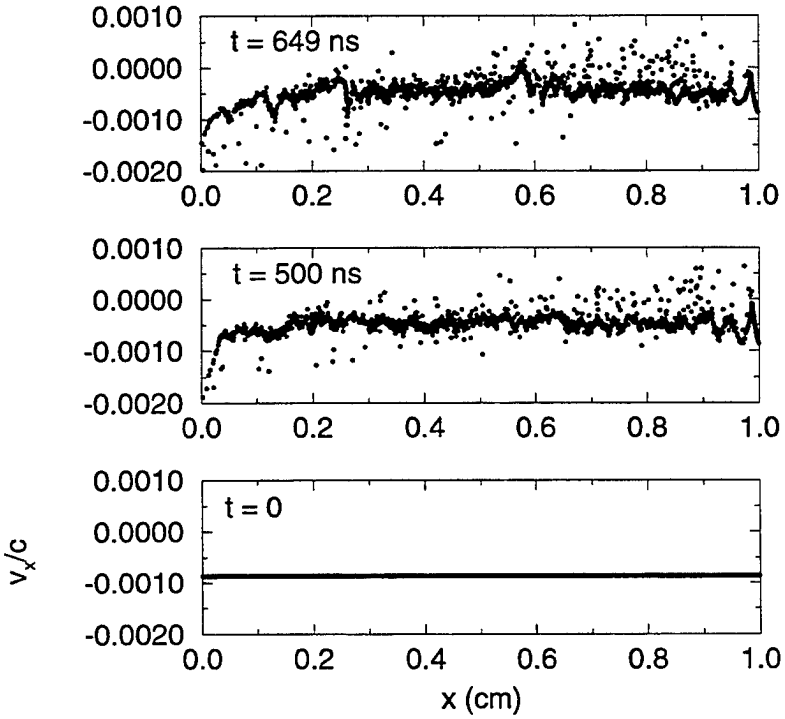

Figure 4-17. Longitudinal phase space of ions at three successive times for simulation in Figure 16 (IVORY run 39).

If the capacitor voltage is raised to 5 kV, (vs. 1 kV in the above simulations), then the electron current drawn exceeds that given by Equation 4.6, and the current has large oscillations about that value, as shown in Figure 4-18.

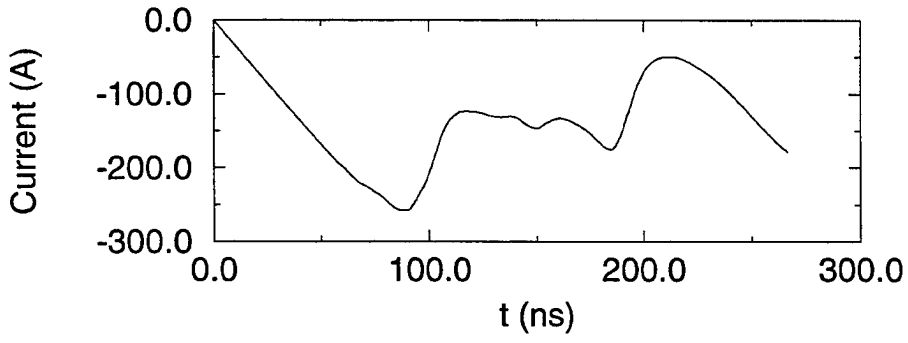

Figure 4-18. Current vs. time for simulation with bank voltage of 5 kV. Other parameters as in Table 4 (IVORY run 34).

If the voltage is raised to the 30 kV used in most of the DCOS experiments, then the initial plasma is essentially completely depleted by the end of the low-impedance phase, and the gap must refill with new plasma before significant current can flow again.

4.2.5.2 High Impedance Regime. The plasma potential generated by the two-stream instability can be estimated from the published expressions for the two-stream saturation amplitude. This can be used to obtain a condition analogous to Equation 4.5 for the two-stream unstable regime.

The energy lost by the beam is equipartitioned between field energy and oscillation energy of the background plasma. For the latter, we have an energy density of[4]

$$E_p \approx 0.2 S n_b \gamma_b m_c^2 \tag{4.7}$$

where n_b is the beam density, n_e is the background plasma density, and $S = \beta_b^2 \gamma_b (n_b/2n_e)^{1/3}$ is the "strength parameter" of Thode and Sudan. We equate this deposited energy to the thermal energy of the plasma to get a temperature

$$\frac{1}{2} n_e kT_{eff} \quad E_p \,, \tag{4.8}$$

and use this to get a rough estimate of the floating potential of the plasma:

$$\phi_{sheath} \approx kT_{eff} \tag{4.9}$$

The criterion for the injected ion energy to exceed ϕ_{sheath} is

$$E_i \equiv \frac{1}{2} M v_i^2 > 0.64 \left(\frac{n_b}{n_e}\right)^{4/3} V_{AK} \tag{4.10}$$

where V_{AK} is the AK potential (which is assumed to be equal to the beam energy in the plasma). If we assume $n_e \approx n_i$, then this can be written

$$\frac{j_b}{j_i} < 1.25 \left(\frac{n_b}{n_i}\right)^{1/3} \sqrt{\frac{M}{m}} \tag{4.11}$$

A general expression for j_b/j_i in a bipolar sheath which takes the injected ion energy E_i into account is[14]:

$$\frac{j_b}{j_i} = \sqrt{\frac{M}{m}} \frac{\sqrt{V_{AK} + E_i} - \sqrt{E_i}}{\sqrt{V_{AK}}} \qquad (4.12)$$

Note that for fixed AK voltage and ion energy, the condition Equation 4.10 is independent of ion density, since the beam and plasma electron densities scale with j_i, keeping the ratio n_b/n_e fixed. This means that if self-opening can be prevented for particular V_{AK} and E_i, then higher electron current can be obtained by increasing the injected ion density.

In Figure 4-19(a), we graph the condition Equation 4.10 vs. ion energy ($n_e \approx n_i$ was not assumed in these plots). Figure 4-19(b) shows the corresponding j_b/j_i ratio from Equation 4.11. We see that lower AK voltages and higher ion energies are favorable, and both of these push one towards lower j_b/j_i ratios.

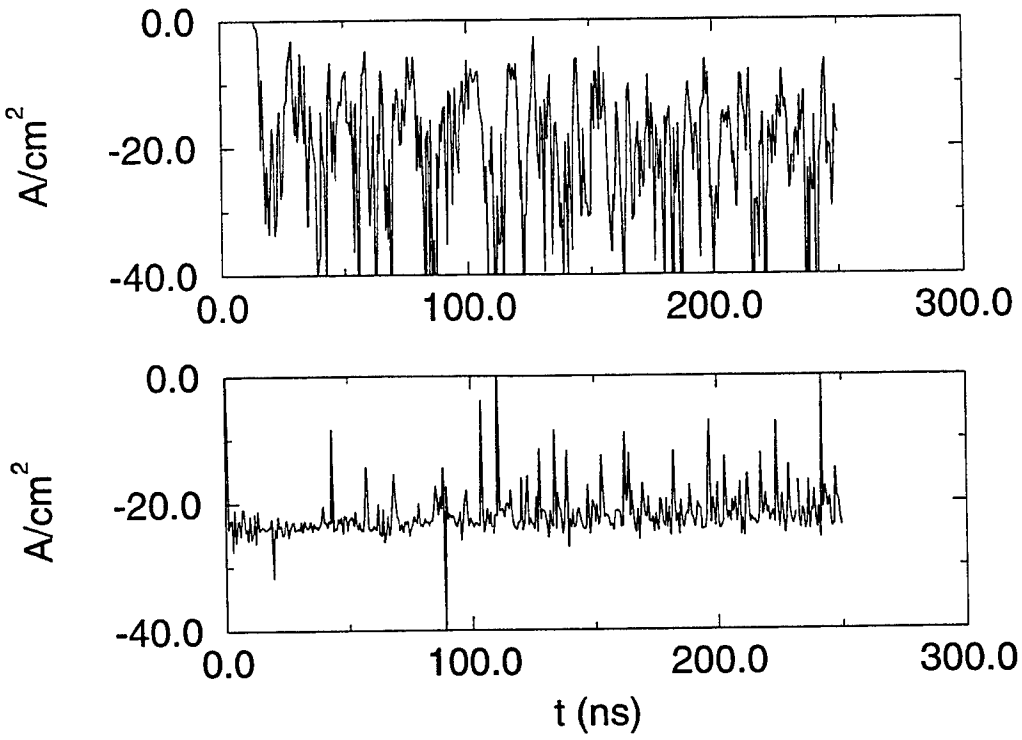

Figure 4-19. Plot shows effect of ion energy E_i on the ratios (a) f_{sheath}/E_i and (b) j_b/j_i. Avoidance of self-opening requires $f_{sheath}/E_i < 1$.

For a simulation which obeys Equation 4.10 we chose an injected ion energy of 2 keV, and an applied (constant) voltage of 2.5 kV. Other parameters are in Table 4-5. For these parameters, the thermal sheath is estimated to have an amplitude of about 0.93 kV. The results in Figure 4-20 show that the ion current at the injection point is relatively constant, indicating, in agreement with the prediction, that the thermal sheath potential is lower than the ion energy. However, ion current reaching the cathode is strongly modulated by the fields in the plasma. The ion current variations are reflected in the conduction current, as shown in Figure 4-21. The ratio of conduction current to ion current is about 20, consistent with Figure 4-19. The results show that avoiding shutoff of the injected ion current does not by itself guarantee a steady conduction current.

Table 4-5. Parameters for high energy ion injection in Figures 4-20, and 4-21.

Injected plasma density	2.4×10^{12} cm^{-3} ($H^+ + e$)
Injected ion velocity	62 cm/μsec (2 keV)
Injected ion current density	23.8 A/cm^2
AK gap length	1 cm
Cathode SCL emission	On
Anode SCL emission	On

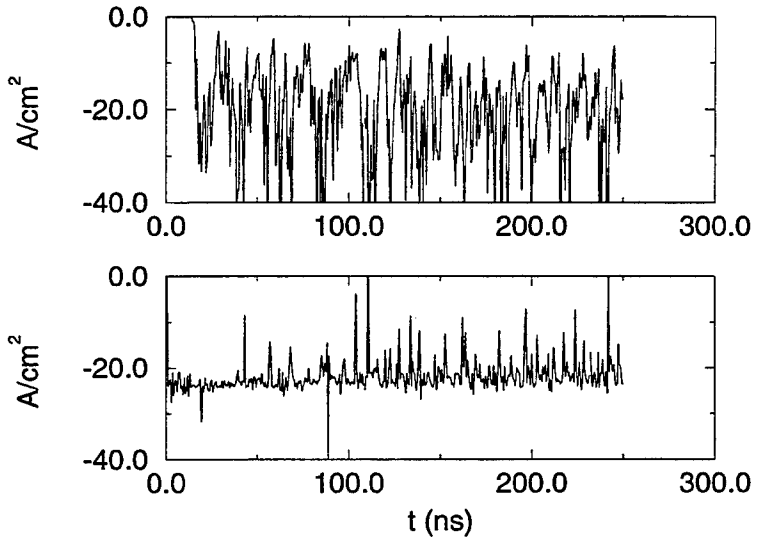

Figure 4-20. Ion current density versus time for 2 keV injection energy (a) near cathode and (b) near injection point (anode). Parameters in Table 4-5 (IVORY run 55).

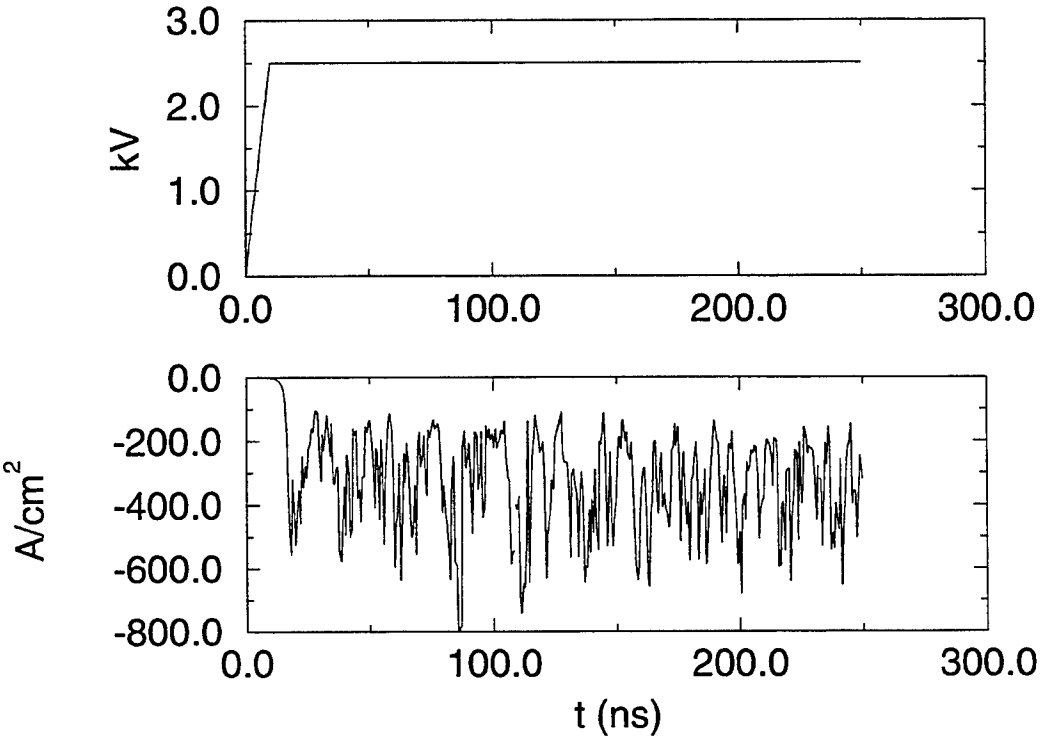

Figure 4-21. Voltage and total current density versus time for 2 keV ion injection. Parameters in Table 4-5 (IVORY run 55).

4.3 2-D ELECTROMAGNETIC SIMULATIONS.

A limited number of 2-D simulations were carried out as a check on the 1-D results, and to look at intrinsically 2-D effects. Because the DCOS opens on the ion motion timescale, but essential physics happens on the time scale of electron oscillations, even 1-D simulations are quite time-consuming. The 2-D simulations are electromagnetic, which further slows them because the time step is then determined by the electromagnetic Courant condition $\Delta t < \Delta x / \sqrt{2c}$, where Δx is the mesh size. To partially offset this, we used a coarser mesh in 2-D. Also, since the simulation particles are relatively slow-moving compared to c, we subcycle on the field-solver, i.e., the fields are advanced several steps for every particle step.

The setup for the 2-D simulations is shown in Figure 4-22. A capacitor discharges into a short transmission line which is connected to the top of the radial line in Figure 4-22. As in 1-D, plasma is injected from the right and electrons are emitted from a space-charge-limited region on the left conductor.

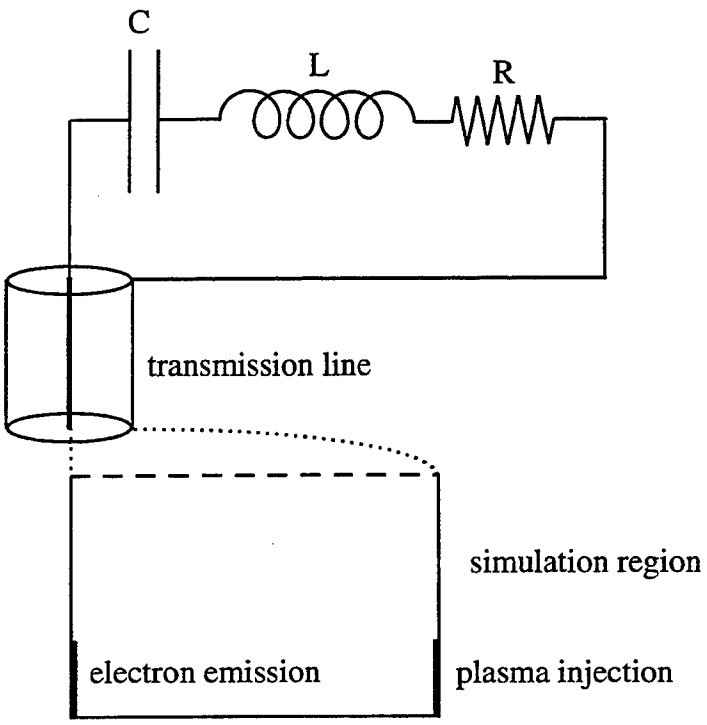

Figure 4-22. Schematic of setup for 2-D simulations.

4.3.1 Low Impedance Regime.

To simulate the low impedance regime where the gap is initially filled with plasma, we used the parameters in Table 4-1, except that the AK gap was 2 cm and the "wall" radius (the boundary where the simulation region connects to the radial transmission line in Figure 4-22) was 3 cm. The current and voltage are plotted on top of the 1-D results (also for a 2 cm gap) in Figure 4-23. The low-impedance phase is about 20 nsec in each case, after which the voltage rises sharply. At this point the 1-D and 2-D results deviate. The spatial resolution of the 2-D run is about 10 times lower than the 1-D run, and we believe that numerical instabilities cause the 2-D run to fail as the voltage rises. For both 2-D and 1-D, the current rises to a value several times larger than measured in the low-density experiments.

4.3.2 Effect Of High Density On Radial Current Profile.

Initially, we tried unsuccessfully to simulate a higher density plasma, 4.8×10^{12} cm^{-3}, with the same grid resolution used to do low-density 2-D simulations, viz. 0.025 x 0.025 cm cells. These simulations exhibited rapid numerical heating which we believe is caused by an "aliasing" instability which has a peak growth rate when the cell size is

about 10 times larger than the plasma Debye length[15]. To avoid this instability it is necessary to increase the resolution, with a consequent increase in running time.

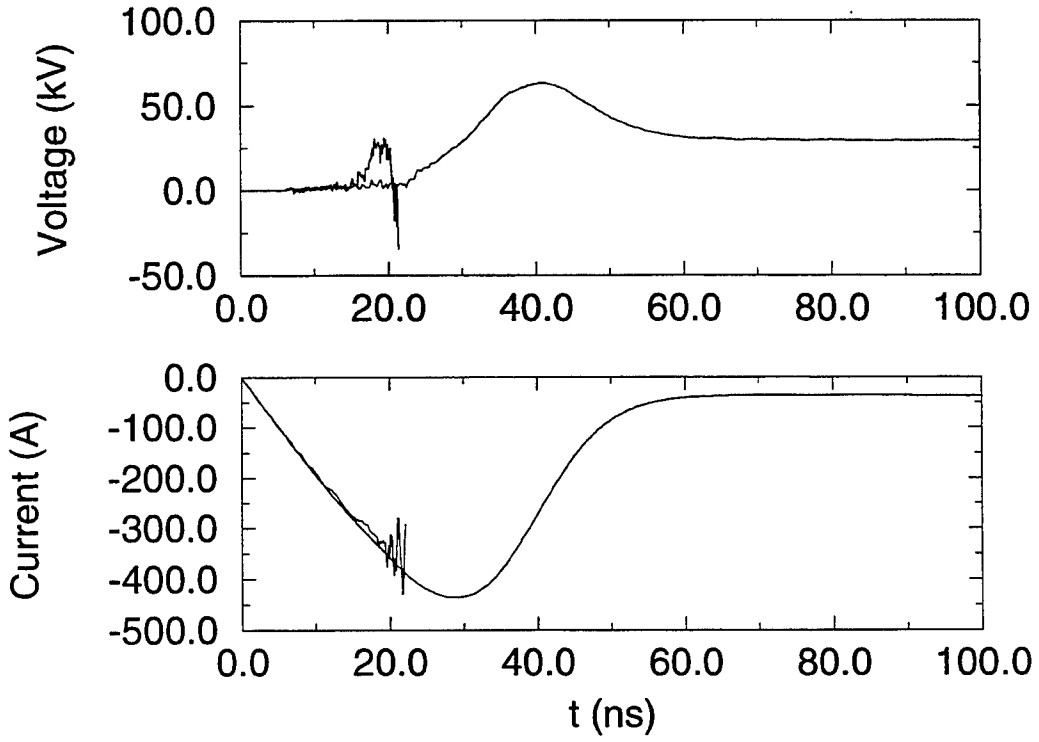

Figure 4-23. Voltage and current versus time for 2-D and 1-D simulation of low-density plasma (IVORY runs 56 and 3b).

A high-resolution (0.004 x 0.004 cm cells) 2-D simulation of the early development of a 4.8 x 10^{12} cm^{-3} plasma is shown in Figure 4-24. With an injection velocity of 10 cm/μsec, this corresponds to a current density of 7.8 A/cm^2. The AK gap of 1 cm is completely filled here, so the plasma enters a low-impedance phase, as in Figure 23. The external circuit is as in Table 4-2. Because of computer time limitations, we were only able to run the simulation to about 6 nsec. For this plasma, c/ω_p ~ 0.25 cm, and we were interested in observing what radial current density profile develops. We find that the cathode emits all across its surface, and generates a hollow current density profile, shown in Figure 4-25. Some gated photographs show what appears to be a hollow light-emitting cylinder of about the plasma radius. This may be related to the formation of a hollow density profile.

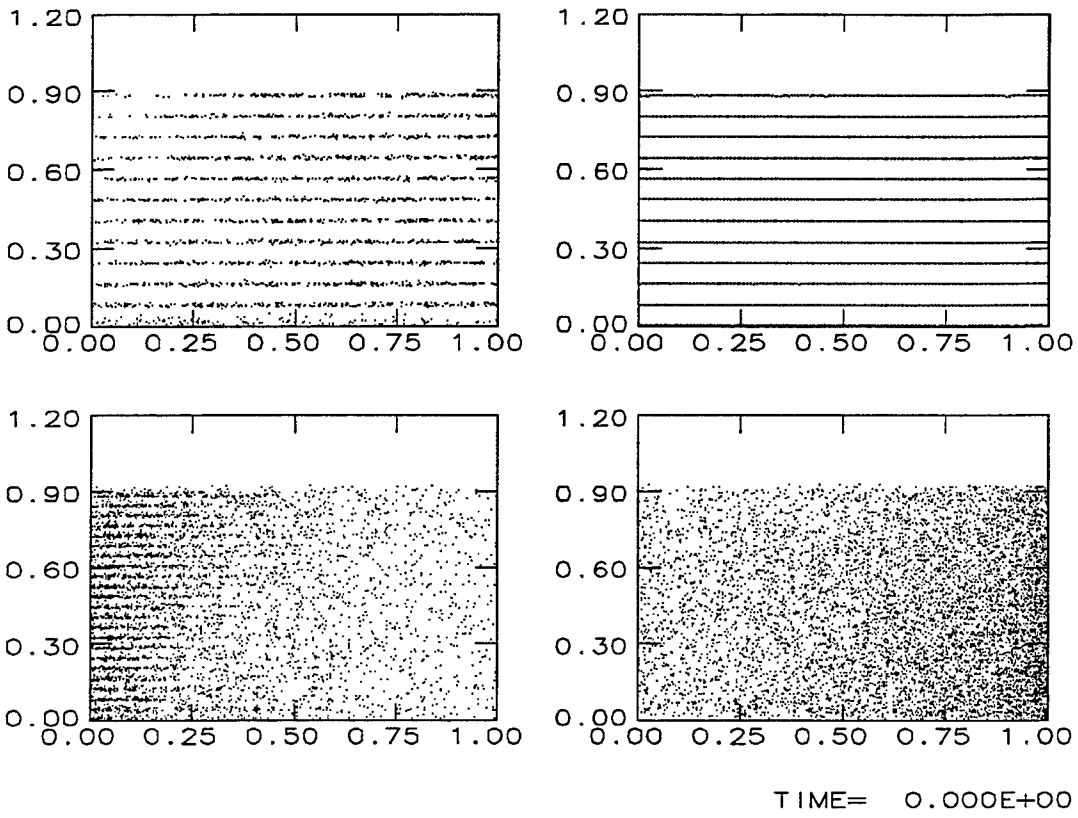

Figure 4-24. Spatial particle plots at t = 4.5 ns of (a) preloaded electrons, (b) preloaded ions, (c) cathode-emitted electrons, (d) anode-emitted electrons for dense plasma simulations (IVORY run 74).

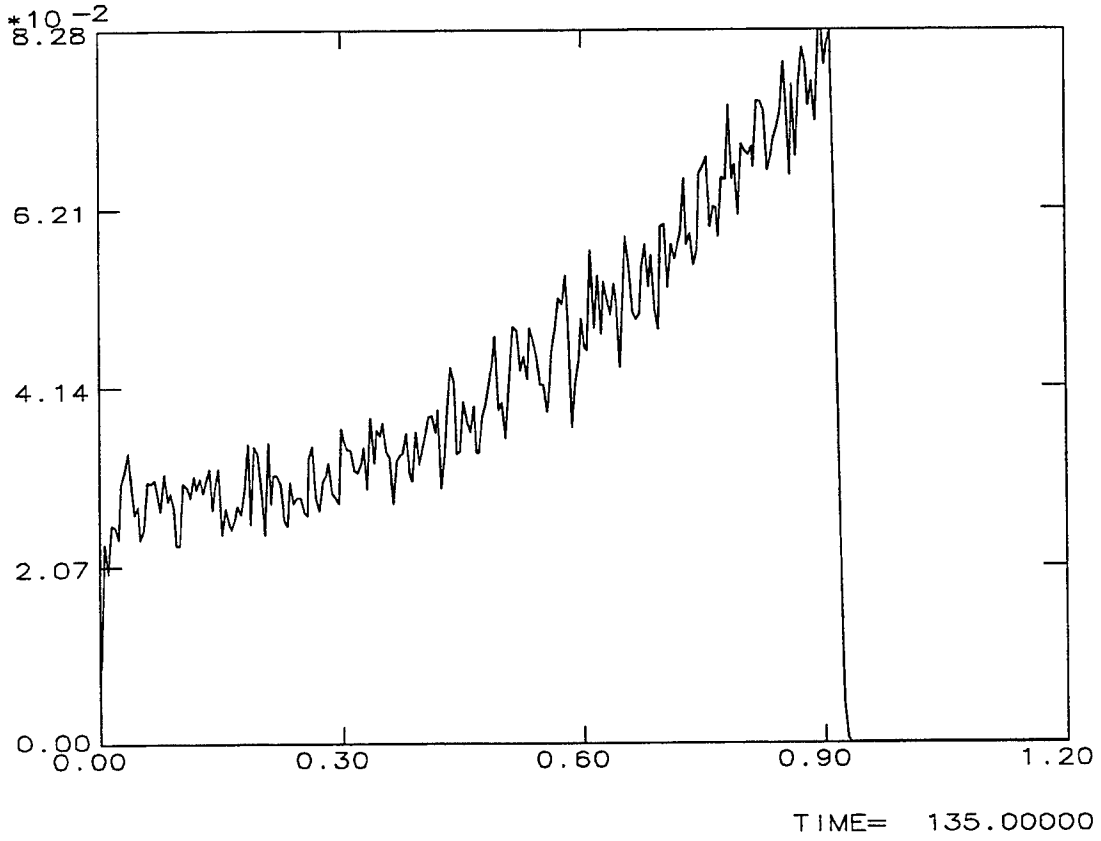

Figure 4-25. Radial current density profile at t = 4.5 ns for dense plasma simulation in Figure 4-24. Units are normalized code units; total current at this time is ~ 400 A (IVORY run 74).

4.3.3 High Impedance Regime.

To initialize two-stream simulations of the two-stream unstable ("high impedance") regime, the AK gap is prefilled with plasma, leaving a gap of 1.25 cm (the bipolar sheath thickness). An axial magnetic field of about 2 kG is applied. The simulation in Figure 4-26 is for the same parameters as the 1-D simulation in Figure 4-11. We see that the peak electron current is more than a factor of two lower than the 1-D case. The two-stream instability strength may be reduced due to the fact that its wavelength (about 1.8 cm) is of the order of the plasma column radius (1.27 cm), so that the fields caused by beam bunching are not purely longitudinal. In addition, there is considerable radial motion of the ions in the bipolar sheath (see Figure 4-27(a)) which reduces the ion space-charge density in the sheath, and thence the space-charge-limited electron current density.

Qualitatively, the behavior of the 2-D case is similar to 1-D. The electron beam phase space in Figure 4-27(d) shows the same coherent bunching as the 1-D simulations.

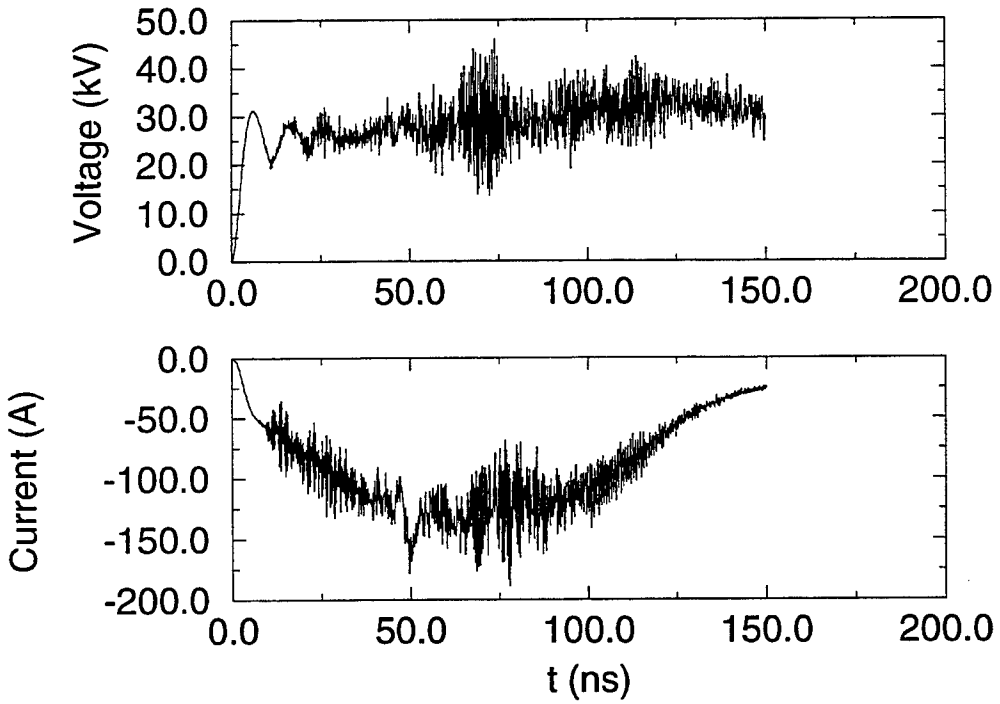

Figure 4-26. Voltage and current obtained from 2-D simulation of low-density parameters, cf Figure 4-11 (IVORY run 65).

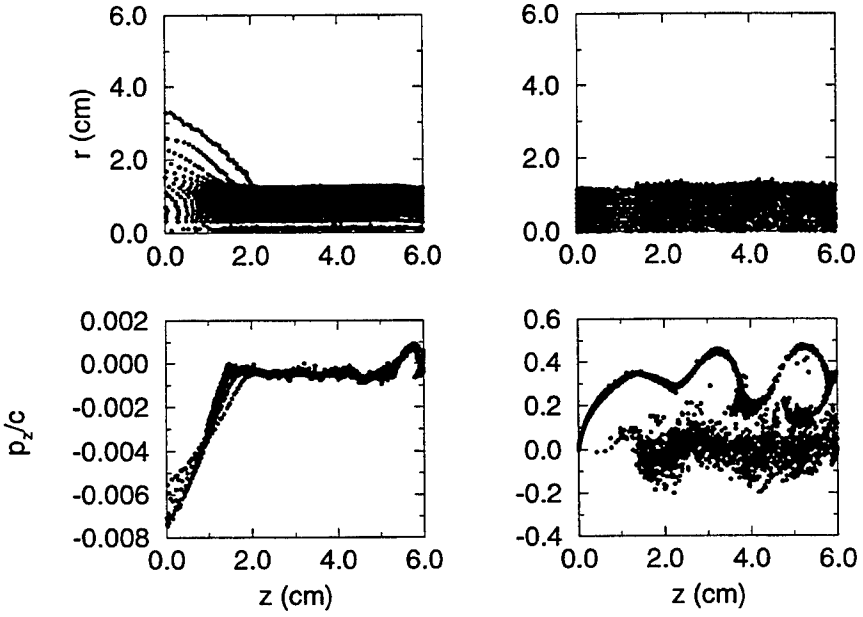

Figure 4-27. Particle plots for ions (a,c) and electrons (b,d) near t = 27 ns in Figure 4-26. Top plots show spatial (r-z) positions, bottom plots show longitudinal phase space (IVORY run 65).

4.3.4 Effect Of Magnetic Mirror Field.

The electron loss which leads to charging of the plasma could potentially be inhibited by a magnetic mirror field. We tried one case where the magnetic field increased by a factor of two, from 1.3 kG at the cathode to 2.6 kG at the anode. We compare this with results for a flat 2 kG field in Figure 4-28. In these simulations, the ion beam current density was 0.6 A/cm^2, the plasma density was 3.8 x 10^{11} cm^{-3}, and the AK gap was 6 cm. We see that there is little difference in the current traces between the two runs. This is probably because most heating occurs towards the anode, and particles heated there see a mirror ratio $B(z)/B_{max}$ which is close to unity.

4.3.5 Effect of Increased Emission Region.

The radial expansion of ions noted in Figure 4-27(a) may lead to cathode turn-on outside the region initially struck by the plasma coming through the anode aperture. This effect is modeled in the simulation shown in Figure 4-29. As the ions expand, we allow the area which they strike to start emitting electrons. These electrons cross the AK gap on the 2 kG field lines and strike the anode, where we in turn allow ion emission. These emission regions outside the plasma column contribute ~ 50% of the

total current (cf Figures 4-26 and 4-30). As seen from the voltage and current plots in Figure 4-30, there is no significant effect on the opening of the switch caused by plasma heating.

(a) Mirror Magnetic

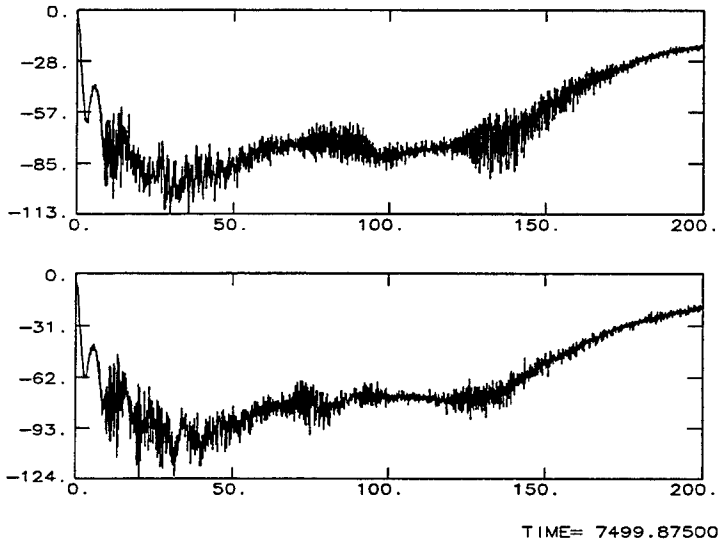

(b) Flat Magnetic Field

Figure 4-28. Current versus time for 2-D simulation.

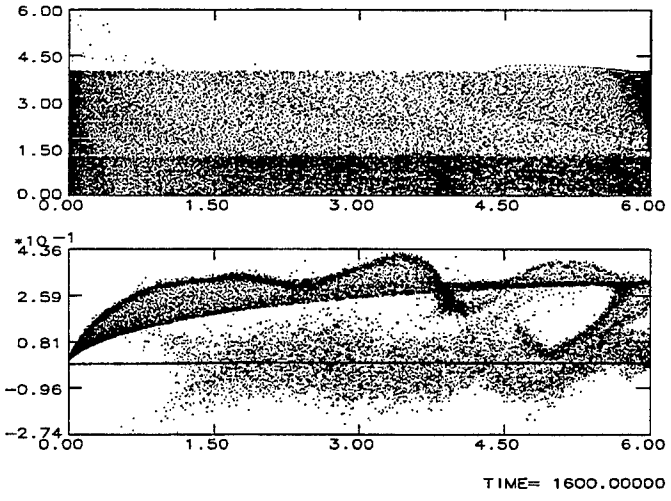

Figure 4-29. Particle plots of (a) spatial (r-z) positions and (b) longitudinal phase-space near t = 53 ns for ions and electrons for case where emission outside channel is allowed (IVORY run 70).

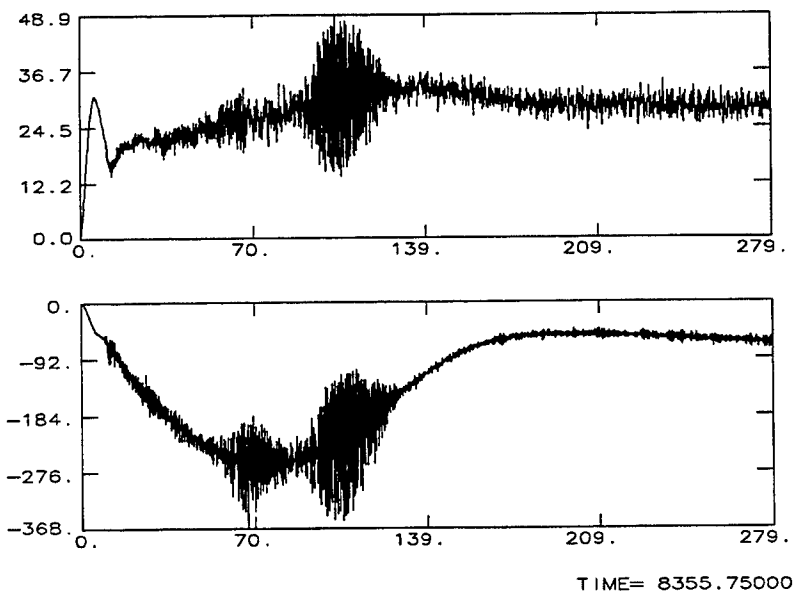

Figure 4-30. Voltage and current for simulation in Figure 4-29 (IVORY run 70).

4.4. ANALYTIC THEORY OF THE PLASMA-FILLED DIODE.

4.4.1 Space-Charge Limited Electron Beam with Immobile Ions.

Kares[1] recently carried out a series of 1-D particle-in-cell (PIC) simulations to study the operating characteristics of a plasma-filled, cold-cathode planar diode (PFD). For the case of space-charge-limited (SCL) electron emission from the cathode, this work revealed a variety of phenomena not included in the standard bipolar erosion model. PFD simulations with a spatially uniform background of immobile ions were typically characterized by a low voltage conduction phase (with length determined primarily by the ion density), followed by an opening phase in which a large diode voltage develops. Dynamics of the beam-plasma interaction initially give rise to a series of small potential humps in the diode gap. Trapping of some fraction of electron current emitted from the cathode occurs primarily at the right hand side of the hump nearest the cathode. As the beam current and the trapping fraction increase during the conduction phase, the potential hump continues to grow in magnitude, and the position of the potential maximum moves steadily away from the cathode. Eventually, the potential hump nearest the cathode spans the full width of the gap, and the opening phase of PFD operation begins with a significant voltage developing across the diode in time.

In an effort to better understand the dynamics of the conduction and opening phases of PFD operation, Kares et al.[13] developed an analytic theory presented in a companion paper to Reference 1. This theory considers the time-independent problem of an SCL electron beam in a fixed, spatially uniform background of positive charge (the immobile ion limit). In addition, it explicitly includes the space-charge contribution due to the trapped electrons, following a treatment of the reflex triode problem developed by Creedon et al.[12,17] This treatment assumes that at each instant of time the system may be treated as if it is in a steady-state, and that once an electron is trapped it reflexes back and forth inside the potential hump with constant energy. Therefore, a potential $\phi(x)$ is accessible to a trapped electron with total energy E if

$$\frac{1}{2}mv^2 = E + e\phi(x) \geq 0 \tag{4.13}$$

These assumptions lead to the following expression for the density of trapped electrons at $\phi(x)$:

$$n_t = 2\int_{-e\phi}^{0} \frac{df}{dE}\left[\frac{2}{m}(E+e\phi)\right]^{-\frac{1}{2}} dE \tag{4.14}$$

where the factor of two in front of the integral accounts for required balance between the negative- and positive-going flux in steady-state. In Equation 4.14, df/dE is the energy spectrum of the trapped electrons at $x = x_m$ (the position of the maximum of the potential hump ϕ_m), and is determined by the details of the trapping process. Below we consider two possible shapes for the spectral distribution and discuss their effect on agreement between the analytic theory and the PFD simulations.

Energy and current conservation yield the usual expression for the density of beam electrons (current density j_b):

$$n_b = \left(\frac{j_b}{e}\right)\left(\frac{m}{2e}\right)^{1/2} \phi^{-1/2} \tag{4.15}$$

Substituting from Equations 4.14 and 4.15 into Poisson's equation gives

$$\frac{\partial^2\phi}{\partial x^2} = \left(\frac{j_b}{\varepsilon_o}\right)\left(\frac{m}{2e}\right)^{1/2} \phi^{-1/2} - \frac{n_i e}{\varepsilon_o} + \frac{2e}{\varepsilon_o}\left(\frac{m}{2}\right)^{1/2} \int_{-e\phi}^{0} (E+e\phi)^{-1/2} \frac{df}{dE} dE \tag{4.16}$$

where n_i is the spatially uniform background ion density. In order to proceed further, we assume a spectral distribution of the form

$$\frac{df}{dE} = C\left(\frac{-E}{e\phi_m}\right)^n \tag{4.17}$$

with the proportionality constant C determined by the normalization condition

$$\int_{-e\phi_m}^{0} \frac{df}{dE}\, dE = f_t \frac{j_b}{e} \tag{4.18}$$

where f_t is the fraction of the total electron current that is trapped. One integration of Equation 4.16 together with the boundary conditions df/dx = 0 at both $x = 0$ and $x = x_m$ yields

$$\left[\frac{2en_i}{\varepsilon_o\phi_m(1+\gamma)}\right]^{\frac{1}{2}} x = \int_0^{\psi} \frac{du}{F(u)} \tag{4.19}$$

with

$$\phi_m = \left(\frac{2m}{e}\right)\left(\frac{j_b}{en_i}\right)^2 (1+\gamma)^2 \tag{4.20}$$

$$F(u) = \left[u^{1/2} - (1+\gamma)u + \gamma u^{n+\frac{3}{2}}\right]^{\frac{1}{2}} \tag{4.21}$$

where we have introduced the normalized potential $\psi = \phi/\phi_m$. The constant γ in Equations 4.19 to 4.21 is proportional to the trapping fraction f_t with constant of proportionality dependent on the choice of n in Equation 4.17. Equation 4.19 is an implicit relation for $\psi(x)$ which depends on the parameters j_b (electron current), n_i (ion density), and f_t (trapping fraction). If we set $x = x_m$ and $\psi = 1$ in Equation 4.19 it becomes a relation for the half-width of the potential hump as a function of these same parameters.

In Reference 13, a flat spectral distribution for the trapped electrons (n = 0 in Equation 4.17) was chosen primarily for analytical simplicity. This choice results in

$$\gamma = \frac{4}{3} f_t \tag{4.22}$$

and the following expression for the trapped electron density at $x = x_m$:

$$n_t(x_m) = \frac{3}{2}\frac{\gamma}{2(1+\gamma)} n_i \quad . \tag{4.23}$$

If we use the electron current and the trapping fraction as a function of time from the PFD simulation, Equation 4.19 can provide a prediction from the analytic theory for the position of the potential hump as a function of time. The result of such an exercise is plotted in Figure 4-6 of Reference 13. Using a flat spectral distribution of trapped electrons gives qualitative agreement between the analytic theory and simulation for the expansion of the potential hump, but falls substantially short of providing what might be called "close" quantitative agreement.

Improvement of the analytic theory can be accomplished by considering a more realistic spectral distribution. Kares[13] points out that the actual trapped electron distribution observed in the simulation is peaked at its lower energy end at E = $-e\phi_m$ (zero kinetic energy) and falls off with increasing E. The simplest distribution which has this property is obtained by using n = 1 in Equation 4.17 (see also Ref. 12). Assumption of this linear distribution results in

$$\gamma = \frac{16}{15} f_t \tag{4.24}$$

and

$$n_t(x_m) = \frac{5}{2}\frac{\gamma}{2(1+\gamma)} n_i \tag{4.25}$$

From Figure 4-6 of Reference 13, we see that the peak value of the trapping fraction is $f_t \simeq 0.3$, which, using Equation 4.24, gives a γ value of 0.32. Returning to Equation 4.19 (using n = 1) with this value of γ, we now predict a value of $x_m/\Delta x$ of approximately 65, much closer to the value observed in the simulation. We conclude that the analytic theory, modified to include a trapped electron spectral distribution which more closely resembles that observed in the simulations, provides excellent agreement for the observed expansion of the potential hump as a function of time.

4.4.2 Space-Charge Limited Electron Beam with Mobile Ions and Reflexing Electrons at the Anode

In Section 4.2.4.4 we showed 1-D PIC simulations in which reflexing of electrons at the anode was used to inhibit the loss of hot electrons from the diode gap. Some insight into the results of these simulations can be gained by considering the analytic theory of the reflex triode developed by Creedon, et al.[12,17] We generalize this theory to include ions injected at the anode with kinetic energy $E_i = eV_i$. We again assume SCL electron emission and trapped electrons characterized by a family of spectral distributions given by Equation 4.17. Under these assumptions, Poisson's equation becomes

$$\frac{\partial^2 \phi}{\partial x^2} = \left(\frac{j_b}{\varepsilon_o}\right)\left(\frac{m}{2e}\right)^{1/2} \phi^{-1/2} - \left(\frac{j_i}{\varepsilon_o}\right)\left(\frac{M}{2e}\right)^{1/2} (V_i + \phi_m - \phi)^{-1/2} \qquad (4.26)$$
$$+ \frac{2e}{\varepsilon_o}\left(\frac{m}{2}\right)^{1/2} \int_{-e\phi}^{0} (E + e\phi)^{-1/2} \frac{df}{dE} dE$$

where ϕ_m is the value of the potential at the anode (applied potential). The second term on the RHS of Equation 4.26 is the ion density, and the third term is the trapped electron density due to reflexing at the anode. Again taking $\partial\phi/\partial x = 0$ at the cathode ($x = 0$), one integration of Equation 4.26 leads to (with $\psi = \phi/\phi_m$ as before)

$$\frac{x}{d} = -\frac{3}{4}\left(\frac{j_b}{j_o}\right)^{-1/2} \int_o^{\psi} \frac{du}{G(u)} \qquad (4.27)$$

where

$$G(u) = \left\{ u^{1/2} - \alpha\left[\left(\frac{V_i}{\phi_m} + 1\right)^{1/2} - \left(\frac{V_i}{\phi_m} + 1 - u\right)^{1/2}\right] + \gamma u^{n+\frac{3}{2}} \right\}^{1/2} \qquad (4.28)$$

where j_o is the Child-Langmuir current density,

$$\alpha = \left(\frac{j_i}{j_b}\right)\left(\frac{M}{m}\right)^{1/2} \qquad (4.29)$$

and d is the width of the diode gap. γ again depends on the choice of spectral distribution for the trapped electrons (choice of n in Equation 4.17). We see that $V_i = 0$ (ions emitted from the anode with zero velocity) corresponds to the limit considered by Creedon et al. (see Equation 4.11 of Ref. 17). Finally, $V_i \rightarrow \infty$ in Equation 4.28 gives the immobile ion limit considered in the previous section (constant ion density).

Equation 4.27 is an implicit relation for the potential in the diode gap as a function of distance from the cathode x. For the case in which the ion current is also space-charge limited, the parameter α is given by

$$\alpha = \frac{(1+\gamma)}{\left[\left(\frac{V_i}{\phi_m} + 1\right)^{1/2} - \left(\frac{V_i}{\phi_m}\right)^{1/2}\right]} \qquad (4.30)$$

We use this assumption in the sample calculations presented below. Figure 4-31 displays the results of three calculations of the potential distribution in the diode gap, corresponding to three different assumptions for the trapped electron spectral distribution: n = 0 in Equation 4.17 gives a flat spectral distribution; n = 2 a quadratic dependence on energy peaked at E = $-e\phi_m$ (or zero kinetic energy); n = 4 a quartic dependence more strongly peaked at zero kinetic energy. Increasing the value of n in Equation 4.17 decreases the effective temperature of the trapped electron distribution. Each curve corresponds to 30 kV applied across a 3 cm gap, H^+ ions injected with a velocity of approximately 13 cm/μsec, and an ion current density of 5 A/cm^2. The corresponding electron current densities are 16, 74, and 99 A/cm^2 for the n = 0, 2 and 4 cases respectively. In each case, the trapped electrons account for nearly 70% of the total electron density in the region of flat potential near the center of the diode. Note that the ratio of electron to ion current density is always smaller than the bipolar ratio $\sqrt{M/m}$ = 43. Furthermore, the "hotter" the trapped electron distribution (i.e. the lower the value of n), the lower the ratio of electron to ion current. Note also that as n decreases, a smaller fraction of the total potential drop occurs in the sheath at the cathode.

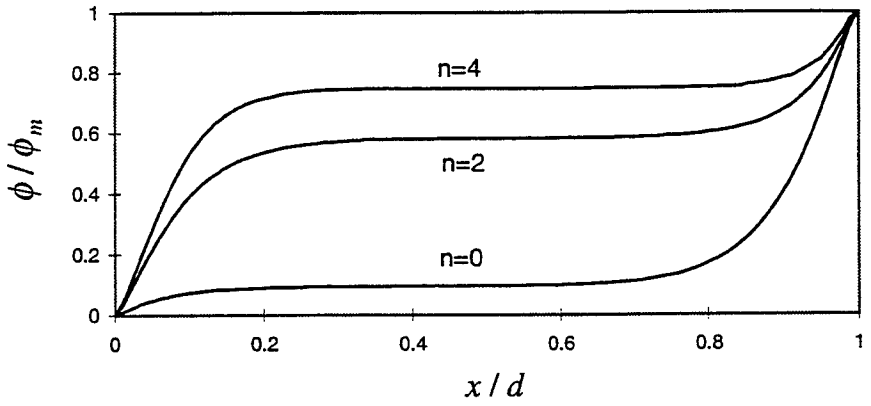

Figure 4-31. Potential distributions from Eq. 27 with flat (n = 0), quadratic (n = 2), and quartic (n = 4) spectral distributions for trapped electrons.

SECTION 5

REFERENCES

1. R.J. Kares, "One-Dimensional Particle-in-Cell Simulations of Sheath Erosion in a Plasma-Filled Diode", J. Appl. Phys. 71, 2155 (1992). (U)

2. W.S. Lawson, "Computer Simulation of Bounded Plasma Systems", UCB/ERL M87/14, U.C. Berkeley, 1987. (U)

3. J.J. Ambrosiano and J.L. Geary, "A One-Dimensional PIC-Circuit Code for Simulating a Reflex Triode", Comp. Phys. Comm. 67, 210 (1991). (U)

4. J.P. Lidestri, "Data Collection of PSI Plasma Opening Switch Experiments, 1/22/93-4/28/93", Pulse Sciences, Inc. (U)

5. L.E. Thode and R.N. Sudan, "Two-Stream Heating of Plasmas by Relativistic Electron Beams", Phys. Rev. Lett. 30, 732 (1973). (U)

6. R.J. Briggs, in Advances In Plasma Physics, edited by A. Simon and W.B. Thompson (Interscience, NY, 1971). (U)

7. D. Welch, private communication.

8. B.N. Breizman and D.D. Ryutov, Sov. Phys. JETP 30, 759 (1970); Nucl. Fusion 14, 873 (1974). (U)

9. G. Schmidt, Phys. Rev. Lett. 33, 287 (1974). (U)

10. M.E. Jones and M.A. Mostrom, "The Effects of Plasma Density Gradients on the Beam Plasma Instability", Bull. Am. Phys. Soc. 27, 982 (1982). (U)

11. S. Humphries, J.J. Lee and R.N. Sudan, "Generation of Intense Pulsed Ion Beams", Appl. Phys. Lett. 25, 20 (1974). (U)

12. J.M. Creedon, I.D. Smith, and D.S. Prono, "Method of Generating Very Intense Positive-Ion Beams", Phys. Rev. Lett. 35, 91 (1975). (U)

13. R.J. Kares, J.L. Geary, and J.M. Grossmann, "A New Theory of the Plasma-Filled Diode", J. Appl. Phys. 71, 2168 (1992). (U)

14. J.M. Grossmann, S.B. Swanekamp, and P.F. Ottinger, Phys. Fluids B4, 44 (1992). (U)

15. J.A. Byers, "Noise Suppression Techniques in Macroparticle Models of Collisionless Plasmas", Proc. of Fourth Conference on Numerical Simulation of Plasmas, J.P. Boris and R.A. Shanny, eds., Naval Research Laboratory, 1971, p. 496. (U)

16. H. Okuda, "Nonphysical Instabilities in Plasma Simulations Due to Small λ_D/Dx, ibid, p. 511. (U)

17. D.S. Prono, J.M. Creedon, I. Smith, and N. Bergstrom, J. Appl. Phys. 46, 3310 (1975). (U)

DISTRIBUTION LIST

DEPARTMENT OF DEFENSE

DEFENSE TECHNICAL INFORMATION CENTER
8725 JOHN J KINGMAN RD., STE 0944
FORT BELVOIR, VA 22060-6218
ATTN: DTIC/OCP

DEFENSE THREAT REDUCTION AGENCY
45045 AVIATION DRIVE
DULLES, VA 20166-7517
ATTN: NSSA, W SUMMA
ATTN: NSSS, K WARE
ATTN: NSSS, R GULLICKSON
ATTN: NSSS, R SCHNEIDER
ATTN: TRC

DEFENSE THREAT REDUCTION AGENCY
ALBUQUERQUE OPERATIONS
1680 TEXAS ST. SE
KIRTLAND AFB, NM 87117-5669
ATTN: SWP, G BALADI

DEPARTMENT OF DEFENSE CONTRACTORS

BERKELEY RSCH ASSOCIATES, INC.
P O BOX 241
BERKELEY, CA 94701-0241
ATTN: R KARES
ATTN: S BRECHT

ENERGY COMPRESSION RESEARCH CORP
6355 NANCY RIDGE DRIVE
SAN DIEGO, CA 92121
ATTN: D S WEIN

FORD MOTOR COMPANY CORPORATION
4800 EAST RIVER ROAD
MINNEAPOLIS, MN 55421
ATTN: M MOSBROOKER

GA TECHNOLOGIES, INC.
P O BOX 85608
SAN DIEGO, CA 92138-5608
ATTN: DOCUMENT CONTROL

ITT INDUSTRIES
ITT SYSTEMS CORP
ATTN: AODTRA/DASIAC
1680 TEXAS ST SE
KIRTLAND AFB, NM 87117-5669
ATTN: DASIAC
ATTN: DASIAC/DARE

ITT SYSTEMS CORP
2560 HUNTINGTON AVENUE
ALEXANDRIA, VA 22303
ATTN: D MOFFETT

JAYCOR
1410 SPRING HILL ROAD
SUITE 300
MCLEAN, VA 22102
ATTN: DR CYRUS P KNOWLES

LOCKHEED MARTIN VOUGHT SYSTEMS
P O BOX 650003
DALLAS, TX 75265-0003
ATTN: LIBRARY EM-08

LOGICON RDA
2100 WASHINGTON BLVD
ARLINGTON, VA 22204-5706
ATTN: I VITKOVITSKY

MAXWELL TECHNOLOGIES
8888 BALBOA AVE., BLDG. 1
SAN DIEGO, CA 92123
ATTN: WILLIAM H RIX

MINNESOTA MINING &
MANUFACTURING COMPANY
3 M FEDERAL SYSTEMS DEPARTMENT
3 M CENTER BUILDING 224-2S-25
ST. PAUL, MN 55144-1000
ATTN: D REDMOND
ATTN: E HAMPL

MISSION RESEARCH CORP.
P O BOX 542
NEWINGTON, VA 22122-0542
ATTN: B GOPLEN

PRIMEX TECHNOLOGIES, ORDNANCE
& TACTICAL SYSTEM
1840 FAIRWAY DRIVE
P O BOX 2055
SAN LEANDRO, CA 94577-0205
ATTN: C STALLINGS
ATTN: D PRICE
ATTN: P SINCERNY

PULSE SCIENCES, INC.
600 MC CORMICK STREET
SAN LEANDRO, CA 94577
ATTN: JOE LIDESTRI
ATTN: P W SPENCE
ATTN: PHIL GREEN
ATTN: SID PUTNAM
ATTN: TOM GENOINI

DISTRIBUTION LIST

DEPARTMENT OF DEFENSE CONTRACTORS

PULSE SCIENCES, INC.
600 MC CORMICK STREET
SAN LEANDRO, CA 94577
ATTN: TOM HUGHES

TETRA CORP
3701 HAWKINS ST, NE
ALBUQUERQUE, NM 87109
ATTN: W MOENY

TEXAS TECH UNIVERSITY
P O BOX 5404
LUBBOCK, TX 79417
ATTN: DR M KRISTIANSEN

TRW SPACE & DEFENSE SECTOR SPACE &
TECH GROUP OGDEN ENG OPERATIONS
P O BOX 804
CLEARFIELD, UT 84015-0804
ATTN: OUT6/HL DEPT/LIBRARY

UNIVERSAL VOLTRONICS CORP
27 RADIO CIRCLE DRIVE
MT KISCO, NY 10549
ATTN: W CREWSON

UNIVERSITY OF MISSOURI-COLUMBIA
W 1025 ENGINEERING BLDG EAST
COLUMBIA, MO 65211
ATTN: DR W NUNNALLY

W J SCHAFER ASSOCIATES, INC.
1901 NORTH FT MYER DRIVE
SUITE 800
ARLINGTON, VA 22209-1681
ATTN: E ALCARAZ

WESTINGHOUSE STC
1310 BEULAH ROAD
PITTSBURG, PA 15235
ATTN: DR A H COOKSON

DEPARTMENT OF ENERGY

SANDIA NATIONAL LABORATORIES
ATTN: MAIL SERVICES
P O BOX 5800
ALBUQUERQUE, NM 87185-0459
ATTN: J HARRIS/MS 0523
ATTN: J MARTIN/MS 0523
ATTN: M BUTTRAM/MS-1153
ATTN: V HARPER-SLABOSZEWICZ
ATTN: W BEEZHOLD\MS-1155

DEPARTMENT OF THE AIR FORCE

AIR FORCE OFFICE OF SCIENTIFIC RSCH
BLDG 410
BOLLING AFB, DC 20332-6448
ATTN: DR. R. BARKER

AIR WEATHER SERVICE, MAC
DEPARTMENT OF THE AIR FORCE
SCOTT AFB, IL 62225
ATTN: AWS TECH LIBRARY, FL4414

ARNOLD ENGINEERING DEVELOLPMENT CENTER
1099 AVENUE C
ARNOLD AFB, TN 37389-9011
ATTN: MAJ J ROWLEY/DOT

DEPARTMENT OF THE NAVY

NAVAL POSTGRADUATE SCHOOL
411 DYER ROAD
MONTEREY, CA 93943-50002
ATTN: CODE 61SW F SCHWIRZKE

NAVAL RESEARCH LABORATORY
4555 OVERLOOK AVE, SW
WASHINGTON, DC 20375-5000
ATTN: CODE 6700 S OSSAKOW
ATTN: CODE 6750/R MEGER
ATTN: CODE 6770 G COOPERSTEIN
ATTN: CODE 6770/R COMMISSO

NAVAL SURFACE WARFARE CENTER
17320 DAHLGREN ROAD
DAHLGREN, VA 22448-5000
ATTN: CODE B-20

DIRECTORY OF OTHER (LIBRARIES AND UNIVERSITIES)

AUBURN UNIVERSITY
231 LEACH SCIENCE CENTER
AUBURN, AL 36849
ATTN: M ROSE

CALIFORNIA-DAVIS, UNIVERSITY OF
DEPARTMENT OF APPLIED SCIENCES
DAVIS, CA 95616
ATTN: J S DEGROOT

NEW YORK-BUFFALO,
STATE UNIVERSITY OF
BONNER HALL, ROOM 312
BUFFALO, NY 14260
ATTN: R DOLLINGER

DISTRIBUTION LIST

OTHER GOVERNMENT

OTHER GOVERNMENT

CENTRAL INTELLIGENCE AGENCY
WASHINGTON, DC 20505
ATTN: OSWR, J PINA

NATIONAL AERONAUTICS AND
SPACE ADMINISTRATION
LANGELY RESEARCH CENTER
HAMPTON, VA 23681-0001
ATTN: MS-493 J LEE

NATIONAL INSTITUTE OF STANDARDS AND
TECHNOLOGY
PHYSICS BLDG., RM B157
GAITHERSBURG, MD 20899
ATTN: R HEBNER, BLDG 220, 8344